
Neutrinos in Core-Collapse Supernova Nucleosynthesis

Neutrinos in der Kernkollaps Supernova Nucleosynthese

Zur Erlangung des Grades eines Doktors der Naturwissenschaften (Dr. rer. nat.)

genehmigte Dissertation von Andre Sieverding aus Heppenheim

Tag der Einreichung: 15.05.2018 , Tag der Prüfung: 11.06.2018

Darmstadt 2018 – D 17

1. Gutachten: Prof. Dr. Gabriel Martínez-Pinedo
2. Gutachten: Prof. Dr. Karlheinz Langanke



TECHNISCHE
UNIVERSITÄT
DARMSTADT

Fachbereich Physik
Institut für Kernphysik
Theoretical Nuclear Astrophysics

Neutrinos in Core-Collapse Supernova Nucleosynthesis
Neutrinos in der Kernkollaps Supernova Nukleosynthese

Genehmigte Dissertation von Andre Sieverding aus Heppenheim

1. Gutachten: Prof. Dr. Gabriel Martínez-Pinedo
2. Gutachten: Prof. Dr. Karlheinz Langanke

Tag der Einreichung: 15.05.2018

Tag der Prüfung: 11.06.2018

Darmstadt 2018 – D 17

Bitte zitieren Sie dieses Dokument als:

URN: [urn:nbn:de:tuda-tuprints-75742](https://nbn-resolving.org/urn:nbn:de:tuda-tuprints-75742)

URL: <http://tuprints.ulb.tu-darmstadt.de/7574>

Dieses Dokument wird bereitgestellt von tuprints,
E-Publishing-Service der TU Darmstadt
<http://tuprints.ulb.tu-darmstadt.de>
tuprints@ulb.tu-darmstadt.de



Die Veröffentlichung steht unter folgender Creative Commons Lizenz:
Namensnennung – Weitergabe unter gleichen Bedingungen 4.0 International
<https://creativecommons.org/licenses/by-sa/4.0/>

*In loving memory of my father,
Franz Sieverding*



Abstract

The environment of supernova explosions is dominated like no other known scenario by neutrinos. In addition to their crucial role for initiating the explosion itself, neutrinos have an important impact on the production of chemical elements in supernovae. An extensive set of improved neutrino-induced reaction cross-sections is compiled, covering almost the whole nuclear chart. The majority of the cross-sections are calculated based on Random Phase Approximation (RPA) with single- and multi-particle evaporation channels based on statistical model codes. Individual cross-sections that are of particular importance, are derived from experimental data or dedicated shell model calculations, while previous results from the literature were also included.

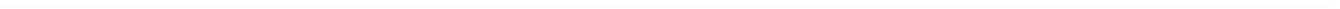
With these cross-sections the ν process accompanying the explosive nucleosynthesis is studied with a one-dimensional supernova model based on progenitors of solar metallicity with initial main sequence masses between 13 and 30 M_{\odot} . Modern supernova simulations find that neutrinos are less energetic than what was assumed in previous studies of the ν process. Using average neutrino energies compatible with modern simulations we investigate the production of ${}^7\text{Li}$, ${}^{11}\text{B}$, ${}^{19}\text{F}$, ${}^{138}\text{La}$ and ${}^{180}\text{Ta}$ and find reduced yields compared to previous studies assuming higher neutrino energies. As a result the yields of ${}^{11}\text{B}$, ${}^{138}\text{La}$ and ${}^{180}\text{Ta}$ are in agreement with their solar abundances, when contributions from other sources are to be taken into account. Implementing a set of neutrino-nucleus cross-sections that is complete in the sense that it includes reactions on all nuclei that are included in the nucleosynthesis calculations, allows to get an overview of the whole extend of process. As a results we can conclude that effects on stable nuclei that have not been discussed previously in the literature are limited to the order of 10%. Dependencies on stellar structure aspects are discussed in detail for the most relevant cases.

We also explore the impact of ν -nucleosynthesis on the production of the long-lived radioactive isotopes ${}^{22}\text{Na}$, ${}^{26}\text{Al}$ and ${}^{36}\text{Cl}$. We find that the yield of ${}^{26}\text{Al}$ is increased by a factor of 1.4 and ${}^{22}\text{Na}$ is found to be efficiently produced in the Carbon-rich zones of some progenitors, providing a possible explanation for radiogenic ${}^{22}\text{Ne}$ found in meteorites. Additionally, the reaction flows relevant for the production of the (very) long-lived isotopes ${}^{92}\text{Nb}$, ${}^{98}\text{Tc}$, ${}^{138}\text{La}$ and ${}^{180}\text{Ta}$ are studied. We find significant contributions of the ν -process to the production of these nuclei, in agreement previous calculations and estimates.

Furthermore, we show the importance of going beyond the standard description of supernova neutrino properties for nucleosynthesis by including the predictions of the neutrino signal from a sophisticated supernova simulation. This shows that the definition of an appropriately averaged neutrino temperature is difficult and underestimates the efficiency of the ν process because elevated neutrino energies for short periods of time are not appropriately captured. We also identify effects of the dynamics that have only minor consequences for the nucleosynthesis.

For the first time the ν process in the innermost supernova ejecta is addressed by using thermodynamic tracers from a two-dimensional supernova simulation. We conclude that the contribution of the α -rich freeze out to the production of the light elements B and Li is negligible in this model. However, we can confirm a substantial production of ${}^{138}\text{La}$ and ${}^{180}\text{Ta}$ in a self-consistent model.

To investigate the production of ${}^{92}\text{Nb}$ we also include its production in the νp process in the neutrino driven winds ejected from the hot proto-neutron star, including the effects of recently measured nuclear masses. We find that the production is also significantly affected by neutrino spallation reactions, in particular on ${}^4\text{He}$. With the contribution we find a ${}^{92}\text{Nb}/{}^{93}\text{Nb}$ ratio that is compatible with values found in primitive meteorites. Finally, an overview of the combined contribution of supernovae to the production of the elusive p nuclei is given.



Zusammenfassung

Supernova Explosionen sind wie kein anderes Szenario von Neutrinos bestimmt. Sie sind nur entscheidend für die Einleitung der Explosion selbst, sondern haben auch einen wichtigen Einfluss auf die Produktion chemischer Elemente in Supernovae. Ein umfangreicher Satz von Wirkungsquerschnitten für Neutrino-induzierte Reaktionen wurde zusammengestellt, der nun fast die ganze Nuklidkarte abdeckt. Die meisten davon wurden basierend auf der Random Phase Approximation (RPA) berechnet und kombiniert mit Evaporationskanälen für einzelne oder mehrere Teilchen mit Hilfe des Statistischen Modells. Einzelne Wirkungsquerschnitte die von besonderer Bedeutung sind, wurden von experimentellen Daten hergeleitet oder nutzen die Ergebnisse von Schalenmodellrechnungen, während andere von früheren Ergebnissen aus der Literatur übernommen wurden. Mit diesen Wirkungsquerschnitten wurde der ν -Prozess, der die explosive Nukleosynthese begleitet, mit eindimensionalen Supernovamodellen basierend auf Vorgängersternen von solarer Metalizität und anfänglichen Hauptreihenmassen zwischen 13 und 30 M_{\odot} untersucht. Moderne Supernova Simulationen zeigen, dass Neutrinos weniger Energie tragen als in vorherigen Studien zum ν Prozess angenommen wurde. Mit mittleren Neutrino Energien die kompatibel mit modernen Simulationen sind, untersuchen wir die Produktion von ${}^7\text{Li}$, ${}^{11}\text{B}$, ${}^{19}\text{F}$, ${}^{138}\text{La}$ und ${}^{180}\text{Ta}$, und finden einen reduzierten Beitrag im Vergleich zu vorherigen Studien, die von höheren Energien ausgingen. Dadurch ist die Produktion von ${}^{11}\text{B}$, ${}^{138}\text{La}$ und ${}^{180}\text{Ta}$ nun in Übereinstimmung mit den solaren Häufigkeiten, wenn man Beiträge von anderen Quellen berücksichtigt. Die Implementierung eines Satzes von Neutrino Reaktionen der vollständig ist, insofern dass Reaktionen an allen Kernen die in der Nukleosynthese Rechnung berücksichtigt werden, gibt einen Überblick über alle möglichen Effekte ohne von vornherein auf eine bestimmte Spezies zu konzentrieren. Außerdem erscheint es notwendig zu sein, einen solchen, vollständigen Ansatz zu wählen, um das ganze Spektrum von sekundären Effekten zu erfassen, d.h Nukleosynthese durch Teilchen die von Neutrino-induzierten Reaktionen erst erzeugt werden.

Mit diesem, nun vollständigen Satz von Reaktionen können wir feststellen, dass die Auswirkung auf stabile Kernen, die bisher noch nicht in der Literatur diskutiert wurden, auf die Größenordnung von 10% beschränkt sind. Die Abhängigkeiten von der stellaren Struktur werden für die wichtigsten Fälle im Detail diskutiert.

Der Einfluss der Neutrino-induzierten Nukleosynthese auf die Produktion von den langlebigen radioaktiven Isotopen ${}^{22}\text{Na}$, ${}^{26}\text{Al}$ und ${}^{36}\text{Cl}$ wird betrachtet. Die produzierte Masse an ${}^{26}\text{Al}$ erhöht sich durch die Neutrinos um einen Faktor von höchstens 1.4 und ${}^{22}\text{Na}$ wird in Kohlenstoffreichen Zonen einiger Sternmodelle sehr effektiv produziert, wodurch sich eine mögliche Erklärung für radiogenes ${}^{22}\text{Ne}$ in Meteoriten ergibt. Das Verhältniss ${}^{36}\text{Cl}/{}^{35}\text{Cl}$ wie es in primordialen Meteoriten gefunden wird lässt sich ebenfalls mit den Ergebnissen erklären. Außerdem werden die Reaktionsflüsse, die zu Nukleosynthese der (sehr) langlebigen Isotope ${}^{92}\text{Nb}$, ${}^{98}\text{Tc}$, ${}^{138}\text{La}$ und ${}^{180}\text{Ta}$ beitragen genau untersucht. Der ν Prozess alleine liefert keinen ausreichenden Beitrag um das Verhältniss ${}^{92}\text{Nb}/{}^{93}\text{Nb}$ wie es in primordialen Meteoriten gefunden wird, zu erklären.

Weiterhin wird gezeigt, dass es wichtig ist, über die einfache Standardbeschreibung der Eigenschaften von Supernovaneutrinos hinauszugehen, indem die Vorhersagen einer Simulation für das Neutrino Signal verwendet werden. Dies zeigt, dass die sich Festlegung einer angemessenen mittleren Neutrino Energie problematisch ist und die Effektivität des ν Prozesses unterschätzt, da die Effekte von kurzzeitig erhöhten Energien durch einen gemittelten Wert nicht ausreichend repräsentiert werden können. Effekte der Dynamik des Neutrino signals auf die Nukleosynthese werden identifiziert, zeigen allerdings keinen signifikanten Einfluss auf die integrierte Nukleosynthese.

Zum ersten Mal wird zudem der ν Prozess in den innersten Bereichen des Supernova Auswurfs be-

trachtet, indem die Nukleosynthese für thermodynamische Tracer einer selbstkonsistenten zweidimensionalen Supernova Simulation berechnet wird. Es zeigt sich, dass in diesem Model der Beitrag des α -reichen Ausfrierens auf die Produktion der leichten Elemente B und Li vernachlässigbar ist. Allerdings wird die Produktion von einem substantielles Maß an ^{138}La and ^{180}Ta nun basierend auf einem selbstkonsistenten Model bestätigt.

Zur genaueren Untersuchung der Produktion von ^{92}Nb berechnen wir ebenfalls den νp Prozess in Neutrinogetriebenen Winden unter Berücksichtigung vor Kurzem experimentel bestimmter Kernmassen. Eine signifikante Menge von ^{92}Nb kann produziert werden, die auch sensitiv zu Neutrino-induzierten Spallationsreaktionen, insbesondere an ^4He , ist. Mit dem Beitrag des Neutrinogetriebenen Windes zur integrierten Nukleosynthese, lässt sich das Verhältniss $^{92}\text{Nb}/^{93}\text{Nb}$ gemessen in primordialen Meteoriten erklären. Abschließend wid ein Überblick über den kombinierten Beitrag von Supernovae zur Produktion der p -Nuklide gegeben.

Contents

1. Motivation - The Quest for rare isotopes	1
2. Nuclear Theory for Astrophysics	5
2.1. Nuclear reaction rates	5
2.1.1. Particle induced reactions	5
2.1.2. Statistical model	9
2.1.3. Detailed balance and inverse reaction rates	10
2.1.4. Nuclear reaction network	12
2.1.5. Equilibria, NSE and alpha-rich freeze out	17
2.2. Neutrino interactions in the standard model	19
2.3. Nuclear structure: RPA	22
3. Astrophysical considerations	25
3.1. Principles of stellar evolution	25
3.2. Massive star evolution	27
3.2.1. Initial Mass Function (IMF)	31
3.3. Supernova Explosions	32
3.3.1. Core collapse	32
3.3.2. The neutrino driven explosion mechanism	34
3.3.3. Explosive nucleosynthesis	37
3.4. Nucleosynthesis of heavy elements	39
3.4.1. Neutron capture processes	39
3.4.2. The γ -process	40
3.4.3. The νp -process in neutrino driven winds	41
4. Methods	43
4.1. A simple explosion model	43
4.2. Neutrino signal	44
4.3. KEPLER hydrodynamics code	46
4.4. Piston model	46
4.5. Post-processing and comparison	49
5. The ν process in the light of an improved understand of neutrino spectra	51
5.1. Neutrino-nucleus cross-sections	51
5.2. Stable isotopes	58
5.2.1. The light elements Li and B	61
5.2.2. ^{13}C	67
5.2.3. ^{15}N , and ^{19}F	68
5.2.4. Long-lived ^{138}La and nature's rarest element ^{180}Ta	71
5.2.5. Further effects on stable isotopes	76
5.3. Radioactive nuclei	78
5.3.1. Overview	80
5.3.2. Short-lived radionuclides ^{36}Cl , ^{92}Nb and ^{98}Tc in the late input scenario	82
5.3.3. γ -ray sources ^{22}Na and ^{26}Al	87

5.4. Time dependent neutrino properties	93
5.4.1. Neutrino properties from simulation data	93
5.5. Innermost ejecta and NSE	103
6. The ν process with tracer particles of a two-dimensional supernova simulation	105
6.1. The simulation data and classification of tracer particles	106
6.2. Extrapolation of the simulation data	108
6.3. Nucleosynthesis results	111
7. The νp process in neutrino driven winds	115
7.1. Impact of new experimental masses for neutron deficient Zr, Y and Nb isotopes	118
7.2. Production of ^{92}Nb	122
7.3. Combined nucleosynthesis	126
8. Conclusions and outlook	129
Appendices	131
A. REACLIB reaction rates	133
B. Galactic cosmic ray contribution	135

1 Motivation - The Quest for rare isotopes

When we look at the abundances of different elements and their isotopes in our solar system as shown in Figure 1.1, we are able to discern patterns, that can be attributed to different processes and sites that contribute to the chemical enrichment of the universe. The abundance patterns we observe are the fingerprint of the whole history of nucleosynthesis and allow us to construct a large-scale picture of the past and to gain an understanding of the processes that determine the chemical composition of the universe. Despite significant achievements in the last decades, many aspects of how to explain the chemical evolution of our galaxy are still uncertain.

Nuclear processes in stars are the main drivers of chemical evolution (Côté et al., 2016; Timmes et al., 1995b; Arnett, 1971). Stars form, evolve and die, ejecting in many cases a large amount of chemically enriched material, from which in turn the next generation of stars is formed. Ever since nuclear processes in stars and stellar explosions have been understood as the origin of the isotopic composition of the universe and the solar system, the goal of nuclear astrophysics has been to understand the main features of observed abundance patterns from first principles and to pin down the astrophysical sites for the production of different parts of the overall abundance pattern. The main processes have in principle been identified by Burbidge et al. (1957) and Cameron (1957). Fusion reactions in stars can explain the abundances of isotopes up to Iron, where only the more massive ones ($\gtrsim 10 M_{\odot}$) really complete all the nuclear burning processes of Hydrogen-, Helium-, Carbon-, Neon- and finally Oxygen- and Silicon burning and form an Iron core (Rauscher et al., 2002; Woosley et al., 2002; Woosley & Weaver, 1995). A massive star is expected to exhibit at the end of its life a typical compositional onion-shell structure that is indicated schematically in Figure 1.2.

Once Iron has been formed, nuclear processes cease, because fusion reactions no longer lead to a gain of energy. The stellar core is bound to collapse and threatens to lock up the important nucleosynthesis products in a compact remnant. Core-collapse-supernovae are therefore very important as mechanism to allow the products of stellar nucleosynthesis to be ejected and mixed into the interstellar medium (Arnett, 1969).

While the necessity of core-collapse supernova explosions is evident, both from direct astronomical observations as well as from nucleosynthesis arguments, the mechanism that enables the explosion has proven to be as elusive as the particles that are most likely to be responsible. In our current understanding, that follows what has been laid out by Bethe et al. (1979), neutrinos are the key to the supernova explosion mechanism. Emitted due to a variety of processes from the hot and dense interior of the core, they transfer a small fraction of the gravitational binding energy of the compact remnant to the supernova shock to allow it to push through the outer Fe core of a massive star (Janka et al., 2003; Janka, 2012; Müller, 2016). Since this scenario is shaped like no other by the interactions of these particles, it should not come as a surprise that they also affect the final

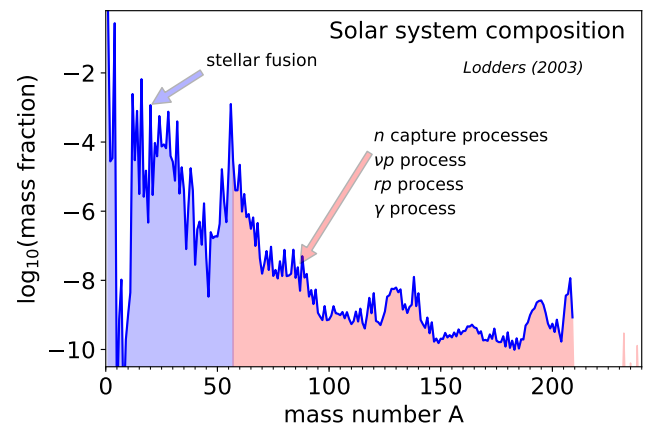


Figure 1.1.: Solar abundances from reference Lodders (2003), based on combination of photospheric data and isotopic abundances from carbonaceous chondritic meteorites.

composition of supernova ejecta. Domogatsky & Nadyozhin (1977) were the first to suggest that neutrino-induced reactions in the stellar mantle, either via the charged current (inverse β -decay) or via inelastic neutral current scattering, as illustrated schematically in Figure 1.3, could produce some of the rarest isotopes found in the solar system (Domogatsky & Nadyozhin, 1977). This idea was at first met with strong skepticism (Woosley, 1977) because neutrinos interact exclusively via the weak interaction and as the name of the interaction implies the probability for such interactions is small.

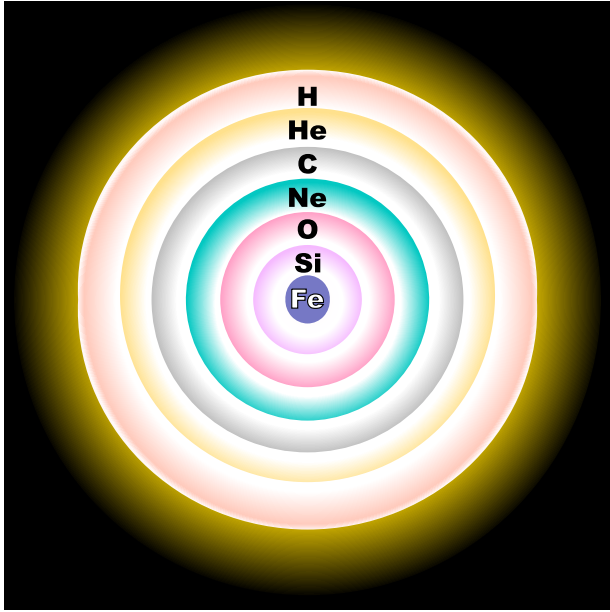


Figure 1.2.: Schematic compositional layers of a massive star at the end of its life [image credit: R. J. Hall].

Neutrino cross-sections on nuclei are typically of the order of 10^{-42} cm² and would thus be expected to be negligible in a hot explosive environment. However, just because of this low interaction cross-sections, neutrinos can carry the high energies that they acquire in the very dense and hot interior of the core all the way out into the mantle. Only the enormous numbers of neutrinos $\sim 10^{58}$ expected from a core-collapse allow for noticeable effects. The exploration of these effects was at first driven by the search for the astrophysical site for the production of heavy elements. The solar abundances decline at first very quickly with increasing atomic number reflecting the characteristics of the increasing Coulomb barrier for charged particle reactions. The abundance pattern for heavier elements is more flat hinting at neutron captures processes. For a long time it was unclear whether the very neutron rich conditions required to produce the heaviest elements can be achieved by any astrophysical scenario (Qian & Wasserburg, 2007). This has led Epstein et al. (1988) to investigate the neutrino reaction ${}^4\text{He} + \nu \rightarrow {}^3\text{He} + n$ in the He-shells of massive stars as a source of neutrons. Even though this process has turned out not to be the most important site for the rapid neutron capture process - in short r -process - to occur, it has been found to provide important contributions to rare isotopes that cannot be produced otherwise. Following a decade of order-of-magnitude estimates Woosley et al. (1990) included a wide range of reactions of the type depicted in Figure 1.3 in a nuclear reaction network calculation and coined the term ν process for the effects of neutrino-induced reactions on the composition in the stellar mantle during a supernova explosion. While proving on the one hand, that this is not the site of the r -process, they found that the ν -process contributes significantly to the production of some rare elements, especially ${}^7\text{Li}$ and ${}^{11}\text{B}$. They also found localized enhancements of ${}^{15}\text{N}$, ${}^{19}\text{F}$, ${}^{22}\text{Na}$ and ${}^{26}\text{Al}$, as well as a significant production of ${}^{138}\text{La}$ and ${}^{180}\text{Ta}$. Estimates for the neutrino properties at that time were based on the very first supernova simulations that predicted much more energetic neutrinos than modern studies. Several studies of the ν process have followed, employing mostly the same scheme and focused on individual reactions with a limited scope with respect to the range of stellar models (Kolbe et al., 1992; Heger et al., 2005; Byelikov et al., 2007; Cheoun et al., 2010, 2012). Interest in this process has also been revived by the discovery of neutrino oscillations in astrophysical scenarios (Yoshida et al., 2006; Wu et al., 2015) While the effects of flavor oscillations remain controversial (Väänänen & McLaughlin, 2016; Wu et al., 2016; Duan et al., 2010) and are neglected also in this work, supernova neutrino properties are increasingly well understood with a growing number of self-consistent simulations of successful supernova explosions and a wide range of supernova progenitor models that are available. This motivates the aim of this thesis to provide an updated view of the ν process, including both, improvements on the neutrino reaction cross-

Neutrino cross-sections on nuclei are typically of the order of 10^{-42} cm² and would thus be expected to be negligible in a hot explosive environment. However, just because of this low interaction cross-sections, neutrinos can carry the high energies that they acquire in the very dense and hot interior of the core all the way out into the mantle. Only the enormous numbers of neutrinos $\sim 10^{58}$ expected from a core-collapse allow for noticeable effects. The exploration of these effects was at first driven by the search for the astrophysical site for the production of heavy elements. The solar abundances decline at first very quickly with increasing atomic number reflecting the characteristics of the increasing Coulomb barrier for charged particle reactions. The abundance pattern for heavier elements is more flat hinting at neutron captures processes. For a long time it was unclear whether the very neutron rich conditions required to produce the heaviest elements can be achieved by any astrophysical scenario (Qian & Wasserburg, 2007). This has led Epstein et al. (1988) to investigate the neutrino reaction ${}^4\text{He} + \nu \rightarrow {}^3\text{He} + n$

sections and a better understanding of supernova neutrino properties. While the impact of the ν process on stable isotopes is limited to contributions to a few rare species, a wide range of radioactive nuclei are affected. Among those are ^{22}Na , ^{26}Al , ^{36}Cl and ^{92}Nb , that lead to observable signatures either via the observation of γ -rays associated to the decay (Diehl et al., 2006; Woosley et al., 1989) or anomalies in the composition of primitive meteorites (Banerjee et al., 2016; Wasserburg et al., 2006; Zinner, 1998). With the results from modern simulations that model the emission and propagation in great detail, it is now also possible to address the question whether the simplified model for the neutrino properties with constant spectral temperatures, that has been commonly applied in the literature, is valid in the first place. Furthermore, multi-dimensional fluid flows have been found to be crucial for successful supernova explosions and multi-dimensional simulations are the only way to properly model the dynamics of the innermost supernova ejecta. While Woosley (1977) has rightfully argued, that neutrinos cannot produce fragile elements in regions where temperatures are high, multi-dimensional fluid flows allow the material that is closest to the proto-neutron star to be ejected very fast and cool down before the neutrino emission has ceased. The ν process has never before been studied in the context of multi-dimensional simulations, even though it was already suggested by Nagataki et al. (1997) that neutrinos could have an effect on material that undergoes an α -rich freeze-out. We explore these effects here by calculating the nucleosynthesis for thermodynamic histories of tracer particles from a self-consistent two-dimensional supernova simulation (Bruenn et al., 2016).

Due to the elusive nature of neutrinos, the effects of the ν process in regions at a large distance from the stellar core are bound to be subtle and on the very edge of being observable. At the surface of the proto-neutron star – the forming remnant of the supernova explosion – neutrinos dominate the dynamics and can drive a supersonic outflow, a wind (Duncan et al., 1986; Arcones et al., 2007), for which neutrino interactions play a major role. The neutrino driven wind is a promising scenario of the νp process – the neutrino-induced rp process (Fröhlich et al., 2006) – in which a sequence of proton captures can bypass waiting points with the help of neutrons from $\bar{\nu}_e + p$ reactions. This allows to create heavier elements than in the regular rp process (Schatz et al., 2001), in particular several of the elusive p -nuclei (Wanajo et al., 2011; Bliss et al., 2018). While $\bar{\nu}_e + p$ is the most important reaction in this scenario, other neutrino-induced reactions, in particular on ^4He cannot be ignored. While the details of the neutrino driven wind are highly model dependent, it is important to explain the solar abundance of several p -nuclei (Travaglio et al., 2018).

The present thesis is organized as follows. In chapter 2 an overview of the most important ingredients from nuclear physics that enter into the calculation of nuclear reaction rates is given. This includes in particular and outline of the statistical model in Section 2.1.2, that is the basis for many of cross-sections regularly used for nucleosynthesis calculations and an extended discussion on neutrino-induced reactions in Section 2.2. The neutrino cross-sections that were used are based on the modeling of nuclear properties within the framework of the random phase approximation (RPA) that is summarized in Section 2.3. In chapter 3 the astrophysical background is discussed. We put special emphasis on the evolution and nucleosynthesis of massive stars in Section 3.2 and discuss the supernova explosion mechanism in 3.3.2. Sections 3.3.3 and 3.4 give an overview over the nucleosynthesis in supernovae and other processes. Following a description of the methods used to model the astrophysical conditions in Chapter 4, the improvements of the neutrino-nucleus cross-sections are discussed 5.1. With

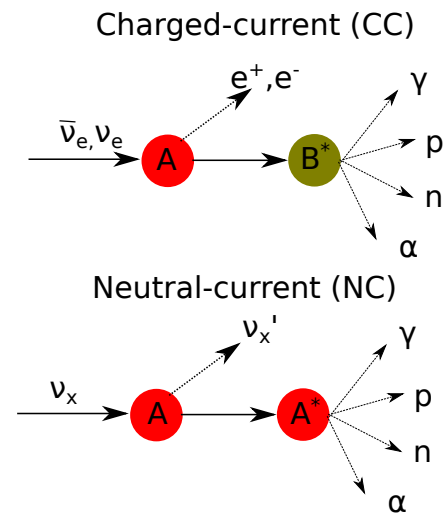


Figure 1.3.: Types of neutrino-induced reactions that affect the production of elements.

this background we present the nucleosynthesis result in Chapter 5.2 focusing on the nuclei that are affected by the ν process the most. Following a discussion of the stable isotopes that are relevant for the composition of the solar system today, the impact on radioactive nuclei is discussed with special attention to those that have clear observable signatures. In Sections 5.4 and 6 the ν process is discussed in models that go beyond the current standard treatment - first by including the neutrino properties from a modern supernova simulation and also in post-processing tracer particles from a self-consistent two-dimensional supernova simulation. To complete the picture of the role of neutrinos for supernova nucleosynthesis, Chapter 7 presents the results for the νp process in the neutrino driven wind. Combining these results the role of core-collapse supernovae and in particular of neutrinos for the production of the p -nuclei is can be discussed in the context of current research.

2 Nuclear Theory for Astrophysics

In this section we first provide an overview over the part of nuclear theory that enters in calculating the nuclear reaction rates from basic nuclear properties. This is particularly important when we want to compare the uncertainties due to unknown neutrino properties in the ν process to the uncertainties due to nuclear reaction rates. In Section 2.2 we also introduce the framework in which the neutrino interaction cross-sections have been calculated. This involves first of all the general features of our current understanding of the weak interaction and the nuclear structure model, the Random Phase Approximation (RPA), that is used to calculate the nuclear properties that enter in the calculation of the cross-sections.

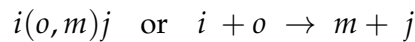
2.1 Nuclear reaction rates

The dynamic modeling of nucleosynthesis processes requires thousands of temperature dependent nuclear reaction cross-sections as input. Those are taken from libraries that have been evaluated and compiled over the last decades and keep on being updated in step with experimental efforts for ever more precise determinations of nuclear reaction rates, which is in turn motivated not only by the investigation of the structure of nuclei itself, but today also by the prospect to answer fundamental questions about the origin of matter and the elements.

In this section we give an overview about the information that is necessary from nuclear physics for the calculation of astrophysical reactions rates and how those are defined in the first place. The discussion in this Section is mostly based on [Cowan et al. \(in prep.\)](#) and [Iliadis \(2007\)](#).

2.1.1 Particle induced reactions

The central quantity to describe the likelihood of a nuclear reaction between isotopes i and o producing nuclei m and j , denoted as



is the reaction cross-section defined as

$$\sigma = \frac{\text{number of reactions per target per second}}{\text{flux of incoming projectiles}} = \frac{r/n_i}{n_o v}$$

where the second equality defines the reaction rate r as reactions per second and volume for a number density n_i of targets and n_o of projectiles moving with constant relative velocity v . The cross-section has the units of an area and can be thought of as the effective target surface which a projectile needs to hit for a reaction to occur. Reaction cross sections can be measured directly in experiments with well defined target and projectile properties and known kinematics in accelerator facilities.

In a stellar plasma the velocities of non-relativistic particles with number density n nucleons and ions are not constant but follow a Maxwell-Boltzmann distribution. The fraction of particles with mass m with velocities between $v = |\vec{v}|$ and $|\vec{v} + d\vec{v}|$ in an ensemble with temperature T is then

$$\frac{dn}{n} = \frac{1}{(2\pi m k_B T)^{3/2}} \exp\left(-\frac{m v^2}{2 k_B T}\right) d^3 v, \quad (2.1)$$

where k_B is the Boltzmann constant. In order to calculate the rate of reactions we need to average over the distribution for targets and projectiles. We define the velocity averaged cross-section as (Longland et al., 2010)

$$\langle \sigma v \rangle_{io} = \int \sigma(|\vec{v}_i - \vec{v}_o|) |\vec{v}_i - \vec{v}_o| \frac{dn_i}{n_i} \frac{dn_o}{n_j}. \quad (2.2)$$

With equation (2.1) and assuming that the reactants are non-relativistic we can write Equation (2.2) as an integral over the center of mass energy E

$$\langle \sigma v \rangle_{io} = \frac{1}{N_A} \frac{3.7318 \times 10^{10}}{T_9^{3/2}} \sqrt{\frac{m_i + m_o}{m_i m_o}} \int E \sigma(E) e^{-11.605E/T_9} dE, \quad (2.3)$$

where N_A is Avogadro's number and E is the energy in the center of mass system in MeV. T_9 is the temperature of the stellar plasma in GK. With $\langle \sigma v \rangle$ the reaction rate r for non-identical particles ($i \neq o$) per volume can be expressed conveniently as

$$r = \frac{1}{1 + \delta_{io}} n_i n_o \langle \sigma v \rangle_{io}. \quad (2.4)$$

Values for $\langle \sigma v \rangle$ are important ingredients for nuclear reaction network calculations discussed in Section 2.1.4. Since $\langle \sigma v \rangle$ can always be calculated for a given cross-section and temperature, the term "cross section" will be often used synonymous to $\langle \sigma v \rangle$ here.

The cross-section for the process of capturing a particle can be related to the transmission coefficients $T(E, J, \Pi)$ depending on angular momentum J and parity Π .

$$\sigma = \frac{\pi}{k_o^2} \frac{1 + \delta_{io}}{(2I_i + 1)(2I_o + 1)} \sum_{J, \Pi} (2J + 1) T(E, J, \Pi) \quad (2.5)$$

The transmission coefficients describe the probability of the incoming particle to be capture by the potential of the target and can be found by solving the quantum mechanical scattering problem with an appropriately chosen potential (c.f. Krane (1988) or other textbooks).

This does not yet consider the subsequent decay of reaction product that is typically produced in an excited state.

We can use Equation (2.5) to estimate the cross-section for neutron capture. In this case we do not require the projectile to overcome the Coulomb barrier and the transmission coefficient for direct s-wave ($l = 0$) capture with a neutron energy E goes as $T_0 \propto 1/\sqrt{E}$ for mean field potential that $V_0 \gg E$. Form equation (2.5) we then get

$$\sigma \propto \frac{1}{\sqrt{E}} = \frac{1}{v}. \quad (2.6)$$

From this we immediately see that $\langle \sigma v \rangle$ for neutron capture should be relatively independent of the particle velocity, and thus of the plasma temperature.

For charged particle interactions the Coulomb potential needs to be taken into account. In a classical approach, a particle with energy E can never enter a region where $E < V(x)$. In the classical picture, the particle will be reflected at the classical turning point x_{turn} defined by $V(x_{turn}) = E$. However, in quantum mechanics there is a probability for tunneling through the barrier. This allows charged

particles to penetrate a nucleus despite the Coulomb repulsion even with a low energy. The tunneling probability through the Coulomb barrier depends exponentially on the Sommerfeld parameter

$$\eta = \sqrt{\frac{m_{\text{red}}}{2E}} \frac{Z_i Z_j e^2}{\hbar}$$

where m_{red} is the reduced mass of target and projectile and E is the center of mass energy. The cross-section for s-wave capture, i.e. orbital angular momentum $\ell = 0$, is

$$\sigma_{\ell=0} = \frac{\hbar^2 \pi}{2m_{\text{red}} E} e^{-2\pi\eta} \quad (2.7)$$

Due to the exponential dependence of the direct process on the energy, the value of a cross-section can range over many orders of magnitude. Therefore, it is convenient to look at the astrophysical S-factor defined as

$$S(E) = \sigma E e^{2\pi\eta} \quad (2.8)$$

which then exhibits a more moderate sensitivity to the energy for non-resonant reactions. In experiment, resonances and higher order effects will appear on top of the direct channel. Inserting Equation (2.8) in (2.3) gives

$$\langle \sigma v \rangle \propto \int S(E) e^{-\frac{E}{k_B T}} e^{-2\pi\eta}. \quad (2.9)$$

In the absence of resonances $S(E)$ is a smooth function and since $\eta \propto E^{-1/2}$ we see that the integrand contains the product of an exponential that increases with energy and one that decreases with energy. At a low energy the reaction is suppressed by the low tunneling probability. At a high energy a larger tunneling probability is compensated by the low probability to actually find a particle with that energy in a Boltzmann distribution. Assuming that the S-factor does not vary a lot for that energy range, the integrand exhibits a distinct peak that defines the energy at which the reaction is the most efficient. This is called the Gamow peak and it is a very useful clue for experiments to decide at which particle energy to measure a reaction cross-section for the application in an astrophysical scenario.

So far we have only described the capture of the projectile in the mean field potential of the target, i.e. a direct capture to the ground state. This is the non-resonant or also called direct capture which is mostly relevant for light nuclei when there are no suitable resonances available. However, the cross-section is often mostly dominated by resonances with particular nuclear states. A resonance of a state n with total angular momentum J at energy E_n is characterized by its total width Γ_n which is in turn the sum of all the partial widths $\Gamma_n = \sum_i \Gamma_{i,n}$ that correspond to different channels for the population and decay of the state n . For example, the decay by emission of photon is called the radiative width $\Gamma_{\gamma,n}$ or gamma-strength function. The width of a state is related to its lifetime by Heisenberg's uncertainty relation as $\tau = \hbar/\Gamma$. The cross-section of a resonant reaction of the form $i(o, m)j$ via a set of resonances n can be expressed by the one-level Breit-Wigner formula as a Lorentzian

$$\sigma_{BW}(E) = \frac{\pi}{k_o^2} \frac{1 + \delta_{io}}{(2J_i + 1)(2J_o + 1)} \sum_n (2J_n + 1) \frac{\Gamma_{o,n} \Gamma_{m,n}}{(E - E_n)^2 + (\Gamma_n/2)^2}, \quad (2.10)$$

where k_o is the momentum of the projectile o , δ_{io} is the Kronecker delta to account for identical particles and $J_{i,o}$ are the total angular momenta of the target and projectile. At low energies the cross-section can

be dominated by individual isolated resonances. For a sufficiently narrow resonance the Boltzmann factor is approximately constant over the width of the resonance and the rate can be expressed as

$$N_A \langle \sigma v \rangle = \frac{1.5399 \times 10^{11}}{T_9^{3/2}} \left(\frac{m_i + m_o}{m_i m_o} \right)^{3/2} \sum_n (\omega \gamma)_n e^{-11.605 E_n / T_9}, \quad (2.11)$$

with the resonance strength $\omega \gamma$ that is defined as

$$\omega \gamma = \frac{2J + 1}{(2J_i + 1)(2J_o + 1)} \frac{\Gamma_o \Gamma_m}{\Gamma}. \quad (2.12)$$

For such a narrow resonance the resonance strength can be measured directly. The experimental determination of the partial widths is important to calculate reaction rates accurately. If not all partial widths are experimentally known, they can be taken from theory and phenomenological models. At high energies and for heavier nuclei a large number of resonances usually contributes and they start to overlap. Hence, instead of considering individual levels, we can think in terms of average widths $\langle \Gamma \rangle$ that can be identified with the transmission coefficient as

$$T_j(E, J, \pi) = 2\pi \rho(E, J, \pi) \langle \Gamma_j(E, J, \pi) \rangle, \quad (2.13)$$

with the average level density $\rho(E, J, \pi)$.

2.1.2 Statistical model

The nucleus that forms after the capture of a projectile with energy E will gain an energy of $E + Q$, where $Q = B_j - B_i$ is the reaction Q -value that is the difference of the nuclear binding energies of the target i and product j . In the compound nucleus model which forms the basis for the statistical Hauser-Feshbach model, this energy is immediately distributed among the nucleons and we have a compound state J^π with energy $E_C = E + Q$. If the equilibration of the compound system is much faster than its lifetime, the state is completely independent of the process by which it was formed. Starting from equation (2.10) we can then take the average over many resonances and exchange multiplication of strengths with taking the average. Using relation (2.13) we then end up with the Hauser-Feshbach formula for a reaction of nucleus i in state μ producing state ν in nucleus j (i.e. a reaction of the form $i^\mu(o, m)j^\nu$). Effectively, we multiply the transmission coefficients for absorption on the target $T_o^\mu(E_C, J, \pi, E_i^\mu, J_i^\mu, \pi_i^\mu)$ and emission of the product $T_m^\nu(E_C, J, \pi, E_j^\nu, J_j^\nu, \pi_j^\nu)$ and normalize to the sum of all channels involving this compound state

$$T_{tot}(E_C, J, \pi) = \sum_{i,\mu} T_i^\mu(E_C, J, \pi, E_i^\mu, J_i^\mu, \pi_i^\mu) \quad (2.14)$$

The Hauser-Feshbach formula reads

$$\sigma^{\mu,\nu} = \frac{\pi \hbar^2 / (2\mu_{io} E_{io})}{(2J_i^\mu + 1)(2J_o + 1)} \sum_{J,\pi} (2J + 1) \frac{T_o^\mu(E_C, J, \pi, E_i^\mu, J_i^\mu, \pi_i^\mu) T_m^\nu(E_C, J, \pi, E_j^\nu, J_j^\nu, \pi_j^\nu)}{T_{tot}(E_C, J, \pi)}. \quad (2.15)$$

In laboratory experiments it is justified to assume that the target nucleus is in the ground state ($\mu = 0$). However, in an astrophysical plasma the excited states can be thermally populated and for the total cross-section we need to sum over those states and get

$$\sigma(E_{io}) = \frac{\sum_\mu \left[(2J_i^\mu + 1) e^{-E_i^\mu / k_B T} \sum_\nu \sigma^{\mu\nu}(E_{io}) \right]}{\sum_\mu (2J_i^\mu + 1) e^{-E_i^\mu / k_B T}}. \quad (2.16)$$

This also includes the summation over all final states ν in the product nucleus of the cross-section given by equation (2.15) and hence the summation over the Transmission coefficients T^ν . However, in general not all of these states are experimentally known. Here we can use the fact that levels at high energies are very close together and can be described by a level density $\rho(E, \Pi, J)$ that depends in general on energy E , angular momentum J and parity Π . Several phenomenological expressions for the level densities exist. [Rauscher et al. \(1997\)](#) have shown that a constant temperature Fermi-gas model (CTM) by [Gilbert & Cameron \(1965\)](#) is very successful in reproducing experimentally measured level densities. Other methods include the back-shifted Fermi-gas model ([Dilg et al., 1973](#)) or a more recent approach by [Goriely \(1996\)](#) that tries to account for shell and pairing effects. Numerically computed values tabulated from microscopic Hartree-Fock calculations ([Goriely et al., 2001b](#)) are also available. With a given description of the nuclear level density $\rho(E, J, \Pi)$ we can generalize the total transmission coefficient as

$$T_m = \sum_{\nu=0}^{\nu_j} T_m^\nu(E, J, \pi, E_j^\nu, J_j^\nu, \pi_j^\nu) + \int_{E_j}^{E-S_{j,m}} \sum_{J_j, \pi_j} T_m^\nu(E, J, \pi, \epsilon, J_j, \pi_j) \rho(\epsilon, J_j, \pi_j) d\epsilon, \quad (2.17)$$

where we continue after the summation of all known discrete levels up to ν_j with integrating over the level density $\rho(\epsilon, J, \Pi)$.

Nuclear reaction codes employ equation (2.15) with a extended databases of experimental information and microscopic and phenomenological descriptions of gamma strength functions, optical potential and level densities to calculate cross-sections for nuclear reactions. Among the most commonly used and well established, maintained and verified codes are the NON-SMOKER (Loens, 2010) and TALYS (Koning et al., 2007) codes. Many of the reaction rates that are included in our calculations are based on such calculations (e.g. Rauscher & Thielemann (2000) and Iliadis et al. (2001)). For Section 7 the TALYS code has been used to calculate reaction rates for a range of reactions affected by recently measured nuclear masses. For this we used the constant temperature Fermi gas model. The statistical model is only applicable if the use of average transition coefficients is appropriate, i.e. when the density of states available for transitions is sufficiently large. This is usually the case for intermediate to heavy nuclei and at high energies. Rauscher et al. (1997) have estimated that around 10 levels should be reachable by a reaction.

The population of the compound nucleus can also occur via weak interactions, in particular by interaction with neutrinos. In this case we can still use the same statistical approach to calculate the branching ratios for the decay channels. In this way, Huther (2014) has used the Modified Smoker code (see ref. Loens (2010)) at low energies. This code considers experimentally known states and their properties explicitly and then matches the experimental spectrum to a level density. However, it is restricted to treat single-particle decays. To allow for multi-particle decay, Huther (2014) has adopted the Monte-Carlo code ABLA Kelic et al. (2009) at higher excitation energies, which has been well validated to properly describe multi-particle decays and fission. The results of the two statistical model codes have been smoothly matched at moderate energies above the single-particle thresholds.

2.1.3 Detailed balance and inverse reaction rates

The calculation of reaction cross-sections usually follows the compound nucleus picture. The incident projectile with energy E reacts with the target to form a temporary compound state $|c\rangle$ in an excited state at an energy of $E + Q$ above the target state. This compound nucleus can now decay in various ways. For a reaction of the form $i(o, m)j$ with particles of non-zero mass with angular momenta J_i, J_o, J_m and J_m for each reactant mediated by an interaction with Hamiltonian \mathcal{H} the cross-section formally can be written as

$$\sigma_{i(o,m)j} = \pi \left(\frac{\hbar^2}{2\mu_{io}E_{io}} \right)^2 \frac{2J_C + 1}{(2J_i + 1)(2J_o + 1)} (1 + \delta_{io}) |\langle mj | \mathcal{H}_2 | C \rangle \langle C | \mathcal{H}_1 | io \rangle|^2 \quad (2.18)$$

with reduced mass $\mu_{io} = m_i m_o / (m_i + m_o)$ and the center of mass energy E_{io} . $\langle C | \mathcal{H}_1 | io \rangle$ is the matrix element for the formation of the compound nucleus and $\langle mj | \mathcal{H}_2 | C \rangle$ for the decay of the compound state to the final state in j .

Analogously for the inverse reaction $j(m, o)i$ we have

$$\sigma_{j(m,o)i} = \pi \left(\frac{\hbar^2}{2\mu_{jm}E_{jm}} \right)^2 \frac{2J_C + 1}{(2J_j + 1)(2J_m + 1)} (1 + \delta_{jm}) |\langle oi | \mathcal{H}_1 | C \rangle \langle C | \mathcal{H}_2 | jm \rangle|^2 \quad (2.19)$$

For the strong, the weak and the electromagnetic interaction, the Hamiltonian is invariant with respect to time-reversal transformations. Therefore, the absolute of matrix elements in (2.19) are identical for both directions and we get

$$\frac{\sigma_{j(m,o)i}}{\sigma_{i(o,m)j}} = \frac{(2J_i + 1)(2J_o + 1)}{(2J_j + 1)(2J_m + 1)} \frac{\mu_{io}E_{io}}{\mu_{jm}E_{jm}} \frac{(1 + \delta_{jm})}{(1 + \delta_{io})}. \quad (2.20)$$

For the velocity averaged cross-section one obtains

$$\frac{\langle \sigma v \rangle_{j(m,o)i}}{\langle \sigma v \rangle_{i(o,m)j}} = \left(\frac{\mu_{io}}{\mu_{jm}} \right)^{3/2} \frac{(1 + \delta_{jm}) (2J_i + 1)(2J_o + 1)}{(1 + \delta_{io}) (2J_j + 1)(2J_m + 1)} e^{-Q/k_B T}. \quad (2.21)$$

The exponential factor $e^{-Q/k_B T} = e^{-(m_j - m_i)/k_B T}$ arises from the ratio of the factors $e^{-\frac{m v^2}{2k_B T}}$ in the Maxwell-Boltzmann distributions (see equation (2.1)). This relationship between forward and reverse reactions is known as detailed balance which allows to determine the solution of equilibrium problems without knowledge of the reaction rates themselves as we will show in the next section. Furthermore, it means that from experimentally measured reaction rates in one direction, the reverse reaction can be determined if all the relevant states are covered. A priori there is no definition of which direction to call forward which to call reverse. However, in order to avoid inaccuracies from states not covered by the "forward" rate it is better to calculate and endoergic inverse rate based on an exoergic reaction (Rauscher & Thielemann, 2000).

Equation (2.21) is valid for massive particles. For radiative capture $i(o, \gamma)j$ and the reverse photodissociation $j(\gamma, o)i$ one can obtain the following relationship

$$\frac{\lambda_{j(\gamma,o)i}}{\langle \sigma v \rangle_{i(o,\gamma)j}} = \left(\frac{2\pi}{h^2} \right)^{2/3} (\mu_{io} k_B T)^{3/2} \frac{(2J_i + 1)(2J_o + 1)}{(2J_j + 1)} \frac{1}{1 + \delta_{io}} e^{-\frac{Q}{k_B T}} \quad (2.22)$$

These relations are for transitions between individual angular momentum states. For the total cross section it is necessary to sum over all involved states and the corresponding compound states. As a result we need to replace the angular momentum factors in equations (2.22) and (2.21) by the temperature dependent partition functions

$$(2J + 1) \rightarrow G(T) = \sum_i (2J_i + 1) e^{-E_i/k_B T} + \int_{E_{\text{elast}}}^{\infty} \sum_{J_j, \pi_j} (2J_j + 1) e^{-\epsilon/(k_B T)} \rho(\epsilon, J_j, \pi_j) d\epsilon, \quad (2.23)$$

to take into account that excited states can be populated by thermal excitations in a stellar plasma. As in equation (2.17) the sum is continued as an integral beyond the last known discrete state. In practice, the integral is usually cut at an upper limit of around 30 MeV beyond which no significant contributions can be expected at stellar temperatures. Values for the partition functions are available in tabulated form. Some details on the format and evaluation of the reaction rates from the REACLIB library and their numerical advantages are elaborated on in Section A.

This very short overview of the nuclear physics involved in evaluating and calculating the nuclear reaction rates for astrophysical applications hopefully illustrates that despite decades of effort, many reactions are still rather uncertain. Longland et al. (2010) have developed a Monte-Carlo approach to evaluate the how the uncertainties of experimentally measured parameters propagate into the reaction rates. In this work we evaluate the effects of neutrino interactions in particular in comparison to the uncertainties of the nuclear reaction rates that are involved. In these cases we use the uncertainties estimated by Iliadis et al. (2010). Several reaction rates evaluated in this framework are relevant for the production of the nuclei we study here.

2.1.4 Nuclear reaction network

In this section we derive the differential equations that govern the evolution of nuclear abundances and discuss how they are numerically formulated, implemented and solved.

Consider the material in a volume V as a mixture of different nuclei i with number densities $n_i = N_i/V$ where N_i is the number of nuclei contained in the volume V .

The change of the number density of particles of species i due to nuclear reactions producing j are described by the reaction rate $r_{i,j} = (\partial n_i / \partial t)_{\rho=const}$. Additionally, if the number of particles N_i does not change, changes of the fluid density $\frac{\partial \rho}{\partial t}$ will also affect the number density by compressing or expanding the volume element such that

$$\frac{dn_i}{dt} = -r_{i,j} + \left(\frac{\partial n_i}{\partial t} \right)_{N_i=const.} \quad (2.24)$$

which also implies

$$\frac{dn_j}{dt} = +r_{i,j} + \left(\frac{\partial n_j}{\partial t} \right)_{N_j=const.} \quad (2.25)$$

To avoid this complication we rather evolve the abundance defined as the ratio

$$y_i = \frac{N_i}{N_B} = \frac{n_i}{n_B} = n_i \left(\frac{m_u}{\rho} \right) \quad (2.26)$$

where $n_B = \rho/m_u$ is the total number density of baryons with the atomic mass unit m_u . Note that $1/m_u = N_A/g$ is Avogadro's number N_A . When we assume that there is no mixing between mass zones, the total number of baryons n_B is conserved. Therefore, $N_i = const.$ implies $y_i = const.$ We normalize to the number of baryons because the number of leptons, i.e. electrons, positrons and neutrinos as well as photons are not evolved explicitly.

Inserting definition (2.26) into (2.24) and (2.25) gives

$$\frac{\partial y_i}{\partial t} \frac{\rho}{m_u} + y_i \frac{1}{m_u} \frac{\partial \rho}{\partial t} = -r_{i,j} + y_i \frac{1}{m_u} \frac{\partial \rho}{\partial t} \quad \rightarrow \quad \frac{\partial y_i}{\partial t} = -r_{i,j}, \quad (2.27)$$

where we use that the derivative on the right hand side is for constant N_i and therefore constant y_i . such that the density dependence cancels. The abundance of i is in general affected by several reactions and we need to sum over all the contributions.

We now have a closer look at the form of the reaction rates $r_{i,j}$ connecting a nucleus i with j . The rate for a one-body reaction $j \rightarrow i$ depends on the number density of particles of the mother nucleus j and a rate λ , which now gives the reactions per time and per particle j , as

$$\frac{\partial y_i}{\partial t} = a_j^i \lambda y_j. \quad (2.28)$$

Here a_j^i is the number of particles i produced per reaction. At the time we also need to account for the destruction of j with

$$\frac{\partial y_i}{\partial t} = a_i^j \lambda y_j, \quad (2.29)$$

where a_i^j is negative. For nuclear decays like β^\pm , electron capture or α decay, the rate is a constant $\lambda = \ln(2)/T_{1/2}$ that is related to the half-life $T_{1/2}$. If temperatures are sufficiently high, nuclear decays may proceed not only from the ground state, but also from excited states. If the quantum numbers of

such states allow for a stronger transition to the daughter nucleus, the decay rate can be significantly modified. In such a case we need to sum over the decays of the excited states weighted with their probabilities of being thermally populated

$$\lambda \rightarrow \lambda(T) = \frac{1}{G(T)} \sum_i \lambda_i (2J_i + 1) e^{-E_i/k_B T} \quad (2.30)$$

with the partition function $G(T) = \sum_i (2J_i + 1) e^{-E_i/k_B T}$. Such a summation requires the knowledge of the energies and angular momentum of the nuclear states and of their decay transitions. While the properties of excited states can be determined relatively well by different methods of nuclear spectroscopy, the transition strengths are difficult to obtain experimentally under laboratory conditions. Therefore, such rates are usually based on theory, most notably nuclear shell model calculations. The temperature dependent decay rates for wide range of nuclei are available in tabulated form [Fuller et al. \(1982\)](#) and have been improved and extended to heavier nuclei by shell model calculations by [Langanke & Martínez-Pinedo \(2000\)](#).

Electron capture rates depend on the density and energies of the electrons that are sensitive to the matter density under degenerate conditions. This is mostly important for the fate of low-mass progenitors at the edge of the minimum mass for CCSNe that develop highly degenerate stellar cores. Whether or not these stars leave a remnant of not hinges on the details of how the explosion unfolds ([Jones et al., 2016](#)) that is also affected by electron capture reactions during the last phase of their evolution ([Schwab et al., 2016](#)).

The massive stars we consider stay mostly non-degenerate except for the final phase of collapse that we do not try to model here. Formally, neutrino-induced reactions are similar to electron captures. They depend on the cross-section that scales with the neutrino energy E_ν as well as on the local flux ϕ_ν . Similar to the Maxwell-Boltzmann velocity average for thermonuclear reactions, the dependence on E_ν can be reduced to a can be removed by taking the spectral average of the cross-section. Supernova simulations have shown, that the neutrino spectra actually deviate from a pure Fermi-Dirac distribution. But this deviation has only a minor effect on the averaged cross-section and in this work we always employ Fermi-Dirac averaged cross-sections

$$\langle \sigma_\nu \rangle (T_\nu) \int_0^\infty E_\nu^2 f(E_\nu, T_\nu) \sigma(E_\nu) dE_\nu \quad \text{with} \quad f(E_\nu) = \frac{2}{3T_\nu^3 \zeta(3)} \frac{1}{1 + e^{E_\nu/T_\nu}} \quad (2.31)$$

with a normalized Fermi-Dirac spectrum, and the Riemann Zeta function ζ . The neutrino temperature T_ν is here related to the average energy as

$$\langle E_\nu \rangle = \frac{7\pi^4}{180\zeta(3)} T_\nu \approx 3.15 T_\nu. \quad (2.32)$$

For neutrino-induced reactions also depends on the neutrino flux ϕ_ν , i.e. the number of neutrinos per area and time,

$$\lambda_\nu = \phi_\nu \langle \sigma_\nu \rangle = \frac{L_\nu \langle \sigma_\nu \rangle}{4\pi r^2 \langle E_\nu \rangle}, \quad (2.33)$$

where we express ϕ_ν in terms of the luminosity L_ν which gives the energy emitted per time.

Photodissociation reactions $j(\gamma, o)i$ can be written in the same way with a temperature dependent constant λ_γ that is related to the forward reaction $i(o, \gamma)j$ direction by detailed balance (see Section 2.1.3, equation (2.22)). The rate for a general two-body reaction of the form $i(o, m)j$ depends on the number of target nuclei and projectiles as well as on the frequency of interactions that depends on the

particles' velocities. Therefore, the rate is expressed in terms of the averaged cross-section $\langle\sigma v\rangle$ defined in equation (2.4) as

$$\frac{\partial y_i}{\partial t} = a_{oj}^i \langle\sigma v\rangle_{io} \frac{\rho}{m_u} y_i y_o. \quad (2.34)$$

with

$$a_{oj}^i = \frac{N_{oj}^i}{1 + \delta_{io}}, \quad (2.35)$$

where N_{oj}^i accounts for the number of particles of i that are destroyed or produced in this reaction. N_{oj}^i is positive if i is produced and negative if i is destroyed by the reaction. $1/(1 + \delta_{io})$ accounts for double counting in case of identical particles. Multi particle reactions are in general suppressed for kinematic reasons because they require all particles to be at the same spot at the same time and in the case of charged particles require to overcome the Coulomb repulsion of all particles. However, in a few exceptional cases three-body reaction can be very important, as for the case of the triple α reaction through which He burning proceeds. For a three body reaction $i + o + k \rightarrow j$, the rate can be expressed as

$$\frac{\partial y_i}{\partial t} = a_{okj}^i \langle iok\rangle \left(\frac{\rho}{m_u}\right)^2 y_i y_o y_k, \quad (2.36)$$

where $\langle iok\rangle$ plays a similar role as $\langle\sigma v\rangle$ and another power of the density enters because we multiply by one more abundance. Furthermore, the coefficient

$$a_{okj}^i = \frac{N_{okj}^i}{1 + \delta_{io} + \delta_{ik} + \delta_{ok} + 2\delta_{iok}}, \quad (2.37)$$

accounts for the multiplicity and proper counting. Each nucleus is affected by these three types of reactions and in total we can write down the equations to determine the evolution of the composition as

$$\frac{\partial y_i}{\partial t} = \sum_j a_j^i \lambda_{ij} + \sum_{oj} a_{oj}^i \langle\sigma v\rangle_{io} \frac{\rho}{m_u} y_i y_o + \sum_{ojk} a_{okj}^i \langle iok\rangle \left(\frac{\rho}{m_u}\right)^2 y_i y_o y_k \quad (2.38)$$

where the sums run over the one-, two-, and three-body reactions involving the nucleus i . Equation (2.38) represents one element of a set of non-linear differential equations that need to be solved to determine the evolution of the composition. The reaction rates and abundances can span many orders of magnitude and the timescales associated with different reactions often differ significantly. Therefore, this set of equations poses in general a very stiff initial value problem that requires an implicit method to solve [Hix & Thielemann \(1999\)](#).

Furthermore, due to non-linear character of the problem, an iterative solution, e.g. via a Newton-Raphson approach, is necessary.

Formally, the equation poses a problem of the form

$$\dot{\vec{y}}(t) = \vec{\mathcal{F}}(\vec{y}, t) \quad (2.39)$$

where $\vec{y}(t) = (y_1(t), y_2(t), \dots, y_n(t))$ represents the abundances of n nuclear species in the reaction network and $\vec{y}(t) = \partial \vec{y} / \partial t$ and \mathcal{F} is the nonlinear functional that also depends explicitly on the conditions and thus on time as the reaction rates vary with temperature and density.

In order to solve this problem we need to discretized it in time and linearize the functional.

Define a time step Δt as $t^{(n+1)} = t^{(n)} + \Delta t$ and correspondingly $y(t^{(n)}) = y^n$.

With this discretization we can write equation (2.39) as

$$\frac{1}{\Delta t}(\bar{y}^{n+1} - \bar{y}^n) - \left(\Theta \vec{\mathcal{F}}(\bar{y}^n) + (1 - \Theta) \vec{\mathcal{F}}(\bar{y}^{n+1}) \right) = 0, \quad (2.40)$$

with Θ between 0 and 1. For $\Theta = 1$ we have the explicit forward Euler method for which \bar{y}^{n+1} can be calculated directly with the knowledge of \bar{y}^n . Such an explicit method would be numerically unstable because of the stiffness of the equations. Using $\Theta = 1$ formally requires evaluating \mathcal{F} at the unknown point \bar{y}^{n+1} . This is the implicit backward-Euler method. Since \mathcal{F} is nonlinear, this formulation cannot give us an immediate solution. We will now consider two different approaches to solve this set of equations.

First, we can linearize $\vec{\mathcal{F}}$ and get

$$\frac{1}{\Delta t}(\bar{y}^{n+1} - \bar{y}^n) - \vec{\mathcal{F}}(\bar{y}^n) + \left. \frac{\partial \vec{\mathcal{F}}}{\partial \bar{y}} \right|_{\bar{y}^n} (\bar{y}^{n+1} - \bar{y}^n) = 0 \quad (2.41)$$

where the Jacobian matrix $\left(\frac{\partial \vec{\mathcal{F}}}{\partial \bar{y}} \right)$ has elements $\left(\frac{\partial \vec{\mathcal{F}}}{\partial \bar{y}} \right)_{ij} = \left(\frac{\partial \mathcal{F}_i}{\partial y_j} \right)$. This linearization reduces the problem to a linear set of equations

$$\left(\frac{1}{\Delta t} + \left. \frac{\partial \vec{\mathcal{F}}}{\partial \bar{y}} \right|_{\bar{y}^n} \right) \Delta \bar{y} - \vec{\mathcal{F}}(\bar{y}^n) = 0 \quad (2.42)$$

that can be solved numerically for the difference vector $\Delta \bar{y} = \bar{y}^{n+1} - \bar{y}^n$ with standard methods from linear algebra packages. This method is applied in the co-processing nuclear reaction network included in the KEPLER code. However, this approach assumes that the linearization of (2.41) is valid. Our network code applies an iterative Newton-Raphson method to cope with the nonlinearity. With the index i to count the number of iterative solutions in additions to n for the time steps, we can define $\Delta \bar{y}_{i+1} = \bar{y}_{i+1}^{n+1} - \bar{y}_i^{n+1}$ for the improvement with respect to previous iteration. Solving

$$\left(\frac{1}{\Delta t} + \left. \frac{\partial \vec{\mathcal{F}}}{\partial \bar{y}} \right|_{\bar{y}_i^{n+1}} \right) \Delta \bar{y}_{i+1} - \frac{1}{\Delta t}(\bar{y}^n - \bar{y}_i^{n+1}) + \vec{\mathcal{F}}(\bar{y}_i^{n+1}) = 0 \quad (2.43)$$

until convergence for $\Delta \bar{y}_{i+1}$ is reached gives an improved estimate for the solution to the nonlinear equations at time t^{n+1} .

This requires an initial guess for $\bar{y}_{i=0}^{n+1}$ for which we take \bar{y}^n , the converged result from the previous time step or the initial composition for the first time step. The first iteration of 2.43 is the same as equation 2.42. For convergence we require

$$\sum_j \frac{(\Delta \bar{y}_{i+1}^{n+1})_j}{(\bar{y}_{i+1}^{n+1})_j} < 10^{-4} \quad (2.44)$$

to be achieved within 10 Newton-Raphson iterations. Otherwise, the time step is reduced and iteration resumed. For the calculation presented in Sections 5.2 and 5.4 our network includes 1988 nuclear species. In Section 7 we include more nuclei further away from stability, mostly on the proton rich side of the nuclear chart, leading to a total count of 2608 nuclei. To make the calculations more efficient we can exploit the fact that nuclei are mostly only connected to their direct neighbors - with the exception of neutron, protons and α particles. As a result, the Jacobian in equation (2.42) is sparse, i.e. most of

the matrix elements are zero. This allows to use a memory-efficient scheme to store the matrix and an optimized solver routine (Petra et al., 2014).

We take the thermonuclear reaction rates of the JINA REACLIB V2.2 library. Beta decay rates are taken from the evaluation of experimental data by Wang et al. (2014) and extended by the theoretical prediction of the FRDM model by Möller et al. (1997) where not measurements are available.

Solving the equations of the nuclear reaction network gives us the evolution of the abundances as a result of the combination of all the reactions involved. However, in many cases we are interested in which particular reactions contribute the most to the evolution of the abundance of a nuclear species. In order to quantify the contribution of a reaction we can look at the reaction flow between

$$F_{ij} = \int \left[\left(\frac{\partial y_i}{\partial t} \right)_{j \rightarrow i} - \left(\frac{\partial y_i}{\partial t} \right)_{i \rightarrow j} \right] dt, \quad (2.45)$$

where $(\partial y_i / \partial t)_{j \rightarrow i}$ is the change of the abundance y_i due to reaction $j \rightarrow i$ and $(\partial y_i / \partial t)_{i \rightarrow j}$ the change due to the inverse reaction. The shape of these terms depends on the type of the reaction. The reaction in general depends not only on the temperature and density, but also on the abundance of the nucleus under consideration and also on the abundances of other nuclei involved. Those are in turn affected by a range of other reactions. In practice F_{ij} is calculated assuming that all abundances are constant during the time step Δt . This does not capture non-linear effects. In conditions close to equilibrium at high temperatures any net abundance change results from small differences of between large numbers of the forward and reverse rates. In such a situation we would not expect to get a reliable representation of the flow F_{ij} with this approach. However, for sufficiently small time steps and away from equilibrium conditions the reaction flow is very useful give an indication for the most important reactions.

2.1.5 Equilibria, NSE and alpha-rich freeze out

It is not necessary to always evolve the composition with the whole set of nuclear reaction network equations. If the conditions evolve much slower than the typical timescales of the nuclear reactions convenient equilibria are established that help to set up initial conditions and to speed up the calculations. Such equilibria are reached if either the conditions are stable for a very long time or if the timescale for the nuclear reaction becomes short. The latter case occurs at very high temperatures which is particularly important because the solution of the reaction network equations becomes increasingly computationally expensive at higher temperatures because the time steps need to be chosen small according to the reaction time scales.

From equation (2.22) we can see that for any particle induced reaction, the cross-section for inverse process becomes comparable to the forward direction at sufficiently high temperatures. As an example we can consider radiative proton captures $i(p, \gamma)j$ in equilibrium with $j(\gamma, p)i$. The equilibrium abundance of i will then be determined by

$$\frac{\partial y_i}{\partial t} = \lambda_\gamma y_j - \frac{\rho}{m_u} \langle \sigma v \rangle_{p,\gamma} y_p y_i = 0$$

Using equation 2.22 we get

$$\frac{y_j}{y_i} = \frac{\rho}{m_u} y_p \frac{\langle \sigma v \rangle}{\lambda_\gamma} = \frac{\rho}{m_u} y_p \frac{G_j}{g_p G_i} \left(\frac{m_j}{m_p m_i} \right)^{3/2} \left(\frac{2\pi \hbar^2}{k_B T} \right)^{3/2} e^{Q/k_B T} \quad (2.46)$$

Thus, the ratio of two neighboring nuclei depends only on the Q-value between them and the abundance of free protons in this case. In particular it is independent of the reaction cross-section. Since nuclear reaction cross-sections also come with much larger uncertainties than the Q-value, the determination of such equilibria is also more precise in regions where the nuclear masses are well known. For processes that operate far from stability, like the r process in very neutron rich conditions or the rp process in very proton rich conditions, the concept of (n, γ) - (γ, n) or (p, γ) - (γ, p) has been very successful to gain qualitative insights into the nucleosynthesis of heavy elements.

At sufficiently high temperature or on long timescales all reactions are in equilibrium and we can construct a set of equations like (2.46) to determine the complete composition. Such a situation is called nuclear statistical equilibrium (NSE). If any two neighboring nuclei are in equilibrium that also means that any nucleus i with mass number A , neutron number N and charge Z is in equilibrium with the complete disintegration into Z protons and N neutrons. This can be expressed in terms of chemical potentials as $\mu_A = N\mu_n + Z\mu_p$. With

$$\mu_i = k_B T \ln \left(\frac{\rho}{G_i m_u} y_i \left(\frac{2\pi}{m_i k_B T} \right)^{3/2} \right) + m_i c^2 \quad (2.47)$$

we get an expression for the abundance of any nucleus

$$y_i = G_i \left(\frac{\rho}{m_u} \right)^{A-1} \frac{A^{3/2}}{2^A} \left(\frac{2\pi}{m_u k_B T} \right)^{3/2(A-1)} e^{-B_i/k_B T} y_n^N y_p^Z \quad (2.48)$$

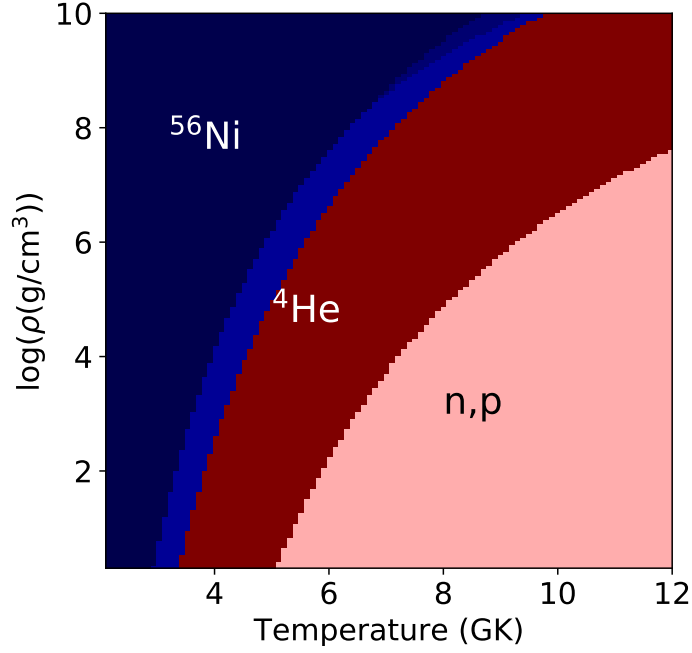


Figure 2.1.: Dominant species in nuclear statistical equilibrium for a range of temperature and density for $Y_e = 0.5$ based on the numerical solution of Equation (2.48). At high temperatures, free nucleons are favored and in between we find mostly α particles. In the region of transition to ^{56}Ni , ^{55}Co and ^{54}Fe are the dominant species, indicated by a lighter blue color.

as a function of the abundances of free protons y_p and neutrons y_n .

In addition to these equations, we have the condition of mass conservation

$$\sum_i A_i y_i = 1 \quad (2.49)$$

and charge neutrality

$$Y_e = \sum_i y_i Z_i. \quad (2.50)$$

Thus, for a given electron fraction Y_e the composition under NSE conditions is determined entirely by the nuclear binding energies. Figure 2.1 shows the dominant species - by mass fraction - in the NSE composition for a range of temperatures and densities for $Y_e = 0.5$. In this study we assume that NSE is achieved for temperatures above 6 GK. Such conditions are only reached by the innermost mass zones of the Si-shell in our 1D supernova models. At very high temperatures around 10 GK the composition in NSE is dominated by free particles. From Equation (2.48) this can be easily seen from the exponential factor that becomes small for high temperatures. Since all abundances of nuclei are small, equations (2.49) and (2.50) demand that all the mass consists of neutrons and protons with a ratio depending on the given Y_e . It can also be understood from the presence of a large number of high energy photons at high temperatures that lead to the photodissociation of nuclei. The nucleus with the largest binding energy, ^4He is the first nucleus to become abundant as temperature decreases at an electron fraction around 0.5. With decreasing temperature heavier nuclei are formed and because of their relatively large binding energy, the composition is dominated by the Fe-group nuclei and in particular ^{56}Ni for Y_e around 0.5. In Figure 2.1 we also see a transition region where the composition is dominated by ^{54}Fe and ^{55}Co in the high density and high temperature regime (upper right corner). Starting from ^{56}Ni the first reaction to set in as the temperature increases is $^{56}\text{Ni}(\gamma, p)$. If the density is too low to capture the proton again, equilibrium shifts in favor of the lighter ^{54}Fe or ^{55}Co and additional free protons.

Equilibrium is only achieved if the dynamical timescale of the system is sufficiently long, i.e. longer than the timescale of the nuclear reactions. Since nuclear reactions are very fast at high temperatures around 10 GK this is easily achieved. However, as material cools and expands, it is easy to see that the timescale of nuclear reaction becomes longer than the expansion timescale. This point is referred to as freeze out of the equilibrium. When this happens depends on the dynamical timescale of the system. [Seitenzahl et al. \(2008\)](#) have shown, that the freeze out conditions of neutron- and proton-rich NSE are very different. While neutron rich NSE favors the nucleus with a mass over charge ratio A/Z corresponding to the Y_e of the medium, proton rich NSE ($Y_e > 0.5$) is always dominated by ^{56}Ni and free protons. This is of great importance for the nucleosynthesis of heavy elements in neutrino driven winds that are discussed in Section 7

In the case of a very fast expansion, the freeze out can happen when still a large amount of free ^4He is present, leading to an α -rich freeze-out. One of the last reactions to achieve equilibrium is the triple-alpha reaction and consequently it is also one of the first to fall out of equilibrium when we look a decreasing temperature. Once this link is broken, material can still be rearranged in the Fe -group but the abundance of α particles is effectively set. This has been found in many of the early models of exploding stars ([Arnett et al., 1971](#)).

2.2 Neutrino interactions in the standard model

In this section the background of our calculations of neutrino nucleus cross-sections is provided. Our modern understanding of the weak interaction is based on the Glashaw-Salam-Weinberg theory of the standard model ([Weinberg, 1996](#)). Within this framework, the weak interaction is mediated by the charged W^\pm and neutral Z^0 gauge bosons with masses of $80 \text{ GeV}/c^2$ and $90 \text{ GeV}/c^2$ respectively. Since the masses of the bosons are much larger than the relevant momentum and energy scales of the processes considered here the propagator can be integrated and absorbed into an effective coupling constant, the Fermi coupling constant G_F . Since the same interaction is responsible for the nuclear β decay, this approach also connects the standard model to Fermi's theory of decay ([Fermi, 1934](#)). The Hamiltonian reduces to a current-current contact interaction. In this case each of the currents, the nucleon current as well as the lepton current have the vector - axial vector (V-A) structure:

$$\mathcal{H}_I = \frac{G_F}{\sqrt{2}} \int d\vec{x} \mathcal{J}^\mu(\vec{x}) j_\mu(\vec{x}). \quad (2.51)$$

Here, \mathcal{J} is the nucleon current and j is the lepton current. With the lepton fields ℓ the current j can be split into the charged (c.c.) or neutral (n.c.) current

$$j_{CC}^\mu = \bar{\ell} \gamma^\mu (1 - \gamma_5) \tau_\pm \ell \quad (2.52)$$

and

$$j_{NC}^\mu = \bar{\ell} \gamma^\mu (1 - \gamma_5) \frac{\hat{t}_3}{2} \ell + 2 \sin^2(\Theta_W) \bar{\ell} \gamma^\mu \frac{(1 - \hat{t}_3)}{2} \ell \quad (2.53)$$

where $G = G_F c_{ud}$ with the up-down mixing factor from the Cabibbo-Kobayashi-Makasawa matrix that accounts for the fact that the eigenstates of quarks with respect to the strong and weak interactions are not the same. The second term in equation (2.53) is the electromagnetic interaction that only acts on protons due to the isospin operator. In order to calculate the cross-section for the excitation of a nucleus from an initial state $|i\rangle$ to a final state $|f\rangle$ we need the corresponding matrix element. The

partial differential cross section for a neutrino interaction can then be calculated according to the Fermi's Golden Rule as

$$\frac{d\sigma}{d\Omega} = \frac{k \varepsilon}{2\pi^2} F(Z \pm 1, \varepsilon) \frac{1}{2J_i + 1} \sum_{M_i} \sum_{M_f} |\langle f | \mathcal{H}_{int} | i \rangle|^2, \quad (2.54)$$

where ε is the energy and k the momentum of the outgoing lepton. For the processes we are interested in, we can assume extremely relativistic leptons, i.e. the lepton energy is much larger than the lepton mass $\varepsilon_\ell \gg m_\ell$. Here we are interested in semi-leptonic processes, such as

$$\begin{aligned} \nu_e + A(Z, N) &\rightarrow B^*(Z + 1, N - 1) + e^-, \\ \bar{\nu}_e + A(Z, N) &\rightarrow B^*(Z - 1, N + 1) + e^+ \quad \text{and} \\ \nu_x + A(Z, N) &\rightarrow A^*(Z, N) + \nu'_x. \end{aligned} \quad (2.55)$$

Here $A(Z, N)$ represents a nucleus with Z protons and N neutrons and A^* indicates that the nucleus is typically in an excited state that might decay by particle emission or an electromagnetic transition. ν_x is any type of neutrino or antineutrino. While the first two processes proceed via the charged current (c.c.), the last process in (2.55) is a neutral current process (n.c.). The differential cross-section for a general semi-leptonic process can then be expressed as (Engel, 1998; Engel et al., 1993)

$$\left(\frac{d\sigma}{d\Omega_e} \right)_\nu = \frac{G_F^2 \varepsilon_f^2}{2\pi^2} \frac{4\pi \cos^2 \Theta_W / 2}{2J_i + 1} F(Z \pm 1, \varepsilon_f) \left[\sum_{J=0}^{\infty} \sigma_{CL}^J + \sum_{J=0}^{\infty} \sigma_T^J \right] \quad (2.56)$$

with a Coulomb plus Longitudinal part

$$\sigma_{CL}^J = |\langle J_f | \hat{M}_J(q) + \frac{\omega}{q} \hat{L}_J(q) | J_i \rangle|^2 \quad (2.57)$$

and a transversal part

$$\begin{aligned} \sigma_T^J &= \left(-\frac{q_\mu^2}{2q^2} + \tan^2 \frac{\Theta}{2} \right) [|\langle J_f | \hat{J}_J^{mag}(q) | J_i \rangle|^2 + |\langle J_f | \hat{J}_J^{el}(q) | J_i \rangle|^2] \\ &\pm 2 \tan \frac{\Theta}{2} \sqrt{-\frac{q_\mu^2}{q^2} + \tan^2 \frac{\Theta}{2}} \operatorname{Re} \left[\langle J_f | \hat{J}_J^{mag}(q) | J_i \rangle \langle J_f | \hat{J}_J^{el}(q) | J_i \rangle \right] \end{aligned} \quad (2.58)$$

where \pm corresponds to antineutrino or neutrino reactions respectively and q is the four-momentum transfer $q_\mu = (\omega, \vec{q})$ with energy transfer ω and $q = |\vec{q}|$. $\hat{M}_J, \hat{L}_J, \hat{J}_J^{mag}, \hat{J}_J^{el}$ are the Coulomb, longitudinal, transverse electric, and transverse magnetic multipole projections of the leptonic current operators. Since we have states with definite angular momentum we can use the reduced matrix elements $\langle J_f | \hat{O} | J_i \rangle$ with respect to the angular momentum projection according to the Wigner-Eckart theorem (Brussaard & Glaudemans, 1977).

For low neutrino energies the Fermi function $F(Z \pm 1, \varepsilon_f)$ that only appears for charged current reactions accounts for the change of the Coulomb potential for the outgoing charged lepton in s-wave. Haxton et al. (1982) and Bühring (1982) have shown that it can be derived as Coulomb correction from the relativistic Dirac equation as

$$F(Z, \varepsilon_f) = 2(1 + \gamma) (2p_\ell R)^{2(\gamma-1)} \left| \frac{\Gamma(\gamma + iy)}{\Gamma(2\gamma + 1)} \right|^2 e^{\pi y}, \quad (2.59)$$

with

$$\gamma = \sqrt{1 - (\alpha Z)^2} \quad \text{and} \quad y = \alpha Z \frac{\varepsilon_f}{p_\ell},$$

with the fine structure constant α . Here, p_ℓ is the lepton momentum in units of the mass m_ℓ of the lepton ℓ , which will always be an electron for the applications here. At energies for which higher order partial waves become relevant, the effect can be taken into account by replacing the momentum of the outgoing lepton by an effective momentum

$$p_{\text{eff}}^2 = E_{\text{eff}}^2 - m_\ell^2 c^4 \quad \text{with} \quad E_{\text{eff}} = E_\ell - 3 \frac{Z e^2}{2R}, \quad (2.60)$$

with an effective energy E_{eff} that is the lepton energy E_ℓ corrected for the Coulomb potential. Since we only consider charged current reactions for neutrinos with average energies of less than 15 MeV, we only use the Fermi function. To obtain the total cross-section, equation (2.56) is integrated over the solid angle $d\Omega$. The reduced matrix elements of the operators in equation (2.56) need to be evaluated in the framework of the random phase approximation (RPA) explained in Section 2.3. In order to do so, following [Walecka \(1975\)](#) these operators that can be written as one-body operators in second quantization in the many-body Hilbert space as

$$\hat{j}^\mu(0) = \sum_{\alpha, \alpha'} \langle \alpha | \hat{j}^\mu | \alpha \rangle a_{\alpha'}^\dagger a_\alpha \quad (2.61)$$

At the low neutrino energies that are relevant for us, neutrino-induced reactions are typically dominated by Fermi- and Gamow-Teller transitions. For Fermi transitions the angular momentum does not change ($\Delta J = 0$) but the projection of the isospin does $\Delta T_z > 0$. Such transitions are only possible between Isobaric Analog States which must be located at sufficiently low excitation energies to contribute noticeably. Neglecting isospin mixing which is small according to [Towner & Hardy \(1995\)](#) the Fermi transition strength can be calculated as

$$B^{if}(F) = T(T+1) - T_{z,i} T_{z,f} = |N - Z| \quad (2.62)$$

where T is the total isospin that is conserved in the transition while $T_{z,i}$ and $T_{z,f}$ are the initial and final isospin projections. The Gamow-Teller strength is

$$B^{if}(GT) = \left(\frac{g_A}{g_V} \right) \frac{|\langle f | \sum_k \hat{\sigma}^k \hat{t}_\pm^k | i \rangle|^2}{2J_i + 1} \quad (2.63)$$

Where $\hat{\sigma}^k \hat{t}_\pm^k$ is the Gamow-Teller operator consisting of the Pauli spin matrices and isospin lowering/raising operators $\hat{t}_\pm = 1/2(\hat{\tau}_x \pm i\hat{\tau}_y)$ that transform protons into neutrons $\hat{t}_+ |p\rangle = |n\rangle$ and vice versa $\hat{t}_- |n\rangle = |p\rangle$. Following the Racah convention the matrix elements are reduced only with respect to the spin operator $\hat{\sigma}$. These transition strengths provide a connection to experimentally measured values and therefore benchmarks for theoretical calculations of neutrino nucleus cross-sections.

2.3 Nuclear structure: RPA

The Random Phase Approximation considers particle hole excitations in terms of spin 1/2 single particle states $|k\rangle = |l m j\rangle$ with energies ε_k from an independent particle model (IPM). These states are calculated as solutions for a mean-field Woods-Saxon potential of the form

$$V(r) = -\frac{V_0}{1 + \exp\left(\frac{r-R}{a}\right)} - V_{s.o.} R^2 \frac{1}{R} \frac{\partial}{\partial r} \left(\frac{1}{1 + \exp\left(\frac{r-R}{a}\right)} \right) \vec{L} \cdot \vec{S} + \frac{1}{2}(1 - \hat{\tau}_3)V_C(r) \quad (2.64)$$

with a central term V_0 , a spin-orbit coupling term $V_{s.o.}$ and a Coulomb term $V_C(r)$. The nuclear radius R is assumed to be the same as the radius of the spin-orbit part and the nuclear diffuseness a is also taken to be identical to the spin-orbit diffuseness. The depth of the potentials V_0 and $V_{s.o.}$ together with a and R are free parameters that are adjusted for each nucleus to be calculated. The potential depth V_0 for neutrons and protons are chosen such that the last occupied single particle state reproduces the corresponding particle separation energy in the compound nucleus. The derivative in the second term of Equation (2.64) makes the spin-orbit interaction strongest at the surface and due to the isospin operator $(1 - \tau_3)$ the Coulomb interaction only acts on protons. For neutral current reactions the compound is the same as the target nucleus. For the charged current reactions the potential is adjusted to the separation energies of the corresponding product after the neutrino capture. Following Zinner (2007) $a = 0.53$ fm was assumed for all nuclei in our calculations and $r = 1.22$ fm $\cdot A^{1/3}$ was chosen according to a liquid drop model approach (Ring & Schuck, 2000). In Huther (2014) it is assumed that the IPM states $|k\rangle$, where k represents the set of quantum numbers that describe the state, are a good approximation for the ground state $|IPM\rangle$. Particle-hole excitations can then be written in terms of creation/annihilation operators a_k^\dagger and a_k . We now want to describe particle-hole excitations $\propto a_i^\dagger a_\alpha$ where Latin indices are for particle states and Greek indices for hole states, i.e. states below the Fermi surface which is defined by the last occupied state of the IPM ground state. In order to describe nuclear states with well defined angular momentum J and projection M the operators for particle/hole creation still need to be projected onto good angular momentum quantum numbers J and M as

$$A_{i\alpha}^\dagger(J, M) = \sum_{m_i m_\alpha} (-1)^{j_\alpha + m_\alpha} \langle j_i j_\alpha J | m_i m_\alpha M \rangle a_{j_i m_i}^\dagger a_{j_\alpha - m_\alpha}. \quad (2.65)$$

In this way, the particle-hole states can be constructed as (Ring & Schuck, 2000)

$$|\nu\rangle = \sum_{i,\alpha} X^{i,\alpha} A_{i\alpha}^\dagger |IPM\rangle - \sum_{\alpha,i} Y^{\alpha,i} A_{i\alpha} |IPM\rangle. \quad (2.66)$$

The assumption that the real many-body ground state is the IPM ground state would be exact if the particle-hole creation/destruction operators satisfied the commutation rules for bosonic fields. However, we apply it to Fermions and therefore this is called *quasi-boson approximation*. To describe the particle-hole excitations we also need a residual interaction \hat{V} to take into account correlations among particles and holes and between the excited particles and the IPM ground state. In Huther (2014) a phenomenological interaction of the Landau-Migdal type suitable for collective excitations is assumed. The interaction is based on an expansion in momentum space that translates into a δ function in space, i.e. a contact interaction, but also contains spin and isospin dependent terms:

$$V(\vec{r}_1, \vec{r}_2) = C_0 \delta^{(3)}(\vec{r}_1 - \vec{r}_2) (f + f' \vec{\tau}_1 \cdot \vec{\tau}_2 + g \vec{\sigma}_1 \cdot \vec{\sigma}_2 + g' (\vec{\sigma}_1 \cdot \vec{\sigma}_2) (\vec{\tau}_1 \cdot \vec{\tau}_2)) \quad (2.67)$$

with $C_0 = 302 \text{ MeV/fm}$, $g = 0.55$ and $g' = 0.8$. Following [Guman & Birbrair \(1965\)](#) the interaction is taken to be density dependent with

$$f = f^{ex} + \frac{(f^{in} - f^{ex})}{1 + \exp(\frac{r-R}{a})}, \quad (2.68)$$

where the density is described by a Fermi distribution with the parameters for radius R and diffuseness a as Equation (2.64). The values have been chosen following [Rinker & Speth \(1978\)](#) as $f^{ex} = -2.45$ and $f^{in} = 1.5$. The internal isospin coupling factor $f^{in} = 0.2$ has been adjusted to reproduce the isobaric analog states in ^{48}Ca and ^{208}Pb ([Plumley et al., 1997](#)).

The residual interaction defines

$$\hat{v}_{\alpha i, j\beta} = n_i n_j \langle \alpha i | \hat{V} | j\beta \rangle - n_i n_j \langle \alpha i | \hat{V} | \beta j \rangle, \quad (2.69)$$

accounting for particle-hole \rightarrow hole-particle and particle-hole \rightarrow particle-hole scattering with occupation numbers n_i and n_j taken from the mother nucleus to account for partial occupancy in open-shell nuclei ([Kolbe et al., 1999](#)). With

$$A_{i\alpha, j\beta} = (\epsilon_i - \epsilon_\alpha) \delta_{ij} \delta_{\alpha\beta} \quad \text{and} \quad B_{i\alpha, j\beta} = \hat{v}_{\alpha i, j\beta} \quad (2.70)$$

the secular equation of the RPA

$$\begin{pmatrix} A & B \\ -B^* & -A^* \end{pmatrix} = E_\nu \begin{pmatrix} X^\nu \\ Y^\nu \end{pmatrix} \quad (2.71)$$

gives the nuclear excitation spectrum E_ν that allows to compute the matrix elements for the one-body operators as described in Equation (2.61). Cross-sections are calculated taking into account excitations of order up to $J = 4$ with positive and negative parities. In order to improve the absolute energy scaling of our RPA calculations, the energies of the single particle states are shifted globally, such that the dominant contribution to the 0^+ Fermi transition reproduces the position of the isobaric analog state that can be quite well approximated by the analytic expression

$$E_{\text{IAS}} \approx \Delta M \mp \Delta m_{\text{np}} \pm \frac{6 Z \alpha \hbar c}{5 R} \quad \text{with} \quad R = 1.12 \text{fm} A^{1/3} + 0.78. \quad (2.72)$$

Here, Δm_{np} is the proton-neutron mass difference and the respective upper signs correspond to the case of neutrinos while the bottom signs are for antineutrinos. Since this shift is applied globally to all single particle states, it can lead to states being shifted to negative energies in the product nucleus. This happens for example for the reaction $^{26}\text{Mg} + \nu_e$ that is discussed in detail in Section 5.1.



3 Astrophysical considerations

In this work we use a range of stellar models for massive stars as the starting point of our calculations. Here we give a short overview of the principles that determine the evolution of stars.

3.1 Principles of stellar evolution

A major part of the evolution of stars is governed by the timescales of the nuclear processes at the center that are of the order of thousands to billions of years. Thus, it is important to understand that observations never allow us to see the dynamics of stellar evolution. Only by observing samples with different ages we can infer how the evolution should proceed. In terms of numerical modeling, this justifies the assumption of hydrostatic equilibrium, i.e. the stellar plasma settles into the equilibrium configuration corresponding to the composition and temperature effectively instantaneously. Furthermore, observational evidence suggests that most stars do not rotate at significant speeds. Therefore, distortions by rotation can be neglected in the most general cases and the assumption of spherical symmetry is well justified. This reduces the modeling of stellar structure effectively to a one-dimensional problem with the radial coordinate r . However, the size of stars varies significantly during their evolution and since the composition is a major aspect that determines the evolution, it is more convenient to look at mass elements that move with the velocity of the fluid, which we assume to be zero in hydrostatic equilibrium. In this picture, we replace the radial coordinate by the mass coordinate $M(r)$, or the enclosed mass, which is defined as

$$M(r) = \int_{\text{center}}^{\text{surface}} 4\pi r^2 \rho(r) dr, \quad (3.1)$$

corresponding to

$$dr = \frac{1}{4\pi r^2 \rho(r)} dM. \quad (3.2)$$

The equilibrium configuration is described by the balance between gravity and the pressure gradients for each mass element. Thus, stellar structure is determined by the equation

$$\frac{dP}{dM} = \frac{1}{4\pi r^2} \frac{GM(r)}{r^2} \quad (3.3)$$

The Pressure results from the thermal pressure of the ions, electrons, radiation and in the case of very high density also neutrinos need to be included

$$P = P_{\text{ion}} + P_e + P_{\text{rad}} + P_\nu. \quad (3.4)$$

Thermal pressure and the contribution from equilibrium photons are connected to density and temperature by an equation of state. Massive stars in the mass range we study here, remain non-degenerate for most of their evolution. Then the thermal pressure can be taken from the ideal gas law as

$$P_{\text{ion}} = n_{\text{ion}} k_B T = \frac{\rho}{\mu m_u} k_B T \quad (3.5)$$

where k_B is the Boltzmann constant, n_{ion} the number density of ions, m_u the atomic mass unit and μ the mean molecular weight of the gas particles. For low densities the electron pressure can also be described as $P_e = n_e k_B T$. However, towards the end of their lives, also massive stars reach conditions where the electrons in the core become degenerate and contribute a significant component to the pressure. In general the pressure can be calculated by integrating over the distribution function f_e as

$$P_e = \frac{8\pi}{3h^3} \int_0^{\infty} p^3 v(p) f_e(p_e) dp_e, \quad (3.6)$$

where p_e is the electron momentum and v the velocity. Electrons follow a Fermi-Dirac distribution

$$f_e(E) = \frac{1}{1 + \exp((E_e - \mu_e)/k_B T)} \quad (3.7)$$

with chemical potential μ_e . Under degenerate conditions the Pressure is almost independent of the temperature $P_e \approx P_e(\rho)$ which has important contribution for the evolution, because the temperature can increase, e.g. due to nuclear reactions, without a corresponding increase in pressure. This can lead to a thermonuclear runaway and explosive flashes, particularly in the evolution of low- and intermediate mass stars.

For radiation we have $P_{\text{rad}} = \frac{1}{3}aT^4$ with the radiation constant a . Neutrinos only play a role for the pressure at very high densities. When the density gets close to the nuclear saturation density of around $2.3 \times 10^{14} \text{g/cm}^3$, ions become degenerate and the nuclear interaction contributes to the pressure. The equation of state of nuclear matter plays a crucial role for the final core collapse and the explosion of massive stars and various approaches have been developed to describe nuclear matter (Oertel et al., 2017). In Section 5.4 the effect of two different models on the neutrino properties is discussed. In addition to these equation we get equations from the conservation of energy and for energy transport including the luminosity. The full set of equations can be found in textbooks on stellar evolution, e.g. Kippenhahn et al. (2012) or Lamers & Levesque (2017).

3.2 Massive star evolution

In this work a wide range of stellar models that differ in their initial mass are discussed. The final nucleosynthesis yields from the supernova are strongly affected by the structure and composition of the star before the explosion, which results from the hydrostatic evolution. In order to understand the resulting nucleosynthesis, including the role of neutrinos in the final explosive phase, the most important aspects of the evolution of massive stars are summarized. The birth of a star is the point at which a gravitationally self-bound cloud of gas has collapsed to provide the density and temperature to ignite Hydrogen fusion. Hydrogen fusion releases about 8×10^{18} erg/g. In terms of energy generation Hydrogen is the most efficient fuel. Therefore, it is also the coldest and longest phase because only a few reactions are necessary to produce enough pressure to maintain hydrostatic equilibrium as defined in Equation (3.3). Stars spend most of the time of their lives in the Hydrogen burning phase and therefore most stars that are observed are Hydrogen burning stars. This phase is also referred to as main sequence. Depending on their initial mass and age the surface properties of main sequence stars, e.g effective temperature T_{eff} and luminosity L_* differ. T_{eff} is the temperature of a black-body spectrum that produces the observed luminosity. A hotter surface also means that light is emitted mostly in the blue part of the optical spectrum while low temperatures correspond to red stars. The black-body spectrum that is fitted to the observed spectrum gives the color temperature.

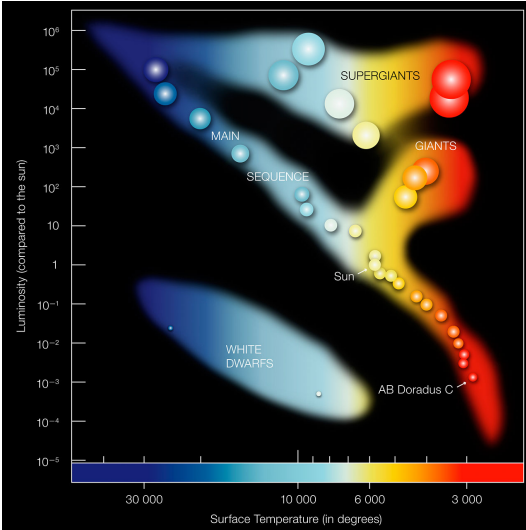


Figure 3.1.: Schematic HR-diagram [Image credit: ESO]

More massive stars need to burn hotter to maintain hydrostatic equilibrium and with the larger radiation pressure the envelope expands, increasing the luminosity. This allows astronomers to infer the mass of stars from their position in the $T_{\text{eff}} - L_*$ plane, which is called Hertzsprung-Russell diagram which was introduced by Hertzsprung in 1905 [Hertzsprung & Hermann \(1976\)](#) and refined by Russell in 1914 [Russell \(1914\)](#) who were working on the classification of stellar spectra. Figure 3.1 shows a schematic modern HR-diagram. Hydrogen burning stars are located on the main sequence. With more massive star burning brighter and hotter. Branches correspond to evolved stars that have expanded to luminous giants due to advanced nuclear burning stages or white dwarfs, which are the remnants of low and intermediate mass stars.

The position of a Hydrogen burning star on the main sequence is determined mostly by its mass. The width of the observed main sequence is mostly due to the different age of the stars. Empirically the luminosity of a star L_* can be related to the stellar mass M_* by a power law scaled to the solar values as

$$\frac{L_*}{L_{\odot}} \approx \left(\frac{M_*}{M_{\odot}} \right)^{\alpha}, \quad (3.8)$$

where L_{\odot} and M_{\odot} indicate the solar luminosity and mass respectively. About 80-90% percent of all stars that are observed in our stellar neighborhood are currently on the main sequence. The main sequence is not a perfectly straight line but has a finite width, that results varying initial composition and different stages of evolution. The mass of a star can change dramatically during its evolution, as we will discuss later, but the mass that determines it's initial position on the HR-diagram, i.e. its mass at the onset of Hydrogen burning also largely determines the whole evolution of single stars. Therefore, the Zero-age main sequence (ZAMS) mass is usually taken to identify a stellar model.

In low to intermediate mass stars and for very old stars that contain essentially nothing but Hydrogen, the nuclear burning during the main sequence proceeds through the pp chains that start from the reaction $p(p, e^+ + \nu_e)^2\text{H}$. Since this reaction involves the weak interaction it is the slowest process with a timescale of approximately 10^9 years. As soon as a deuteron is produced it undergoes $^2\text{H}(p, \gamma)^3\text{He}$ on a much shorter timescale. If no ^4He has been produced yet, the only way to proceed is $^3\text{He}(^3\text{He}, 2p)^4\text{He}$ which is responsible for the bulk of the energy generation with a Q-value of 12.9 MeV. This process is the ppI chain. If ^4He is already present and the temperature is sufficiently high, Hydrogen burning can proceed via $^3\text{He}(\alpha, \gamma)^7\text{Be}(e^-, \nu_e)^7\text{Li}(p, \alpha)^4\text{He}$ (ppII chain). These reactions are also very important or the production of ^7Li by the ν process. At even higher temperatures the electron capture on ^7Be is replaced by a proton capture and the resulting ^8B quickly β decays to ^8Be that dissolves in to two α particles. Detailed discussions of these processes can be found e.g. in [Iliadis \(2007\)](#) and [Maeder \(2009\)](#). Details about the evolution of metal-free stars are discussed e.g. by [Heger & Woosley \(2010\)](#).

For massive stars with solar metallicity in the mass range that is discussed in this thesis, Hydrogen burning typically proceeds via the Carbon-Nitrogen-Oxygen (CNO) cycles. In these cases the weak interaction process $p(p, e^+ + \nu_e)^2\text{H}$ of the ppI chain is bypassed by reaction sequences initiated by (p, γ) reactions on ^{12}C , ^{14}N or ^{16}O . These processes can proceed much faster than the pp-chains and lead to a characteristic rearrangement of the abundances of the involved nuclei. The $^{14}\text{N}(p, \gamma)$ is the slowest reaction and the abundances of ^{14}N increases substantially. ^{13}C and ^{18}O are produced which is important for the production of ^{19}F in the explosive burning phases as discussed in Section 5.2.2. Due to the higher Coulomb barriers in the CNO cycles, the reactions are more sensitive to temperature and large temperature gradients develop. As a consequence the H burning cores of massive stars are convective. In a convective core the entropy profile is flat and due to convective mixing the composition is the same over the whole region where convection is active. We see such effects in the mass fraction profiles of the various models discussed in the results. This also allows the burning process to proceed uniformly throughout the core. Massive stars have a basically flat entropy profile at birth with value around $20 - 30 k_B$ per baryon ([Woosley & Weaver, 1986](#)). Convective stability requires the profile to stay either flat or to increase towards the surface. As central nuclear burning proceeds, entropy is carried away, first by photon and during later stages increasingly by neutrinos.

As Hydrogen is converted to Helium, the Helium ashes accumulate in the center. Once the Hydrogen fuel is depleted, the He core contracts. Depending on the progenitor mass Hydrogen burning can be ignited in a shell around the core dumping more He onto it and accelerating the contraction. According to the virial theorem, a fraction of the gravitational binding energy gained by contraction is turned into internal energy. Therefore, a star's interior must heat up, as it continues to contract ([Kippenhahn et al., 2012](#)).

The next viable fuel for fusion reactions is ^4He . However, Helium fusion is problematic, because the immediate fusion product ^8Be is unstable with a very short half-life of 8.17×10^{-17} s. Therefore, the reaction needs to proceed through an effective 3-body reaction, the triple α process. In order to explain the existence of Carbon - and thus life - in the universe, [Hoyle \(1954\)](#) postulated the existence of a resonant state in ^{12}C to speed up the process which was later experimentally confirmed ([Almqvist et al., 1959](#)).

Despite this particular resonance, the triple α reaction is kinematically unfavorable because it requires three particles to be in the same spot at the same time. Therefore, $3^4\text{He} \rightarrow ^{12}\text{C}$ is in direct competition with $^{12}\text{C}(\alpha, \gamma)^{16}\text{O}$. For massive stars with a ZAMS mass of more than $20 M_\odot$, He burning occurs under very hot conditions and the product is mostly ^{16}O . Furthermore, the formation of a Hydrogen burning shell towards the end of convective He burning leads to the addition of fresh fuel that also decreases the production of ^{12}C .

The reaction rates for the triple α process and $^{12}\text{C}(\alpha, \gamma)^{16}\text{O}$ are therefore of paramount importance for stellar evolution. At the same time, those reactions are particularly challenging to measure because they involve the interfering tails of sub-threshold resonances and the energies relevant in the astrophysical context are very low. High precision measurements of these rates require very long-term experiments

with high current and low energy beam and extremely low background. One of the most successful facilities for the measurement of reaction cross-sections relevant for hydrogen and He burning in recent years is the LUNA (Laboratory for Underground Nuclear Astrophysics) project deep underground at the Gran Sasso Laboratory (Broggini et al., 2018; Strieder & Rolfs, 2007) or future shallow underground experiments (Bemmerer et al., 2016).

These rates determine how much Carbon a massive star can produce and set the prerequisite for the following evolution. Weaver & Woosley (1993) have even suggested to constrain the $^{12}\text{C}(\alpha, \gamma)^{16}\text{O}$ reaction rate by nucleosynthesis arguments, requiring that the yields of the key products of He burning should agree with their solar values. The He-burning reaction rates even have a significant impact on the production of light elements by the ν process Austin et al. (2014) because it affects the size and composition of the Carbon-rich zones.

In addition to the production of ^{12}C and ^{16}O the high temperatures also allow for the further α captures that result in mass fractions of ^{20}Ne of around 1% at the end of He burning. Also ^{22}Ne is produced from the CNO abundance of ^{14}N via $^{14}\text{N}(\alpha, \gamma)^{18}\text{F}(\beta^+ \nu_e)^{18}\text{O}(\alpha, \gamma)^{22}\text{Ne}$. The ^{18}O produced in this process is very important for the thermonuclear production of ^{19}F that complements its production via the ν process that is discussed in Section 5.2.2. We will also see that ^{22}Ne is the seed for the production of ^{22}Na in the ν process. He core burning in massive stars (i.e. with ZAMS masses exceeding $11 - 13 M_{\odot}$) is also the site for the weak component of the s -process (The et al., 2000) that is discussed in more detail in Section 3.4 and can lead to the production of nuclei with masses up to around $A \approx 90$. These heavy elements can be important seeds for the production of radioactive isotopes via the ν process. The neutron source for this process is $^{22}\text{Ne}(\alpha, n)$ which is also an important source of neutrons during the explosion. In the case of He burning ^{22}Ne requires the presence of ^{14}N that is a product of the CNO cycle. Therefore, the weak s -process is suppressed in low-metallicity stars.

The modeling of stellar evolution beyond the main sequence is a complex multi physics problem but it has been understood for a long time that Supernovae are an important component of nucleosynthesis (Burbidge et al., 1957). After He burning the composition of the core is dominated by ^{12}C and ^{16}O . Even though Oxygen is typically more abundant than Carbon for massive stars, the next burning process to ignite is $^{12}\text{C} + ^{12}\text{C}$ because it has the lower Coulomb barrier compared to $^{12}\text{C} + ^{16}\text{O}$ and $^{16}\text{O} + ^{16}\text{O}$. The Q-Value of Carbon fusion is 14 MeV and therefore the highly excited ^{24}Mg mostly sheds its energy by particle emission. The most important reactions in C-burning are $^{12}\text{C} + ^{12}\text{C} \rightarrow ^{20}\text{Ne} + ^4\text{He}$ with a Q-value of 2.24 MeV, $^{12}\text{C} + ^{12}\text{C} \rightarrow ^{23}\text{Na} + p$ with a Q-value of 4.62 MeV and $^{12}\text{C} + ^{12}\text{C} \rightarrow ^{23}\text{Mg} + n$, which is endothermic and requires 2.6 MeV of additional energy. While ^{16}O remains the most abundant nucleus the main product of C burning which takes of the order of 1000 years till C exhaustion is ^{20}Ne , followed by ^{24}Mg which is produced by $^{20}\text{Ne}(\alpha, \gamma)$ and $^{23}\text{Na}(p, \gamma)$ and not directly by the Carbon fusion. The released α particles also induce $^{22}\text{Ne}(\alpha, n)$. During central Carbon burning the stellar core can heat up to 0.6 – 1.0 GK and the liberated free protons and neutrons lead to the production of ^{25}Mg , ^{26}Mg and ^{27}Al - nuclei with neutron excess - while the abundance of ^{22}Ne is reduced by about a factor 10, removing an important neutron source and the seed for ^{22}Na in the ν process. ^{22}Ne , ^{25}Mg , ^{26}Mg and ^{27}Al remain with mass fractions of around 10^{-3} at core C exhaustion.

Following Carbon burning the core contracts again and heats up further. Before Oxygen fusion becomes possible, the temperature exceeds values of 1.5 GK at which $^{20}\text{Ne}(\gamma, \alpha)$ becomes important. With a Q-value of -4.7 MeV this reaction alone cannot stabilize the star against contraction. However, the released α particles power the conversion of ^{20}Ne to ^{28}Si with a Q-value of almost 20 MeV as well as $^{23}\text{Na}(\alpha, n)^{26}\text{Mg}(\alpha, n)^{29}\text{Si}$ which have a combined Q-value of 1.85 MeV. The net reaction flow is $2 ^{20}\text{Ne} \rightarrow ^{16}\text{O} + ^{24}\text{Mg}$. The energy release of around 5.3×10^{17} erg/g can support the star only for a few hundred days. ^{26}Al is produced by $\text{Mg}(p, \gamma)$ during core and shell Ne-burning. $^{21}\text{Ne}(\alpha, n)$, $^{25}\text{Mg}(\alpha, n)$ and $^{26}\text{Mg}(\alpha, n)$ provide a small flux of neutrons that drive (n, γ) reactions, further increasing the abundances of ^{26}Mg , ^{27}Al and ^{29}Si . ^{16}O remains the most abundant nucleus.

Following Ne burning the stellar core contracts again and heats up. For the next fusion reaction the Oxygen ions need to overcome a 13 MeV Coulomb barrier giving a Gamow peak at or 6.6 MeV. At

such energies, the reaction cross-section could be measured (e.g. by [Thomas et al. \(1986\)](#); [Fernandez et al. \(1978\)](#)) for energies close to the Gamow window and well within the energy range relevant for the explosive burning. and it does not exhibit any isolated resonances because the reaction proceeds through many overlapping states in ^{32}S .

Depending on the initial mass and composition of the star, at a temperature of between 1.5 and 2.7 GK the Oxygen burning process sets in. The compound nucleus ^{32}S is created with high excitation energy and decays mostly by the emission of light massive particles, yielding mostly ^{28}Si , ^{30}Si , ^{31}S and ^{31}P . In endothermic reactions also ^{24}Mg and ^{30}P can be produced. As in Carbon burning, the released protons, neutrons and α particles can engage in variety of secondary reactions with the products of Ne burning. These secondary reactions also contribute substantially to the energy budget of the burning process. The proton, neutron and α separation energies of the most abundant nuclei ^{16}O , ^{24}Mg and ^{28}Si are relatively large and therefore at these temperature they are affected by photodissociation reactions and in particular for ^{16}O the fusion reaction is dominant channel for its depletion. Oxygen burning, including the most important secondary reactions releases about 3.24×10^{23} erg/g, exceeding the energy generation during C and Ne burning. Due to the large Coulomb barrier the reaction rate is extremely sensitive to the temperature with $\propto T^{34}$. In addition to ^{28}Si , the main products of Oxygen burning are ^{32}S , $^{36,38}\text{Ar}$ and $^{40,42}\text{Ca}$. In the ν process ^{36}Ar is a seed for the production of ^{36}Cl and ^{40}Ca leads to the production of ^{40}K by neutrino absorption. The reaction cross-section for $^{35}\text{Cl}(p, \gamma)^{36}\text{Ar}$ is based on measurements in the relevant energy range ([Iliadis et al., 2001](#)) as well as $^{30}\text{Si}(p, \gamma)^{31}\text{P}$, $^{32}\text{S}(\alpha, p)^{35}\text{Cl}$, $^{24}\text{Mg}(\alpha, p)^{27}\text{Al}$ and $^{30}\text{P}(\gamma, p)^{29}\text{Si}$, reducing the uncertainty of these reaction rates to the level of 20%. This is particularly important for the scope of this thesis because the ν process accompanies explosive Oxygen burning that also involves these reactions. For this burning process, only a few reactions remain that are still based on statistical model calculations ([Rauscher & Thielemann, 2000](#)), $^{31}\text{S}(\gamma, p)^{30}\text{P}$, $^{33}\text{S}(n, \alpha)^{30}\text{Si}$ and $^{29}\text{Si}(\alpha, n)^{32}\text{S}$. Oxygen burning reaches completion typically on the timescale of ~ 100 days.

In contrast to Carbon burning, the nuclear reaction do not cease once Oxygen is depleted. Due to the high temperatures that are reached towards the end of Oxygen burning some radiative capture reactions come into equilibrium with their inverse photodissociation reactions. In that way, the abundances of free protons and α particles remain almost constant. This leads to whole groups of nuclei to achieve equilibrium within quasi-equilibrium-clusters that exchange material by non-equilibrium flows between them.

As the core heats up further the number of nuclear reactions in equilibrium increases. Direct ^{28}Si fusion never occurs but for core temperatures between 2.8 – 4.1 GK a nuclear rearrangement usually called Si burning sets in. During this phase, the composition changes via quasi-equilibrium reaction flows. Two major QSE clusters form around $A = 25\text{--}40$ and $A = 46\text{--}64$, with the later including the Fe-group. The reactions within these two groups of nuclei are in equilibrium but while the abundance of the nuclei around ^{28}Si decreases, the total abundance in the Fe-group increases. Thus, in total the net reaction flow proceeds as $2\ ^{28}\text{Si} \rightarrow\ ^{56}\text{Ni}$ via a range of α and proton capture reactions that are give a net energy gain. Compared to the previous burning processes the energy release is small and the reactions need to proceed fast. The equilibrium (NSE, see Section 2.1.5) composition dominated by Fe group nuclei is reached on the timescale of hours. Once this condition is reached there is no further energy release from nuclear reactions.

[Truran et al. \(1967\)](#) were the first to show with numerical calculations how the Fe peak that can be seen in the solar system abundances can be obtained from the nucleosynthesis in a supernova shock wave from NSE material. Before calculations of whole stellar models have been computationally feasible, a large range of simplified models have been calculated, modeling individual burning stages under static conditions ([Rakavy et al., 1967](#)). Piecing together the composition of different phases of stellar evolution quickly lead to the first studies on the impact on a galactic scale [Truran & Cameron \(1971\)](#) [Weaver et al. \(1978\)](#) finally developed a computational model for stellar evolution and collapse that allowed to follow the evolution of a massive star all the way from its formation to core collapse.

The fate of stars in an intermediate regime of 9-11 M_{\odot} is determined by a complex competition between degeneracy, weak interactions and possible explosive burning (Woosley & Heger, 2015a). In this work we concentrate on stars heavier than this, which are expected to mostly form iron cores and end their lives in spectacular supernova explosions. Some of the stars more massive than 20 M_{\odot} could finally form black holes. Multiple studies have addressed the connection between a stars ZAMS mass and its final fate (Ebinger et al., 2018; Ertl et al., 2015; Ugliano et al., 2012), but due to the unknowns involved in the explosion mechanism explained in Section 3.3.2 this connection remains highly uncertain at this point.

What we have discussed in this section mostly applied to the evolution of single massive stars. However, most stars are actually found with a companion and depending on their distance they can exchange mass and influence the evolution of one another. See Langer (2012) for a review on the evolution of binary stars. Furthermore, stars can rotate. While the rotational frequencies of many observed stars are relatively small and unlikely to have a significant effect on the stellar evolution, this is not always the case and for example Ekström et al. (2012); Hirschi et al. (2004) have investigated stellar models with rotation in great detail. In this work we always use non-rotation models of single stars.

3.2.1 Initial Mass Function (IMF)

The composition of the solar system is not the result of a single supernova explosion, by many generations of stars with different masses contribute. In order to judge the agreement between a nucleosynthesis model and observations it would in principle be necessary to model the whole history of star formation, evolution and explosion (Côté et al., 2016). As a first approximation however, it is useful to just look at the most recent generation of stars that have formed from material with solar metallicity and take an average over a suitable range of main sequence masses taking into account that less massive stars are more common than more massive ones.

In 1955 Salpeter Salpeter (1955) has developed the concept of a initial mass function (IMF) that is still commonly used today The IMF gives the probability to find that a star of a mass m_* form as $P \propto m_*^{-(\alpha+1)}$ and $\alpha = 1.35$ has been inferred from observations. Knowing the yield $Y_A(m_*)$ for a range of stellar masses m_* , we can define the IMF averaged yield of a nucleus A as

$$\langle Y_A \rangle_{\text{IMF}} = \frac{1}{m_2^{-\alpha} - m_1^{-\alpha}} \int_{m_2}^{m_1} Y_A(m_*) m_*^{-(\alpha+1)} dm_* \quad (3.9)$$

In the same way we can calculate an average production factor, which we define here always normalized to ^{16}O as

$$P_A^f(m_*) = \frac{Y_A(m_*)/Y_A^{\odot}}{Y_{(^{16}\text{O})}(m_*)/Y_{(^{16}\text{O})}^{\odot}}, \quad (3.10)$$

where Y_A^{\odot} is the solar abundance of the isotope under consideration. This factor takes into account that Supernovae are the main producers of ^{16}O and hence the abundances of isotopes that are co-produced in Supernovae should scale in the same way. A production factor $P_A^f(m_*) \approx 1$ indicates that Supernovae are likely to be the main source of this isotope and using the IMF average, we can include the contributions from a whole range of stars.

3.3 Supernova Explosions

Finally, after all the hydrostatic burning stages are completed and the nuclear fuel is exhausted, a massive star ejects most of the material outside the Iron core in a brilliant supernova explosion. As the explosion shock propagates through the star, the final phase of nucleosynthesis occurs on a much shorter timescale and under the influence of neutrinos. In this section the process of core collapse and the mechanism that leads to the supernova explosion are presented.

3.3.1 Core collapse

Once a star has formed an Iron core, it cannot generate more pressure by nuclear reactions and the collapse becomes inevitable. A sufficiently small core can be sustained like a white dwarf by the pressure of degenerate electrons. For vanishing entropy the maximum mass that can be supported by relativistic degenerate electrons is the Chandrasekhar mass

$$M_{Ch,0} = 1.44 M_{\odot} \times (2 Y_e)^2 \quad (3.11)$$

that depends on the electron fraction Y_e . In contrast to a cold and isolated white dwarf, the iron core of a massive star is hot and surrounded by the stellar plasma. Due to finite temperature effects [Baron & Cooperstein \(1990\)](#) have derived an improved estimate for the maximum mass of a stellar Fe core with corrections due to Coulomb interactions as well as thermal pressure from electrons and ions as

$$M_{Ch}^{(b)} = M_{Ch,0} \left[1 - 0.057 + \left(\frac{s_e}{\pi Y_e} \right)^2 + 1.21 \left\langle \frac{1}{A} \right\rangle s_e \right] \quad (3.12)$$

depending on the electronic entropy

$$s_e = 0.56 k_B \left(\frac{Y_e}{0.5} \right)^{2/3} \left(\frac{10^{10} \text{g/cm}^3}{\rho} \right)^{1/3} \left(\frac{T}{\text{MeV}} \right). \quad (3.13)$$

Here, $\langle \frac{1}{A} \rangle$ is the inverse atomic mass averaged over the composition. (3.12) gives the maximum mass for a static configuration. For the hydrodynamic stability of the core against small perturbations an effective adiabatic index $\partial P / \partial \rho > 4/3$ is required ([Janka, 2012](#); [Woosley et al., 2002](#)). However, there are three main effects that do not allow the formation of a stable Fe white dwarf as a remnant of a massive star. First, as the core continues to contract, the increasing temperature leads to a shift of the composition determined by nuclear statistical equilibrium (NSE). At high temperature, NSE increasingly favors free α particles and nucleons over the heavy Fe group nuclei. This process of photodissociation is endothermic and the abundance of high energy photons effectively shrinks. This reduces the radiation pressure and decreases the adiabatic index. From Equation (3.12) it is not obvious that the maximum mass is also decreased. Increasing the number of particles increases the ionic entropy and since the process is adiabatic except for neutrino losses, the electronic entropy s_e must decrease. This effect is more relevant for more massive stars which form hotter and less degenerate Fe cores. If the core is dominated by electron degeneracy, a more important effect is the reduction of the electron fraction Y_e . As density increases the Fermi energy of the degenerate electrons also increases and electron captures first on nuclei and later on nucleons become more frequent. This lowers the electron fraction Y_e and hence the contribution from electron degeneracy to the pressure. From Equation (3.11) we can also see that it decreases the supportable mass. Electron captures also have an important impact on the composition that is dominated by increasingly neutron rich nuclei and later free neutrons. Furthermore, Si burning can continue in a shell around the core, increasing its mass even further. All of these effect accelerate the

collapse and the timescale for the neutrinos to diffuse out of the core eventually becomes longer than the free-fall timescale that we estimate at a position r where a mass of $M(r)$ is enclosed via the average density $\bar{\rho}$ following [Woosley & Heger \(2015b\)](#) and [Müller et al. \(2016a\)](#) as

$$t_{\text{ff}} = \sqrt{\frac{\pi}{4G\bar{\rho}}} \quad \text{with} \quad \bar{\rho} = \frac{4\pi}{3} \frac{M(r)}{r^3}. \quad (3.14)$$

As a result, the neutrinos cannot leave the core and become trapped leading to a constant lepton content that effectively blocks further electron captures because the available phase space for the emission of neutrinos becomes small. While the core contracts the gravitational binding energy of the central object increases. The long-standing basic conundrum at the core of supernova explosions lies in the link between the large amount of energy available in the form of the gravitational binding energy of the neutron star - which is of the order of 10^{53} erg - and the observed kinetic energy of the ejected material. The explosion energy is only of the order of 10^{51} erg and hence, it seems plausible that some mechanism transfers about one percent of the energy to the stellar mantle, to eject it. This already shows, that this mechanism must be comparatively inefficient. The dominant cooling mechanism that carries away the gravitational energy of the proto-neutron star is the emission of neutrinos and [Colgate & White \(1966\)](#) have already suggested the neutrino driven mechanism to turn the collapse into an explosion. In the next Section this mechanism which is the basic assumption of the work presented in this thesis, is discussed.

3.3.2 The neutrino driven explosion mechanism

While the observational signatures and energetics of supernova explosions are readily inferred, the mechanism behind the explosion has remained elusive and controversial for decades.

As the collapsing core reaches nuclear densities around $2.7 \times 10^{14} \text{ g/cm}^3$, the equation of state becomes dominated by effects of the strong interaction. The repulsion between nucleons provides a new pressure component to resist the infalling material.

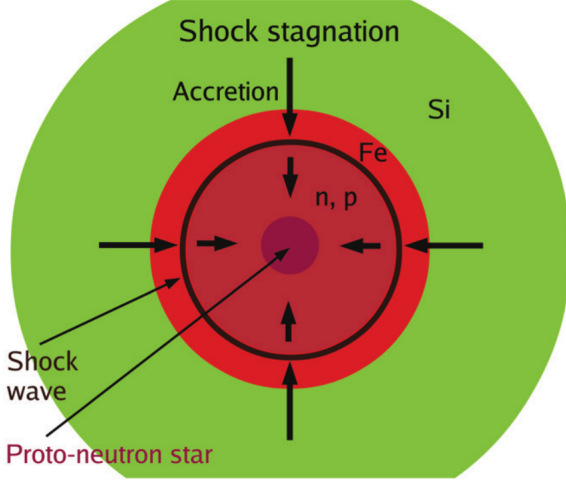


Figure 3.2.: Schematic illustration of the standing accretion shock following core bounce. The initial bounce shock has lost most of its initial energy due to the dissociation of the Fe core material into free nucleons. Figure from Janka (2012).

matter behind the shock consists of free neutrons and protons while the Fe core material is in front of the shock. This is illustrated in Figure 3.2. The deceleration of the shock leads to a negative entropy gradient that gives rise to an episode of prompt post-shock convection which is an important source of gravitational waves (Kotake, 2013; Ott, 2009). Without any further energy input, even though the shock keeps moving outward in mass, the radial velocity decreases and the shock stagnates. A standing accretion shock is formed through which material keeps on falling onto the proto-neutron star. The early phase of bounce shock and shock stagnation has been studied by many groups and general agreement has been reached (Buras et al., 2006; Liebendörfer et al., 2001). In simulations without neutrino effects, the shock starts to recede and the collapse continues leading to the formation of a black hole. In the neutrino driven mechanism the neutrinos that govern the dynamics of the contraction and cooling of the proto-neutron star by carrying away the potential energy are able to revive the stalled supernova shock. The almost adiabatic infall of the accreted matter results in a temperature profile as $T \propto r^{-1}$ and a density profile as $\rho \propto r^{-3}$. Absorption of mostly electron neutrinos and antineutrinos depends of the neutrino properties and gives a heating rate as

$$\dot{q}_{\text{heat}} \propto \frac{L_{\nu} \langle E_{\nu} \rangle}{4\pi r^2}. \quad (3.15)$$

In contrast to that the neutrino cooling has a very steep temperature dependence

$$\dot{q}_{\text{cool}} \propto T^6 \propto r^{-6}. \quad (3.16)$$

Based on these relations [Bethe \(1993\)](#) has motivated the existence of a gain layer between the neutrinosphere and the supernova shock, a region where the neutrino heating dominates. If the energy deposition by neutrinos in this layer is sufficient the stalled shock can be revived and [Janka \(2001\)](#) has developed the notion of a critical neutrino luminosity that is required for a successful explosion. Hence, the explosion is very sensitive to the neutrino emission and a useful picture for qualitative understanding of the general features of the neutrino properties are the neutrinospheres.

The radius of the neutrinosphere R_ν for a given neutrino species is defined as the radius at which the optical depth is $2/3$. It marks the position where the neutrinos can no longer be considered to be in thermal equilibrium with matter. Since opacities are energy dependent, there is in principle no unique neutrinosphere for a neutrino species but an energy averaged value can be defined. [Liebendörfer et al. \(2003\)](#) have pointed out that this picture is overly simplified, but it is sufficient for the general discussion at this point. The average neutrino energies are of the order of a few to maximally 20 MeV. Thus, they are not sufficient for the production of heavy flavor leptons μ^\pm or τ^\pm .

Only electron neutrinos and antineutrinos interact via the charged currents which leads to larger opacities and shorter mean free paths for ν_e and $\bar{\nu}_e$. Consequently the corresponding neutrinospheres are at lower densities, larger radii and thus lower temperature. Therefore, a general hierarchy of the average neutrino energies is expected

$$\langle E_{\nu_e} \rangle < \langle E_{\bar{\nu}_e} \rangle \leq \langle E_{\nu_x} \rangle. \quad (3.17)$$

As matter behind the accretion shock keeps on falling in, the mass of the proto-neutron star increases. As a consequence, temperature and density increase and the neutrinospheres move inward. This leads to a rise in the average neutrino energies that is roughly proportional to the mass of the remnant $E_\nu \propto M_{\text{PNNS}}$ ([Müller & Janka, 2014](#)). The neutrino heating rate also increases and makes the conditions more favorable for an explosion as time evolves. Due to the larger cross-section of charged current reactions, electron flavor neutrinos also dominate the heating. However, the unbinding of the material by neutrino heating competes with the ongoing accretion.

[Müller et al. \(2016a\)](#) have developed a semi-analytical model to predict the explosion properties of a stellar model based on the criterion that the heating timescale τ_{heat} for depositing enough energy by neutrino heating to unbind the material needs to be shorter than the advection timescale τ_{adv} that corresponds to the average time material spends in the gain region. The advection timescale can be increased substantially by convective overturns that can not be modeled in one-dimensional simulations. While the first spherically symmetric simulations including neutrino transport by [Bethe & Wilson \(1985\)](#) have shown successful explosions, improvements of the numerical treatment of neutrino transport and advances in the relevant microphysics have lead to the conclusion that one dimensional supernova simulations do not predict explosions for most cases ([Liebendörfer et al., 2001](#)). There are only a few cases of light progenitor models ([Nomoto & Hashimoto, 1988](#)) with ZAMS masses below $10 M_\odot$ that have been shown to successfully explode in one-dimensional simulations ([Hashimoto et al., 1993](#); [Kitaura et al., 2006](#)). These models have a very steep density gradient at the edge of the core and dilute He and H shells and only lead to very weak and faint explosions. It has been found that the multi-dimensional nature of supernovae is indeed crucial for the explosion. Two-dimensional supernova models have shown that self-consistent explosions with the neutrino driven mechanism are possible and in particular it has been found that convective overturns allow material to remain in the neutrino heating region for an extended period of time while the simultaneous accretion downflows feed the neutrino luminosity. In two-dimensional simulations the resulting explosion energies tend to be consistently too small to explain observations ([Summa et al., 2016](#); [O'Connor & Couch, 2018](#)).

This has lead to the realization that the behavior of turbulent energy cascades is fundamentally different between two- and three-dimensions ([Kraichnan, 1967](#); [Hanke et al., 2012](#); [Couch, 2013](#); [Couch & Ott, 2015](#)). The growth of large-scale turbulence is favored by two-dimensional simulations and

hence fast and weak explosions are found. While this is a large caveat for the predictive power of two-dimensional simulations they are important tools to improve the understanding of the fundamental physics that drive supernova explosions (Janka, 2012). In particular they include the important effects of multi-dimensional fluid flows and allow us to at least qualitatively explore possible effects on nucleosynthesis.

The first three-dimensional self-consistent supernova simulations have been performed (Couch & O'Connor, 2014; Melson et al., 2015) but Radice et al. (2016) have pointed out that the crucial scales are not yet fully resolved. While three-dimensional simulations of core-collapse supernova are improved, several methods have been proposed to incorporate the physics of multi-dimensional simulations in a parametrized way in one-dimensional models. This mostly involves systematically increasing the neutrino heating in with parameters adjusted to reproduce observations (Perego et al., 2015) or replacing the proto-neutron star with an fine-tuned engine (Ertl et al., 2016). Such approaches allow relatively cheap calculations of supernova explosions that are very well suited for nucleosynthesis studies. However, their predictive power remains to be evaluated.

The modeling of the dynamics is one important aspect for the modeling of successful explosions but Melson et al. (2015) have also shown that changes of the neutrino opacities of the order of 20% can be sufficient to turn non-exploding three-dimensional models into successful explosions. This shows that a successful supernova model requires a treatment of neutrino interactions in hot and dense matter with unprecedented precision. One aspect that significantly complicated the treatment of neutrino transport in the case of core collapse supernovae is, that it involves neutrino interactions on nucleons and nuclei in the hot and dense environment of a nascent proto-neutron star. Under such conditions, correlations between the particles and the medium become important for the interaction cross-section (Burrows & Sawyer, 1998). For example, Bartl et al. (2014) have found a significant enhancement of the rate for neutrino pair bremsstrahlung and absorption at supranuclear densities. Recently, Kotake et al. (2018) have systematically analyzed the effect of various improvements on top of the baseline set of neutrino opacities given by Bruenn (1985) the calculation of neutrino opacities for one-dimensional core-collapse supernova simulations. The neutrino luminosities are depend on the mass accretion rates and the rate at which the core contracts and heats up which in turn is determined by the equation of state that connects pressure, density and temperature for a given composition. However, for matter at densities beyond the nuclear saturation density at around, the equation of state is not very well known and the impact of different models on the supernova explosions has been the subject of various studies (e.g. O'Connor & Ott (2013) and Janka et al. (2012)). Softer equations of state for nuclear matter lead to a faster contraction that favors explosions because it leads to larger neutrino luminosities. such as the creation of muons in the PNS (Bollig et al., 2017) help to achieve explosions.

The final kinetic energy of the ejecta mostly results from the energy of nuclear recombination (Scheck et al., 2006). Nucleons recombine mostly to α particles and some heavier nuclei, gaining about 5 MeV per nucleon as estimated by Müller et al. (2016a). This is illustrated in Figure 3.3. As a result the final explosion energy is not set by the energy deposited by the neutrinos. Even after the shock is successfully

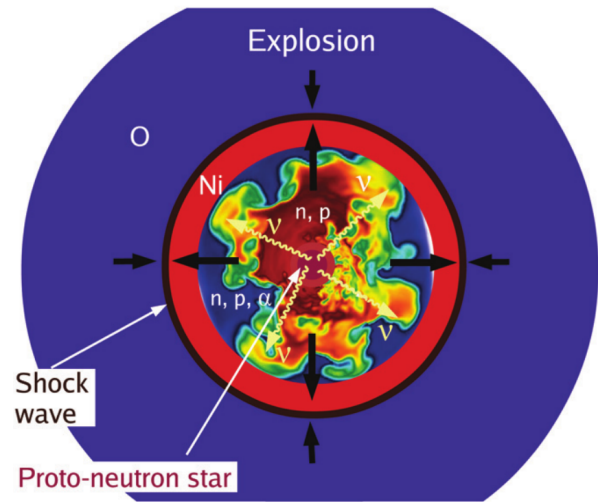


Figure 3.3.: Schematic illustration of a successfully revived shock. The shock front gains energy from the recombination of nucleons while the proto-neutron stars keeps on cooling by the emission of neutrinos. Figure from Janka (2012).

launched, the proto-neutron star keeps on contracting radiating away the gravitational binding energy mostly as neutrinos over a timescale of several seconds. The substantial fraction of the neutrinos, in particular the heavy flavor neutrinos, are produced thermally by nucleon-nucleon bremsstrahlung and electron-positron annihilation as

In this way all types of neutrinos are produced equally giving rise to the assumption that the total energy is distributed equally among the neutrino species which we also use to parametrically model the neutrino luminosities in Section 5.2. However, note that this is in principle only valid for the late cooling phase. The interior of the core is optically thick to neutrinos and they escape diffusively. As the shock runs into the Silicon, Oxygen and Neon shells, explosive nucleosynthesis (see Section 3.3.3) is triggered and the material is unbound. While the supernova shock is already moving out it has left behind a low density region above the proto-neutron star. The neutrinos from the hot core interact with the material in the outer parts of the neutron star crust which mostly consists of neutrons and a few protons. Simulations have shown that the energy deposition can be large enough to produce a neutrino driven wind which is discussed in detail in Section 3.4.3.

In this work we use a parametric explosion model calculated with a piston approach as already developed by (Weaver et al., 1978) (cf. Woosley & Weaver (1995) for updates on the model). A detailed description and evaluation of the approach along with and employed parameters for our models are given in Section 4.4. The delayed neutrino driven explosion mechanism is the currently favored explanation for supernovae and albeit low statistics forbid strong conclusions this picture is consistent with the observation of neutrinos associated with SN1987A (Arnett, 1987; Bethe, 1990). There are also other models, such as a hadron-quark phase transition (Fischer et al., 2011), jet-driven supernovae (Papish & Soker, 2014) and magneto-rotationally driven supernovae (Winteler et al., 2012; Mösta et al., 2015). that could account for an unknown fraction of all observed supernovae but could also make important contributions to the nucleosynthesis of heavy elements (Nishimura et al., 2015).

3.3.3 Explosive nucleosynthesis

Compression by the supernova shock heats material to temperatures far in excess of the hydrostatic burning stages. In these cases the timescale for nuclear processes are much longer than the hydrodynamic timescale. If, however, the dynamic timescale of the system and the one of nuclear reactions are similar, one speaks of explosive nucleosynthesis. For all the nuclear burning processes that have been discussed above, there are explosive equivalents that occur at a higher temperature proceed much faster. Towards the end of a star's life the nuclear reactions speed up and can come close to the hydrodynamic timescales. This happens in particular in the case of intense convective shell burning when the convective velocities can almost reach the speed of sound. (Woosley et al., 2002). In these cases explosive Carbon, Neon and even Oxygen burning can occur before the explosions. This has important consequences for the nucleosynthesis as we will see later. In most cases the explosive nucleosynthesis takes place during the supernova explosion. The He and C shells of massive stars are typically not heated sufficiently by the shock to ignite He or C burning explosively. However, the Si layer is entirely processed by explosive burning and a significant fraction of the O/Ne layer undergoes explosive Ne and O burning. The main reactions and also the products of the explosive burning are very similar to the hydrostatic cases discussed above. One important difference that was already pointed out by Arnett (1969) is the absence of weak interactions in the explosive process because of the comparatively low reaction rates of electron captures and β decays. Therefore, while hydrostatic Oxygen and Silicon burning leads already to a substantial neutron excess, i.e. decrease of the electron fraction Y_e , this is not the case for explosive Si-burning. This has important consequences for the nucleosynthesis, because the products of hydrostatic Silicon burning tend to deviate significantly from the solar abundances and Arnett (1969) suggests that it never leaves the star. How-

ever, Si-burning is required to explain the Fe peak. Explosive Si-burning is the solution to this problem.

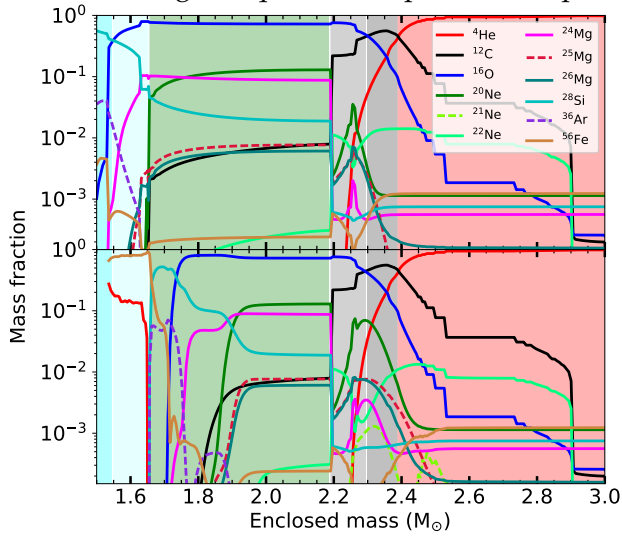


Figure 3.4.: Effects of the explosive nucleosynthesis for the $15 M_{\odot}$ progenitor model. The top panel shows the pre-supernova mass fraction profiles while the lower panel shows the profile for the supernova ejecta based on the calculations presented in 4.4.

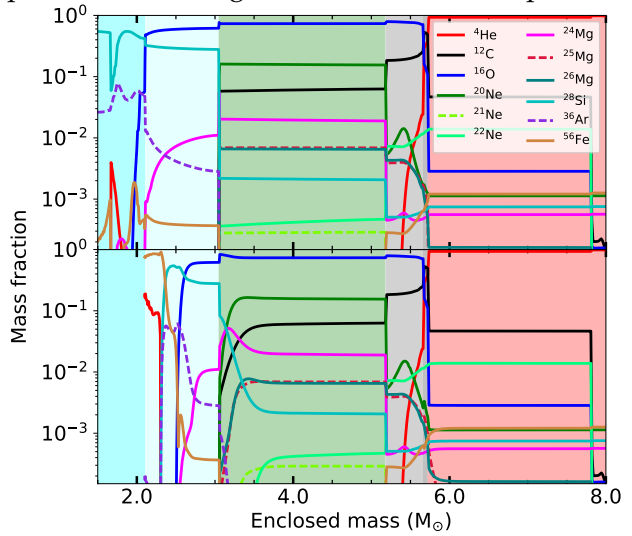


Figure 3.5.: Same as Figure 3.4 but for the more massive $25 M_{\odot}$ progenitor model.

Figures 3.4 and 3.5 illustrate the compositional layers and the effect of explosive nucleosynthesis for two different progenitor models. Here we go through the compositional structure from the core outward and explain the major features. Those are important for the connections between the ν process and the progenitor models discussed in Section 5.2. The background colors indicate the compositional layers in the pre supernova model. This color scheme is kept throughout this work and is used in all of the Figures showing compositional profiles to provide some orientation. The innermost layer is dominated by ^{28}Si and ^{56}Fe . Here Oxygen burning has been completed and Silicon burning has already set in. Further out ^{16}O and ^{28}Si , dominate the composition indicated by a different background color. Here, O-burning has not yet been completed but is ongoing or at least partially completed. Therefore, we refer to this region also as Si shell. The gradient in the composition indicates that the burning process is not fully convective. In the $15 M_{\odot}$ model we see a small region (small in terms of mass coordinate) where Ne burning has been completed and the composition is dominated by ^{16}O , ^{24}Mg and ^{28}Si . To avoid introducing another color we include this as Si shell. The next major compositional shell is dominated by ^{16}O and ^{20}Ne . This is one of the most important layers for the ν process. In addition to Oxygen and Neon, this region also contains residual ^{12}C that can vary significantly from star to star as we see here for the 15 and $25 M_{\odot}$ models. The C rich shells are indicated by gray background colors. As mentioned in Section 3.2, He burning often ends with a larger abundance of ^{16}O than ^{12}C . Therefore we distinguish between a region where ^{16}O is the most abundant species followed by ^{12}C (lighter gray), and a usually very narrow region where ^{12}C is the most abundant nucleus (darker gray). Only a bit further out, where He burning is incomplete a layer where the most abundant species is actually ^{12}C exists. This layer is also characterized by a substantial abundance of ^4He . Together with ^{22}Ne these α particles provide an important neutron source during the explosion. Finally, indicated in red is the He shell. Here, very little happens during the explosions as the temperature barely not exceeds 1 GK. However, the ν process allows for the production of ^7Li in this region. Epstein et al. (1988) suggested a neutrino-induced r -process in this region. This idea was not confirmed by the detailed calculations of Woosley et al. (1990) but remains a possibility for very compact metal-poor stars (Banerjee et al., 2011).

Comparing the upper and lower panels in Figures 3.4 and 3.5 show that explosive Si, O and Ne burning take place for a substantial fraction of the O/Ne shell. Beyond that, the explosion changes the main components of the composition only marginally. In the $15 M_{\odot}$ model, even before the explosion, the inner part of the O/Ne shell undergoes explosive burning that reduces the ^{12}C and ^{20}Ne abundances and increases ^{28}Si . As a by-product that is not show, this region is enhanced in more neutron rich isotopes such as ^{27}Al and as a consequence of the high temperatures a partial γ process already takes place before the explosion. The consequences of that for the production of ^{180}Ta are discussed in section 5.2.4. For the later discussion it is also important to note that explosive Oxygen burning at the bottom of the O/Ne shell leads to a substantial mass fraction of ^{36}Ar . The lighter α elements, O, Ne and Mg are depleted by the explosive Oxygen burning. In the transition region, where explosive O burning is not possible, the remaining ^{12}C is burnt leading to an increase of the ^{16}O abundance. Together with this, the secondary C-burning product such as ^{23}Na , ^{27}Al and also the radioactive ^{26}Al are produced. ^{26}Al is an important source of γ rays that can be detected for thousands of years after a supernova explosion. The neutrons that are released in these processes are responsible for the production of ^{60}Fe which also decays slowly and emits observable γ -rays in the process. The picture is in principle very similar for the $25 M_{\odot}$ progenitor. Note, however, that the pre-supernova model does not exhibit the decline of the ^{12}C abundance at the bottom of the O/Ne shell which has a very uniform composition. Such uniformity is the consequence of full convective, hydrostatic burning. The $25 M_{\odot}$ progenitor also exhibits an exceptionally large abundance of ^{12}C in the O/Ne shell.

3.4 Nucleosynthesis of heavy elements

3.4.1 Neutron capture processes

Fusion processes in stars can only produce the elements up to Iron because the nuclear binding energy reaches a maximum and further fusion or capture reactions are endothermic, i.e. they require energy input from the medium and can thus not help to stabilize a star against gravitational collapse. Since charged-current reactions on heavy elements have to overcome the Coulomb barrier, the most promising way to proceed to heavier elements is neutron captures. In the presence of a moderate amount of neutrons a sequence of neutron captures and subsequent β^- -decays proceed to heavier nuclei along the valley of stability. This is called the slow neutrino capture process (*s*-process). The analysis of branching points along this path has lead to the conclusion that there are two components that contribute to the solar *s*-process abundances (Ward & Newman, 1978; Kappeler et al., 1989). During He-burning in massive stars the reaction $^{22}\text{Ne}(\alpha, n)$ can provide a continuous source of moderate neutron exposure on the timescale of thousands of years that allows for the production of elements in the range $A \sim 60-90$ (Couch et al., 1974). Since this process cannot account for a large part of heavy elements, it is called the weak *s*-process. A much stronger source of neutrons is the $^{13}\text{C}(\alpha, n)$ reaction that is activated in quasi-periodic He-shell flashes of AGB stars. In intervals that can last hundreds of thousands of years these stars ignite He-burning in a shell that has ingested protons from the H envelope on top of it. The free protons lead to the production of ^{13}N that decays to ^{13}C and acts as a neutron source in a very thin layer of the star of typically $10^{-4} M_{\odot}$. On the timescale of hundreds of days the neutron exposure is strong enough to produce heavy elements up to Bismuth. This is called the main *s*-process. Mixing is a critical ingredient for the computational modeling of the conditions of this ^{13}C -pocket in AGB stars and a very active field of research (Doherty et al., 2014; Battino et al., 2016). The *s*-process requires intermediate mass elements as seeds for neutron captures. Therefore, it is a secondary process that depends on the metallicity of the site. The *s*-process proceeds along the valley of stability and the final abundance pattern reflects the neutron capture rates. Since nuclei with magic neutron numbers are more reluctant to capture another neutron, the abundances of these nuclei are particularly high and give a characteristic pattern that we can also find in the solar system abundances. In addition to that, the solar abundances show another,

slightly shifted pattern of peaks. This results from the r -process, the rapid neutron capture process. Recently, an electromagnetic transient compatible with the expected signatures of the r -process as predicted by Metzger et al. (2010) have been detected following the gravitational wave event GW170817 associated with the merger of two neutron stars (Abbott et al., 2017; Cowperthwaite et al., 2017). In the r process the neutron capture rates are much faster than β -decay rates and the nucleosynthesis proceeds on timescales of milliseconds on a path that involves very neutron rich nuclei close to the drip-line. See e.g. reference Qian (2003) for a general review. Also in this process material accumulates at the neutron magic numbers, but on the very neutron rich side of the nuclear chart. After β decays this leads to the second set of characteristic peaks that can be seen in the solar abundance pattern. Even though neutron star mergers have recently been identified as at least one site for the r -process Qian & Wasserburg (2007) have shown that there are indications for multiple components. One other such site are jet-like explosions of magnetorotational core-collapse supernovae (Nishimura et al., 2015). A “light” r -process has also been discussed for high entropy outflows from nascent proto-neutron stars in core collapse supernova explosions (Martínez-Pinedo et al., 2014), which is however at the same time a possible site of the νp process discussed below.

Most of the heavy nuclei can be produced by the neutron capture processes, but there are several so called p -nuclei that can be found in the solar system and that require different types of nucleosynthesis. Neutron capture cross-sections increase with the mass number and thus size of a nucleus, but proton captures have to overcome increasingly strong Coulomb repulsion. Photodissociation and competition with (p, α) reactions can prevent the production of heavier nuclei in proton-rich conditions. Only in rather extreme conditions a rapid proton capture process, the rp process can operate. The conditions for the rp -process are expected to be found in X-ray bursts or Thorne-Zytkow objects (van Wormer et al., 1994; Schatz et al., 1998). Even for the most extreme conditions the rp -process has been shown to be unable to produce much material beyond the waiting-point nuclei ^{62}Se , ^{64}Ge and ^{72}Kr (Schatz et al., 2001). Conditions for the rp process are expected to be found close to compact objects and it is not clear how much of the nucleosynthesis products escapes to contribute to the chemical enrichment of the galaxy.

3.4.2 The γ -process

p -nuclei with $A > 100$ can be produced by sequences of photodissociation reactions (γ, n) and (γ, α) in massive stars. During the final burning stages, the heavy nuclei that are inherited from the metallicity of the molecular cloud are processed to form the heavy p -nuclei. This process is expected to be most efficient in the O/Ne shells of massive stars. The process has been studied in detail e.g. in references Prantzos et al. (1990); Rayet et al. (1995) where stellar regions with peak temperatures between 1.8 and 3.3 GK have been selected as relevant layers. Rayet et al. (1995) identify different temperature ranges for the production of the p -nuclei. The heavier species with $N > 82$ only survive in the coolest regions with $T_9 < 2.5\text{GK}$ from the pre-existing seed nuclei by sequences of (γ, n) reactions. These conditions are the most likely site for an appreciable production of ^{180}Ta . At higher peak temperatures (γ, p) and (γ, α) reactions become important and drive the nucleosynthesis to lower atomic numbers after (γ, n) pushed it to the neutron-deficient side of the valley of stability. The released neutrons can in turn again be captured on the products of the photodissociation chain. Up to a temperature of around 3.3 GK the intermediate p -nuclei with $50 < N < 82$ can be produced. The temperature range where a particular nucleus is produced, is usually relatively narrow, leading to a distinct peak in the mass fraction profile. Most stellar models of massive stars contain a region where the optimal conditions can be achieved. Therefore, the γ -process has been found to be relatively robust with respect to the progenitor model. Due to the photodissociation chains the abundances of heavier nuclei are depleted. In even hotter regions the photodissociation proceeds to nuclei with $N < 50$. Here, more complicated reaction flows involving also capture reactions make the production of the lighter p -nuclei more sensitive to the details of the explosion and the structure of the progenitor model. Hoffman et al.

(2001) have found that p -nuclei with $A < 90$ can already be made before the explosion in hydrostatic O-burning for some progenitors. Rauscher et al. (2002) also find a strong contribution to the p -nuclei from hydrostatic burning for some progenitors. This behavior is particularly sensitive to convective mergers of hydrostatic burning shells, that can mix the fuel for hot shell burning phases into deeper regions to allow for the γ -process. The modeling of such convective processes can now be addressed with multi-dimensional numerical simulations of the fluid flows in a stellar plasma, which is an active field of research (Ritter et al., 2018; Edelmann et al., 2017).

The γ -process is particularly sensitive to the branching ratios photon-induced reactions on heavy nuclei. It also includes a number of nuclei that are radioactive and hence reactions for which cross-sections are more difficult to measure directly. Only recently modern facilities have been developed and are being developed to perform such measurements routinely (Shimizu et al., 2011; Gade & Sherrill, 2016). Therefore, the first models for γ -process nucleosynthesis have become possible with progress in the calculation of reactions rates within the framework of the statistical model (Thielemann et al., 1987).

Following progress in the experimental determination of (n, γ) cross-sections Dillmann et al. (2008) have investigated the effect on the γ -process yields and found a significant reduction of the overproduction factors of most p -nuclei.

Despite advances in the experimental and theoretical determination of the cross-sections for the involved reactions, this process significantly underproduces the lighter p -nuclei in the range $60 < A < 100$.

3.4.3 The νp -process in neutrino driven winds

While the rp -process could produce heavy, neutron deficient nuclei it is not expected to contribute to the chemical enrichment because the process is always connected to the formation of compact objects. The production of heavier nuclei by proton captures is slowed down by the relatively long β -decay lifetimes for the waiting point nuclei with low proton capture rates on the neutron deficient side of stability. The νp -process overcomes this problem by introducing free neutrons produced via $\bar{\nu}_e + p \rightarrow e^+ + n$. This process has first been discussed by Fröhlich et al. (2006). Due to the large cross-sections for (n, p) reactions on neutron deficient nuclei this can overcome the waiting points and allow to proceed to higher mass numbers. The conditions for this process could be found in the neutrino driven winds in the late phases of supernova explosions.

After the supernova explosion has been launched, the neutrinos from the cooling remnant keep depositing energy in the layers on the surface of the PNS. The existence of steady-state outflow solutions from the surface of a hot PNS has first been discussed by Duncan et al. (1986) and was also explored by Woosley et al. (1994) and Takahashi et al. (1994). Modern supernova simulations including detailed neutrino transport that have been run long enough to capture the late phase of the PNS evolution (Arcones et al., 2007; Fischer et al., 2010; Hüpdepohl et al., 2010) confirm that due to the neutrino energy deposition a supersonic outflow can be launched. This is referred to as the neutrino driven wind (NDW). The material expands into the low density region behind the supernova shock. Due to high velocities, the wind outflow quickly catches up with the shock and collides with the slow moving ejecta a few milliseconds after being launched. This collision marks the wind termination. The material is decelerated and shock heated. The expansion proceeds much more slowly afterwards. Wanajo et al. (2011) have studied the impact of the time of wind termination on the nucleosynthesis and found that the νp -process can operate efficiently if the wind termination occurs while the material is in the temperature range between 3 and 1.5 GK. The Y_e at the time of wind termination is found to be crucial for the production of heavier p -nuclei. In particular, the production of p -nuclei with mass number of up to $A = 152$ can be achieved. Heavier masses are not reached because (n, γ) reactions start to compete with (p, γ) and the nucleosynthesis moves towards the neutron rich side of stability.

The νp -process is particularly interesting to explain the solar abundances of the p -nuclei $^{92,94}\text{Mo}$ and $^{96,98}\text{Ru}$ which cannot be produced by neutron capture processes and are underproduced by the γ

process. Furthermore, this process is a primary process and may be applied to explain the observed large abundances of Sr and other p -isotopes in extremely metal-poor stars (Travaglio et al., 2004; Frebel et al., 2005).

The material of the PNS is very neutron rich in the beginning and the wind expands from very high temperatures. The proton to neutron ratio is finally determined by the competition between electron neutrino captures on neutrons and electron antineutrino captures on protons. Qian & Woosley (1996) found that the equilibrium value of the electron fraction Y_e depends sensitively on the difference of the energies of electron neutrinos and electron antineutrinos. Due to the energy threshold to overcome the proton-neutron mass difference in $\bar{\nu}_e$ absorption on protons Y_e will tend to increase, as the neutrino luminosities and energies decrease. Hence, neutron rich conditions would only be expected in an early phase. Simulations (e.g. Martínez-Pinedo et al. (2012)) confirm that the wind is expected to be proton-rich most of the time and the electron fraction can reach values of up to 0.7. Martínez-Pinedo et al. (2014) have studied the nucleosynthesis of neutrino driven wind, based on long-term one-dimensional simulation including important mean-field effects (Martínez-Pinedo et al., 2012; Roberts et al., 2012) that tend to reduce the neutron-richness of the ejected material, concluding that the NDW is not a suitable site for the r-process. While the composition of moderately neutron rich NSE after freeze out is dominated by nuclei, a slightly proton-rich freeze-out results in ^{56}Ni accompanied by a relatively large fraction of free protons of approximately $Y_p \approx 2Y_e - 1$ (Pruet et al., 2006; Seitenzahl et al., 2008). For high entropy conditions, therefore even slightly proton rich conditions are sufficient to provide large proton-to-seed ratios.

4 Methods

4.1 A simple explosion model

The ν process has first been studied in detail by [Woosley et al. \(1990\)](#). For this first study a simplified explosion model was used. While this approach is not a very good approximation for the innermost supernova ejecta we employ it in Chapter 6 to extrapolate the evolution of the outer zones based on the results from a self-consistent supernova simulation. Assuming that the whole explosion energy of a supernova is contained as radiation behind the shock, we can estimate the evolution of the peak temperature to which the material is heated by the outward moving shock. The explosion energy E_{expl} can in principle be derived from observations by looking at the kinetic energy of the ejected material. Assuming that the internal energy of the material behind the shock is dominated by radiation and keeps most of the explosion energy we arrive at the following relation between the peak temperature T_{peak} reached by the shocked material and the radius r

$$E_{\text{expl}} = \frac{4\pi}{3} r^3 a T^4. \quad (4.1)$$

This leads us immediately to an estimate for the peak temperature at radius r :

$$T_{\text{Peak}} = 2.4 \times 10^9 \text{K} \times \left(\frac{E_{\text{expl}}}{10^{51} \text{erg}} \right)^{1/4} \times \left(\frac{r}{10^9 \text{cm}} \right)^{-3/4}. \quad (4.2)$$

The key parameters here are the explosion energy and the initial position of the mass shells. The dependence on the explosion energy seems relatively weak since a 20% increase of the explosion energy results only in a 4.7% increase of the temperature. However, nuclear reaction rates often scale with very high powers of the temperature such that minor changes in the explosion energy can already have a significant impact on the nucleosynthesis. This simple estimate of the peak temperature is already in relatively good agreement with results of a full hydrodynamical calculated piston model. Figure 4.1 shows a comparison of the estimated T_{Peak} from equation 4.2 with the results from hydrodynamic calculations tuned to the same explosion energy of 1.2×10^{51} erg for several progenitor models. The agreement is particularly good in the regions where the peak temperature ranges between 1 and 4 GK. These regions are also particularly important for nucleosynthesis. For peak temperatures exceeding 4-5 GK the composition is mostly determined by NSE and the exact peak temperature is not important for the nucleosynthesis yields. Also,

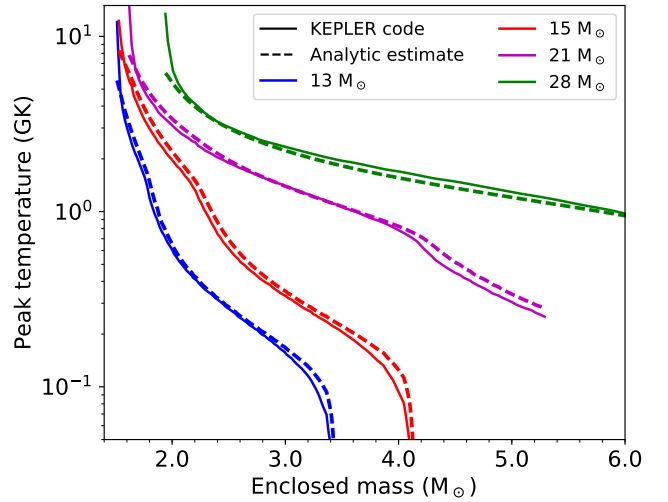


Figure 4.1.: Comparison of the peak temperature estimated with the analytic expression 4.2 and calculated with the Kepler code.

for peak temperatures significantly below 1 GK charged particle reaction are suppressed and the shock heating has only little effect on the composition.

Woosley et al. (1990) have then described the cooling with an exponential decline of temperature and density on the free-fall timescale. Prantzos et al. (1990) have shown, that this approach underestimates the cooling timescale. To describe and extrapolate the temperature evolution in Section 6 we instead follow Ning et al. (2007) who derived an expression for the evolution of temperature and density based on a known post-shock velocity u as:

$$\rho(t) = \frac{\rho_0}{(1 + t/\tau_1)^2 (1 + t/\tau_2)}, \quad (4.3)$$

with

$$\tau_1 = r/u \quad \text{and} \quad \tau_2 = \frac{1}{7(du/dr)}, \quad (4.4)$$

where u is the post-shock velocity of the mass element under consideration. In the outer layer of the star we expect the shock velocity to be almost constant and get $\tau_2 \gg \tau_1$, such that the evolution is determined predominantly by τ_1 . Furthermore, we assume that the shocked material moves with the shock velocity v_{sh} and estimate

$$\tau_1 = \tau = \frac{r}{v_{\text{sh}}} \quad (4.5)$$

4.2 Neutrino signal

In order to study the ν process we need to know the neutrino flux ϕ_ν for the different neutrino species for the whole evolution of the calculation. Assuming a Fermi-Dirac distribution for the neutrinos Equation 2.31 allows us to consider the neutrino nucleus cross-sections as functions of the neutrino temperature which we assume to be constant. Following further the model of Woosley et al. (1990), we use the ansatz $L \propto e^{-t/\tau_\nu}$. Normalizing the integrated luminosity to the total energy emitted in neutrinos E_{total}

$$\int L dt = E_{\text{total}},$$

allows to determine the proportionality factor of the exponential, giving

$$L = \frac{E_{\text{total}}}{\tau_\nu} e^{-t/\tau_\nu}. \quad (4.6)$$

From this, an expression for the flux for one neutrino species is

$$\phi_\nu = \frac{1}{4\pi r^2} \frac{1}{6} \frac{E_{\text{total}}}{\tau_\nu \langle E_\nu \rangle} e^{-t/\tau_\nu}, \quad (4.7)$$

where the factor $1/6$ enters assuming that the energy is equally distributed among all 6 neutrino species. In Sections 5.2 and 5.3.3 we assume the total energy $E_{\text{total}} = 3 \times 10^{53}$ erg which is the typical order of magnitude for the difference of gravitational binding energy of a stellar Fe core and the final neutron star. This energy is radiated away mostly by neutrinos. Burrows & Lattimer (1987) have estimated the neutrino energies and luminosities from the observed neutrinos from supernova 1987A. This remains the only direct detection of supernova neutrinos and the statistics of this observation are very low. Furthermore, the only neutrinos observed were electron flavor neutrinos and hence the best estimates for the neutrino emission properties we have are from supernova simulations. With the

	“high energies”	“low energies”
T_{ν_e}	4.0 MeV	2.8 MeV
$T_{\bar{\nu}_e}$	5.0 MeV	4.0 MeV
$T_{\nu_{\mu,\tau}}$	6.0 MeV	4.0 MeV
$T_{\bar{\nu}_{\mu,\tau}}$	6.0 MeV	4.0 MeV

Table 4.1.: Spectral neutrino temperatures adopted for Chapter 5.2

improvements of the treatment of neutrino transport in last decades the estimated average neutrino energies have been reduced multiple times. While the models calculated by [Bethe & Wilson \(1985\)](#) predict that μ and τ neutrinos could have average energies in excess of 35 MeV and electron flavor neutrinos between 15 and 20 MeV, modern simulations ([Fischer et al., 2009](#); [Hüdepohl et al., 2010](#); [Martínez-Pinedo et al., 2012](#); [Martínez-Pinedo et al., 2014](#); [Mirizzi et al., 2016](#)) predict much lower values, with heavy flavor neutrinos and electron antineutrinos between 12 and 15 MeV, and electron neutrinos below 10 MeV. This reduces the neutrino-nucleus cross-sections and in particular particle spallation cross-sections for neutral-current reactions which are very sensitive to the tail of the neutrino spectra due to the relatively high particle separation thresholds involved. Our choice of neutrino temperatures denoted “*low energies*” is $T_{\nu_e} = 2.8$ MeV ($\langle E_{\nu_e} \rangle = 9$ MeV), $T_{\bar{\nu}_e, \nu_{\mu,\tau}} = 4$ MeV ($\langle E_{\bar{\nu}_e, \nu_{\mu,\tau}} \rangle = 12$ MeV). Recently, [Banerjee et al. \(2016\)](#) have also made a similar choice for the spectral neutrino temperatures. To compare with previous neutrino nucleosynthesis studies ([Woosley et al., 1990](#); [Heger et al., 2005](#)) we have also performed our calculations using the following set of neutrino temperatures: $T_{\nu_e} = 4$ MeV ($\langle E_{\nu_e} \rangle = 12$ MeV), $T_{\bar{\nu}_e} = 5$ MeV ($\langle E_{\bar{\nu}_e} \rangle = 15.8$ MeV), and $T_{\nu_{\mu,\tau}} = 6.0$ MeV ($\langle E_{\nu_{\mu,\tau}} \rangle = 19$ MeV); that we denote as “*high energies*” along the manuscript. For quick reference these values are also summarized in Table 4.1. In section 5.4 we show that the choice of appropriate neutrino energies is not straightforward and their time dependence that we would expect in nature also has an impact on the nucleosynthesis.

4.3 KEPLER hydrodynamics code

In order to model the conditions of the material in a supernova explosion it is necessary to solve the equations of hydrodynamics that determine the evolution of temperature, density, pressure and entropy.

We employ the KEPLER hydrodynamics code which solves the Euler equations in their Lagrangian form as (Landau & Lifshitz, 2012)

$$\frac{\partial v}{\partial t} = -4\pi r^2 \frac{\partial P}{\partial m} - \frac{Gm}{r^2} + \frac{4\pi}{r} \frac{\partial Q}{\partial m} \quad (4.8)$$

for the conservation of momentum. Here, $v = \frac{\partial r}{\partial t}$ and P is the pressure.

With the viscosity term

$$Q = \frac{4}{3} \eta r^4 \frac{\partial}{\partial r} \left(\frac{v}{r} \right). \quad (4.9)$$

Here, η is the dynamic viscosity coefficient (Landau & Lifshitz, 2012) which is important to describe shocks. During the hydrodynamic phase, only a quadratic term is used for the viscosity as

$$\eta = 3/4 l_2^2 \rho \max(0, -\vec{\nabla} \cdot \vec{v}), \quad (4.10)$$

with $l_2 = 2\Delta r$, where Δr is the size of the zone. This spreads shock discontinuities over about $2 \times l_2$. The conservation of energy yield in Lagrangian formalism

$$\frac{\partial \epsilon}{\partial t} = -4\pi P \frac{\partial}{\partial m} (vr^2) + 4\pi Q \frac{\partial}{\partial m} \left(\frac{v}{r} \right) - \frac{\partial L}{\partial m} + \dot{S} \quad (4.11)$$

where ϵ is the energy per unit mass, L is the luminosity passing through a sphere with radius r and \dot{S} is the local energy generation rate per unit mass which is coupled to the nuclear reaction network. The KEPLER hydrodynamics code solves these equation implicitly together with a nuclear reaction network to calculate the nuclear heating and the composition. For fuhrer detail we refer to Weaver et al. (1978).

In a one-dimensional model, the mass coordinate, or enclosed mass is fixed since matter cannot move past the overlying layers. Interactions of material moving through overlying shells are accounted for by a treatment of convection with mixing length theory that is important during stellar evolution. During the explosion, which we are most interested in here, mixing is assumed not to occur because convective timescale are much longer than the dynamical timescales during the explosion.

4.4 Piston model

For the lack of self consistent explosions in one dimension, various methods have been developed to parametrically describe a supernova explosion in order to obtain nucleosynthesis yields (Young & Fryer, 2007). The piston model was among the most successful approaches to model supernova explosions Woosley & Weaver (1995). It is based on the concept that once the supernova shock has been launched the propagation of shock, lightcurve and the dynamics of the ejection of the stellar mantle should be decoupled from the central engine that powers the initial deposition of energy. This motivates the modeling of the explosion with a piston, that acts like a dynamic but externally prescribed boundary condition for the innermost mass zone of a supernova model.

With the neutrino driven mechanism explosions are expected to be delayed by the time it takes the neutrinos to revive the stalled shock inside the Fe core. Therefore, the piston is first moved inward,

following an accelerated trajectory to reach $R_0 = 500$ km, starting from its initial velocity of the pre supernova calculation. For the infall phase the gravitational acceleration is modified by a factor $\beta = 0.25$. Afterwards, the position R of the piston follows a ballistic trajectory according to

$$\left(\frac{dR}{dt}\right)^2 = \alpha GM_{\text{piston}} \left(\frac{1}{R} - \frac{1}{R_0}\right) + v_0^2 \quad (4.12)$$

where M_{piston} is the mass of the piston, v_0 the initial, outward velocity that is adjusted to reach $dR/dt = 0$ at a final radius $R_1 = 10,000$ km.

The mass of the piston is the mass of material below the initial position of the piston. All mass zones below that are removed from the calculation. The piston position is chosen to be at a discontinuity of the electron fraction Y_e that can be typically be found in the outer Fe core as discussed by [Woosley & Weaver \(1995\)](#). In our calculations we neglect the possibility that matter that has first been pushed out by the explosion can still fall back onto the remnant eventually. We assume that all the mass exterior to the piston is ejected. Thus, the mass coordinate of the piston is equal to the remnant mass. The amount of material found to fall back is typically of the order of $1/10$ of a solar mass. This is crucial to determine the amount of ^{56}Ni and also of ^{44}Ti that is ejected. Since we are mostly interested in the ν process here, we neglect fallback. The parameter α in equation (4.12) modifies the gravitational potential and is chosen to achieve a given kinetic explosion energy. The requirement for the piston to stop at R_1 gives a relationship between v_0 and α

$$\alpha = \frac{v_0^2}{GM_{\text{piston}}} \left(\frac{1}{R_0} - \frac{1}{R_1}\right)^{-1} \approx \left(\frac{0.4 M_{\odot}}{(10^9 \text{ cm/s})^2}\right) \times \left(\frac{v_0^2}{M_{\text{piston}}}\right) \quad (4.13)$$

The motion of the piston sets the inner boundary for the innermost mass shell and thus shoves out all the zones above. Figure 4.3 illustrates the radius evolution of the innermost mass shell and piston trajectories for several choices of α . The piston comes to a halt at $R_1 = 10,000$ km for all cases but the momentum imparted on the innermost mass shell is sufficient to eject it. The choice of parameters to achieve the characteristic explosion energy of 1.2×10^{51} erg for the whole range of progenitors used here are summarized in table 4.2. The explosion energy is determined as the total kinetic energy of the ejecta after 100 days, such that internal and gravitational energy can be neglected.

Figure 4.2 shows the trajectory of the innermost mass zone and the corresponding piston for several values of α . The innermost mass zone follows the infall of the piston and is pushed and carried along as it moves outward. The sudden outward movement of the piston produces the hydrodynamic shock and as the mass shell is pushed out by the piston the kinetic energy is increased. This propagates to the zones on top. While the piston trajectory decelerates and stops at R_1 , the mass shell has acquired a sufficient amount of kinetic energy to escape the gravity of the remnant and overcome the pressure

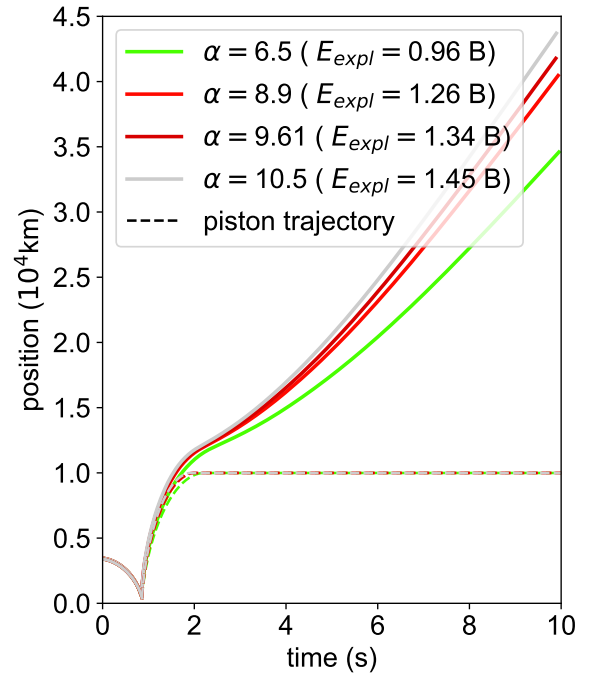


Figure 4.2.: Radius evolution of the innermost mass shell of the $13 M_{\odot}$ model that is shoved outward by the piston as described in the text for different choices of the acceleration parameter α .

of the in-falling layers on top. High values of α correspond to high push velocities v_0 , as can be seen from equation 4.13. A strong effective gravity for the piston means, that the push is short and strong. For the less massive models with low compactness such a quick shove is enough to achieve the required explosion energies and a relatively fast moving shock. For the models with high compactness, the value of the α parameter is smaller and the piston takes longer to reach R_1 . The shock also propagates more slowly because it is decelerated rapidly by the ram pressure of the in-falling shells. This is illustrated by Figure 4.2 which shows the shock radius as a function of time. The shock radius is here taken to be the position of the shell which has reached the maximum temperature at a given time. At first the shock accelerates and propagates very fast while moving through the steep density gradient in the outer Fe-core and Si-shell. As the density profile becomes more shallow, the shock decelerates rapidly. As the piston stops, the shock is decelerated in the dense inner shells. Once it reaches the Hydrogen envelope at around 40 – 60 s the shock is accelerated again slightly and afterwards the velocity remains roughly constant. The time at which the shock starts to propagate is determined by the time it takes the piston to fall to 500 km. This depends on the radius associated with the mass cut.

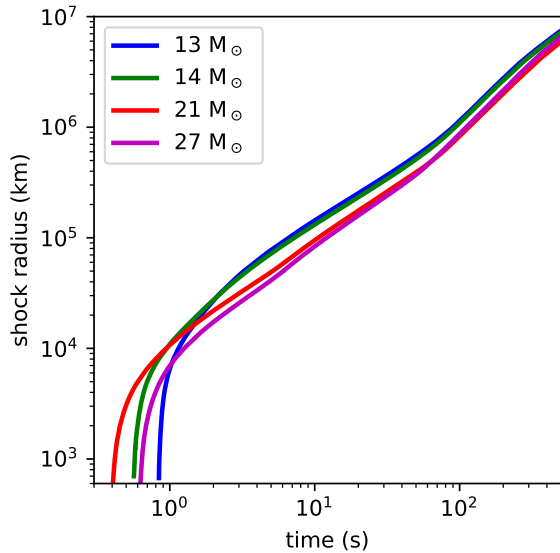


Figure 4.3.: Shock radii for different progenitor models. The evolution of the shock radius is predominantly determined by the density profile of the progenitor model.

Model	α	Mass cut	Ni mass	$\zeta_{2.5}$
s13	8.61	1.51	0.015	0.013
s14	4.57	1.54	0.041	0.023
s15	2.39	1.53	0.108	0.045
s16	2.35	1.55	0.107	0.109
s17	1.86	1.63	0.125	0.164
s18	1.31	1.76	0.142	0.215
s19	2.94	1.53	0.100	0.160
s20	2.72	1.58	0.104	0.185
s21	2.46	1.62	0.112	0.180
s22	1.63	1.80	0.148	0.279
s23	1.92	1.51	0.178	0.223
s24	2.57	1.63	0.114	0.190
s25	0.89	2.10	0.216	0.417
s26	0.89	2.15	0.222	0.441
s27	1.21	2.02	0.195	0.385
s28	1.81	1.94	0.136	0.315
s29	3.26	1.69	0.095	0.230
s30	2.97	1.68	0.110	0.242

Table 4.2.: Piston parameters to achieve explosion energies around 1.2 B. Except for the lightest stars, the amount of Ni ejected is of the order $10^{-1} M_{\odot}$, consistent with observations of SN 1987A.

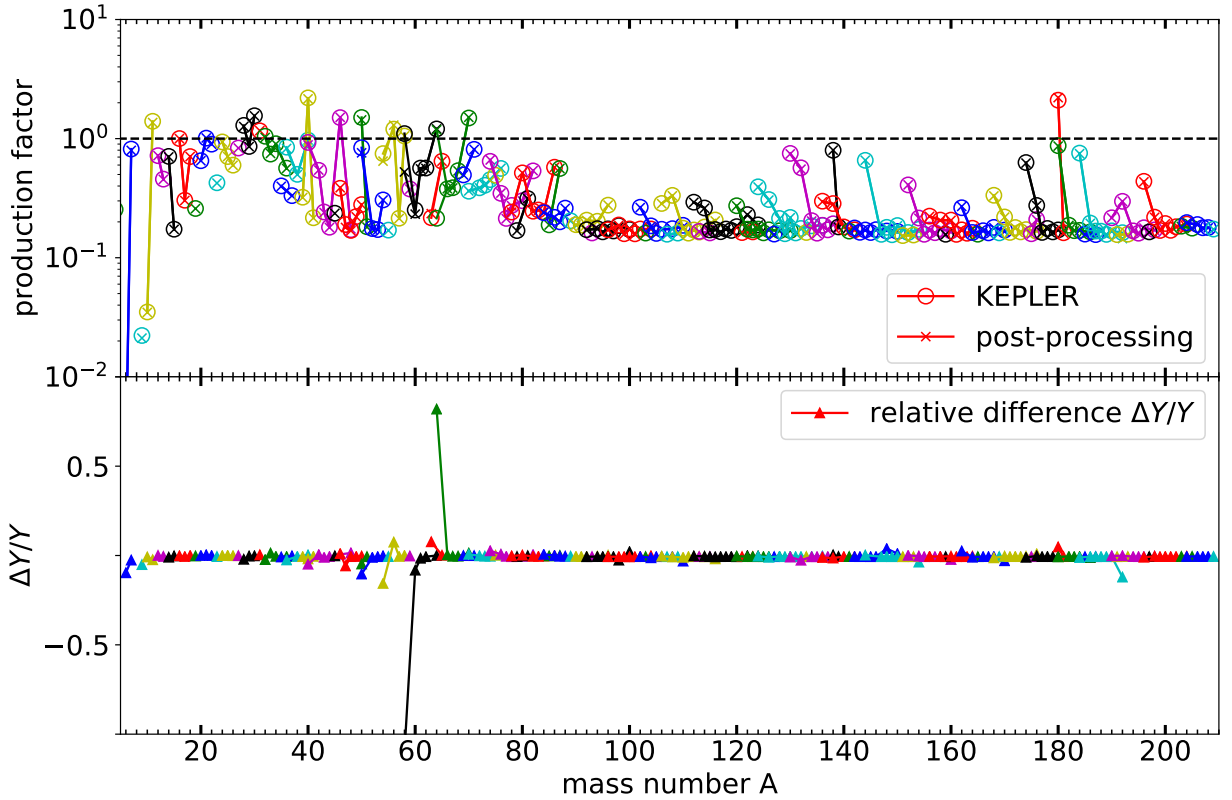


Figure 4.4.: Upper panel: Production factors relative to ^{16}O for the $15 M_{\odot}$ model from calculations with the KEPLER code and from our post-processing calculations. Isotopes of the same elements are connected by lines.

Bottom panel: relative differences of the yields $\Delta Y/Y = (Y_{\text{post}} - Y_{\text{KEPLER}})/Y_{\text{post}}$ from the KEPLER calculation and the post-processing. Except for the Fe peak elements we find a reasonably good agreement.

4.5 Post-processing and comparison

The calculations for this work were done in a hybrid approach, combining the hydrodynamics and stellar evolution code KEPLER to calculate the thermodynamic evolution of a piston driven supernova model with our own nuclear reaction network code described in Section 2.1.4.

The KEPLER code also includes a co-processing reaction network that is adaptive, i.e. the size of the network is increased or decreased as the composition and reactions demand. However, due to the additional computational burden of solving the equations of hydrodynamics and radiation transport at the same time, the equations of the nuclear reaction network are solved in a different way. While our network implements a Newton-Raphson approach as outlined in Section 2.1.4 with a stringent convergence check for the relative change of abundances, the KEPLER code implements a single iteration of the network equations per time step and as a convergence check requires that none of the calculated abundances are negative. However, since KEPLER is solving the equations of hydrodynamics coupled to the network, the code typically takes smaller time steps. Small differences in the temperature and density may also arise from the fact that our post-processing approach interpolates the thermodynamic variable based only on a subset of the time steps of the original calculation. Since our network code takes the thermodynamic variables as given, all mass zones of a given stellar model can be calculated independent of each other. This allows a trivial parallelization of the calculations. As a consistency check we compare our results to those obtained with the KEPLER code. Significant modifications of

the reaction network of the KEPLER code were necessary to include our neutrino cross-sections and the same nuclear reaction rates. However, we do not employ the same β decay and electron capture rates. To cross check the calculations we compare the results based on the $15 M_{\odot}$ model with the KEPLER code to the results obtained with our reactions network code in post-processing of the same thermodynamic history. With our reaction network we process all the mass zones above the final mass cut up to the zones where the temperature never exceeds 10^7 K because we do not expect any nuclear reactions to occur in these regions. We then include the Hydrogen and Helium envelope from the progenitor model in the final yield for all the zones further out. This also includes the mass loss during the pre-supernova evolution which is included in the progenitor data. Figure 4.4 shows the production factors relative to ^{16}O for the $15 M_{\odot}$ model with our post-processing approach and from the KEPLER co-processing reaction network that was modified to use the same nuclear reaction rates and neutrino reactions. We find in general a very good agreement. The lower panel of Figure 4.4 also show the relative differences. The most significant deviations arise for the Fe group nuclei, in particular for ^{58}Ni and ^{64}Zn . These nuclei are produced by the 10 innermost mass zones, all of which reach NSE conditions in our calculations and they are affected by density dependent electron capture rates. The differences most likely arise from a different treatment of NSE and electron captures. The KEPLER code does not assume NSE for temperatures below 10 GK while we take the solution of Equation (2.48) for temperatures above 6 GK. Furthermore, there are also differences in the method to solve the reaction network equations. While our post-processing employs a Newton-Raphson method described in Section 2.1.4, the reaction network in the KEPLER code solves the equations without iterative refinement. Both codes employ screening corrections based on the work of [Alastuey & Jancovici \(1978\)](#) for weak screening and on [Graboske et al. \(1973\)](#) for strong and intermediate screening. However, we found that the two different implementations of these correction factors give slightly different results. Since the production of Fe peak elements is not the main focus of this work we can consider just the material that has reached NSE. When we exclude the innermost layers that exceed a temperature of 6 GK, the total yields agree within 10%.

In total we find that the overall agreement between both codes is at the 10% level for the nuclei we are interested in. We could associate most of the remaining discrepancies to different input physics.

5 The ν process in the light of an improved understand of neutrino spectra

5.1 Neutrino-nucleus cross-sections

One major advance of our calculations with respect to previous studies of the ν process is the implementation of a complete set of neutrino-nucleus reaction cross-sections that have been calculated globally for nuclei with $Z < 76$ extending almost to the drip lines on both, the neutron- and proton- rich sides of stability. The calculation of these cross-sections is discussed in detail by [Huther \(2014\)](#) and follows a two-step strategy presented by [Kolbe et al. \(1992\)](#) and described also in Section 2.3. First, the neutrino-induced nuclear excitation cross-sections to a final state at energy E have been calculated within the Random Phase Approximation following [Kolbe et al. \(2003\)](#). These calculation include multipole transitions up to order four. The single particle energies were adopted from an appropriate Woods-Saxon parametrization, adjusted to reproduce the proton and neutron thresholds and to account for the energies of the Isobaric Analog State and the leading giant resonances. Assuming very high neutrino energies, mainly neutral-current spallation reactions have a significant impact on the nucleosynthesis. These reactions can be computed with sufficient accuracy using simple nuclear models, since they are mainly sensitive to collective excitations. As state-of-the-art SN simulations tend to predict neutrino energies to be lower than expected in the past, charged current channels gain in relative importance. Such reactions, i.e. ν_e and $\bar{\nu}_e$ absorption on abundant stable nuclei need to overcome a positive Q-value and hence they can only excite relatively low lying states. Hence, such reactions are often determined by a few low-energy Gamow-Teller and Fermi transitions. Strengths for these transitions are in some cases known from experiments or can be calculated with high accuracy in the shell model.

The reactions $^{26}\text{Mg}(\nu_e, e^-)^{26}\text{Al}$ and $^{22}\text{Ne}(\nu_e, e^-)^{22}\text{Na}$ affect the production of the radioactive isotopes ^{26}Al and ^{22}Na which are interesting for γ -ray astronomy ([Timmes et al., 1995a](#)).

^{26}Al is a particular case because only 228.3 keV above its long-lived, high-spin 5^+ ground state, there is a 0^+ state with isospin $T = 1$ that decays to ^{26}Mg by an super allowed Fermi transition with a half-life of 6.34 s. Due to the high spin of the ground state, the isobaric analog is effectively isolated. Thermal excitations of higher states, however, allow for transitions between the short-lived state and the ground state. Because of the important role of ^{26}Al in γ -ray astronomy, the population of the excited state by nuclear reactions has received quite some attention and has sparked experimental initiatives to measure the relevant branchings. However, such measurements are a formidable task and the reaction rates are still subject to very large uncertainties. [Iliadis et al. \(2011\)](#) have shown that the theses states are effectively thermally occupied under supernova conditions. Therefore, and for simplicity we do not treat the isomer of ^{26}Al as a separate species in our calculations.

This Fermi transition also enhances the cross-section for the inverse process, i.e. ν_e capture on ^{26}Mg which we have studied here in more detail.

Following the first measurements of anomalous ^{26}Mg abundances in meteorites, [Domogatskij & Nadezhin \(1980\)](#) have suggested $^{26}\text{Mg}(\nu_e, e^-)^{26}\text{Al}$ as the main production mechanism. Even though we now know that the main part of the production results from Hydrogen burning and also explosive O/Ne burning, the neutrino interactions suggested by [Domogatskij & Nadezhin \(1980\)](#) still contribute. At low neutrino energies $^{26}\text{Mg}(\nu_e, e^-)$ is dominated by Gamow-Teller transitions and the Fermi transition to the short lived 0^+ state in ^{26}Al .

In their original work they calculated the cross-section for that reaction using equation 2.62 for the Fermi-transition which gives $B(F) = 2$. The Gamow-Teller strength was inferred from the β^+ decay of the mirror nucleus ^{26}Si . At that time the contribution of the three lowest transitions at 1.058, 1.851 and 2.072 MeV have been known to be $B(GT) = 1.82, 0.96$ and 0.21 . More recently the strength of the Gamow-Teller transitions $B(GT)$ has been measured with high precision by [Zegers et al. \(2006\)](#). Figure 5.1 shows how different states contribute to the cross section. At low energies that correspond to the average energies expected for electron flavor neutrinos from core-collapse supernova simulations the Fermi transition to the isobaric analog state clearly dominates. Its strength and position can be determined to a good approximation with the analytic formulae.

In the RPA the 1^+ Gamow-Teller transitions are represented by two transitions that are fragmented into more than six individual states in the experimental spectrum. Due to the position of the GT strength close to the particle separation thresholds in the RPA, this calculation overestimates the particle emission channels leading to the too low cross section for the channel producing ^{26}Al that can be seen in Figure 5.3. However, Figure 5.4 shows that the summed GT strength and also the total cross section shown in figure 5.3 are in relatively good agreement. Table 5.1 also shows that the deviation of the spectrum averaged total cross-sections based on the RPA calculations from the measurement based values are on the 10% level for low neutrino energies which are the most sensitive to the threshold.

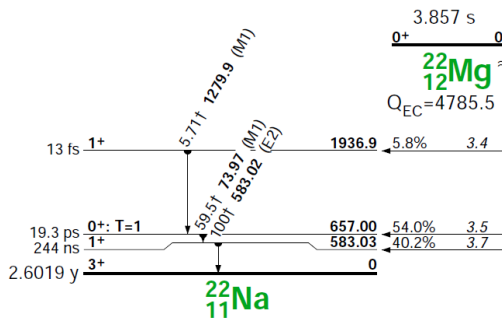


Figure 5.2.: ^{22}Mg decay scheme from [Firestone \(1991\)](#)

We expect that the RPA calculation are even more reliable for heavier nuclei, in particular because the parameters of the mean field potential for the independent particle states are adjusted to properties of ^{208}Pb . At a neutrino energy of 60 MeV the Fermi transition and the low lying Gamow-Teller transitions still dominate the cross-section but higher order transitions start to come into play. Those transitions mostly decay by particle emission. The left panels of Figure 5.1 also show, that due to our strategy to adjust the energy scale of the RPA states to reproduce the position of the isobaric analog state some 1^+ state end up below the Q-value of the transitions. This can be seen in Figure 5.3 and 5.4 where we see major differences at the threshold. In particular, in the RPA calculation a large amount of the GT strength is located above the proton separation energy of 6.3 MeV. As a result, the channel going to the production of ^{26}Al is underestimated. In our nucleosynthesis calculation the cross-sections only enter averaged over the neutrino spectrum. Therefore, the exact position of the threshold is not critical. However, this illustrates that special care needs to be taken for calculating the cross-sections when the effect of deviations of neutrino spectrum from an ideal Fermi-Dirac distribution are to be considered. The reaction $^{22}\text{Ne}(\nu_e, e^-)^{22}\text{Na}$ that has a significant impact on the production of ^{22}Na in massive stars (see Section 5.3.3) is also dominated by the Fermi transition to the isobaric analog state at 657 keV with and two Gamow-Teller transitions. Transitions to those states from the mirror nucleus ^{22}Mg have been measured and $\log ft$ are indicated in Figure 5.2.

For the reaction $^{22}\text{Ne}(\nu_e, e^-)^{22}\text{Na}$ this data from the β -decay of the mirror nucleus ^{22}Mg can be used to determine the strength of the dominant Gamow-Teller transitions.

The cross-sections derived from the measured transition strengths have been supplemented by forbidden transitions calculated within the RPA.

Table 1 compares the cross-sections obtained in that way with the results of a calculation by Marketin et al. using a relativistic Quasiparticle Random Phase Approximation (QRPA) [Paar et al. \(2013\)](#). Values by Woosley and Hoffman [Woosley et al. \(1990\)](#) are also shown. We find a significant increase of the cross-sections which is important for the production of ^{22}Na in the O/C shell as discussed in Section 5.3.3.

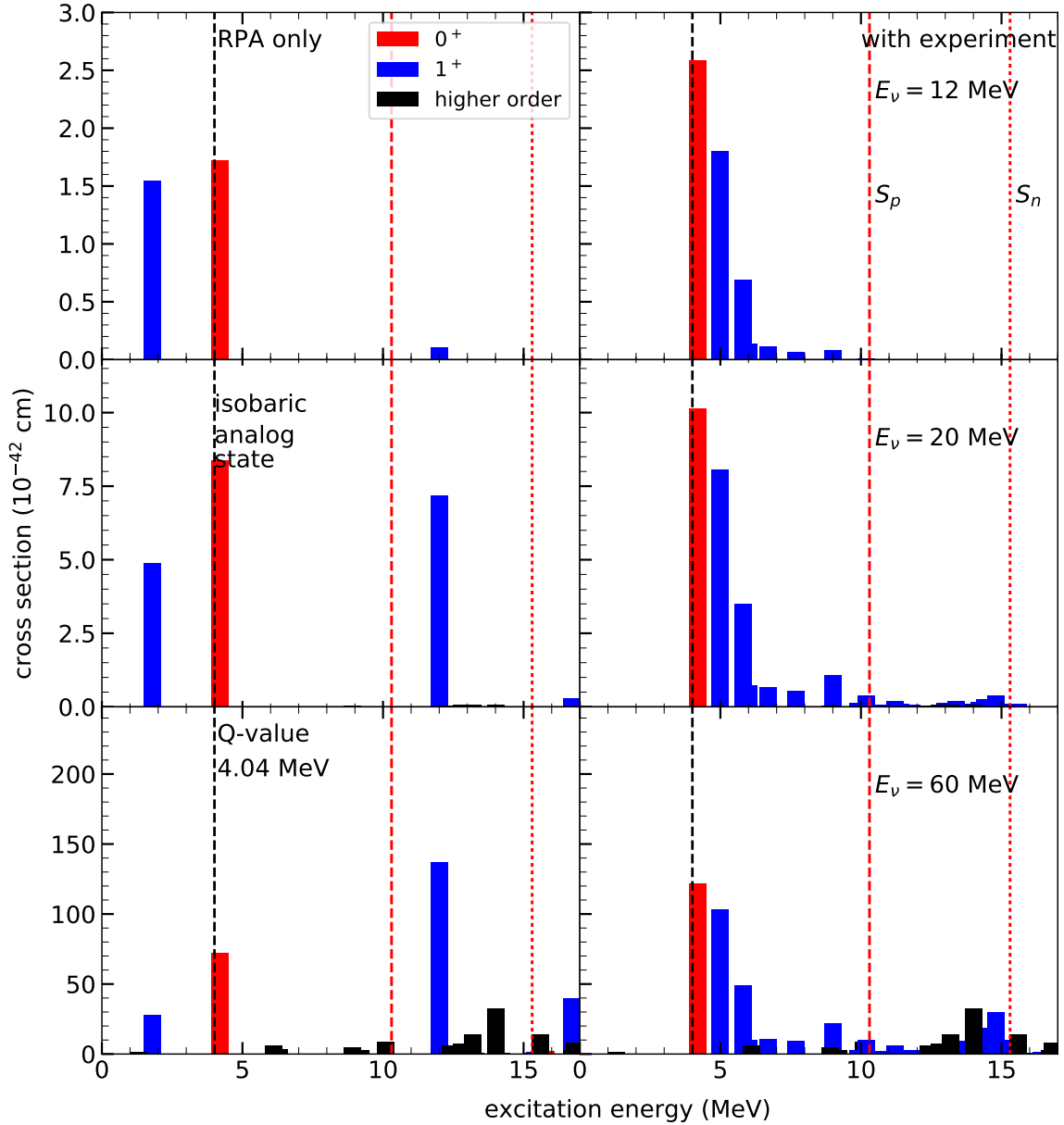


Figure 5.1.: Contribution of different states to the cross-section for the reaction $^{26}\text{Mg}(\nu_e, e^-)$ for three neutrino energies, $E_\nu = 12$ MeV (top row), $E_\nu = 20$ MeV (middle row) and $E_\nu = 60$ MeV (bottom row). The left column shows the results using only our RPA calculations and the right panels show the results including the experimentally measured transitions. The energy scale is relative to the parent nucleus ^{26}Mg and the Q-value of 4.04 MeV is indicated as black dashed line. The proton separation energy S_p and neutron separation energy of ^{26}Al are indicated by dashed and dotted red lines.

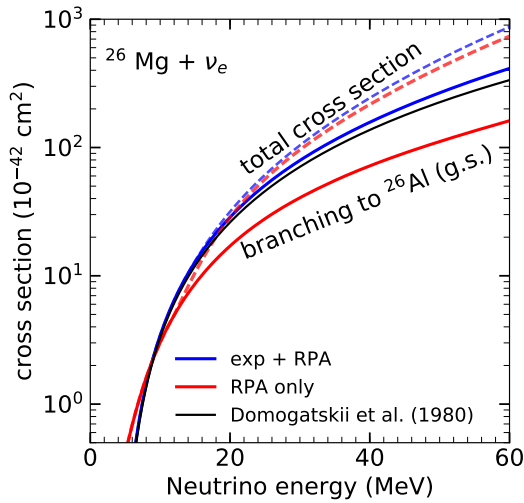


Figure 5.3.: Cross-section for the reaction $^{26}\text{Mg}(\nu_e, e^-)$ as a function of neutrino energy. At very low energies the cross-section is dominated by the experimentally known transitions. The black line indicates the distribution of the neutrinos corresponding to $T_\nu \approx 4$ MeV ($\langle E_\nu \rangle = 12$ MeV). For comparison, also the results based only on the RPA results and the estimate from [Domogatskii & Nadezhin \(1980\)](#) are shown.

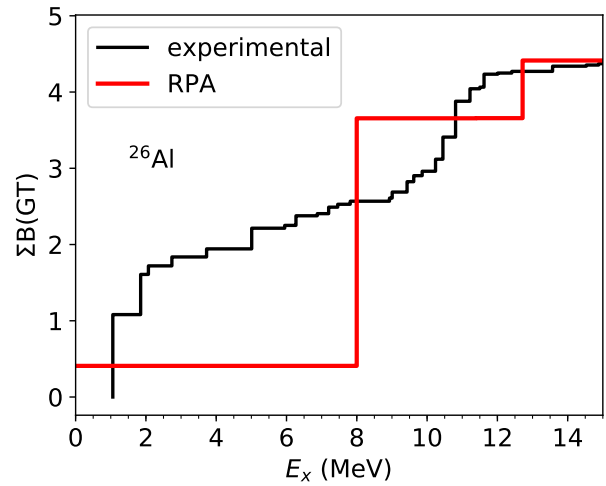


Figure 5.4.: Summed Gamow-Teller strength for ^{26}Al from the experiments and our RPA calculations. The true spectrum is much more fragmented but the total strength is reproduced with good accuracy.

^{36}Cl is of some particular interest because it has been found in material from the early solar system [Murty et al. \(1997\)](#) and its production in core-collapse supernova is discussed in detail in Section 5.3.3. The main channel for the production of ^{36}Cl via neutrinos is the reaction $^{36}\text{Ar}(\bar{\nu}_e, e^-)^{36}\text{Cl}$ that we have determined by combining shell-model calculations for the Gamow-Teller strength and RPA for the forbidden transitions. Table 5.2 compares the cross-sections from [Woosley et al. \(1990\)](#) to our results obtained with the RPA only and including the results from shell model calculations. [Woosley et al. \(1990\)](#) have calculated the cross-section based on full $0\hbar\omega$ shell model calculations based on the interaction matrix elements calculated by [Kuo & Brown \(1968\)](#), here the USDB interaction was used ([Brown & Richter, 2006](#)). [Lisetskiy et al. \(2007\)](#) have compared experimentally determined M1 strength of ^{36}Ar with the predictions from the shell model using the USD interaction and found a good agreement. Our cross-sections are slightly larger than the values by [Woosley et al. \(1990\)](#) but in general agreement.

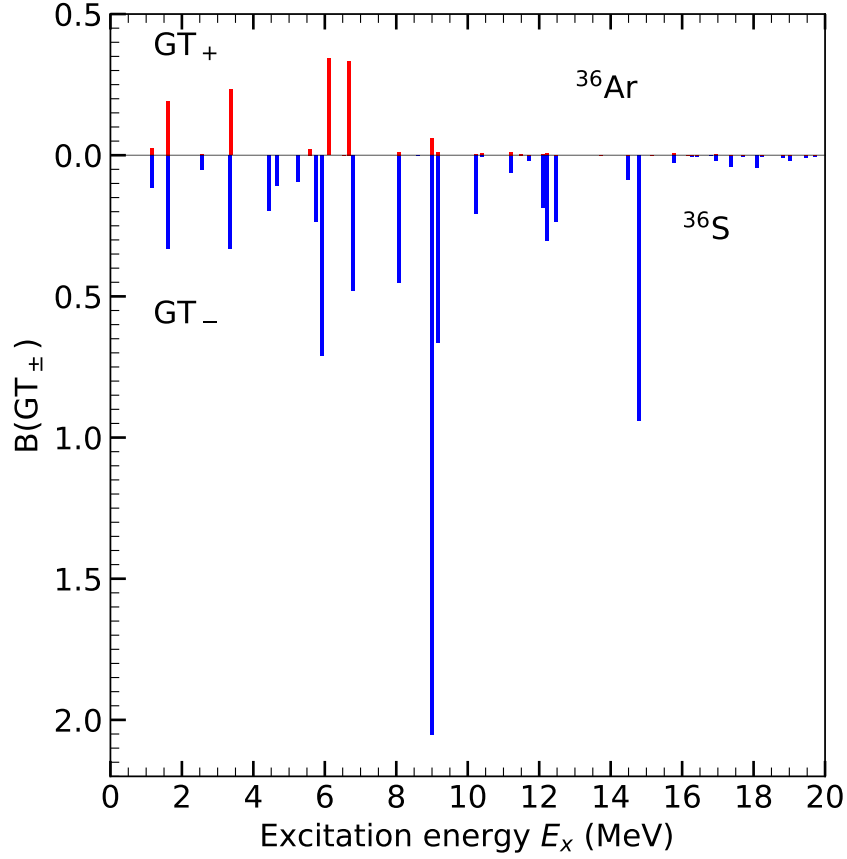


Figure 5.5.: $B(GT_+)$ strength distribution for ^{36}Ar and $B(GT_-)$ strength distribution ^{36}S from shell model calculations with the USDB interaction. This strength dominates the production of ^{36}Cl via electron (anti)neutrino captures on ^{36}S (^{36}Ar).

Another reaction that is relevant in this context is $^{36}\text{S}(\nu_e, e^-)^{36}\text{Cl}$. Data from the mirror β^+ decay of ^{36}Ca gives us information about the Fermi transition to the isobaric analog state which is in this case at 4.3 MeV and the two dominant Gamow-Teller transitions. The Fermi transition gives a significant contribution to the total cross-section, as can be seen in Figure 5.6. We also use the Gamow-Teller strength determined by shell-model calculations using the USDB interaction (Brown & Richter, 2006) with forbidden contributions again determined from the RPA calculations. The values we obtain are also shown in Table 5.2.

From the Gamow-Teller sum rule we find that $S_- = S_+ + 3(N + Z) = S_+ + 12$. Since the product of ^{36}P is not included in the model space of the shell model calculation that was used, $S_- = 12$ and thus already significantly larger than the total GT_+ strength for ^{36}Ar . However, ^{36}S is typically not abundant enough to allow a significant contribution to the production of ^{36}Cl . Again we find a good agreement between the RPA results and the values including the shell model calculations and the experimental β^+ decay. For this reaction also data from QRPA calculations is available and the values agree very well with our calculations. This shows that the typical uncertainties we expect from our RPA calculations are much smaller than what the relatively large discrepancy for ^{26}Al suggests.

In lighter nuclei only few states usually exist and in some cases they can be tackled by ab-initio approaches. Dedicated studies available in the literature provide some of the relevant cross sections. Values for reactions on ^4He are taken from Gazit & Barnea (2007).

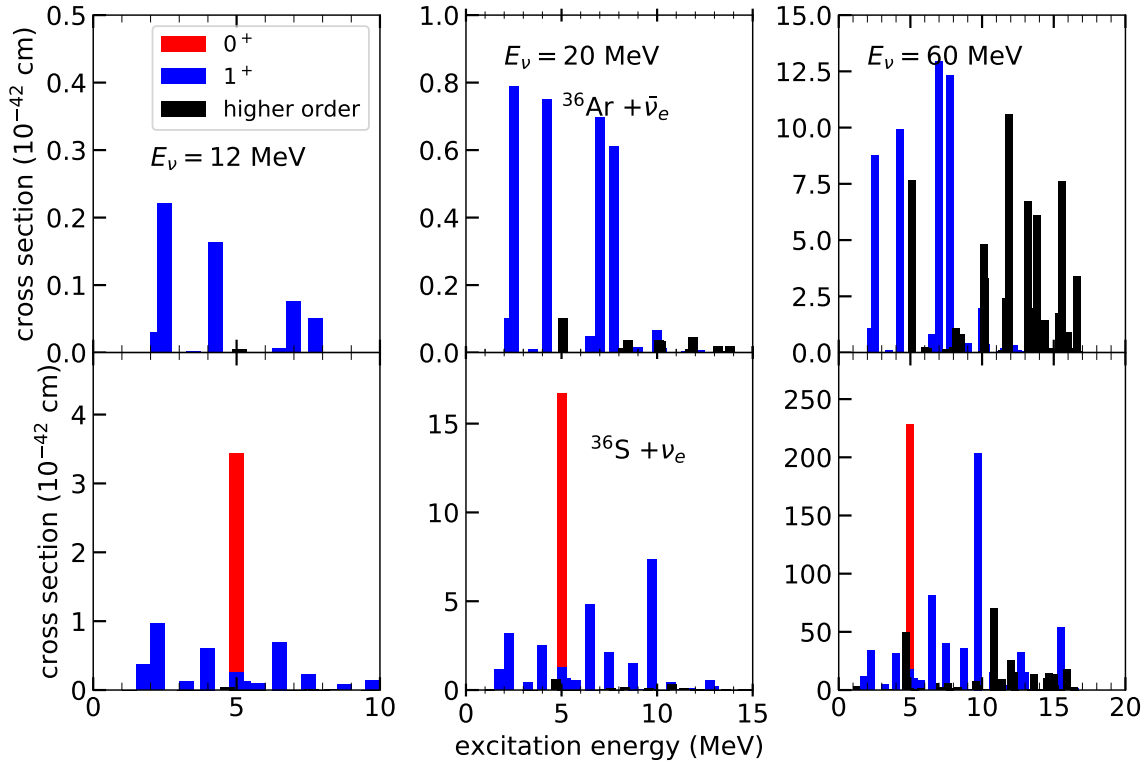


Figure 5.6.: Contribution of different multipoles to the electron (anti) neutrino absorption on ^{36}Ar and ^{36}S relevant for the production of ^{36}Cl . In both cases the Gamow-Teller (1^+) contribution is calculated with the shell model. For ^{36}S the Fermi transition (0^+) and dominant GT transitions are included based on the β decay properties of the mirror nucleus ^{36}Ca .

Reactions on ^{12}C are particularly important and for the emission of single particles, i.e. neutron, proton or α , we adopt values from [Heger et al. \(2005\)](#) that are also based on the measured strength and position of the dominating Gamow-Teller transition. QRPA calculation for ^{12}C have also been performed by [Cheoun et al. \(2010\)](#). The charged current cross-section for $^{12}\text{C}(\nu_e, e^-)^{12}\text{N}_{gs}$ has been experimentally determined for neutrino energies between 30 and 60 MeV from muon decay [Athanasopoulos et al. \(1997\)](#) and was found to be in good agreement with RPA predictions.

Ref. [Woosley et al. \(1990\)](#) provides cross-sections for $^{12}\text{C}(\nu, \nu' ^3\text{He})^9\text{Be}$, $^{12}\text{C}(\nu, \nu' ^3\text{He} \alpha p)^4\text{He}$ and $^{12}\text{C}(\nu, \nu' ^3\text{He} n)^4\text{He}$ that were derived with considerable care, using branching ratios for multi particle emission based on photo absorption experiments. The cross-sections for these channels are small compared to the single nucleon emission channels. Therefore, we just include the additional channels without adjusting the total cross-section.

We use cross-sections on ^{20}Ne based on charge-exchange data ([Anderson et al., 1991](#)) following the approach discussed by [Heger et al. \(2005\)](#) extended to both neutral-current and charged-current cross-sections.

While light to intermediate mass nuclei can be tackled with shell model calculations and for several nuclei direct measurements or data from mirror nuclei is available, these approaches cannot help for heavier nuclei. Only for very few cases experimentally determined transition strengths are available. The Gamow-Teller strengths below particle separation threshold in ^{138}Ba and ^{180}Hf have been measured by [Byelikov et al. \(2007\)](#) with the $(^3\text{He}, t)$ reaction at RCNP in Osaka using a 140 MeV/nucleon ^3He beam. The products were measured at forward angles to maximize the sensitivity to GT transitions. [Fujita et al. \(1999\)](#) had previously shown that charge-exchange reactions are suitable to extract the GT transition strength. Since the experiment only provides data up to the particle separation threshold,

we take the values for the cross-sections stated in [Byelikov et al. \(2007\)](#) for the γ channels, i.e. on $^{138}\text{Ba}(\nu_e, e^-)^{138}\text{La}$ and $^{180}\text{Hf}(\nu_e, e^-)^{180}\text{Ta}$. For the other particle emission channels we adopt the values presented in [Heger et al. \(2005\)](#) that are also very similar to our results. The γ channel is also the most important decay mode for nucleosynthesis as we show in Section 5.2.4. However, due to the relatively low neutron separation energy, the reaction $^{138}\text{Ba}(\nu_e, e^-n)^{137}\text{La}$ and $^{180}\text{Hf}(\nu_e, e^-n)^{179}\text{Ta}$ are found to have actually larger branchings than the γ -channels already at low neutrino energies around 10 MeV. This has already been seen in [Heger et al. \(2005\)](#) but not further explored. In Section 5.2.4 the role of the neutron emission channels is discussed but its contribution depends on the progenitor composition and is found to be minor except for a few cases. Cross-sections for ν_e absorption on ^{138}Ba and ^{180}Hf for example are based on measured Gamow-Teller strengths [Byelikov et al. \(2007\)](#) and have been found to be larger than RPA based values. For most other cases we need to rely on theory. Cross-section for the reactions relevant for the production of ^{92}Nb and ^{98}Tc have previously also been calculated in ref. [Cheoun et al. \(2012\)](#) within the framework of QRPA. For the most relevant reactions $^{92}\text{Zr}(\nu_e, e^-)^{92}\text{Nb}$ and $^{98}\text{Mo}(\nu_e, e^-)^{98}\text{Tc}$ our cross-sections are around 40% larger for $\langle E_{\nu_e} \rangle = 10$ MeV. Multi particle emission channels become only dominant for nuclei far away from stability. Therefore, even though we include all these channels in our nucleosynthesis calculations, they only play a very minor role for supernova nucleosynthesis. [Haxton et al. \(1997\)](#) have pointed out that the r -process abundance pattern of heavy elements could be sensitively affected by neutrino-induced reactions if the r -process occurs in the context of core-collapse supernova explosions. The impact of the set of reactions we use here have been considered in r -process scenarios by [Huther \(2014\)](#) but were found to have only a minor impact on the final yields.

reaction	method/ source	T_ν in MeV		
		2.8	4.0	6.4
$^{26}\text{Mg} + \nu_e$	WH1990	1.10	3.71	26.93
	QRPA	3.14	12.01	52.76
	RPA	4.72	14.37	59.41
	incl. exp	5.28	16.11	67.02
$^{22}\text{Ne} + \nu_e$	WH1990	0.02	1.23	13.91
	QRPA	3.90	13.28	50.03
	RPA	5.806	16.00	59.15
	incl. exp	6.61	18.04	67.03

Table 5.1.: Cross-sections averaged assuming Fermi-Dirac distributions of different temperatures T_ν and $\mu = 0$ in units of 10^{-42} cm². Our values based on RPA combined with experimental data (incl. exp) are shown in comparison to the values by Woosley and Hoffman [Woosley et al. \(1990\)](#) and QRPA calculations [Paar et al. \(2013\)](#).

reaction	method/ source	T_ν in MeV		
		2.8	4.0	6.4
$^{36}\text{Ar} + \bar{\nu}_e$	WH1990	0.68	2.77	14.23
	RPA	0.45	2.00	11.25
	incl. SM	0.75	2.55	12.85
$^{36}\text{S} + \nu_e$	WH1990	0.18	2.48	25.27
	QRPA	5.08	18.47	76.25
	RPA	6.60	21.80	92.19
	incl. SM + exp	9.70	31.60	136.07

Table 5.2.: Same as Table 5.1 but now for the charged current reactions that contribute to the production of ^{36}Cl . For ^{36}Ar no experimental information is available but we have supplemented the RPA transition with results from detailed shell model calculations for the Gamow Teller transitions. For ^{36}S data from the mirror nucleus and shell model results have been used.

5.2 Stable isotopes

After validating our setup in Section 4.5 we now discuss the nucleosynthesis results with the new set of neutrino-nucleus cross-sections presented in 5.1. A major part of this discussion is included in [Sieverding et al. \(2018b\)](#) and [Sieverding et al. \(2018a\)](#). We use a grid of progenitor models with ZAMS masses between 13 and 30 M_{\odot} spaced on an interval of 1 M_{\odot} . The progenitors have been evolved with the setup by [Rauscher et al. \(2002\)](#), including mass loss by [Nieuwenhuijzen & de Jager \(1990\)](#) and an improved treatment of convective overshooting. The progenitor models have been evolved including a full reaction network to follow the He-burning s -process and the γ process during the late phases of the evolution. The final burning episodes can result in merging convective burning shells which need to be modeled with multi-dimensional hydrodynamics coupled to the reaction network ([Ritter et al., 2018](#)) that can result in different nucleosynthesis. In the progenitor we use these phases are treated assuming hydrostatic equilibrium. The models are affected by an error in the implementation of neutrino losses that has recently been identified by [Sukhbold et al. \(2017\)](#). While these changes affect the structure and compactness of the iron core we do not expect a significant modification of the properties of the O/Ne, C and He shells that are the most relevant for the ν process. Furthermore, the parametric explosion model used here, is not affected by changes of the structure of the inner core.

While [Woosley & Heger \(2007\)](#) provide supernova nucleosynthesis yields of massive stars including the ν process in the standard fashion as setup by [Woosley et al. \(1990\)](#) with several updated neutrino-nucleus reaction rates by [Heger et al. \(2005\)](#) and [Kolbe et al. \(1992\)](#) but with the high neutrino energies. The recent set of supernova yield tables by [Pignatari et al. \(2016\)](#) does not include the ν process at all.

The focus of previous dedicated studies of the ν process [Heger et al. \(2005\)](#) has been primarily on the isotopes ${}^7\text{Li}$, ${}^{11}\text{B}$, ${}^{15}\text{N}$, ${}^{19}\text{F}$, ${}^{138}\text{La}$, and ${}^{180}\text{Ta}$, because those are present in the solar system, but nucleosynthesis calculations without including neutrino interactions cannot fully explain the observed abundances. Table 5.3 shows the production factors as defined by equation (3.10) averaged over the range of progenitor models between 13 and 30 M_{\odot} weighted with a Salpeter initial mass function with $\alpha = 1.35$ as in (3.9). The values of the production factors for the calculations without neutrinos clearly show the deficit in their production. The ν process pushes the averaged production factors of those nuclei closer to the solar system values. We find that due to the reduction of the ν energies (see 4.2) the effect of the ν process is diminished which, on the one hand, solves the problem of the slight overproduction of ${}^{11}\text{B}$ ([Heger et al., 2005](#)). On the other hand with the very low electron neutrino temperature ${}^{138}\text{La}$ is produced to less than half of its solar value. While ${}^{180}\text{Ta}$ has potentially other contributions from the s -process ([Käppeler et al., 2004](#)) (c.f. Section 5.2.4), this is not the case for ${}^{138}\text{La}$. In Section 5.4 we show that the early phase of neutrino emission can provide a solution to this problem.

Figure 5.7 shows the dependence of the total yields of these 5 most prominent ν process isotopes that are shown in Table 5.3 on the initial mass of the stellar model on which the composition and the structure depend. Stellar structure affects the ν process by three major aspects. First, as a secondary process the ν process always operates on abundant seed nuclei and the composition therefore determines where and to which extent the process can occur. Secondly, the stellar density and temperature profiles determine how strong the supernova shock affects the regions where the ν process seeds are located. Finally, the stellar model determines the distance of the regions of interest from the proto-neutron star and hence the intensity of the neutrino fluxes.

Stellar structure is determined by the complex interplay of nuclear burning, convection and hydrostatic adjustment and therefore monotonous trends with respect to the initial mass are not to be expected. Still, Figure 5.7 shows that the relative enhancement for the ν process nuclei, and in particular for the light elements Li and B, are quite robust with respect to the progenitor. Trends for the ν process contributions mostly follow trends for the production without neutrinos but tend to have a smoothing effect on variations with initial mass which we also find for the radioactive nuclei discussed in section 5.3.3.

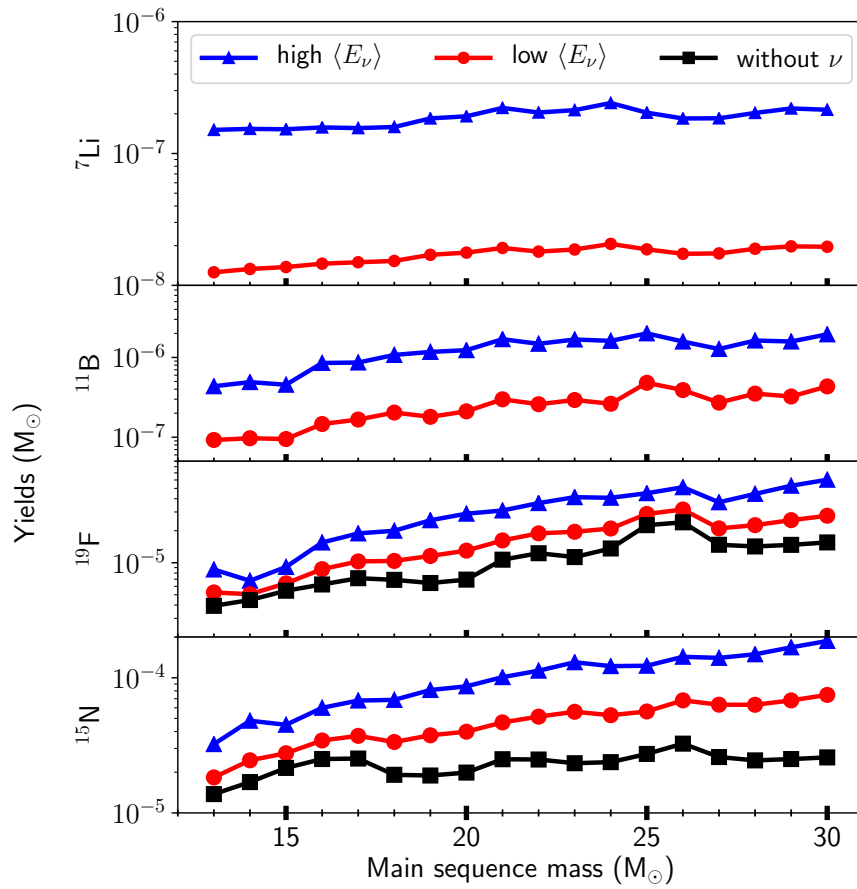


Figure 5.7.: Total yields for the nuclei with largest contributions from the ν process for the range of progenitors studied here. Averaged production factors are summarized in Table 5.3. Note that the scale of the y axis is different for each panel. The production of ${}^7\text{Li}$ and ${}^{11}\text{B}$ without neutrinos is negligible and not shown in the figure.

Nucleus	no ν	Low energies			High energies		
		all ν	only c.c.	only n.c.	all ν	only c.c.	only n.c.
${}^7\text{Li}$	0.002	0.04	0.01	0.03	0.58	0.05	0.57
${}^{11}\text{B}$	0.01	0.31	0.17	0.21	1.57	0.58	1.31
${}^{15}\text{N}$	0.06	0.09	0.08	0.08	0.16	0.10	0.15
${}^{19}\text{F}$	0.13	0.18	0.14	0.16	0.29	0.17	0.26
${}^{138}\text{La}$	0.16	0.46	0.44	0.18	0.77	0.73	0.22
${}^{180}\text{Ta}$	0.20	0.49	0.48	0.24	0.84	0.80	0.33

Table 5.3.: Production factors relative to solar abundances from reference [Lodders \(2003\)](#), normalized to ${}^{16}\text{O}$ production. Shown are the results obtained without neutrino, with our choice of neutrino temperatures (“Low energies”), and with the choice of [Heger et al. \(2005\)](#) (“High energies”) as defined in Table 4.1. For each set of energies, the results are also shown when only charged current reactions (induced by electron flavor neutrinos) are considered and when only neutral current reactions are considered. The values for ${}^{180}\text{Ta}$ are calculated assuming that a fraction of 35% survives in the long-lived isomeric state [Mohr et al. \(2007\)](#).

In the following we will first discuss the production of these nuclei individually in more detail and also include a short discussion of the uncertainties of the thermonuclear reaction rates that are involved.

5.2.1 The light elements Li and B

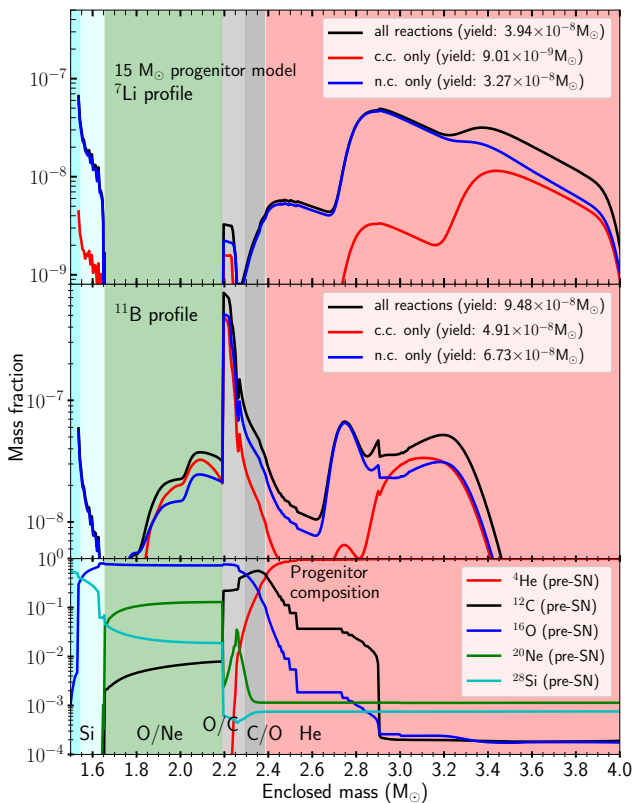


Figure 5.8.: Profiles of ${}^7\text{Li}$ and ${}^{11}\text{B}$ mass fractions for the $15 M_{\odot}$ using the updated low neutrino energies model with solar metallicity. ${}^7\text{Li}$ is mostly made at the base of the He shell by the reaction sequence described in the text and ${}^{11}\text{B}$ is produced in the thin C layer. Also shown are results when only charged current (c.c.) or only neutral current (n.c.) reactions are taken into account. This shows that electron flavor neutrinos contribute to as similar extent as the heavy flavor neutrinos for . The colored regions denote the different stellar regions as in Figures 3.4 and 3.5

equation B.3 one obtains that 42 % of the solar ${}^{11}\text{B}$ remains to be explained by the ν process, which could almost be accounted for even with the lower neutrino energies. This also supports that the more recently predicted lower neutrino energies are in better agreement with nucleosynthesis arguments.

In our current model the contribution to ${}^7\text{Li}$ from the ν process is even lower and GCR can also not account for more than 20% of the solar ${}^7\text{Li}$ (Prantzos, 2012). The nuclear uncertainties in the production of light elements by GCR are relatively small Kneller et al. (2003) because the cross-sections of the involved reactions have been measured at the relevant energies Mercer et al. (2001); Kneller et al. (2003). As discussed e.g. by (Prantzos, 2007), irradiation by galactic cosmic rays (GCR) is a promising scenario but also associated with large uncertainties. Most likely a combination of the contributions from GCR irradiation and the ν process in core-collapse supernovae is required to explain the solar abundance as pointed out by Prantzos (2012) and Austin et al. (2014). A better understanding of the ν process

The light elements ${}^7\text{Li}$ and ${}^{11}\text{B}$ are present in the solar system with abundances of 1.5×10^{-9} and 4×10^{-10} Lodders (2003). Since these nuclei are easily destroyed by charged particle reactions there is no stellar production mechanism and the origin of these abundances is a long-standing problem.

The idea that light isotopes of Li, Be and B could be produced by reaction between nuclei and high energy cosmic rays, in particular protons and α particles in the interstellar medium has been introduced by Reeves (1970) and refined by many authors (Meneguzzi et al., 1971). Cassé et al. (1995) have studied the production of light elements in the environment of very massive stars. The ejection of Carbon and Oxygen at high velocities could lead to reactions with the surrounding medium and spallation reaction would produce the light elements. Including the ν process as contribution to the production of light elements from massive stars along with a contribution from GCR irradiation, Olive et al. (1994) found that the original predictions by Woosley et al. (1990) would have to be tuned down by a factor 2 to be in agreement with the observed trends and the current solar values. Including metallicity dependent yields Vangioni-Flam et al. (1996) found that the yield would need to be reduced by up to a factor 5. More recent work Prantzos (2012) succeeds to explain the high ${}^{22}\text{Ne}/{}^{20}\text{Ne}$ ratios in the ISM with irradiation by GCR irradiation, taking into account the metallicity dependence of the cosmic ray spectra. With the estimate for the ${}^{11}\text{B}/{}^{10}\text{B}$ ratios associated with GCR irradiation it is possible to estimate how large the contribution from the ν process (see B) needs to be (Austin et al., 2011). From

yields is therefore important to constrain the contribution of different sources to the production of light elements. In particular, models of Hot Bottom burning in AGB stars [Karakas \(2016\)](#) and nucleosynthesis in classical novae [Rukeya et al. \(2017\)](#) have been shown to be potential sources of ${}^7\text{Li}$. Estimates for the required contribution of such intermediate mass stars to the galactic ${}^7\text{Li}$ inventory are tied to the predicted yields of light elements from supernova ν process.

To illustrate how the ν process can produce the light elements the upper panel of figure 5.8 shows the ${}^7\text{Li}$ mass fraction as a function of the mass coordinate for a $15 M_{\odot}$ progenitor model for the set of low neutrino energies as defined above. In order to disentangle the impact of electron type (anti)neutrinos and heavy flavor neutrinos results from calculations in which the neutrino reactions either only for charged- (c.c.) or only for neutral current (n.c.) processes have been included are also shown.

At the base of the He-shell the neutral current neutrino-interactions ${}^4\text{He}(\nu, \nu' p)$ and ${}^4\text{He}(\nu, \nu' n)$ contribute to produce ${}^7\text{Li}$ by the reactions ${}^3\text{He}(\alpha, \gamma){}^7\text{Be}(\beta^+){}^7\text{Li}$ and also ${}^{11}\text{B}$ via ${}^3\text{H}(\alpha, \gamma){}^7\text{Li}(\alpha, \gamma){}^{11}\text{B}$.

The n/p branching ratios for the particle emission after the neutral current excitation of ${}^4\text{He}(\nu, \nu')$ is very close to $1/2$ and only slightly favors proton emission. Depending on the composition, the production of ${}^3\text{He}$ can be followed by ${}^3\text{He}(n, p){}^3\text{H}$, giving in total a slightly larger production rate of tritons.

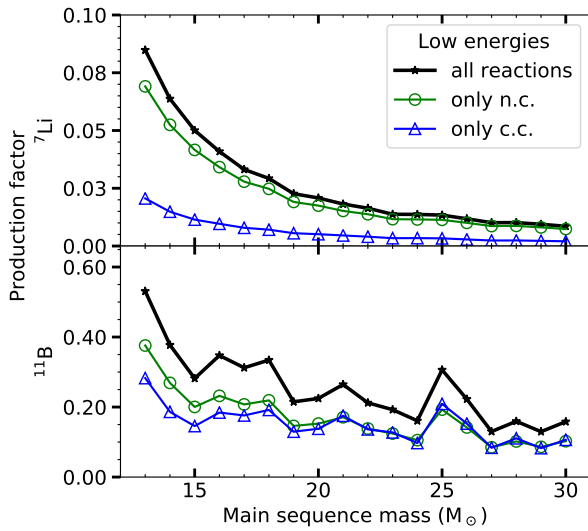


Figure 5.9.: Production factors for ${}^7\text{Li}$ and ${}^{11}\text{B}$ for the range of progenitor model we have studied with the set of low neutrino energies. The results of calculations that only include either charged- or neutral-current reactions are also shown.

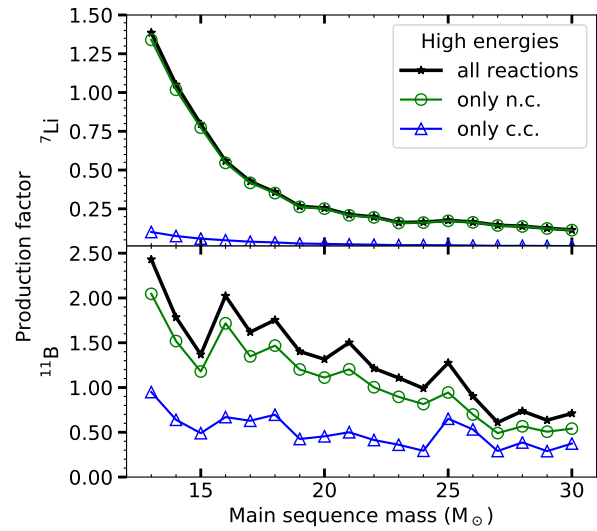


Figure 5.10.: Same as Figure 5.9 but for the high neutrino energies. In this case the neutral-current reactions are clearly dominant.

The upper panel of figure 5.8 shows that we can distinguish two regions for the production of ${}^7\text{Li}$ in the He-shell. In the lower part of the He-shell, ${}^7\text{Li}$ is mostly produced as ${}^7\text{Be}$ and charged current reactions have almost no contribution. Moving outwards, the mass fraction of ${}^7\text{Be}$ goes down and for mass coordinates larger than $3.2 M_{\odot}$ ${}^7\text{Li}$ is produced directly. Figure 5.11 illustrates the reaction flows in the He shell as defined by equation (2.45). In the lower part of the He shell, where the peak temperature ranges between $250 - 400 \text{ MK}$ both ${}^3\text{He}(\alpha, \gamma)$ and ${}^3\text{H}(\alpha, \gamma)$ are active. However, most of the ${}^7\text{Li}$ is destroyed again by further α captures. Due to the larger Coulomb barrier the reaction rate of ${}^7\text{Be}(\alpha, \gamma)$ is lower at this temperature and as shown in panels a and b of Figure 5.11 a large fraction of ${}^7\text{Be}$ survives the explosion. The destruction of ${}^7\text{Li}$ is at the same time the production mechanism for ${}^{11}\text{B}$ which is reflected by the high mass fraction of ${}^{11}\text{B}$ between 2.8 and $3.2 M_{\odot}$ in Figure 5.8. Once

the peak temperature drops below 250 MK as shown in panel c and d of Figure 5.11 the reaction flow through ${}^3\text{He}(\alpha, \gamma)$ is again smaller than ${}^3\text{H}(\alpha, \gamma)$ due to the higher charge of He. As a consequence the production of ${}^7\text{Be}$ decreases dramatically with temperature and an increasing amount of ${}^3\text{He}$ remains unprocessed. However, at such low temperatures also ${}^7\text{Li}(\alpha, \gamma)$ can no longer operate and ${}^7\text{Li}$ can be produced directly until also the rate ${}^3\text{H}(\alpha, \gamma)$ drops. The temperature dependence of these nuclear reactions also determines the dynamics of for each mass shell. Most of the tritons that are produced by neutrinos before the shock hits and while the temperature is still above 250 MK end up as ${}^{11}\text{B}$ while the further ${}^3\text{H}$ that is produced via neutrinos when the temperature is already low can contribute to ${}^7\text{Li}$. This has implications when we consider a time dependent neutrino signal in Section 5.4.

For the direct production of ${}^7\text{Li}$ there is also a much more significant contribution from charged-current reactions. For the production of ${}^7\text{Li}$ via ${}^3\text{H}(\alpha, \gamma)$ electron antineutrinos are relevant by creating ${}^3\text{H}$ via ${}^4\text{He}(\bar{\nu}_e, e^+ n){}^3\text{H}$. For the production of ${}^7\text{Be}$ electron neutrinos are relevant due to ${}^4\text{He}(\nu_e, e^- p){}^3\text{He}$. Since electron neutrinos are assumed to have softer spectra than their antiparticles, charged current reactions play a more important role for the direct production of ${}^7\text{Li}$ than for ${}^{11}\text{B}$ in the He shell.

By the same reaction chain those nuclei can also be produced from the α rich freeze out in the Si shell very close to the proto-neutron star that is subject to the most intense neutrino irradiation. The contribution from this region depends on the choice of the mass cut in parametric 1D simulations and is sensitive to details of the explosion dynamics. The contribution from this region is discussed in detail in Section 6. A final answer to the role of the ν process in this region requires to take into account multi-D effects from self-consistent supernova simulations that we look at in Section 6.

A significant fraction of ${}^{11}\text{B}$ is produced in the thin O/C shell by spallation reactions on ${}^{12}\text{C}$, i.e. ${}^{12}\text{C}(\nu, \nu'/n/p)$ mostly as ${}^{11}\text{C}$ that decays later with a half-life of about 20 minutes. On closer inspection the ${}^{11}\text{B}$ mass fraction profile in the C-rich zones shown in Figure 5.8 shows two components. In the lower part of the C shell the composition is dominated by Oxygen and only very little He is present. Further out, He burning is increasingly incomplete with ${}^{12}\text{C}$ being more abundant than ${}^{16}\text{O}$ and significant fraction of He still available. The presence of these α particles is detrimental to the production of light elements that are easily destroyed by α -capture reactions in the shock. As a result, mostly the neutrino irradiation after the shock has already passed contributes to the final yield of ${}^{11}\text{B}$. For more massive stars He-burning is increasingly complete and the C-dominated region shrinks.

The O/Ne layer also contains a mass fraction of ${}^{12}\text{C}$ of the order of 10^{-3} - 10^{-2} , about a factor 10 lower than what is found in the O/C layer. Therefore, the same channels operate also throughout the whole O/Ne shell. Also here the timing of the neutrino interactions plays a role, because the shock heating is strong enough to produce α particles via photodissociation that destroy most of the light elements.

5.12 shows the contributions from the different layers. The He shell always gives the largest contributions. and for the models between 13 and 18 M_{\odot} the He- and C shells provide the dominant contributions. For more massive stars, the contribution from the O/Ne shell is larger than the contribution from the C shell.

In the following we discuss the dependence of the contributions from the different shells on the progenitor structure. With increasing progenitor mass the O/Ne shell tends to grow in terms of mass coordinate while the O/C shell shrinks because He-burning at higher temperature tends to produce little Carbon. As the O/Ne layer gains mass, the O/C shell also moves outward in radius, reducing the neutrino exposure in O/C region. The composition at the shell interface between the Si/O and O/Ne layers depends sensitively on the dynamics of the final burning phases. Shell O-burning at the bottom of the O/Ne layer removes most of the ${}^{12}\text{C}$ from that region. Depending on the extend of O burning the C-depleted region with ${}^{12}\text{C}$ abundances below 10^{-5} varies significantly. For the 21 M_{\odot} and 24 M_{\odot} the region of O burning is particularly narrow and ends already at typically 2.4 M_{\odot} while it extends to a mass coordinate of 3.7 M_{\odot} for the 25 M_{\odot} model. If O burning affects a smaller fraction of the star, less material has collapsed to the temperature and density required for O ignition. This means that the burning provides enough pressure to prevent the material on top from falling in. Such an intense

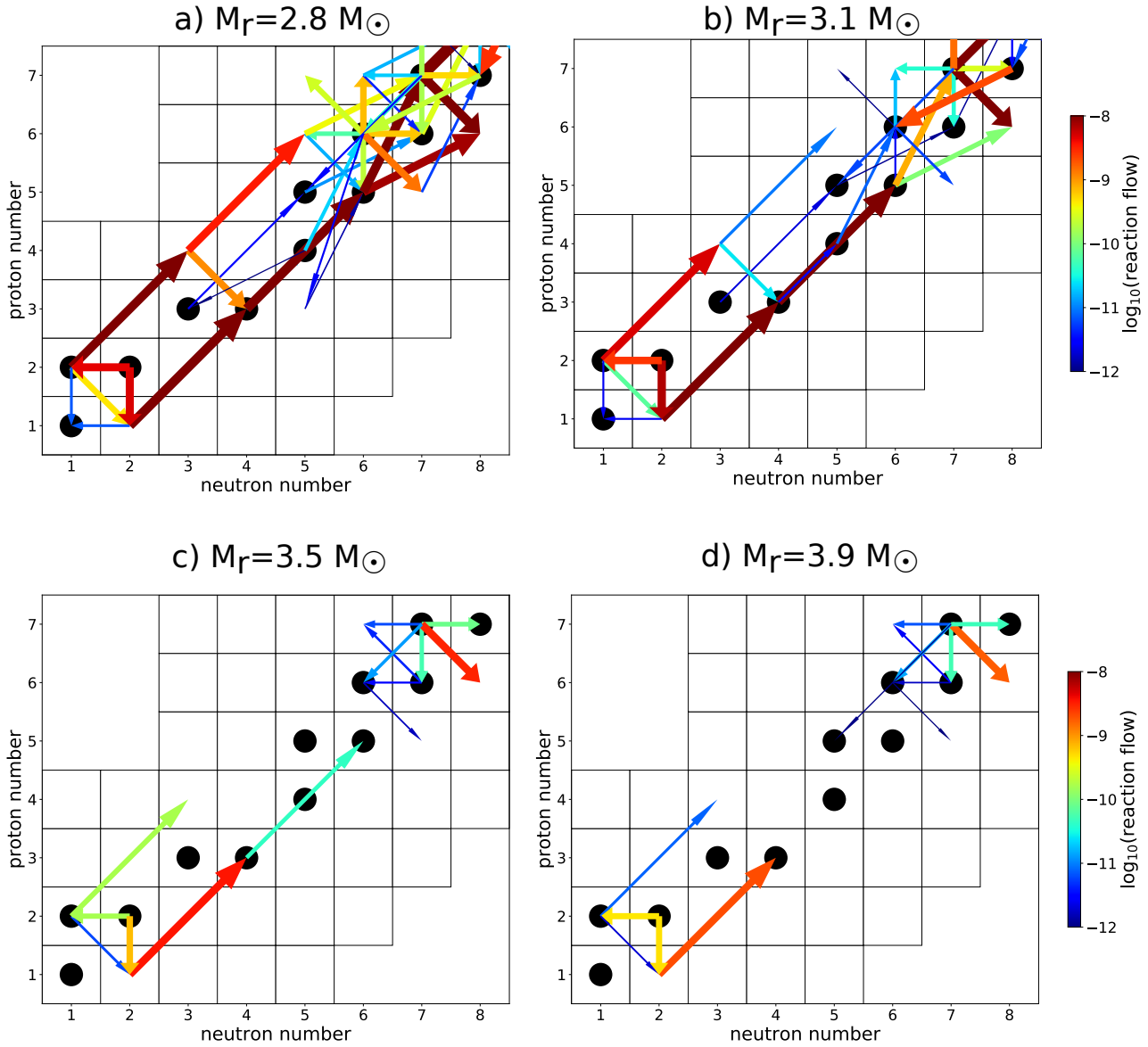


Figure 5.11.: Time integrated reaction flows as in equation (2.45) for the production of ${}^7\text{Li}$ in the He shell for the $15 M_\odot$ progenitor model for four different mass zones. Neutrino reactions on ${}^4\text{He}$ are included in the reaction flows and added to the photodissociation reactions in the same direction. β decays are not included in the reaction flows. The peak temperatures are a) 400 MK, b) 300 MK, c) 190 MK and d) 120 MK. As discussed in the text, ${}^7\text{Li}$ is produced directly for low temperature while only ${}^7\text{Be}$ survives at higher temperatures where also ${}^{11}\text{B}$ is produced.

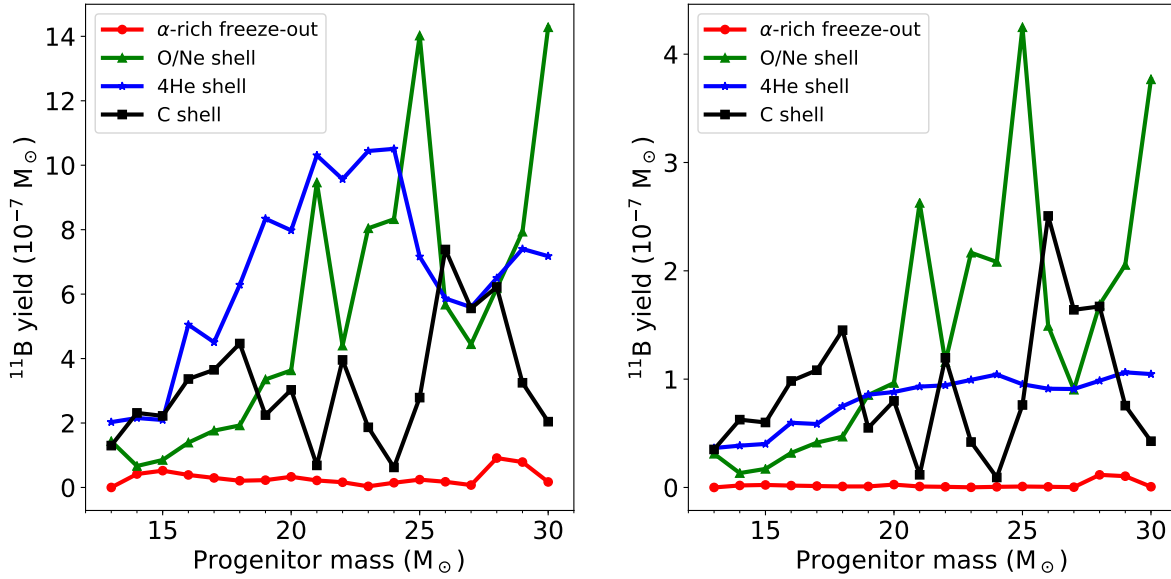


Figure 5.12.: Contributions to the total yield of ^{11}B from the different layers of the progenitor models.

burning would also push out the outer layer to larger radii, moving the C/O layer away from the PNS. This explains the anti-correlation between the contributions from the O/Ne and C shells that we see in 5.12. A large contribution from the O/Ne shell indicates hot He burning that puts the O/C shell far away from the center and implies a narrow O-burning region at high entropy.

In the O/Ne shell there is also a minor contribution from $^{16}\text{O}(\nu, \nu'\alpha p)$ that requires multi-particle emission channels to be taken into account. Since these reactions hinge on the knockout of protons and neutrons from tightly bound ^4He , ^{12}C and ^{16}O high energy neutrinos from the tail of the distribution are important. Consequently, the shift of the neutrino spectra to lower energies has a significant impact on the production of these light elements. The yields obtained in our calculations are consistent with Heger et al. (2005) when we use the same energies. The updated cross-sections for reactions on ^4He from Gazit & Barnea (2007) are slightly larger than what was previously used, giving an increase in the production of ^7Li and ^{11}B . These same cross-sections and also realistic energies have been used in a recent study about the production of radioactive ^{10}Be in low mass supernova Banerjee et al. (2016).

The yields of ^{11}B show more variation than the yields of ^7Li , which is predominantly produced in the He-shell. In contrast to that, ^{11}B has also contributions from deeper layers, in particular from the C/O rich and also the Ne/O layer.

With the previously often used set of high neutrino energies ^{11}B has commonly been overproduced and it has been suggested that the neutrino energies could be constrained by requiring a good reproduction of the solar value of the ^{11}B abundance with respect to ^{16}O (Yoshida et al., 2005).

We find that with the low neutrino energies the production of ^7Li by the ν process is negligible. This is consistent with the observation of the Lithium ‘‘Spite plateau’’ (Spite & Spite, 1982; Sbordone et al., 2010) in metal-poor stars in the metallicity range $-3.0 \lesssim [\text{Fe}/\text{H}] \lesssim -1.5$. Recent calculation of galactic chemical evolution Prantzos (2012) come to the result that about more than 50% of the solar ^7Li is not accounted for even for the more optimistic high neutrino energies. Hot Bottom burning in AGB stars (Karakas, 2016) and classical novae (Rukeya et al., 2017) could contribute minor amounts of ^7Li that are however insufficient to explain the Spite plateau. Observations of metal poor stars, with metallicities in the range between -1.5 to -3 show an almost constant abundance of ^7Li relative to Hydrogen. Since Core Collapse Supernovae are the main contributors to nucleosynthesis as early times, any significant contribution from Supernovae to ^7Li would lead to an accumulation of ^7Li with time.

The top panels of Figure 5.7 show that the neutrino enhanced yields of ${}^7\text{Li}$ and ${}^{11}\text{B}$ are not as sensitive to the progenitor model as e.g. ${}^{19}\text{F}$. That is because in the lower mass stars the relevant zones tend to be closer to the proto-neutron star which compensates for the overall narrower burning shells that contain smaller amounts of relevant seed nuclei. Since the production of ${}^{16}\text{O}$ increases with progenitor mass that also means that the production factor normalized to Oxygen significantly increases towards the low mass end of the progenitor range we studied. Hence, uncertainties in the initial mass function will also play an important role since the weight given to the low mass stars is crucial for the average production factor.

With respect to thermonuclear reactions ${}^7\text{Li}(\alpha, \gamma)$ and ${}^3\text{He}(\alpha, \gamma)$ are the most important reaction rates for the determination of ${}^7\text{Li}$ yields. The reaction rates in this region have been under intense investigation for many years mostly because of their relevance for Big Bang Nucleosynthesis. The cross-sections for ${}^3\text{He}(\alpha, \gamma)$, ${}^3\text{H}(\alpha, \gamma)$ as well as for ${}^3\text{He}(n, p){}^3\text{H}$ and ${}^7\text{Be}(n, p){}^7\text{Li}$ are based on a recent evaluation based on *R*-matrix theory by (Descouvemont et al., 2004) and the uncertainty is quoted as less than 20% at a temperature of 0.1 GK. The important reaction ${}^7\text{Li}(\alpha, \gamma)$ is still based on NACRE (Angulo et al., 1999). Even though the uncertainty for the relevant temperatures around few 100 MK is given as 20% the reaction is currently investigated at the University of Notre Dame.

The production mechanism is very robust with respect to changes of the reaction rates ${}^3\text{He}(\alpha, \gamma)$ and ${}^3\text{H}(\alpha, \gamma)$. Variations of the rates of these reactions within a factor 10 change the final ${}^7\text{Li}$ and ${}^{11}\text{B}$ abundances by less than 1%. Therefore, the nuclear uncertainties associated with the predicted yields are rather small.

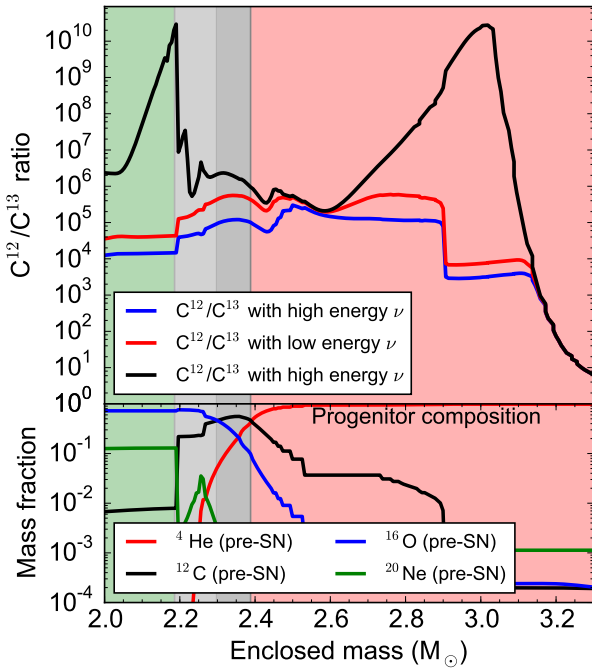


Figure 5.13.: figure

$^{12}\text{C}/^{13}\text{C}$ profile for the $15 M_{\odot}$ progenitor. for the high and low neutrino energies. The ν process can lead to a significant local reduction of the ratio that however never goes down to the solar value.

either in low and intermediate mass stars by convective mixing and associated with the s process or induced by rotational mixing in massive stars Pignatari et al. (2015). A secondary effect of the neutrino process is also the release of free protons from spallation reactions into a medium which is largely depleted in hydrogen. We find that free protons from neutrino reactions lead to a locally significantly increased mass fraction of ^{13}C and hence reduced $^{12}\text{C}/^{13}\text{C}$ that is shown in figure 5.13 for a $15 M_{\odot}$ progenitor. This enhancement has almost no effect on the integrated yield because that is dominated by the much higher ^{13}C mass fraction in the outer He shell. Pre-solar grains do not necessarily reflect the average composition of the environment in which they have formed. Depending on the efficiency of mixing after the ejection by a supernova explosion, material from a particular shell can condense into grains. In this case, however, even the largest localized increase due to the ν process that we find in our models is insufficient to explain the origin of carbon-rich pre-solar grains with the lowest $^{12}\text{C}/^{13}\text{C}$ ratios.

The ν process can contribute to the production of ^{15}N and to ^{19}F in the O/Ne and O/C shells mostly via the neutral current spallation that is discussed in the next section.

The CNO isotopes are copiously produced in many stellar environments and with the improvements in telescopes more and more data on the distribution of their abundances become available Adande & Ziurys (2012). This gives us insights into the evolution of abundances of these element in the universe. The most common isotopes ^{12}C , ^{16}O and ^{14}N are copiously produced by massive stars. More interesting are the rarer variants of these elements, such as ^{13}C , ^{18}O and ^{15}N . More than 40 years ago it has been found that the interstellar medium is enriched in these rare isotopes compared to the solar system. Hence, active astrophysical sources of these isotopes are required. Using prediction of nucleosynthesis yields theoretical models of galactic chemical evolution can reproduce the observations and disentangle the contribution of different astrophysical sources Audouze et al. (1975); Romano et al. (2017). For ^{13}C there is also evidence that it has could have been very abundant in the material from which the solar system has formed. Carbon-rich pre-solar grains have been found that exhibit $^{12}\text{C}/^{13}\text{C}$ ratios in the range 1-10, i.e. even lower than the solar value (see database Washington University Presolar Grains Database (Hynes & Gyngard, 2009) and original references therein). ^{13}C has been found to be most efficiently produced in scenarios of proton ingestion into He burning regions

5.2.3 ^{15}N , and ^{19}F

The ν process can contribute to the production of ^{15}N and to ^{19}F in the O/Ne and O/C shells mostly via the neutral current spallation of protons or neutrons $^{16}\text{O}(\nu, \nu' p/n)$ and $^{20}\text{Ne}(\nu, \nu' p/n)$ respectively, since ^{15}O as well as ^{19}Ne quickly decay to ^{15}N and to ^{19}F respectively. Even the charged current reactions $^{16}\text{O}/^{20}\text{Ne}(\nu_e, e^- p)$ and $^{16}\text{O}/^{20}\text{Ne}(\bar{\nu}_e, e^+ n)$ finally contribute to ^{15}N and to ^{19}F . When we take into account the harder spectrum for the heavy flavor neutrinos we find that the spectrally averaged cross-section for the sum of the two charged current channels is a factor 10 smaller than the combined neutral current channels for the higher neutrino energies. For the lower energies the charged current contribution is still smaller than $1/3$. Heger et al. (2005) have also concluded that the ν process can probably not account for the entire solar abundance of ^{19}F and can only produce small amounts of ^{15}N . Table 5.3 shows that with the low neutrino energies the averaged ^{19}F yield is increased by 30% but still only reaches a production factor of 0.2 and with high energies it is less than 0.3. This is in agreement with the conjecture that the ν process in core-collapse supernovae is not the only source of ^{19}F which is supported by recent observational evidence. Spectral analysis of nearby stars do not show a distinct correlation between O and F abundances that would be expected if supernovae were the main source for Fluorine Jönsson et al. (2017). Galactic chemical evolution models Renda et al. (2004); Kobayashi et al. (2011), still attribute a significant component of the galactic ^{19}F inventory to core collapse supernovae in combination with asymptotic giant branch (AGB) and Wolf-Rayet stars.

The lower panel of Figure 5.7 shows that the ^{19}F yield exhibits a relatively large sensitivity to the progenitor model. Indeed, the mechanism behind the production depends significantly on the mass of the star.

For the $15 M_{\odot}$ model the supernova shock alone, i.e., without neutrinos, increases the pre-supernova ^{19}F content of $4.3 \times 10^{-6} M_{\odot}$ to a yield of $5.5 \times 10^{-6} M_{\odot}$, corresponding to a production factor of 0.15. Neutrinos increase the production factor to 0.20 or 0.28 for low and high energies respectively. The thermonuclear component is mainly due to the reaction sequence $^{18}\text{O}(p, \alpha)^{15}\text{N}(\alpha, \gamma)^{19}\text{F}$ operating on ^{18}O at the lower edge of the He-shell where post shock temperatures reaches 0.67 GK at densities of up to 1500 g cm^{-3} . This requires an episode of convection to mix the ^{18}O from the CNO cycle down to the bottom of the He-shell where the peak temperature in the shock will be optimal. For the least massive star, the $13 M_{\odot}$ model ^{18}O remains concentrated in a narrow region where the peak temperature reaches less than 0.5 GK and as a results the shock heating does not really play a role for the ^{19}F yield without neutrinos which here results almost entirely from the pre explosive hydrostatic burning and gives a production factor of 0.23. Including the ν process in this model however gives the highest production factor among the models studied here of 0.27 for the low energies and 0.37 for high energies.

The profile of the ^{19}F mass fraction for the $15 M_{\odot}$ model is shown in the upper panel of figure 5.14 where one can see that the thermonuclear production at the base of the He shell is confined to a relatively narrow region. The thermonuclear production of ^{19}F requires two components. First the presence of ^{18}O that is a produced via $^{14}\text{N}(\alpha, \gamma)^{18}\text{F}(\beta^+ \nu_e)^{18}\text{O}$. ^{14}N results from the CNO cycle and thus the region for suitable for the thermonuclear production of ^{19}F is sensitive to the physics of Hydrogen burning. Secondly, the peak temperature reached in this region needs to be in the range of 0.4 – 0.5 GK.

Assuming that internal energy after shock passage is dominated by radiation one can relate the explosion energy E_{expl} and the peak temperature T_{peak} at a given radius r can as (Woosley et al., 2002):

$$T_{\text{peak}} = 2.4 \left(\frac{E_{\text{expl}}}{10^{51} \text{ erg}} \right)^{1/4} \left(\frac{r}{10^9 \text{ cm}} \right)^{-3/4} \text{ GK.} \quad (5.1)$$

This illustrates that whether the optimal temperature conditions for ^{19}F production are reached for a given progenitor abundance profile is very sensitive to the radial position of the compositional shell interfaces and also mildly sensitive to the explosion energy. The optimal temperature itself is determined by thermonuclear reaction rates and recent updates on the proton capture rates (Iliadis et al., 2010)

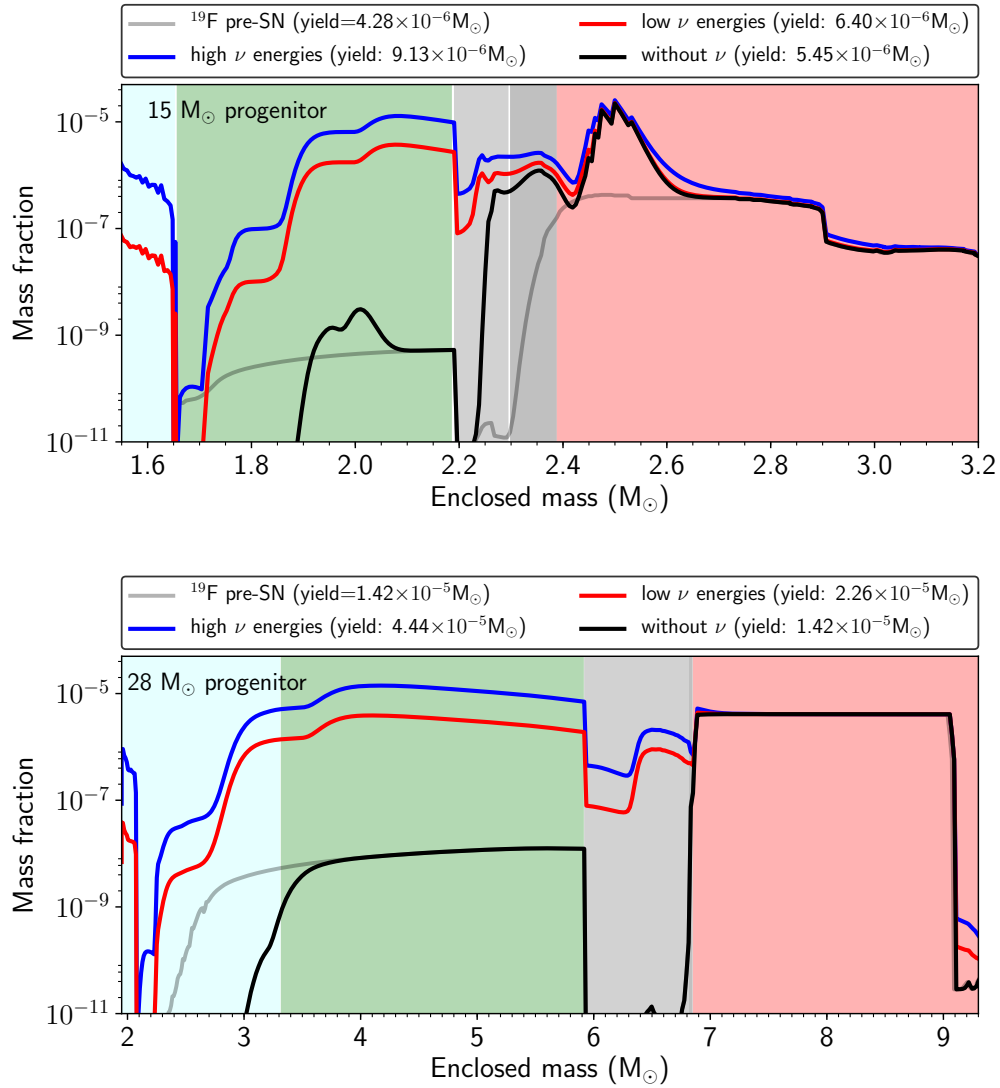


Figure 5.14.: Mass fraction of ^{19}F for the $15 M_{\odot}$ model (upper panel) and the $28 M_{\odot}$ progenitor (lower panel) representative for the lower and upper ends of the range of masses we explore. Shown are the pre-SN mass fractions as well as the final mass fractions without neutrinos, with the updated set of low neutrino energies and the high energies. While the supernova shock leads to a peak in the mass fraction around mass coordinate $2.5 M_{\odot}$, the ν process is much more prominent for the more massive model. The background colors indicate the compositionally differing shells of the progenitor star as shown in detail at the bottom of Figure 5.8

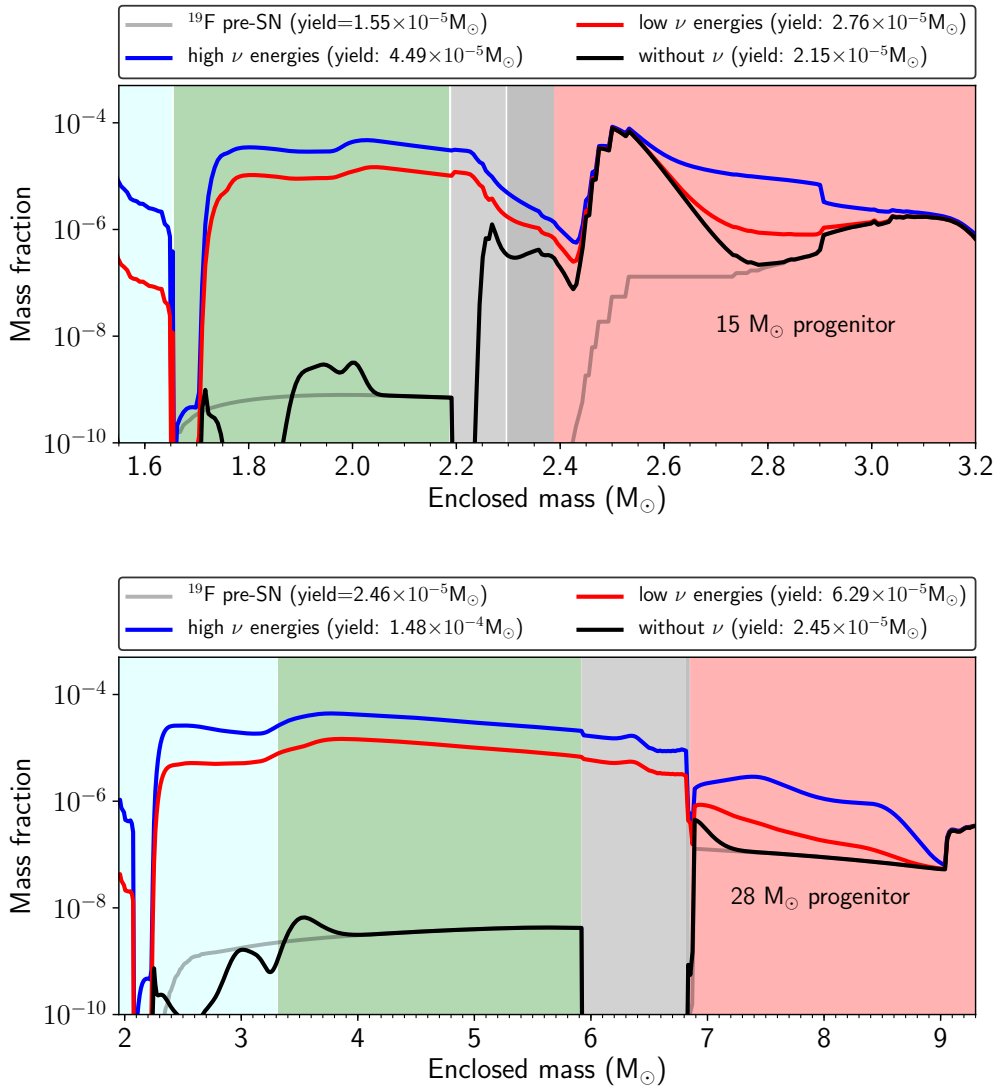


Figure 5.15.: Same as Figure 5.14, mass fraction of ^{15}N for the $15 M_{\odot}$ model (upper panel) and the $28 M_{\odot}$ progenitor (lower panel) including the pre-SN mass fractions as well as the final mass fractions without neutrinos, and with the different sets of neutrino energies and the high energies. While the effect of the ν process is almost negligible for the lower mass progenitor, the yield for the $28 M_{\odot}$ progenitor is increased by a factor 3. Due to the large amount of ^{16}O however, the production factor is only 0.1.

have a significant impact on the production of ^{19}F . Compared to calculations with reaction rates based on [Caughlan & Fowler \(1988\)](#) and [Angulo et al. \(1999\)](#) the updated reaction rates have increased the total yield of ^{19}F by 15% without neutrinos and by 20% with the high neutrino energies for the $15 M_{\odot}$ model.

Trends of the ^{19}F production with respect to the progenitor mass can be related to these sensitivities of the thermonuclear production. With increasing initial stellar mass the ^{19}F production factor without neutrinos tends to decrease because of a larger production of ^{16}O even though the yield of ^{19}F itself also increases substantially as can be seen in Figure 5.7. The ν process has also a larger impact because the mass contained in the O/Ne layer increases while the thermonuclear production is increasingly suppressed. This is illustrated with two examples in Figure 5.14 where the mass fraction of ^{19}F for the $15 M_{\odot}$ and $28 M_{\odot}$ models are shown, representative for lower and upper end of mass range considered here. For the $28 M_{\odot}$ model the contribution from the ν process in the O/Ne layer is the most prominent effect of the explosion while the peak of thermonuclear production at the inner He-shell in the $15 M_{\odot}$ model gives an important contribution. For stars more massive than $17 M_{\odot}$, the ν process can boost the ^{19}F production by factors of up to 1.5-2 and 3-4 for low and high energies respectively.

Finally, we also take a quantitative look at the sensitivity with respect to variations of the thermonuclear reaction rates and compare it directly with the same variation of the neutrino-induced reaction. Table 5.4 shows the effect of changes of different reactions rates on the ^{19}F yield of the $15 M_{\odot}$ model. Note, that changes only affect the explosive nucleosynthesis. The effect such changes would have on the pre supernova evolution and hence the composition of the progenitor are not included. We have again varied the thermonuclear reaction rates within a factor of 10 which exceed the expected uncertainty by far. According to [Sallaska et al. \(2013\)](#) the reaction rates for $^{15}\text{N}(\alpha, \gamma)^{19}\text{F}$ and $^{18}\text{O}(p, \alpha)^{15}\text{N}$ are both known with an uncertainty of less than 10% for temperatures above 1 GK. Even though we also do not expect such a large uncertainty for the neutrino reaction $^{20}\text{Ne}(\nu, \nu'p)^{19}\text{F}$, the comparison shows, that the sensitivity of the ^{19}F yield to the neutrino reaction is similar to the sensitivity with respect to the thermonuclear reaction rates.

Reaction	$\times 10$	$\times 0.1$
$^{15}\text{N}(\alpha, \gamma)^{19}\text{F}$	1.71	0.85
$^{18}\text{O}(p, \alpha)^{15}\text{N}$	1.14	1.00
$^{20}\text{Ne}(\nu, \nu'p)^{19}\text{F}$	2.28	0.86

Table 5.4.: Ratio of the integrated ^{19}F yield with modified reaction rates relative to the standard values for the calculations with a $15 M_{\odot}$ model. The sensitivity to the neutrino reactions is comparable to the sensitivity with respect to nuclear reaction rates.

The thermonuclear production mechanism is additionally sensitive to the temperature and composition. The ν process is mainly sensitive to the distribution of ^{20}Ne in the stellar model as well as the cross-sections for neutrino-induced reactions on ^{20}Ne , which is now based on measured Gamow-Teller strength [Anderson et al. \(1991\)](#); [Heger et al. \(2005\)](#). While the reaction rates of for the thermonuclear process are determined by the ambient temperature of the stellar plasma, the neutrino nucleus interactions are determined by the spectral temperature of the neutrinos. In Section 5.4 we show that an appropriate choice of this temperature is not straightforward.

5.2.4 Long-lived ^{138}La and nature's rarest element ^{180}Ta

The production of the isotopes ^{138}La and ^{180}Ta is of particular interest because they both are present in the solar system but their production mechanism is not yet fully understood.

While ^{11}B is the most sensitive to the neutrino energies mostly via neutral current reactions, the ν process affects ^{138}La and ^{180}Ta almost exclusively via ν_e captures. Therefore, those two isotopes are the most promising species to infer ν_e properties via ν process nucleosynthesis. The cross-sections for $^{138}\text{Ba}(\nu_e, e^-)^{138}\text{La}$ and $^{180}\text{Hf}(\nu_e, e^-)^{180}\text{Ta}$ are well constrained based on experimentally measured transition strengths presented by [Byelikov et al. \(2007\)](#).

Nucleosynthesis calculations by [Käppeler et al. \(2004\)](#) and [Belic et al. \(2002\)](#) have shown that around 80% of the solar ^{180}Ta can be produced by the s process in AGB stars mostly via decays of excited states

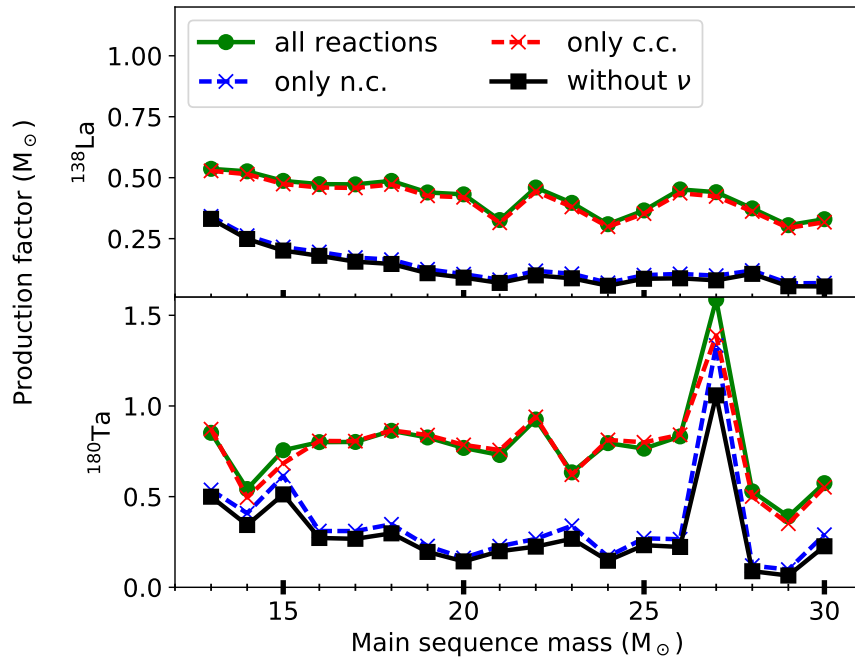


Figure 5.16.: Production factors relative to ^{16}O for ^{138}La and ^{180}Ta for the new set of low neutrino energies. Results including only neutral current (n.c.) and only charged current (c.c.) are also shown. Only for the $14 M_{\odot}$, $15 M_{\odot}$ and $27 M_{\odot}$ models a significant contribution from neutral current reactions to the production of ^{180}Ta appears while ^{138}La is dominated by the c.c. reactions for all the models. The values for ^{180}Ta correspond to the assumption that 35% of the yield survive in the long-lived isomeric state.

of ^{179}Hf and ^{180}Hf . However, [Heger et al. \(2005\)](#) have also found an overproduction of ^{180}Ta due to the ν process in core collapse supernovae.

Understanding the origin of ^{180}Ta is further complicated by the fact that the $J^{\pi} = 1^{+}$ ground state ^{180}Ta decays by electron capture and β^{-} with a half-life of 8.15 h and only its isomeric 9^{-} state at an excitation energy of 75 keV is very long lived. Due to its high spin, the isomeric state is effectively decoupled from the ground state at low temperatures. We do not treat ^{180}Ta and its meta-stable isomeric state $^{180}\text{Ta}^m$ as separate species in our network but following the estimates derived by [Mohr et al. \(2007\)](#) we assume that about 35% of the ^{180}Ta that is present at 200 s after the onset of the explosion survives in the excited state.

With the high neutrino energies, our results for ^{138}La and ^{180}Ta are consistent with those presented by [Heger et al. \(2005\)](#) and [Byelikov et al. \(2007\)](#), giving almost solar production of ^{138}La and ^{180}Ta . The ^{180}Ta production shown in table 5.3 and Figure 5.16 are corrected for the fact that only the isomeric state of ^{180}Ta is long lived. Averaged over the whole range of progenitors ^{180}Ta is underproduced with the new set of lower neutrino energies (see table 5.3) ameliorating the tension with the contribution from the s process in AGB stars. In the following we look in detail at the production mechanism of ^{138}La and ^{180}Ta and the dependence on the progenitor model. Figure 5.18 illustrates the production of ^{180}Ta in the $15 M_{\odot}$ model. The reaction flows have been estimated as integrated instantaneous flows based on the abundances of the beginning of each time step of the calculation as defined by equation (2.45). Dashed lines indicate a negative net reaction flow, i.e. the inverse reaction dominates. At the base of the O/Ne shell, below $1.9 M_{\odot}$ the peak temperature exceeds 2.6 GK and the density reaches $0.5 \times 10^6 \text{ g/cm}^3$ such that not only the pre supernova abundance of ^{180}Ta but also ^{180}Hf are destroyed by photodissociation (see Figure 5.17). Since ^{180}Hf is the seed for the ν process, this forms the lower boundary of the production region. The net reaction flow of (γ, n) dominates over (n, γ) as indicated by the dashed lines in the upper panel of figure 5.18. Further out, as the peak temperature decreases

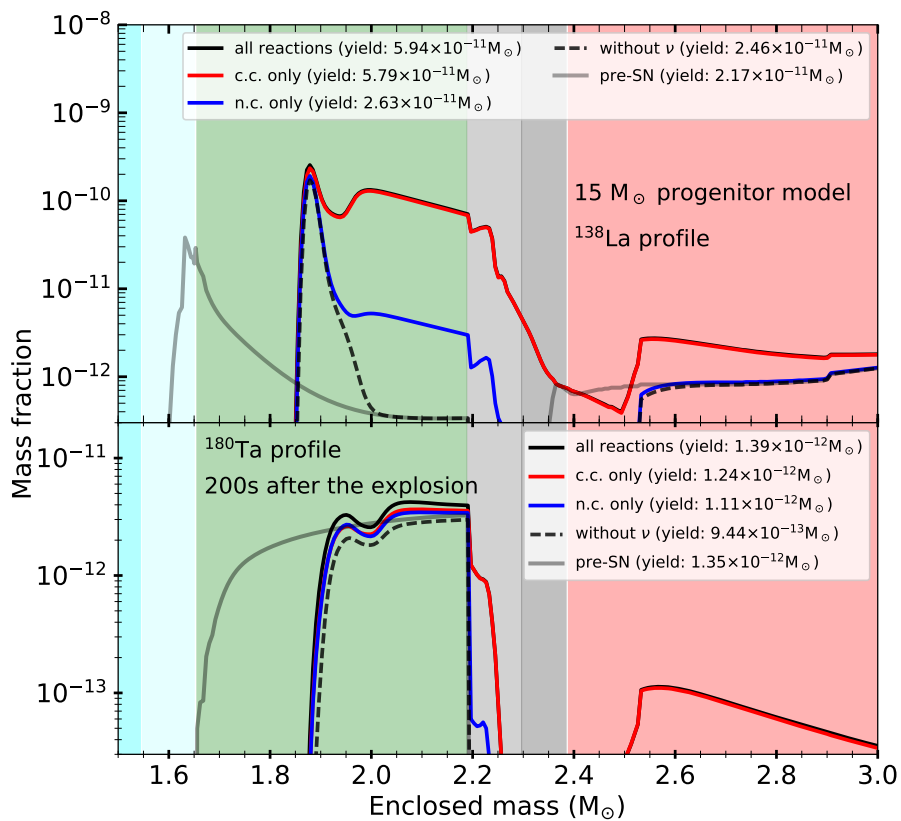


Figure 5.17.: Mass fraction profiles of ^{138}La and ^{180}Ta for the $15 M_{\odot}$ progenitor model. The background colors indicate the compositional zones as in 5.8. Also shown are results with only neutral and charged current reactions. ^{138}La and ^{180}Ta are both affected primarily by the charged current reactions with electron neutrinos.

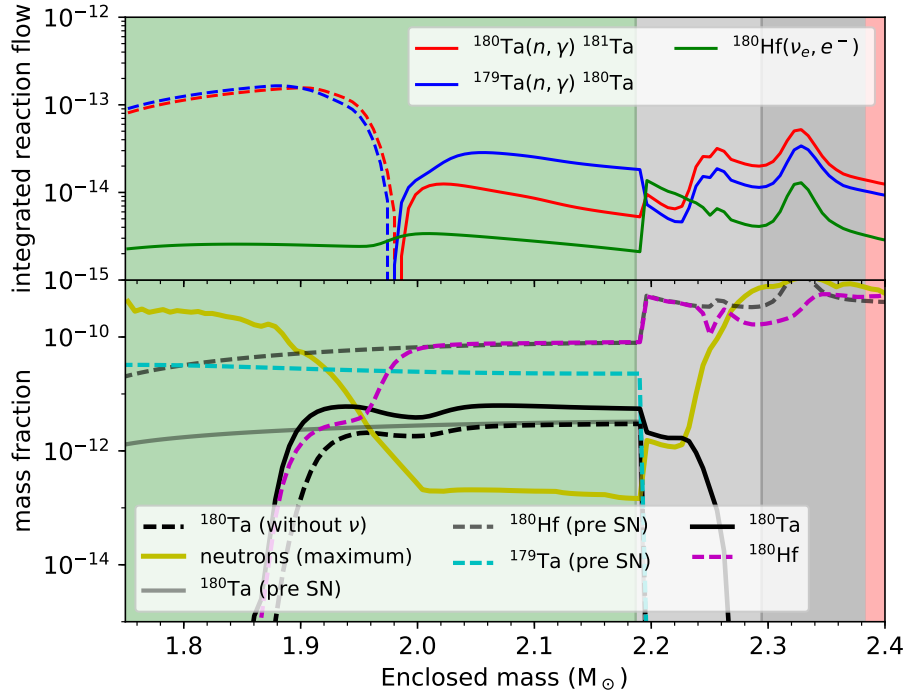


Figure 5.18.: Time integrated reaction flows (top panel) as defined by equation (2.45) and mass fraction profile of ^{180}Ta and relevant nuclei (bottom panel) for the $15 M_{\odot}$ model. If the forward (n, γ) is dominating, flows are shown as solid lines while dashed lines indicate that the inverse process (γ, n) dominates. The neutrino induced reaction flow through $^{180}\text{Hf}(\nu_e, e^-)^{180}\text{Ta}$ is also shown and only dominates in a very narrow region. The background colors indicate the different compositional layers as in figure 5.8.

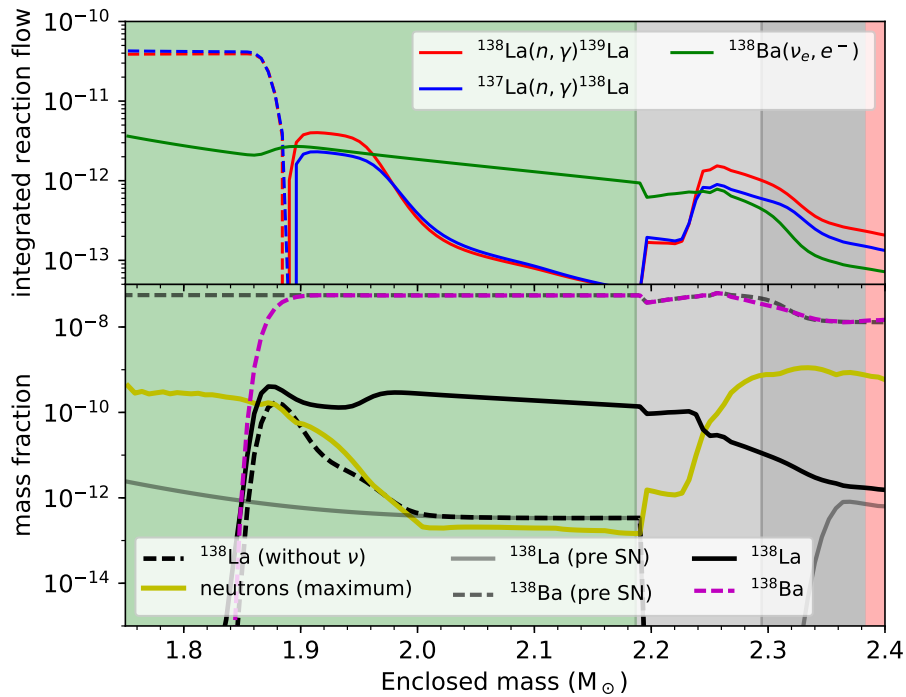


Figure 5.19.: Same as figure 5.18 but for ^{138}La . There is also a peak in the production due to (γ, n) reactions and in this case there is a region between 2.0 and $2.3 M_{\odot}$ where the ν process clearly is the dominant production channel.

below 2.3 GK, the γ process leads to peak in the production of ^{180}Ta in agreement with the temperature ranges suggested by [Rayet et al. \(1995\)](#) (see 3.4.2). The ν process increases the maximum abundance but only operates after the shock has passed and the material has cooled to below 2 GK.

For the particular case of the $15 M_{\odot}$ model shown in Figure 5.17 the pre SN abundance of ^{179}Ta is larger than the ^{180}Ta abundance. Therefore, not only the direct charged current channel $^{180}\text{Hf}(\nu_e, e^-)^{180}\text{Ta}$ plays a role but also free neutrons mainly from $^{16}\text{O}(\nu, \nu' n)$, $^{24}\text{Mg}(\nu, \nu' n)$ and $^{20}\text{Ne}(\nu, \nu' n)$ increase the final yield of ^{180}Ta . Figure 5.17 shows that neutral current reactions alone lead to a significant increase of the final yield even though the contribution from $^{180}\text{Hf}(\nu_e, e^-)^{180}\text{Ta}$ still dominates.

As the maximum temperature decreases towards higher mass coordinate the conditions for an effective production via the γ process are no longer given. In figure 5.18 the time integrated reaction flows change sign, showing that now the neutrons liberated by photo-dissociation actually lead to a reduction in the pre-supernova ^{180}Ta mass fraction. The competition between the $^{179}\text{Ta}(n, \gamma)$ and $^{180}\text{Ta}(n, \gamma)$ is important for the final abundance of ^{180}Ta in this region. [Wisshak et al. \(2018\)](#) have presented measurements for the neutron capture cross-section on $^{180}\text{Ta}^m$ and we use the reaction rates from the KADoNiS database (v0.3, eg. [Dillmann et al. \(2014\)](#)) which are given with an error estimate of less than 10%. We have performed calculations with variations of those two neutron capture rates within factors of ten and find that the effect on the final ^{180}Ta abundance is less than 40%. Hence, we conclude that the uncertainty of the ^{180}Ta yield with respect to the neutron capture cross-section is less than 1% and thus much smaller than the uncertainties that result from the neutrino properties.

At a mass coordinate of $2.0 M_{\odot}$ the main source for free neutrons changes from photodissociation to neutrino spallation. Hence, without neutrinos, the initial ^{180}Ta mass fraction remains unchanged in this region. Since this progenitor model provides a relatively high initial abundance of ^{179}Ta both processes, the direct charged current and the neutral current providing additional free neutrons, are relevant. The reaction flow of the ν_e captures on ^{180}Hf dominates only in a small region between 2.2 and $2.3 M_{\odot}$. Note, that this is a peculiarity of this progenitor model which is enriched in ^{179}Ta . For most other progenitor models the ν_e captures dominate the flow in the whole O/Ne shell. Further out in the He shell, ^{180}Hf is still available. However, free neutrons from $^{22}\text{Ne}(\alpha, \gamma)$ destroy any ^{180}Ta that is produced by neutrinos, forming the upper boundary of the production region.

The role of neutral current and charged current reactions depends significantly on the progenitor structure. In the range of progenitor models studied here the 14 , $15 M_{\odot}$ and $27 M_{\odot}$ models are the only cases for which more than 10% of the ν process contribution to ^{180}Ta results from neutral current neutrino reactions due to the additional neutrons to be captured on ^{179}Ta because those progenitor models are already enriched in ^{179}Ta and ^{180}Ta while at the same time depleted in ^{180}Hf .

The $27 M_{\odot}$ stands out in particular because here ^{180}Ta is already produced to full solar abundance before the explosion and without neutrinos. The ν process increases the production factor to 1.5 and 2.5 for low and high neutrino energies respectively. The pre explosive production of $^{179,180}\text{Ta}$ depends sensitively on the temperatures reached during the last burning stages and merging convective burning shells. If the O/Ne shell becomes hot enough or material is mixed into the hotter layers below, photodissociation can change the abundances significantly. This shows that more detailed modeling of the pre supernova phase as in [Ritter et al. \(2018\)](#) is desirable to understand not only the explosion mechanism as suggested by [Suwa & Müller \(2016\)](#) but it might also have a large effect on the synthesis of individual nuclei.

As can be seen in figure 5.16 The 14 and $15 M_{\odot}$ also show a particularly low ν process contribution to ^{180}Ta and a relatively large ^{180}Ta and low ^{180}Hf abundance before the explosion, as a result of slightly hotter burning conditions during the evolution. This is also reflected in the ^{98}Tc abundances shown in figure 5.21. Due to the relatively low neutron separation energy $S_n = 6.6$ MeV of the odd-odd nucleus ^{180}Ta the reaction cross-section for $^{180}\text{Hf}(\nu_e, e^- n)^{179}\text{Ta}$ is comparable to $^{180}\text{Hf}(\nu_e, e^-)^{180}\text{Ta}$ for average neutrino energies around 10 MeV such that ^{179}Ta can also be produced in-situ. This process contributes 10-20% to the total ^{180}Ta yield.

^{138}La is a very similar case. It is also a p nucleus that is bypassed by the s process that moves along the chain of stable Barium isotopes. Goriely et al. (2001a) have concluded that the decision about origin of ^{138}La requires the determination of the relevant neutron capture cross sections a better understanding of supernova neutrino properties. Recent experimental results do not favor the production via the γ process, leaving it an important candidate for the ν process (Kheswa et al., 2015). Figure 5.19 shows the most important reaction flows affecting ^{138}La . Similar to the case ^{180}Ta , the production of ^{138}La at the base of the O/Ne layer is dominated by the competition between (n, γ) and (γ, n) reactions, leading to a peak of the production even without neutrinos due to photodissociation of ^{139}La at peak temperatures of around 2.6 GK. Figure 5.17 also illustrates that the γ -process contribution to the lighter nucleus ^{138}La is located deeper inside the, i.e. at higher temperatures. As the peak temperature drops below 2 GK neutron captures dominate and tend to move the material back towards ^{139}La . Without neutrinos, the supply of ^{137}La is very small. However, $^{138}\text{Ba}(\nu_e, e^-n)$ can lead to a substantial production of ^{137}La because of the relatively large abundance of ^{138}Ba . In contrast to the case of ^{180}Ta free neutrons from neutral current spallation reactions alone do not have a significant effect because the relevant target nucleus ^{137}La is for all progenitors much less abundant than ^{138}Ba and would need to be produced by the charged current reaction first. In our calculations typically about 10% of the total yield of ^{138}La result from this mechanism via neutron captures on ^{137}La . The reaction channel $^{138}\text{Ba}(\nu_e, e^-n)$ is currently not based on experimental data from Byelikov et al. (2007) that provided Gamow-Teller strength below particle emission. This contribution is also particularly sensitive to the ratio between the $^{137}\text{La}(n, \gamma)$ and $^{138}\text{La}(n, \gamma)$ cross-sections. Therefore, we have taken the reaction rates by Rauscher & Thielemann (2000) in spite of recent experimental constraints on the $^{138}\text{La}(n, \gamma)$ cross-section. In Figure 5.19 one can see, that in the outer half of the O/Ne shell the direct neutrino-induced production is the dominating reaction flow, leading to an extended region where the ^{138}La mass fraction is almost exclusively determined by ν_e . Therefore, the production by the ν process increases with the amount of mass in the O/Ne shell.

The upper panel of figure 5.16 shows the production factor for ^{138}La over the range of progenitor models discussed here with the set of our new more realistic set of lower neutrino energies. This also shows the results of calculations with only neutral current and charged current reactions, illustrating that the charged current channel clearly dominates over the whole range of progenitors. The most striking feature is a overly large production of ^{138}La for the $28 M_{\odot}$ model. This is due to a increased production of ^{138}Ba and other Ba isotopes together with other weak s process nuclei and leads also to a larger production of ^{138}La .

More massive progenitors provide more mass in the O/Ne layer and correspondingly give higher absolute yields of ^{138}La and ^{180}Ta . When looking at the production factors this increase of the yield is compensated by an also increasing yield of ^{16}O and a the decreasing weight of more massive stars in the IMF. ^{138}La and ^{180}Ta are mostly sensitive to electron flavor neutrinos and since the production region in the O/Ne shell is closer to the proto-neutron star they are also the most sensitive to neutrino emission properties. Therefore, those nuclei are also expected to be affected the most by collective neutrino oscillations as suggested by Wu et al. (2015).

5.2.5 Further effects on stable isotopes

Recent studies dedicated to the ν process have focused on individual nuclei and have employed limited sets of neutrino-nucleus cross-sections expected to be relevant for the nuclei of interest. In particular when such approaches focus on a single progenitor model, the question whether there are additional effects in other scenarios or due to different reactions that have not been included always remains open. With our complete set of cross-sections we can survey the whole range of the reaction network at once and study for the first time the complete effect of ν -reactions on the explosive nucleosynthesis in supernovae for a whole range of progenitor models. The abundances of stable nuclei in the solar system are one of our most accurately measured observables making processes that have an effect on

those nuclei particularly important. Unless major changes in the models for the progenitor composition or the supernova mechanism itself are found, we hope to have captured all possible processes and give in the following a summary of the changes of the yields of stable nuclei after decay, before we enter on the discussion of radioactive isotopes in Section 5.3.3.

Table 5.5 summarizes the maximum differences $\delta_{rel} = (Y_{no\nu} - Y_{\nu})/Y_{no\nu}$ in the integrated yields of stable and very long-lived ($T_{1/2} > 10^{10}$ years) nuclei after decay that we find among all the progenitor models studied here. The table shows that large effects that change abundances by a significant factor indeed only appear for nuclei that have been identified in previous studies. On the 10% level we find a few more nuclei that are affected. In most cases the maximum effect is found for the more massive progenitors. That is because the inner regions of more massive stars tend to be more compact, putting the relevant O/Ne layer closer to the PNS. Only the light isotopes ${}^7\text{Li}$ and ${}^9\text{Be}$ that are produced at larger radii in the He-shell are maximally affected in at the low mass end of our progenitor range because here the He-shell is at smaller radii. Even though ${}^9\text{Be}$ and ${}^{10}\text{B}$ are listed in Table 5.5 their yields correspond to production factors of at most 4.5×10^{-2} and 7×10^{-2} respectively, too low to explain their solar abundances or solar ratios with respect to ${}^7\text{Li}$ and ${}^{11}\text{B}$. However, models of GCR nucleosynthesis can account for those nuclei as stated in Section 5.2.1. A modification of ${}^{17}\text{O}$ mass fraction is found throughout the O/Ne shell and is mostly induced by neutron captures on abundant ${}^{16}\text{O}$ where the neutrons are released by neutral-current spallation reactions. Locally the mass fraction of ${}^{17}\text{O}$ is increased by several orders of magnitude. However, the total yield is dominated by the abundance of ${}^{17}\text{O}$ in the He-shell left over from H-burning via the CNO cycle. The modification of ${}^{33}\text{S}$ occurs in the Si/O shell and it is affected by several reactions, including the reaction sequence ${}^{34}\text{S}(\nu_e, e^-){}^{34}\text{Cl}(\gamma, p)$ as well as ${}^{34}\text{S}(\nu, \nu'n){}^{33}\text{S}$. Thus, the contributions of charged- and neutral-current reactions is about equal. At the top of the O/Si shell ${}^{35}\text{Cl}$ is enhanced by ${}^{36}\text{Ar}(\nu, \nu'p)$ where ${}^{36}\text{Ar}$ is a results of the α -rich freeze out. The production factor for ${}^{35}\text{Cl}$ on average around 0.5, making the contribution from massive stars a relevant for the solar system inventory of ${}^{35}\text{Cl}$. The yield of ${}^{41}\text{K}$ is modified mostly by ${}^{41}\text{Ca}(\bar{\nu}_e, e^+)$ and to a lesser extent by ${}^{42}\text{Ca}(\nu, \nu'p)$. Averaged over the range of progenitors the ν process increases the production factor for ${}^{41}\text{K}$ from 0.48 to 0.52 for the low neutrino energies but it reaches values of up to 1.8 for the $20 M_{\odot}$ progenitor for which the effect of neutrinos is negligible. ${}^{113}\text{In}$ and ${}^{176}\text{Lu}$ are affected by electron antineutrino capture on ${}^{113}\text{Sn}$ and ${}^{176}\text{Hf}$ which inherited from the initial metallicity in the O/Ne shell, very similar to the cases of ${}^{138}\text{La}$ and ${}^{180}\text{Ta}$ but interestingly involving antineutrinos in this case. In both the cases the IMF averaged production factor is below 0.2. ${}^{176}\text{Lu}$ can be explained with the main s -process in AGB-stars and subject of current experimental efforts (Roig et al., 2016). The case of ${}^{176}\text{Lu}$ is further complicated by a short-lived 1^- excited state at 122 keV above the 7^- ground state that β decays with a half-life of 3.7 h. The short lived isomer is likely to be populated thermally under supernova conditions and since we do not include it explicitly in our calculations we expect that our results overestimate the yield of ${}^{176}\text{Lu}$. In contrast to that, ${}^{113}\text{In}$ is a p-nucleus that is produced via the γ -process. It is particularly interesting because Travaglio et al. (2011) found that it to be underproduced in type Ia supernovae. However, in our calculation we also find a production factor of at most 0.32. The optical model potentials to describe the involved (γ, α) reactions have recently been studied by Kiss et al. (2013) where a good agreement of the total cross-sections with the theoretical calculations was found. We find that the final integrated yield of ${}^{59}\text{Co}$ is reduced by 11% in the $15 M_{\odot}$ model. This is due to ${}^{59}\text{Ni}(\nu_e, e^-n){}^{58}\text{Cu}$ which reduces the abundance of the long-lived ${}^{59}\text{Ni}$ with a half-life of 7.6×10^4 yr that finally decays to ${}^{59}\text{Co}$. The modification of the ${}^{57}\text{Fe}$ results mostly from the charged-current reaction ${}^{58}\text{Ni}(\bar{\nu}_e, e^+p)$ and also involves ${}^{58}\text{Co}(\nu, \nu'p)$. The 12% increase in the yield of ${}^{54}\text{Cr}$ for the $23 M_{\odot}$ reflects the production of ${}^{54}\text{Mn}$ by $\bar{\nu}_e$ capture on ${}^{54}\text{Fe}$ that reaches a mass fraction of 5×10^{-2} the O/Si shell. We see that in the O/Si shell close to the mass cut reactions on the Fe-peak elements induce some changes on the ejecta composition on the order of few percent. However, since our piston model is not expected to give a very good description of these innermost regions (Young & Fryer, 2007) that are sensitive to the imposed mass cut and potential fallback of material, further studies with self-consistent explosion models are needed to verify the significance of these effects. Heger et al. (2005) have suggested reac-

Nucleus	δ_{rel}^{max} (%)	$Y_{no\nu}(M_{\odot})$	$Y_{\nu}(M_{\odot})$	M_*^{max} (M_{\odot})
${}^7\text{Li}$	2,250	1.69×10^{-9}	3.96×10^{-8}	15
${}^9\text{Be}$	25	7.19×10^{-11}	8.97×10^{-11}	18
${}^{10}\text{B}$	34	1.79×10^{-9}	2.40×10^{-9}	25
${}^{11}\text{B}$	8,208	5.78×10^{-9}	4.80×10^{-7}	25
${}^{15}\text{N}$	188	2.58×10^{-5}	7.45×10^{-5}	30
${}^{17}\text{O}$	16	5.98×10^{-5}	6.91×10^{-5}	30
${}^{19}\text{F}$	88	6.92×10^{-6}	1.30×10^{-5}	20
${}^{33}\text{S}$	14	3.75×10^{-4}	4.26×10^{-4}	19
${}^{35}\text{Cl}$	11	3.91×10^{-4}	4.35×10^{-4}	25
${}^{41}\text{K}$	22	2.82×10^{-5}	3.44×10^{-5}	19
${}^{54}\text{Cr}$	12	3.07×10^{-5}	3.43×10^{-5}	23
${}^{57}\text{Fe}$	13	4.66×10^{-3}	5.25×10^{-3}	25
${}^{59}\text{Co}$	-12	8.42×10^{-4}	7.39×10^{-4}	17
${}^{78}\text{Kr}$	10	3.63×10^{-8}	3.26×10^{-8}	23
${}^{113}\text{In}$	19	5.44×10^{-10}	6.48×10^{-10}	27
${}^{138}\text{La}$	511	5.35×10^{-11}	3.27×10^{-10}	30
${}^{176}\text{Lu}$	14	1.79×10^{-10}	2.04×10^{-10}	30
${}^{180}\text{Ta}$	501	4.93×10^{-13}	2.96×10^{-12}	29

Table 5.5.: Maximum values of the relative difference $\delta_{rel}^{max} = (Y_{\nu} - Y_{no\nu})/Y_{no\nu}$ that are larger than 10% from all progenitor models considered here for the set of low neutrino energies. Also shown are the yields in M_{\odot} for the calculations with and without including neutrino reactions. The last column gives the mass of the progenitor for which the maximum value is found M_*^{max} .

tions that could modify the yields of ${}^{51}\text{V}$, ${}^{55}\text{Mn}$, ${}^{78}\text{Kr}$, ${}^{138}\text{Ce}$ and ${}^{196}\text{Hg}$. Our calculations include all the reactions suggested by [Heger et al. \(2005\)](#) and we find that the yields of these nuclei are increased by 5-9%. The effects on the p -nuclei ${}^{113}\text{In}$, ${}^{137}\text{La}$ and ${}^{180}\text{Ta}$ shown here also illustrate that it is necessary to include neutrino-induced reactions for quantitative predictions of γ -process nucleosynthesis.

Unless significant changes in the progenitor composition or the neutrino properties are found, we can thus exclude and further effects on stable nuclei due to the ν process on supernova nucleosynthesis for stars in the mass range 13-30 M_{\odot} at solar metallicity.

5.3 Radioactive nuclei

The production of radioactive nuclei is particularly interesting because those nuclei can have clear observable signatures. There are three major aspect than can potentially be observed. First, assuming that the environment is sufficiently dense an optically thick, the radioactive decay of nucleus deposits energy in the medium, heating the material. The material in turn cools down by the emitting photons with a black-body spectrum according to its temperature. If nuclear decay is slow enough, this can keep the material emitting light over the timescale of the slowest nuclear decay. In supernovae, the decay of ${}^{56}\text{Ni}$ and ${}^{56}\text{Co}$ is observable in this way. This usually requires a decay lifetime is sufficiently long for observations but short enough for the material to still be optically thick. Furthermore, there needs to be enough radioactive material to achieve a significant heating. If the lifetime of the nucleus is very long, the material is already transparent to photons at the time the decay happens. If the decay proceeds via a state that is associated to a characteristic γ -ray transition, this is also an observable. While γ -rays can be detected with already with very low fluxes, it is rather difficult to infer the amount of this nucleus that is produced. Finally, the inclusion of radioactive isotopes in solids that formed in the early solar system leaves anomalies in the composition of minerals found in meteorites. With high precision mass

spectroscopy this allows the determination of isotopic abundance ratios present at the time when the solar system was formed ([Wasserburg et al., 2006](#)).

In this Section we show that the ν process has significant effects on the yields of radioactive isotopes. In many cases these nuclei do not have a clear observable signature but we discuss the most promising cases here in detail.

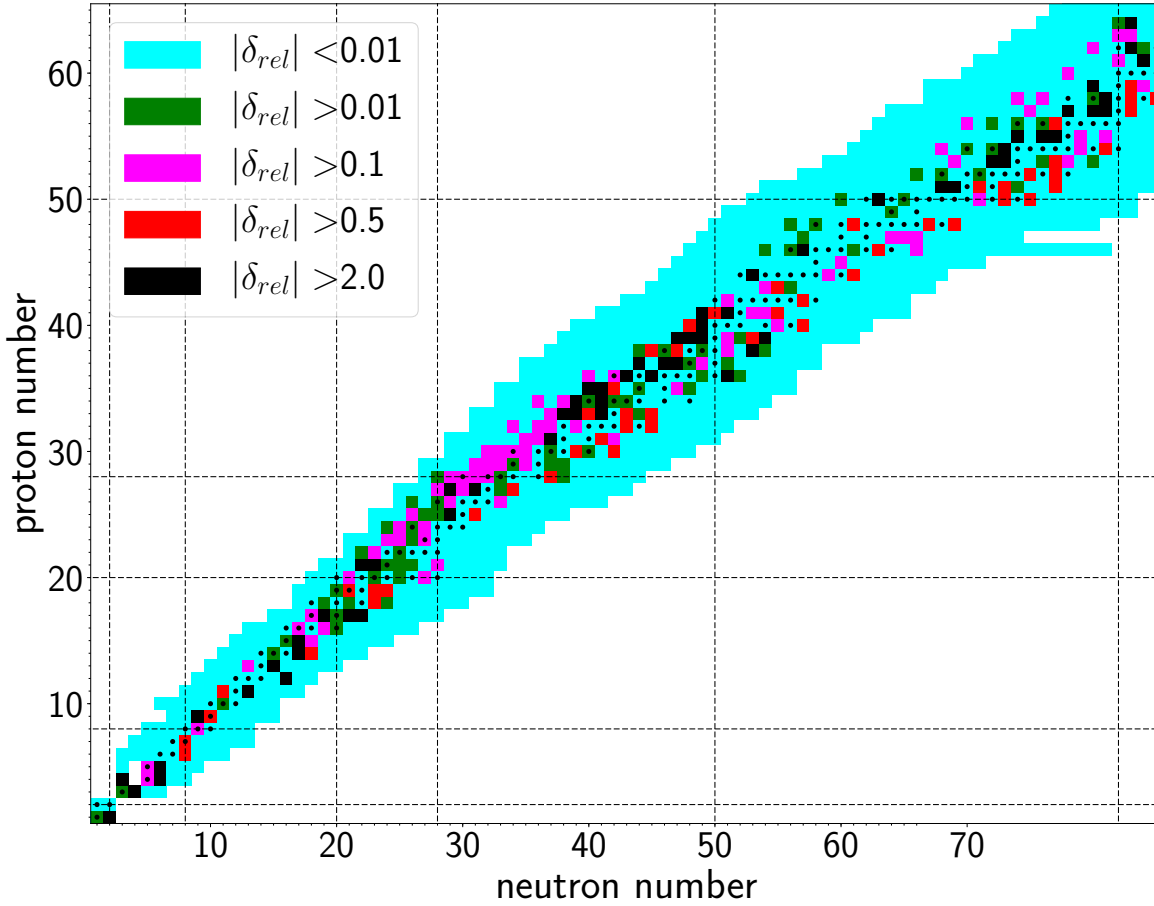


Figure 5.20.: Maximum values among all the progenitors studied here for the absolute of the relative change δ_{rel} as defined in Figure 5.25 with the new set of low neutrino energies at 2.5×10^4 s after core bounce when the very short lived nuclei have already decayed. Only nuclei with a mass fraction larger than 10^{-12} are included.

In addition to the important effect on the yields of stable isotopes we will see in the following that the ν process affects the production of many radioactive nuclei. Mostly, the modification of the abundances of radioactive nuclei does not result in noticeable changes of the yields of stable nuclei after the radioactive isotopes have decayed. However, for some species the decay is accompanied by the emission of characteristic γ -rays and others leave traces in the composition of pre-solar grains. The most interesting cases are discussed in detail in Section 5.3.2 and 5.3.3 but before we give an overview of the effects on radioactive nuclei, focusing on the $15 M_{\odot}$ progenitor model as a representative example for the mass range we have explored.

We find that a large range of radioactive species are substantially affected by the ν process. Figure 5.20 provides an overview of the relative effects of the ν process for the whole range of nuclei included in our calculations at 7 hours after the explosion when very short lived nuclei have already decayed. The relative differences δ_{rel} shown there, are the maximum values we find for the whole range of progenitor models we have looked at. The largest effects appear close to stability where seed nuclei with a large abundances relative to their neighbors are present. Many nuclei are affected on the 10% level and a few show differences exceeding 50% or a factor 2. Below the Iron group the ν process mostly increases the production of isolated rare stable and long-lived nuclei discussed in the previous sections. Spal-

Nucleus	$T_{1/2}$	no ν	Low energies	High energies
^{22}Na	2.61 yr	1.89×10^{-6}	2.42×10^{-6}	3.01×10^{-6}
^{26}Al	0.72 Myr	3.88×10^{-5}	4.19×10^{-5}	4.74×10^{-5}
^{36}Cl	0.30 Myr	2.89×10^{-6}	4.19×10^{-6}	5.01×10^{-6}
^{44}Ti	59.1 yr	3.68×10^{-5}	5.05×10^{-5}	5.17×10^{-5}
^{60}Fe	2.6 Myr	7.20×10^{-5}	7.21×10^{-5}	7.23×10^{-5}
^{72}As	26.0 h	2.38×10^{-10}	3.01×10^{-9}	7.48×10^{-9}
^{84}Rb	32.8 d	3.97×10^{-10}	2.87×10^{-9}	5.50×10^{-9}
^{88}Y	106.6 d	4.14×10^{-10}	1.27×10^{-9}	2.49×10^{-9}
^{92}Nb	34.7 Myr	3.30×10^{-11}	7.38×10^{-11}	1.30×10^{-10}
^{98}Tc	4.2 Myr	2.57×10^{-11}	2.98×10^{-11}	3.61×10^{-11}

Table 5.6.: Impact of the ν process on the yields of radioactive isotopes at the end of our calculation at 2.5×10^4 s. At this time the very short-lived nuclei have already decayed and mostly species that are potentially interesting for observations remain. Shown are the yields in units of M_{\odot} averaged with an IMF as above, obtained without neutrino, with our choice of neutrino temperatures (“Low energies”), and with the choice of [Heger et al. \(2005\)](#) (“High energies”).

lation reactions on the most abundant nuclei like ^{16}O , ^{20}Ne and ^{24}Mg do not change the abundances of the targets noticeably but the neighboring nuclei get produced and they provide light particles that affect other nuclei. Additional neutrons are mostly captured by heavier nuclei, leading to increased abundances on the neutron rich side for $A > 100$ where the seed nuclei are inherited from the initial solar metallicity. Since the γ process also operates on those seed nuclei, the abundances on the proton-rich side are also modified slightly. Around the Iron group many long-lived nuclei exist and they are mainly produced in the Si-shell close to the PNS where the neutrino fluxes are largest. After freeze out from NSE, neutrino interactions reshuffle the abundances of the Fe-peak with differences at the 10% level, leading for example to the modification of the ^{59}Co yields discussed previously. In the region of $A = 60 - 90$ we can see a significant modification of the abundances, both on the neutron- and proton-rich side of stability. This is due to the weak $s - process$ nuclei and the operation of the γ -process that already leads to the production of radioactive nuclei in that region which are then modified further by neutrino interactions. Radioactive, neutron-deficient isotopes of As, Br, Kr, Sr, Y and Zr are particularly enhanced with mass fraction typically between 10^{-12} to 10^{-10} . For progenitors with a weaker γ process free neutrons from spallation reactions are captured on the most abundant s -process nuclei and lead to increased abundances on the neutron-rich side in the same mass region.

The production of radioisotopes by the ν process has hitherto received only limited attention in the literature which has mostly focused on the five isotopes discussed above. In the following we will discuss the overall effect of the ν process on the production of radioactive nuclei, in particular focusing on those that are relevant for observations.

Table 5.6 lists the IMF averaged nucleosynthesis yields for a range of radioactive nuclei that are still present at around 7 hours after the explosion, including ^{32}P , ^{72}As , ^{84}Rb , ^{88}Y . Their yields are increased by factors between 2 and 10 with the realistic neutrino energies and the production of ^{72}As would be increased by almost two orders of magnitude with the choice of high neutrino energies. The typical yields for ^{72}As , ^{84}Rb , and ^{88}Y are $10^{-9} M_{\odot}$, which may allow for the observation of the gamma-ray decay lines only with very high precision observations. Further complicating the detection, their lifetimes are of the order of a 100 days or shorter, putting their decay signal in competition with ^{56}Ni and its daughter ^{56}Co which by far dominates the early lightcurve and therefore outshines the signature of the ν process. However, this shows that the ν process can affect a large range of radioactive nuclei among which we can look for a suitable candidate to provide an observable signature of supernova neutrinos.

5.3.2 Short-lived radionuclides ^{36}Cl , ^{92}Nb and ^{98}Tc in the late input scenario

While ^{138}La and ^{180}Ta are measurable as part of the current composition of the solar system, indications for the presence of other less long-lived p-nuclei like ^{92}Nb and ^{98}Tc have been found in primitive meteorites that are assumed to have conserved the composition of the material from which the solar system has formed. Isotopic ratios mostly derived from mass spectroscopy of grains of meteoritic material offer the possibility to put some constraints on nucleosynthesis models in general and on the ν process in particular. In the late input scenario as suggested by ? a nearby supernova has triggered the formation of the solar system and in this case the composition of the early solar system can be related to a single event. In the following we discuss ^{92}Nb , ^{98}Tc and ^{36}Cl in this context.

Our calculations show (see Table 5.6), that neutrino interactions increase the average yield of ^{36}Cl by factors of 1.4 and 1.7 for low and high neutrino energies respectively and ^{92}Nb by a factors of 2.1 and 3.7. This relatively steep increase indicates that the ν process provides a dominant and independent contribution. The yield of ^{98}Tc is increased on average by less than 20%. Even though the mass fraction of ^{98}Tc in the O/Ne shell is typically increased by one to two orders of magnitude mostly by $^{98}\text{Mo}(\nu_e, e^-)$. Despite the higher average energy of electron antineutrinos $^{98}\text{Ru}(\bar{\nu}_e, e^+)$ is negligible because ^{98}Ru is very rare with mass fraction typically around 10^{-16} , while ^{98}Mo is much more abundant with mass fractions around 5×10^{-9} . A particularly large amount of ^{98}Mo is present in the $27 M_\odot$ which is enriched in γ -process nuclei as discussed for the case ^{180}Ta in Section 5.2.4.

For most progenitor models there is also a direct contribution of the γ process during the shock heating to ^{98}Tc which is typically a factor 10 smaller than the ν process contribution. In spite of this large effects, the relative enhancement of the integrated yield is still small because it is dominated by the pre-supernova content of ^{98}Tc in the He-shell.

Figure 5.21 shows the yields of ^{36}Cl , ^{92}Nb and ^{98}Tc for the stellar models we have studied. ^{36}Cl and ^{92}Nb exhibit very similar systematics with respect to the progenitor mass because they are both very sensitive to the composition and temperature at the inner edge of the O/Ne shell.

^{36}Cl and ^{92}Nb are the two species with the deepest ν process production region. While their yields including the ν process are relatively smooth with respect to the initial progenitor mass, large variations can be seen in the calculations without neutrinos. As a result, also the relative enhancement ranges from factors of 2-5 for most progenitors up to a factor of 600 for the $24 M_\odot$ model which yields particularly little ^{92}Nb without the ν process. The production mechanisms for ^{92}Nb and ^{98}Tc in the ν process are very similar to the production of ^{138}La and ^{180}Ta . The upper panel of Figure 5.22 shows the dominating reaction flows relevant for the synthesis of ^{92}Nb in the $15 M_\odot$ progenitor model. At the bottom of the

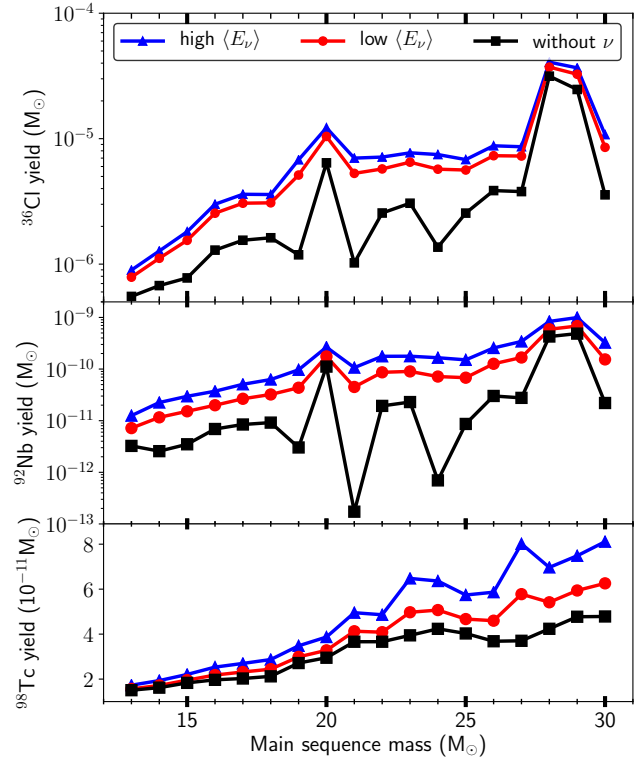


Figure 5.21.: Yields of ^{36}Cl , ^{92}Nb and ^{98}Tc for different sets of neutrino energies and without the ν process over the range of progenitors considered here. Note that the upper two panels are on a logarithmic scale while the ^{98}Tc mass fraction is on a linear scale because it shows a much smaller variation.

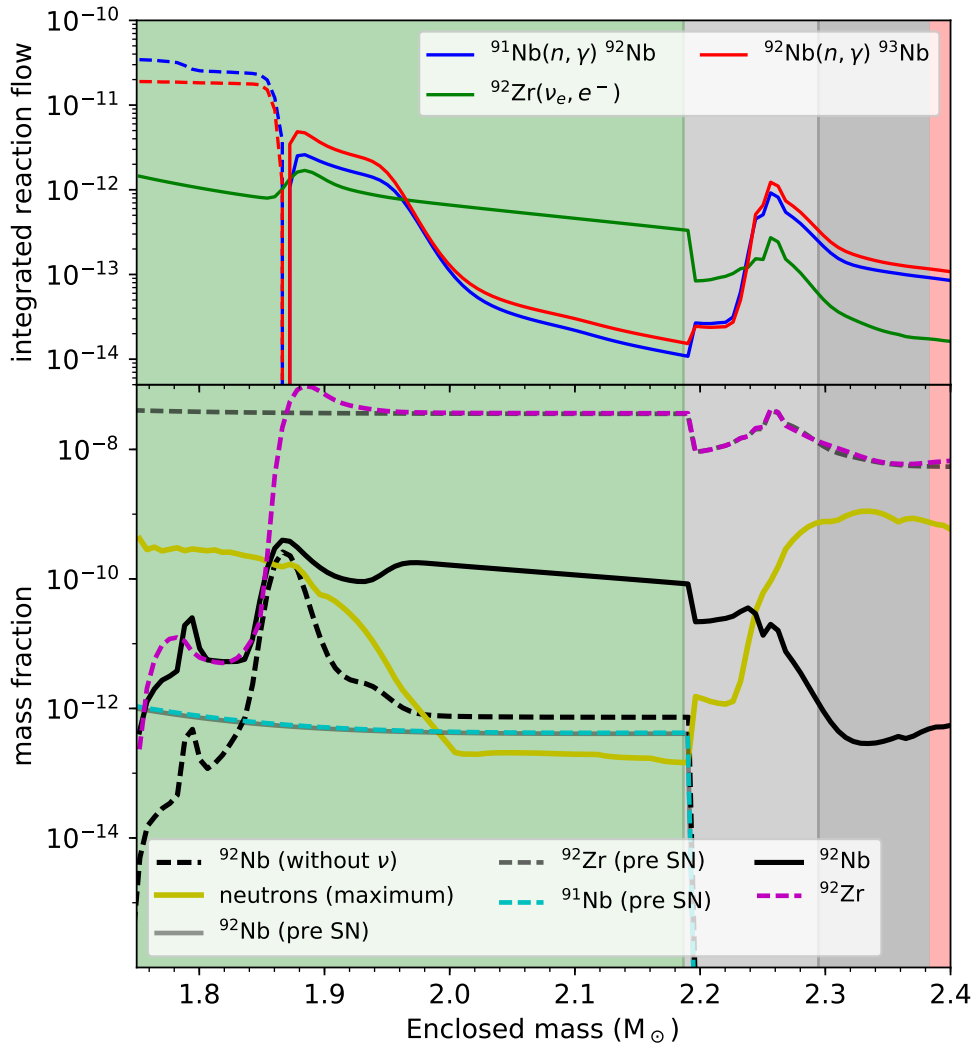


Figure 5.22.: Same as Figure 5.19 for ^{92}Nb . The top panel shows time integrated reaction flows and the lower panel gives an overview over the mass fractions of the involved nuclei. While the production of ^{92}Nb proceeds via (n, γ) - (γ, n) reactions in the deeper, hotter part of the O/Ne shell, the $\nu\nu$ process leads to a moderate production throughout the outer part of the O/Ne shell.

O/Ne shell, photodissociation and neutron captures compete and in an optimal temperature range the ^{92}Nb mass fraction forms a peak even without neutrinos. The ν process contributes evenly through the whole region which contains ^{92}Zr with a mass fraction of around 3×10^{-8} .

For the progenitors more massive than $15 M_{\odot}$ the production region moves to smaller radii, into the upper part of the Si-shell which also contains substantial amounts of Oxygen. The $20 M_{\odot}$ model stands out with a rather large pre-supernova production. In this model the ν process contribution is strongest in the Si/O-O/Ne transition region which consists of Si and Ne in roughly equal amounts. [Cheoun et al. \(2012\)](#) and [Hayakawa et al. \(2013\)](#) have discussed the ν process in supernovae as a production site for the radioactive isotopes ^{92}Nb and ^{98}Tc . In particular ^{92}Nb is interesting a potential chronometer. [Mohr \(2016\)](#) has analyzed the impact of an isomeric state of ^{92}Nb at 135.5 keV on its nucleosynthesis in an explosive environment and found that it does not affect the production. The survival might however be affected by a reduced lifetime at low temperatures.

[Hayakawa et al. \(2013\)](#) have estimated the contribution of the ν process to the ISM inventory of $^{92}\text{Nb}/^{93}\text{Nb}$ based on $11 M_{\odot}$ supernova model with a similar yield as presented here. They conclude that the continuous production is insufficient to explain the isotopic ratio of $\approx 10^{-5}$ inferred from primitive meteorites [Schönbächler et al. \(2002\)](#). While the estimate by [Hayakawa et al. \(2013\)](#) is based on a single progenitor model we can use the IMF weighted average of the stellar models we have studies. We get an average ratio of $\langle ^{92}\text{Nb}/^{93}\text{Nb} \rangle = 7.2 \times 10^{-4}$ without neutrinos. This reaches 1.5×10^{-3} and 2.6×10^{-3} for low and high neutrino energies respectively. Assuming a uniform production model and taking supernovae as the sole production site for both ^{92}Nb and ^{93}Nb we estimate the ratio as ([Huss et al., 2009](#)):

$$\left(\frac{X(^{92}\text{Nb})}{X(^{93}\text{Nb})} \right)_{UP} \approx 2 \langle ^{92}\text{Nb}/^{93}\text{Nb} \rangle \frac{\tau_{92\text{Nb}}}{T} \quad (5.2)$$

Where $\tau_{92\text{Nb}} = 50.1$ Myr is the decay timescale of ^{92}Nb . With a typical isolation time $T = 10$ Gyr we get a maximum ratio of 1.3×10^{-7} in agreement with [Hayakawa et al. \(2013\)](#) and still insufficient to explain the observed ratio. [Hayakawa et al. \(2013\)](#) conclude that a late injection event where the pre-solar material is polluted by the ejecta from a nearby supernova is more likely. [Banerjee et al. \(2016\)](#) have recently consolidated this scenario using the short-lived radioactive ^{10}Be produced by the ν process in low-mass supernovae as indicator. In the case of such a late input scenario, we can relate the measured abundance ratios to a single nucleosynthesis event. If this is the case, properties of this event can be inferred from measured abundance ratios. The main parameters are the delay time between the injection event and the formation of the solar system Δ and the dilution factor f that indicates to which extent the solar system material has been mixed with the ejecta from the last event. Following [Takigawa et al. \(2008\)](#) and [Banerjee et al. \(2016\)](#) we can estimate the number ratio N_R/N_S between a radioactive isotope with mass number A_R and a stable reference nucleus with mass A_S at solar system formation as

$$\left(\frac{N_R}{N_S} \right)_{SSF} \approx \frac{f \times Y_R e^{-\Delta/\tau}}{X_S^{\odot} M_{\odot}} \times \frac{A_R}{A_S}. \quad (5.3)$$

where Δ is the time between the last nucleosynthesis event to produce the isotope of interest and the condensation of the material into solid grains. Y_R is the yield of the radioactive nucleus in solar masses from our calculations and X_S^{\odot} is the solar mass fraction of the reference isotope, taken here from [Lodders \(2003\)](#). Due to its long half-life, ^{92}Nb is not very sensitive to Δ and therefore a good candidate to constrain f . Assuming $\Delta \approx 1$ Myr and the lowest ^{92}Nb yield from the $13 M_{\odot}$ model we require a dilution factor $f \approx 5 \times 10^{-3}$ to achieve the measured ratio of 1.6×10^{-5} ([Schönbächler et al., 2002](#)). This value is significantly higher than what has been suggested in the literature ([Banerjee et al., 2016](#); [Takigawa et al., 2008](#); [Wasserburg et al., 2006](#)). Furthermore, this value is also much larger than the upper limit of $f < 5 \times 10^{-4}$ that results from with the same model from the upper limit on the $^{98}\text{Tc}/^{96}\text{Ru}$

ratio (Becker & Walker, 2003). Thus, in particular with the updated neutrino energies, it does not seem possible to explain the pre-solar abundance of ^{92}Nb with the input by a low mass supernova.

The yields of ^{92}Nb and ^{98}Tc might even be more enhanced by contributions from the neutrino-driven wind (Fuller & Meyer, 1995; Hoffman et al., 1996). The nucleosynthesis of p -nuclei in the neutrino driven wind and its contribution to ^{92}Nb and ^{98}Tc are discussed in detail Section 7. In our model we find that with the contribution of the neutrino driven wind the $^{92}\text{Nb}/^{93}\text{Nb}$ of 1.6×10^{-5} can be reproduced.

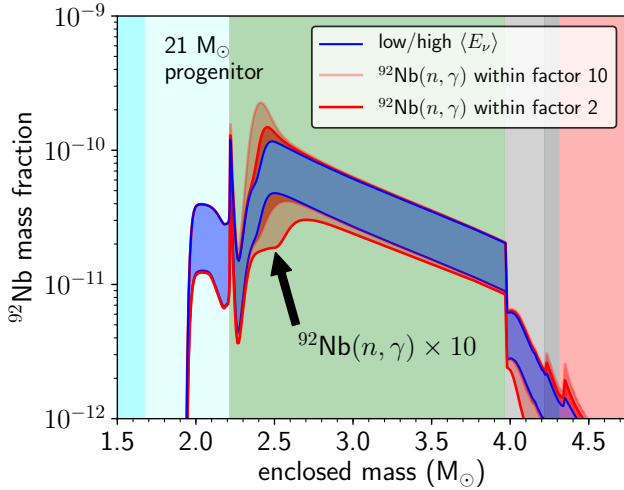


Figure 5.23.: ^{92}Nb mass fraction profile for the $21 M_\odot$ progenitor model. The sensitivity to the $^{92}\text{Nb}(n, \gamma)$ reaction rate is indicated by the red band. The lower mass fractions results from an increase of the rate and are shown for the case of the low neutrino energies. The larger values of the mass fraction result from a decrease of the (n, γ) rate and are shown for the case of high energies. This illustrates the combined sensitivity.

captures that the neutron capture has a destructive effect. Hence, an increase of the reaction rate leads to a decrease of the final ^{92}Nb yield. In the region that is most sensitive to the neutron capture rate at a mass coordinate of around $2.4 M_\odot$, the production of ^{92}Nb is driven by the reaction chain $^{90}\text{Zr}(n, \gamma)^{91}\text{Zr}(p, n)^{91}\text{Nb}(n, \gamma)^{92}\text{Nb}$. ^{90}Zr that is present in the progenitor with a mass fraction of $X(^{90}\text{Zr}) \approx 10^{-6}$. Figure 5.23 summarizes the large uncertainties that are associated with changes of the neutrino energies on the one hand, and the neutron capture rate on the other hand. High neutrino energies combined with a low neutron capture rate lead to the upper limits, while the low neutrino energies with an increased neutron capture rate lead to the lower limit in Figure 5.23. The variation neutron capture reaction rates alone withing a factor 2 results in a change of the integrated yield by a factor of 0.3 and a variation withing a factor 10 changes the yields by factor 2. In combination with the variation of the neutrino energies the yield is affected by a factor 3.8. This gives us an upper limit for the combined uncertainty of the ^{92}Nb yield with respect to the neutrino properties and the most important neutron capture rate involved in its production.

The ^{36}Cl yield without neutrinos results mostly from neutron captures on ^{35}Cl at lower to mid O/Ne shell. ^{35}Cl is product of hydrostatic Oxygen burning in the progenitor but is of its explosive version. Providing additional neutrons, neutrino neutral current spallation reactions have a minor effect on the yield while $^{36}\text{Ar}(\bar{\nu}_e, e^-)^{36}\text{Cl}$ is the most important contribution of the ν process for all of the progenitor

At his point we also want to look at the uncertainties of the ^{92}Nb yield that results from the uncertainties in nuclear reaction rates. We concentrate on the reaction $^{92}\text{Nb}(n, \gamma)$ which is currently based on statistical model calculations and Sallaska et al. (2013) assign an uncertainty of a factor 10.

We have varied the reaction rate and its inverse by factor 2 and 10 up and down. Note that detailed balance always connects the forward and reverse reactions and an increase of the rate in one direction is always accompanied by an increase of the inverse, unless the Q-value changes. Neutron capture rate do not depend strongly on temperature and hence using a global factor for all temperatures is appropriate. In the context of single degenerate Ia supernovae a Monte-Carlo study Travaglio et al. (2014) have explored the sensitivity of the ^{92}Nb yields. In this scenario the production proceed via the γ process from s -process seed nuclei. There it was found that a factor 2 increase of the $^{92}\text{Nb}(n, \gamma)$ reactions rate and associated increase of the reverse reaction leads to a decrease of ^{92}Nb . This is because of the larger (γ, n) rate. In contrast to that, we find for our supernova scenario where ^{92}Nb is predominantly produced by electron neutrino cap-

models. In O-burning ^{36}Ar is produced prolifically to reach mass fractions of the order 10^{-2} in the final Si-shell. A large fraction of this ^{36}Ar -rich material is either burnt to NSE located below the mass cut and not thus part of the ejecta. In explosive Oxygen burning triggered by the explosion, ^{36}Ar is efficiently produced at the bottom of the O/Ne shell where the peak temperatures reach up to 2.5 GK. The most important reactions are $^{35}\text{Cl}(p, \gamma)$ and $^{32}\text{S}(\alpha, \gamma)$. While for most other nuclei that are affected by the ν process, the parent nucleus is already present in the progenitor, ^{36}Ar and also ^{35}Cl need to be produced by the shock heating first. Hence, ^{36}Cl is also particularly sensitive to the shock propagation and the explosion energy.

Jacobsen et al. (2009) have given a value of $(17.2 \pm 2.5) \times 10^{-6}$ for the ratio $^{36}\text{Cl}/^{35}\text{Cl}$ from grains of the Allende meteorite. Since ^{36}Cl decays faster than ^{92}Nb it is more sensitive to the time delay Δ in equation (5.3). For $\Delta = 1\text{Myr}$ the yield of the $13 M_{\odot}$ model requires a dilution factor of $f = 1.1 \times 10^{-3}$ to 1.7×10^{-4} , in agreement with the value of 5×10^{-4} suggested by Banerjee et al. (2016). However, due to the relatively large uncertainty of the measured abundance ratio, this can already be achieved without neutrinos. Note that Jacobsen et al. (2011) have suggested that ^{36}Cl could also be produced in-situ in the early solar system by high energy photons from the early sun. The meteoritic ratios of ^{36}Cl are currently the only direct constraint on its production because ^{36}Cl decays mainly to the ground-state of ^{36}Ar without characteristic γ -rays.

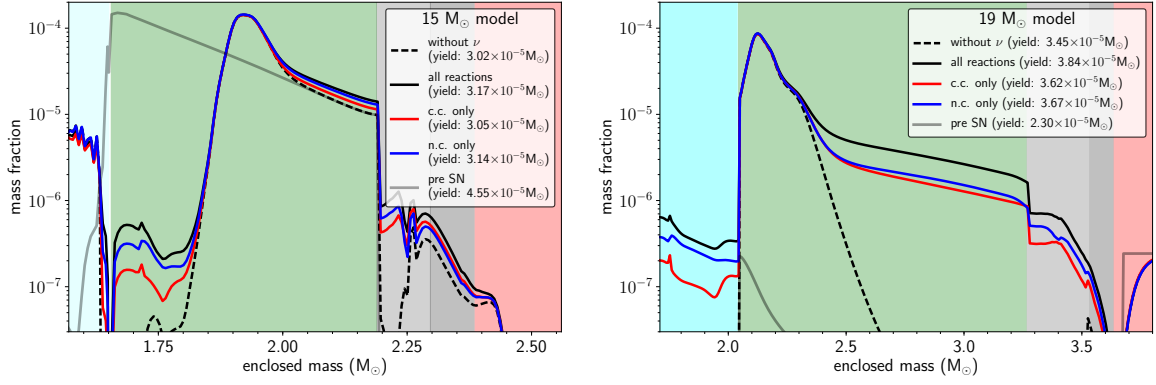


Figure 5.24.: Mass fraction of ^{26}Al for the $15 M_{\odot}$ (left) and $19 M_{\odot}$ (right) progenitor models. Shown are the results for calculations with and without including neutrino interactions, with charged-current reactions only, and neutral-current reactions only for the low neutrino energies. The pre-supernova mass fraction are also shown. Comparison of the two models illustrates that the contribution from hydrostatic C-burning almost irrelevant for the final yield.

5.3.3 γ -ray sources ^{22}Na and ^{26}Al

^{26}Al decays by electron capture and β^+ with a half-life of 0.72×10^6 to an excited state in ^{26}Mg . The following decay to the ground state leads to the emission of a characteristic γ -ray line at 1.8 MeV. The observation of this signature has allowed [Diehl \(2013\)](#) to estimate its present-day equilibrium content of ^{26}Al in the Galaxy to be $2.8 \pm 0.8 M_{\odot}$. While the sensitivity of ^{26}Al yields from massive stars with respect to thermonuclear reaction rates has been studied in detail by [Iliadis et al. \(2011\)](#), we here explore the uncertainties related to the ν process.

The yield of ^{26}Al is known to be enhanced by neutrino nucleosynthesis ([Domogatskij & Nadezhin, 1980](#); [Woosley et al., 1990](#); [Timmes et al., 1995a](#)). With the cross-section derived as discussed in Section 5.1 we also find an increase on average by factors between 1.1 and 1.4 for the range of progenitor models studied (see Table 5.6 and Figure 5.25). For low energies the maximum increase is limited to a factor of 1.13 for the most massive progenitor in our set. These effects are already within the precision of the galactic ^{26}Al content estimate. In massive stars ^{26}Al can be produced in core H burning, C burning in the core, and in a convective shell as well as during explosive Ne/C burning in the supernova shock. ^{26}Al from H core burning survives largely in the envelope and is partly blown away by stellar winds especially for more massive stars. It contributes 25%–55% of the total yield with the exception of the $13 M_{\odot}$ progenitor for which the H burning component constitutes 70%. This component is unaffected by the explosion and by the neutrinos.

Figure 5.24 shows the ^{26}Al mass fraction profile for the $15 M_{\odot}$ model which contains a significant amount of ^{26}Al from C-burning in the O/Ne shell before the supernova explosion. Most of this ^{26}Al is destroyed by the shock, mainly by $^{26}\text{Al}(n, p)^{26}\text{Mg}$ and $^{26}\text{Al}(n, \alpha)^{23}\text{Na}$. The $19 M_{\odot}$ model shown in the right panel of Figure 5.24 differs significantly in its pre-supernova ^{26}Al mass fraction which is almost negligible. However, both cases lead to a rather similar distribution and yield of ^{26}Al at the end. When looking at the whole range of progenitors we find that the final ^{26}Al yield in the ejecta is effectively independent of the inner C-burning component of pre supernova ^{26}Al . Similar results have been obtained by [Limongi & Chieffi \(2006\)](#) for a different set of progenitor models.

Shock heating produces a peak in the mass fraction distribution during explosive C/Ne burning. The reactions chain $^{20}\text{Ne}(\alpha, \gamma)^{24}\text{Mg}(n, \gamma)^{25}\text{Mg}(p, \gamma)^{26}\text{Al}$ competes with neutron induced reactions on ^{26}Al and photodissociation at higher temperatures. The optimal conditions for the production of ^{26}Al are found where the peak temperature reaches around 2.3–2.5 GK, depending on the progenitors density structure. With the explosion model used here we find for all progenitors a peak in the O/Ne shell.

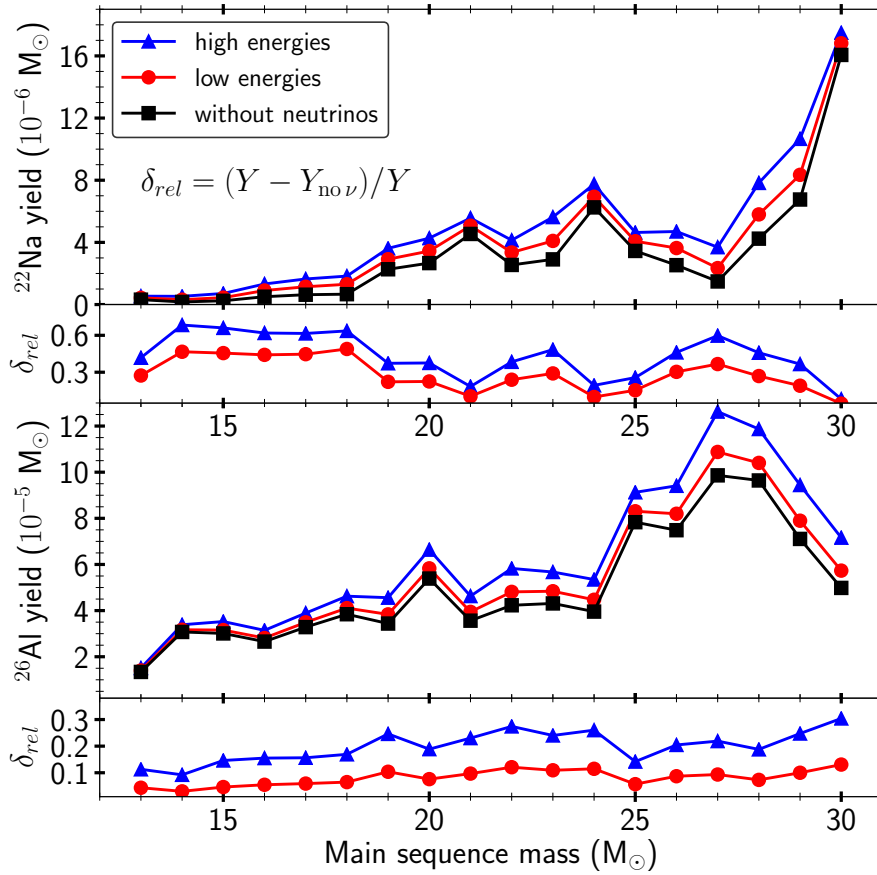


Figure 5.25.: Yields of ^{22}Na (upper panel) and ^{26}Al (lower panel) for the set of progenitor stars considered here. Shown are the yields without neutrinos and including neutrinos with the high energies and the more realistic low energies. Below each panel the relative differences $\delta_{rel} = (Y - Y_{\text{no}\nu})/Y$ between the yields with and without neutrinos are shown in smaller panels.

Deeper inside, i.e., left of the peak, no ^{26}Al survives the shock heating while the ν process can operate further out.

Neutrinos contribute to the production of ^{26}Al during the explosive phase by two different mechanisms. Neutrino-induced spallation reactions on the most abundant nuclei in the O/Ne shell, ^{20}Ne , ^{24}Mg , and ^{16}O increase the number of free protons, enhancing the reaction $^{25}\text{Mg}(p, \gamma)$, which is also the main production channel without neutrinos. Additionally, the charged-current reaction $^{26}\text{Mg}(\nu_e, e^-)$ also contributes with a cross-section that is now based on experimental data as described in Section 5.1. Figure 5.24 illustrates the neutral-current and charged-current contributions. With the softer neutrino spectra, we find that both charged- and neutral-current reactions contribute to a similar extent to the production of ^{26}Al in the O/Ne layer. The enhancement of the $^{25}\text{Mg}(p, \gamma)$ is confined to a narrow region of optimal temperature, whereas the $^{26}\text{Mg}(\nu_e, e^-)$ contributes more evenly but to a lesser extent throughout the entire layer, decreasing with the neutrino flux at larger radii. The strength of the ν process also depends on the position of the ^{26}Al production peak within the O/Ne shell which in turn depends on the peak temperature. The deeper inside the peak is, the more mass is on the right hand side of the peak where the ν process can operate efficiently. While the total mass of the O/Ne layer scales with the initial progenitor mass, the condition of the peak temperature is more sensitive to the detailed structure of the individual stellar models. Comparing the two cases in Figure 5.24 also illustrates this dependence of the ν process region on the position of the ^{26}Al peak. The systematics of the total yield with respect to the progenitor mass that are shown in figure 5.25 follow the trend of the ^{20}Ne content of the pre-supernova models, modulated by structural details affecting the position of the ^{26}Al peak within the O/Ne layer. The relative differences δ_{rel} due to neutrinos to Figure 5.25 can be understood from these aspects. For the 13–18 M_\odot progenitors, the ^{26}Al peak is located in the middle of the O/Ne shell, such that only a fraction of that shell is cold enough for the ν process to contribute. Within this range of progenitors the mass in the O/Ne shell increases giving rise to a slight increase with progenitor mass. In all of these models a substantial amount of ^{26}Al is present from hydrostatic burning but little of it survives the high temperatures during the explosion. Starting from the 19 M_\odot the ^{26}Al peak is right at the bottom edge of the O/Ne shell. As discussed by [Woosley et al. \(2002\)](#) energy generation in central C burning in stars heavier than this can no longer overcome the neutrino losses which leads to substantial changes in structure and nucleosynthesis, including a reduced abundance of ^{26}Al in the O/Ne shell. In the mass range between 19–25 M_\odot there is basically no contribution from C burning and the ν process has the strongest relative effect on ^{26}Al because most of the O/Ne shell is cold enough. The 20 M_\odot is a particular exception for which a convective merger of shells has occurred and altered the structure and composition (see also [Woosley et al., 2002](#)). The relatively large yields for the 25–28 M_\odot progenitor models result from a drastic increase of the contribution from hydrostatic C burning that decreases again in the 29 and 30 M_\odot progenitors. The 25–28 M_\odot progenitors also exhibit the largest compactness parameter [O’Connor & Ott \(2011\)](#)

Reaction	$\times 10$	$\times 0.1$
$^{21}\text{Ne}(p, \gamma)$	2.03	0.87
$^{22}\text{Na}(p, \gamma)$	0.98	1.09
$^{22}\text{Na}(n, \gamma)$	0.93	1.00
$^{22}\text{Na}(n, p)$	0.31	1.00

Table 5.7.: Ratio of the integrated ^{22}Na yield with modified reaction rates relative to the standard values for the calculations with a 15 M_\odot model. The sensitivity to the neutrino reactions is comparable to the sensitivity with respect to nuclear reaction rates.

$$\zeta_{2.5} = \frac{2.5M_\odot}{R(M_r = 2.5M_\odot)/1000\text{km}} \quad (5.4)$$

in the range between 0.31–0.45 and also the largest pre-SN content of ^{25}Mg . Note that according the explosion criterion suggested by [Ugliano et al. \(2012\)](#), stars with $\zeta_{2.5} > 0.35$ are likely to fail to explode as supernovae.

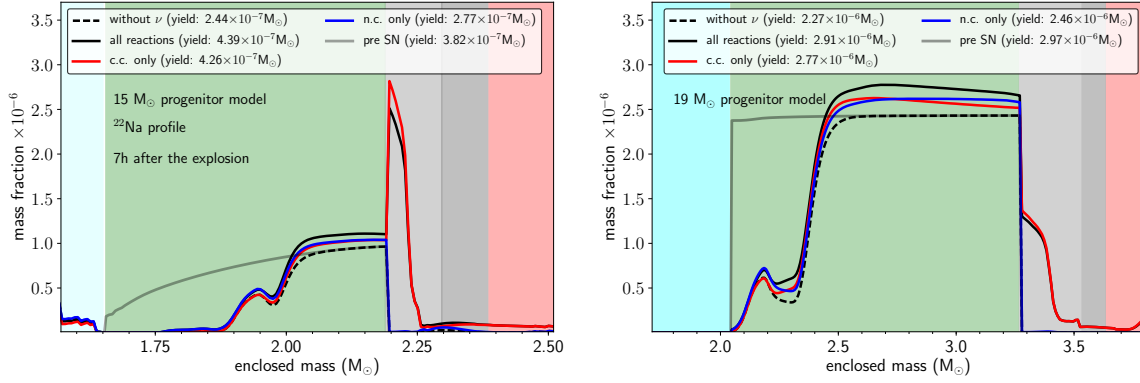


Figure 5.26.: ²²Na mass fraction profile for the 15 (left) and 19 M_⊙ (right) progenitors for the set of low neutrino energies. While O/C shell contains the largest amount of ²²Na the 15 M_⊙ model the contribution from this region is negligible for the 15 M_⊙ progenitor.

The fact that the ν process mostly adds to ²⁶Al in a secondary way, i.e., by enhancing the abundance of protons, makes its contribution to scale smoothly with the ν energy compared to the weak dependence with the neutrino energy seen in Sections 5.2.4 and 5.3.2.

Since the position of the ²⁶Al production peak depends on the peak temperature at that radius we can see from equation 5.1 that it also depends on the explosion energy. For less energetic explosions the optimal temperature is reached for smaller radii and a stronger impact of ν process can be expected because the neutrino fluxes are higher closer to the PNS.

The short-lived isomeric state of ²⁶Al is not treated explicitly in our calculation, but we assume a thermal equilibrium and use an accordingly adjusted β -decay rate Fuller et al. (1982). The validity of this assumption in a supernova environment has been confirmed by Iliadis et al. (2011).

Our results show that the major uncertainty for the yields of ²⁶Al from massive stars originates from thermonuclear reaction rates. Iliadis et al. (2011) have estimated such a uncertainty to be a factor 3. As experiment and theory advance, these uncertainties are bound to shrink and the predictions can approach the precision of the observations.

The radioisotope ²²Na has a relatively short half-life of 2.6 yr and decays to ²²Ne emitting a positron followed by the emission of a γ ray line at 1.275 MeV and two 0.511 MeV γ rays from the annihilation of the positron. Woosley et al. (1989) have estimated the contribution of ²²Na to the bolometric lightcurve and emission lines from SN1987A based on a model that did not include the ν process. They conclude that a detection of the γ -ray line emission might become possible with future instruments. In the following we describe how the ν process affects the production of ²²Na for our range of progenitor models and discuss the detectability of this enhancement in photometry and as radiogenic ²²Ne in presolar grains.

Figure 5.25 shows that supernovae could eject even larger amounts of ²²Na.

Just like in the case of ²⁶Al the peak temperatures reached in the O/Ne shell are the determining factor for the ejected amount of ²²Na. In general, there is no contribution from the pre-supernova wind, the He shell or H envelope because most of the ²²Na that has been produced there during hydrostatic burning has decayed at the time of core collapse. Figure 5.26 illustrates the distribution of the mass fraction of ²²Na for the 15 and 19 M_⊙ progenitor models.

The last phases of shell burning produce mass fractions around $1-4 \times 10^{-6}$ of ²²Na O/Ne shell. Without taking into account the ν process the final ejected amount of ²²Na is only determined by how much of it survives the shock heating which destroys ²²Na in explosive O/Ne burning mostly via ²²Na(γ, p)²¹Ne for temperatures above 1.8 GK which is below mass coordinate 1.9 M_⊙ for the 15 M_⊙ model. At the outer edge of explosive burning, there is a peak at mass coordinates around 1.9 M_⊙ for

the $15 M_{\odot}$ model and around $2.1 M_{\odot}$ for the $19 M_{\odot}$ model the mass fraction of ^{22}Na that results mostly from $^{21}\text{Ne}(p, \gamma)^{22}\text{Na}$.

The ν process also affects this peak by increasing the abundance of free protons as in the case of ^{26}Al discussed above. This peak is however always negligible compared to the bulk of the ^{22}Na in the outer part of the O/Ne shell which remains mostly unchanged by the passage of the supernova shock without taking into account neutrinos. The ν process liberates free protons that increase of the ^{22}Na mass fraction in the outer O/Ne shell as can be seen in Figure 5.26 and also the charged current reaction $^{22}\text{Ne}(\nu_e, e^-)^{22}\text{Na}$ contributes. $^{23}\text{Na}(\nu, \nu'n)^{22}\text{Na}$ has been suggested by [Woosley et al. \(1990\)](#) as an additional source of ^{22}Na . We find that this channel contributes 50% of the neutral current effects for the $16 M_{\odot}$ model. Figure 5.26 illustrates that both channels contribute to about the same extend in the outer O/Ne shell. This can be understood from the pre-supernova composition because the O/Ne shell consists of roughly equal mass fractions of ^{22}Ne and ^{21}Ne that range between 5×10^{-5} to 5×10^{-4} in the O/Ne shell of this progenitor.

More striking is the effect of the charged current $^{22}\text{Ne}(\nu_e, e^-)^{22}\text{Na}$ reaction that increases the mass fraction of ^{22}Na in the O/C shell and produces the very prominent peak for the $15 M_{\odot}$ progenitor that can be seen in the left panel of Figure 5.26. In contrast, this production channel is negligible in the $19 M_{\odot}$ model shown in the right panel. The O/C shell contains very little ^{21}Ne and ^{23}Na such that the thermonuclear and also neutral current contributions to ^{22}Na are suppressed. The mass fraction of ^{22}Ne in the O/C shell which has not undergone C-burning is between $1 - 1.5 \times 10^{-2}$ and very similar for all progenitor models studied here. Still, only the $14-18 M_{\odot}$ models show a major production of ^{22}Na in the O/C shell due to the ν_e capture on ^{22}Ne . For these progenitor models the charged current reaction in the O/C shell contribute at least 80% of the total ν process enhancement. That is reflected in larger values for δ_{rel} in Figure 5.25. As described above, the energy balance of C burning changes and consequently also the star's structure, when going from the 18 to the $19 M_{\odot}$ model. While the inner edge of the O/C shell is located between $17,000$ and $20,000$ km for progenitor models below $19 M_{\odot}$, its position moves out to more than $30,000$ km for most of the more massive models. This reduces the maximum neutrino flux by more than a factor two and the neutrino-induced production is suppressed. The abundance of ^{22}Na in the outer part of the O/Ne shell is then much larger than at the bottom of the O/C shell for the more massive models. The $27 M_{\odot}$ model is again an exception for which the abundances in both regions are similar again. That is because the $27 M_{\odot}$ model has very little ^4He left in the O/C shell, such that the neutron production via $^{22}\text{Ne}(\alpha, n)$, which drives the destruction of ^{22}Na by neutron captures, is suppressed. For all the cases studied here, the ^{22}Na yield with only charged current reactions is larger than with only neutral current reactions. For the low neutrino energies the charged current alone contributes at least 70% of the total ν process enhancement and for the higher energies it is at least 60%.

Assuming a total yield of $2 \times 10^{-6} M_{\odot}$ of ^{22}Na [Woosley et al. \(1990\)](#) found that the contribution of the ^{22}Na decay to the supernova lightcurve is of the order of 10^{36} erg/s, very similar to the contribution from ^{44}Ti decay during the first 2-3 years. During this time, the decay of ^{56}Co still dominates the bolometric luminosity with $10^{40}-10^{38}$ erg/s. Later ^{44}Ti with a half-life of 59 years dominates the luminosity while most of the ^{22}Na has already decayed. Therefore, we do not expect the enhancement of ^{22}Na due to the ν process to make a difference for the bolometric lightcurve of a supernova (see also [Kozma & Fransson \(1998\)](#) and [Diehl & Timmes \(1998\)](#)). The γ -ray line at 1.275 MeV has been detected with the COMPTEL experiment on board the Compton Gamma-Ray Observatory associated with Nova Cassiopeia 1995. From this observation [Iyudin \(2010\)](#) has estimated the total amount of ejected ^{22}Na to be $\approx 10^{-7} M_{\odot}$ with large uncertainties remaining due to the distance (≈ 3 kpc) and total ejected mass ($\approx 10^{-3} M_{\odot}$). Scaling the results from [Woosley et al. \(1989\)](#) for a supernova at a distance of 10 kpc with an escape fraction of 20% at 400 days after the explosion we find a photon flux of $5.3 \times 10^{-6} \text{ cm}^{-2}\text{s}^{-1}$ per $10^{-6} M_{\odot}$ of ejected ^{22}Na . [Teegarden & Watanabe \(2006\)](#) give the sensitivity of the SPI γ -ray telescope on the INTEGRAL satellite as 1.2×10^{-4} for the 1.275 MeV γ -ray line. The expected photon flux for the largest amount of ^{22}Na we find for the $30 M_{\odot}$ model would barely lead to such a photon flux.

In order to distinguish between the low and high energy scenario discussed here, we would require to resolve a flux difference of 5×10^{-6} photons $\text{cm}^{-2}\text{s}^{-1}$ which might become feasible with future space based γ -ray telescopes like the proposed e-ASTROGAM mission (Tatischeff et al., 2016).

In addition to the emission in the electromagnetic spectrum ^{22}Na might also be relevant as the progenitor of ^{22}Ne found in meteoritic grains. Clayton (1975) has already pointed out that the ^{22}Ne -rich Ne-E(L) component in low density graphite grains from meteorites first found by Black & Pepin (1969) could be a consequence of ^{22}Na decay, i.e., the Ne found in these grains would be pure ^{22}Ne originally condensed as ^{22}Na . More recently Amari (2009) has concluded that the O/Ne shell of massive stars are the most likely origin of the material with very low $^{20}\text{Ne}/^{22}\text{Ne}$ ratios below 0.01. The condensation of graphite grains in O-rich material is problematic (Lattimer et al., 1978) even though models exist that would allow for it (Clayton et al., 1999). The C/O ratio in the O/Ne shell is typically $\text{C/O} \approx 0.01$ while this ratio reaches $\text{C/O} \approx 0.3$ in the O/C shell where charged current reactions produce most of the ^{22}Na . Modest mixing with the C/O shell right on top of it could easily lead to material satisfying $\text{C/O} > 1$ and strongly enriched in ^{22}Na . The ν process allows for the production of a large fraction of ^{22}Na in more C-rich supernova ejecta but the ratio of $^{12}\text{C}/^{13}\text{C} \approx 10^4\text{--}10^5$ in these layers still requires mixing with the outer He or H rich layers to explain the high $^{12}\text{C}/^{13}\text{C}$ ratio of 313 ± 2 found in the same grains Meier et al. (2012).

Table 5.7 shows the sensitivity of the ^{22}Na yield to variations of several important reactions rates that are involved in its production and destruction.

In the following we take a look at the sensitivity of ^{22}Na to thermonuclear reaction rates. Table 5.7 shows the effect for several reactions on the final yield of ^{22}Na . We find that $^{21}\text{Ne}(p, \gamma)^{22}\text{Na}$ and $^{22}\text{Na}(n, p)^{22}\text{Ne}$ are the most relevant reactions.

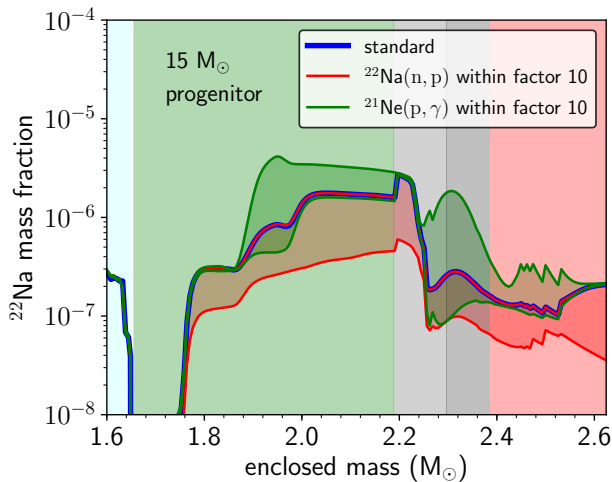


Figure 5.27.: Mass fraction profile of ^{22}Na for the $15 M_{\odot}$ model with the set of high neutrino energies illustrating the largest effects of the reaction rate variations indicated in Table 5.7 and discussed in the text. The variation of the $^{21}\text{Ne}(p, \gamma)^{22}\text{Na}$ cross-section is exaggerated compared to experimental uncertainties for the sake of comparison. Also note that this is on a logarithmic scale.

fraction at around $1.9 M_{\odot}$ leading to a mass fraction even higher than the production in the C shell by the ν process. This also shows again that the role of the ν process depends on the efficiency of the thermonuclear reaction mechanism - which depends on the combination of temperature, composition and reaction cross-section.

We have seen before that there is a small peak at mass coordinates around $1.9 M_{\odot}$ for the $15 M_{\odot}$ model and around $2.1 M_{\odot}$ for the $19 M_{\odot}$ model the mass fraction of ^{22}Na that results mostly from $^{21}\text{Ne}(p, \gamma)^{22}\text{Na}$.

This reaction rate has been studied extensively by theory and experiment resulting in relatively low uncertainty. Sallaska et al. (2013) estimate an uncertainty of less than 10% at a temperature of 1 GK. For the sake of comparison we show here in Table 5.7 and Figure 5.27 the results for changes of this rates by a factor 10 up and down. An effective increase or decrease of the reaction rate can also result from changes of temperature or composition. Therefore, the variation shown in Figure 5.27 also illustrates the sensitivity to these aspects and clearly shows in which region the reaction is important. A larger rate can significantly enhance the production even though it also implies a larger $^{22}\text{Na}(\gamma, p)^{21}\text{Ne}$ rate. In particular, Figure 5.27 shows that the increased rate leads to a pronounced peak in the mass

The neutron capture cross-section on ^{22}Na is currently based on statistical model calculations (Caughlan & Fowler, 1988; Cyburt et al., 2010) and Sallaska et al. (2013) assign an uncertainty of a factor 10 to it. In Section 2.1.2 we have discussed the assumptions and model dependencies that go into such calculations. Table 5.7 shows that the ^{22}Na yield is particularly sensitive to an increase of the (n, p) reaction rate that could reduce the yield by 70%. A reduction of this reaction rate by the same factor does not affect the yield. This is because the reaction is already negligible for the standard neutron capture rate such that available free neutrons are predominantly captured by ^{25}Mg in the O/Ne shell. Figure 5.27 illustrates that the reduction of the ^{22}Na due to an increased neutron capture rate is extended over the whole O/Ne shell and even affects the O/C and He layers.

^{44}Ti has been detected in supernova remnants (Iyudin et al., 1994; Grefenstette et al., 2014). It is produced mainly in the inner ejecta in an α -rich freeze out of NSE Woosley et al. (2002). At high temperatures, photon- and charged particle induced reactions dominate over any neutrino contribution. Therefore, we find no significant effect of neutrinos on the yield of ^{44}Ti . The production of ^{60}Fe in supernovae is discussed in detail by Limongi & Chieffi (2006), where the neutron density reached during the shock is identified as a key parameter for the yield. Despite the increase in the density of free nucleons due to neutrino spallation reactions, we find no significant modification of the ^{60}Fe yield because neutrons are mostly captured by other, in particular heavier nuclei.

5.4 Time dependent neutrino properties

In previous studies of the ν process and also in the last section it is assumed, that only the thermally produced neutrinos from the neutron star cooling phase are relevant for the nucleosynthesis. In the cooling phase, all neutrino flavor are produced equally and hence the total luminosity is distributed equally among the flavors. However, as we will see in this section modern simulations with a detailed treatment of neutrino transport give us information about the earlier phases of neutrino emission that are also described in Section 3.3.2. In first few seconds of the supernova explosion the neutrino luminosities and the energies can exceed the values during cooling by far.

One reason why the time evolution of the neutrino properties has hitherto not been taken into account for studies including the ν process is the argument that the efficiency of the ν process is determined mostly by integral quantities such as the total energy and number of neutrinos emitted. Those quantities can to some extent be constrained by the difference of the gravitational binding energy of the stellar Iron core and the final remnant under the assumption that all the neutrinos are produced during the proto-neutron star cooling. By comparing the ν process nucleosynthesis with neutrino properties from a detailed simulation to the common parametrization adjusted to result in the same integrated quantities we try to assess the validity of the parametric approach. We first use the data for neutrino luminosities and average energies obtained from a one-dimensional, artificially exploded supernova simulation (Mirizzi et al., 2016) including detailed treatment of neutrino transport by a two-moment scheme with a variable Eddington factor as closure relation (Rampp & Janka, 2002) that is equivalent to a direct solution of the full Boltzmann transport (Liebendörfer et al., 2005).

5.4.1 Neutrino properties from simulation data

Here we use the data for neutrino luminosities and average energies from an artificially exploded one-dimensional supernova simulation by R. Bollig presented in Mirizzi et al. (2016) that includes a complete and consistent treatment of neutrino transport. This model has also been used in Bartl et al. (2016) to study the effects of an improved treatment of nucleon-nucleon bremsstrahlung on the proto-neutron star cooling phase. At this point we have to resort to artificially triggered one-dimensional supernova simulations because self-consistent models are computationally very expensive and are usually not run to cover the whole proto-neutron star cooling phase. This simulation for a $27 M_{\odot}$ progenitor star is

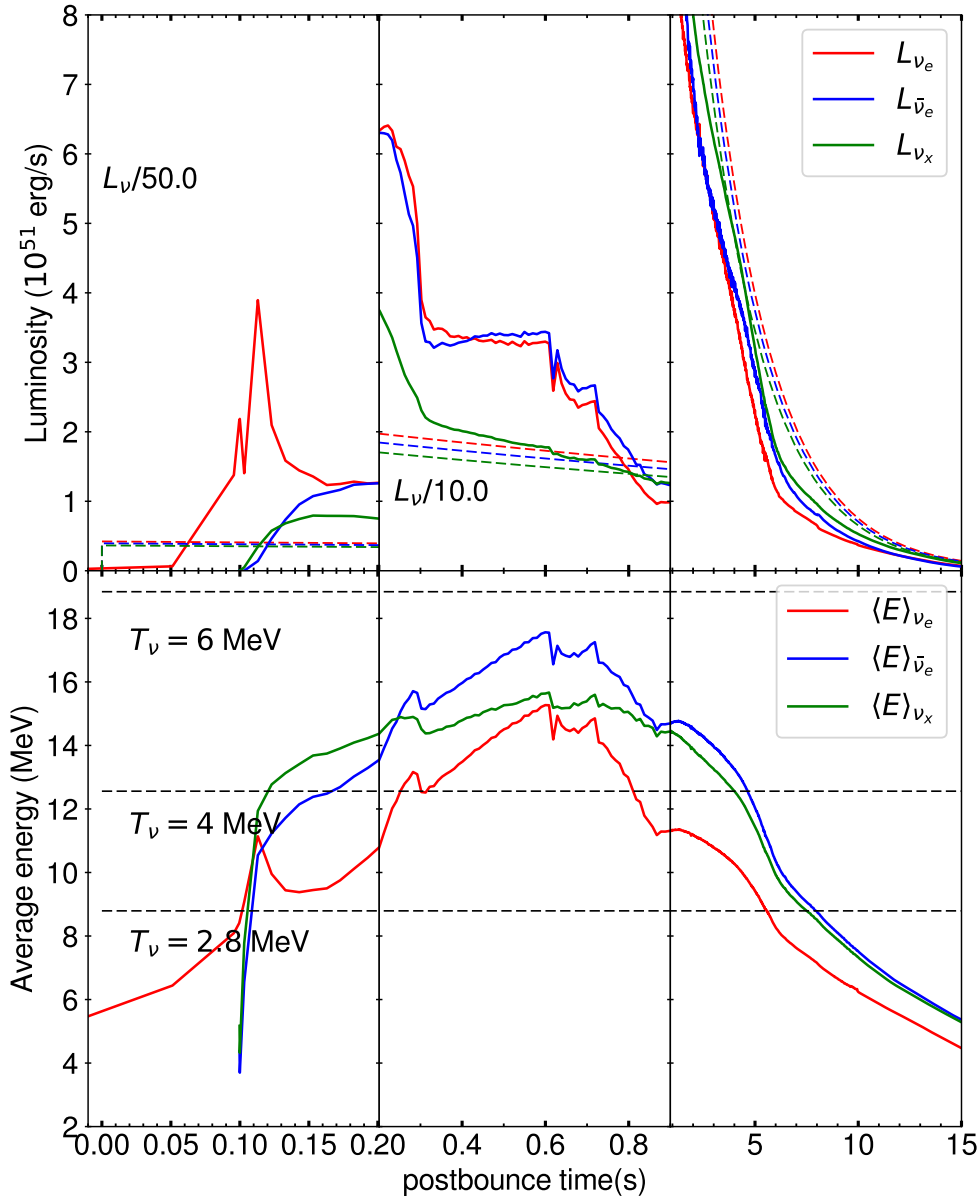


Figure 5.28.: Time evolution of neutrino luminosities and energies from a one-dimensional, artificially triggered supernova simulation. The top panels show the luminosities and the bottom panels the average neutrino energies. For comparison the evolution of the luminosity according to the exponential ansatz with a timescale of 3 s as in Equation 4.6 is also shown as dashed lines. The luminosity in Equation 4.6 was adjusted to give the same total neutrino energy as the full numerical signal.

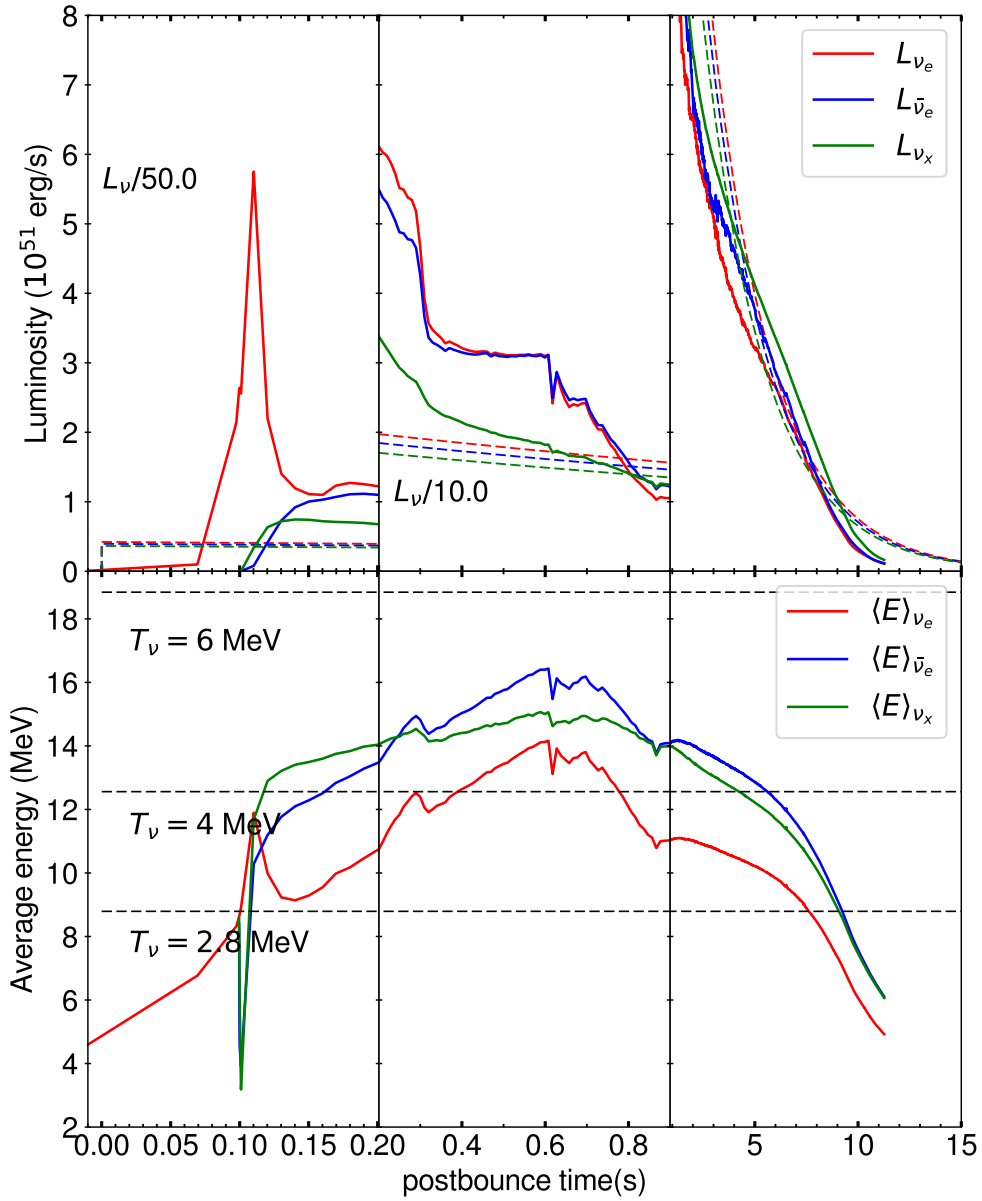


Figure 5.29.: Same as Figure 5.28 but from a simulation using the SFHo equation of state developed by [Steiner et al. \(2013\)](#) to based on a relativistic mean field model to agree with observational constraints from neutron star masses and properties of matter at nuclear saturation density derived from experiments.

suitable for our purposes because it exhibits all the relevant features of the neutrino signal that are qualitatively also found in self-consistent multi-dimensional models and we can consistently combine it with the $27 M_{\odot}$ progenitor model. Figures 5.28 and 5.29 show the three phases of the neutrino signal in detail for simulations based on two different equations of state. The top panels show the luminosities and the bottom panels the average neutrino energies. For comparison the evolution of the luminosity according to the exponential ansatz with a timescale of 3 s as in equation (4.6) is also shown as dashed lines where the luminosity in equation (4.6) was adjusted to result in same total neutrino energy of 3.42×10^{53} erg.

The cooling phase that starts after around one second after bounce is relatively well described by the parametrization of equation (4.6) with $\tau = 3$ s. However, there are two key features that are not accounted for. First, the electron neutrino burst during the first 10 ms that appears at shock breakout from the neutrino trapping regime. The burst alone contains about 10 % of the total energy that is emitted as electron neutrinos. This is followed by a prolonged phase of accretion as material falls through the stalled shock. During this time the neutrino energies are set by the position of the neutrinospheres that slowly move inward, leading to a slow, almost linear increase of the average neutrino energies. Consequently, the longer the accretion takes, the more effective can the neutrinos be for the nucleosynthesis. The explosion is then artificially revived at 0.5 s, effectively ending the accretion phase. The neutrino properties around that time are affected by the trigger and therefore not to be considered as self-consistent. In a one-dimensional model, the accretion ends immediately as soon as the explosion shock is revived because matter cannot move around the outward moving material.

First, we consider the full signal that results from the simulation. We shift the time of the data such that the peak in the electron luminosity coincides with the “bounce” in our piston model which we take to be the time when the innermost of the ejected mass zones reaches the lowest radius. The total energy emitted as neutrinos is 3.42×10^{53} erg and thus slightly more than the value of 3×10^{53} erg that we have taken previously. The distribution among flavors is also not exactly equal as assumed in all our calculations so far. Instead, ν_e contribute 0.62×10^{53} erg, $\bar{\nu}_e$ amount to 0.58×10^{53} erg and the heavy flavors μ and τ give 2.2×10^{53} for neutrinos and antineutrinos together. The mass fractions that result from the calculations with the fully time-dependent neutrino data from the simulation are marked as “full signal” in Figure 5.30.

The neutrino properties can be characterized by two main integral quantities. First, the total energy emitted as neutrinos

$$E_{\nu,tot} = \int L_{\nu}(t)dt, \quad (5.5)$$

and secondly the total number of neutrinos that are emitted

$$N_{\nu} = \int \frac{L_{\nu}(t)}{\langle E_{\nu} \rangle(t)} dt. \quad (5.6)$$

Both can be defined for each neutrino species individually. In order to judge the effect of taking the neutrino properties from a simulation compared to using the simple description of equation (4.6) we construct a reference case where we adjust the luminosity of equation (4.6) to give the same total energy as the simulation, keeping $\tau = 3$ s. Then we take average energies as

$$\langle E_{\nu} \rangle = 3.15 \times T_{\nu} = \frac{E_{\nu,tot}}{N_{\nu}}. \quad (5.7)$$

For the simulation data shown in Figure 5.28 we find $T_{\nu_e} = 3.46$ MeV, $T_{\bar{\nu}_e} = 4.01$ MeV, $T_{\nu_x} = 3.72$ MeV and $T_{\bar{\nu}_x} = 3.96$ MeV. Except for the higher electron neutrino energies this is effectively the same as our set of “low” neutrino energies discussed previously. The higher temperature of ν_e mostly results for the elevated energies during the accretion phase. If we start integrating equations (5.5) and

Nucleus	Production factor				
	cooling (low)	adjusted	full signal (SFHo)	full signal (LS220)	cooling (high)
${}^7\text{Li}$	0.01	0.02	0.04	0.05	0.16
${}^{11}\text{B}$	0.15	0.21	0.31	0.34	0.65
${}^{15}\text{N}$	0.05	0.05	0.06	0.07	0.10
${}^{19}\text{F}$	0.10	0.10	0.12	0.13	0.18
${}^{138}\text{La}$	0.53	0.70	0.84	0.89	1.00
${}^{180}\text{Ta}^m$	1.16	1.17	1.41	1.50	1.94

Table 5.8.: Production factors for the ν process nuclei as discussed in Section 5.2 now for the calculations with the numerical neutrino signals from simulations with two different equations of state for the $27 M_{\odot}$ model.

(5.6) up from 1 s post-bounce we find $T_{\nu_e} = 3.2$ MeV. This already shows that the accretion and shock breakout have important effects on the average neutrino properties. This reference case reproduced the total neutrino energy and the number of neutrinos from the simulation and is denoted as “only cooling (adjusted)” in Figure 5.30. We also compare to the cases of “low” and “high” neutrino energies. In these cases we adjust the ansatz in equation (4.6) to result in the same total neutrino energy and distribution among flavors, but the standard neutrino temperatures. The results from this approach are tagged as “cooling only (low)” and “cooling only (high)” in Figure 5.30. In order to disentangle the effects of the time dependent luminosities from the effects of different energies we consider combinations of luminosities and energies from the simulation data and from the parametrization. For once, we take the parametric luminosities from equation 4.6 with the time dependent average energies from the simulation. We find that this leads within a few percent to the same results as taking the full signal. Vice versa we use the constant energies from our parametric models with the time dependent luminosities from the simulation and find that the results are practically the same as in the completely parametric model. This shows, that the time dependence of the luminosities only plays a minor role, while the neutrino energies are crucial.

Figure 5.30 shows that there are significant differences in the nucleosynthesis of light elements ${}^7\text{Li}$ and ${}^{11}\text{B}$ when we compare our adjusted parametrized neutrino properties (“only cooling (adjusted)”) to the properties from the simulation data. We also see differences for the integrated yields given in Table 5.8. In particular we find that the full signal leads to 50% more ${}^{11}\text{B}$ and 20% more ${}^{138}\text{La}$ even though in both cases the total energy and the number of neutrinos are the same. In the following we discuss how these differences can be explained.

Since we have discussed the production of ${}^{11}\text{B}$ and ${}^7\text{Li}$ in detail in Section 5.2.1 we can start from our well known low energy case. The adjusted parametrization differs from the low energies case mostly by the higher electron neutrino temperature. This increases the production of ${}^{11}\text{B}$ in the C shell because we have already shown in Section 5.2.1 that the charged current reactions contribute almost half of the ${}^{11}\text{B}$ in that layer. However, the mass fraction is still below the results using the simulation data. For ${}^7\text{Li}$ there is a stronger contribution from the electron neutrinos in the He shell and therefore we see an increased mass fraction compared to the case with low energies. Remember that electron neutrinos lead to the production of ${}^3\text{He}$ which leads to the production of ${}^7\text{Be}$ that is more likely to survive. ${}^{11}\text{B}$ is produced in the He shell only via ${}^3\text{H}$ and since the spectral temperatures of $\nu_x, \bar{\nu}_x$ and $\bar{\nu}_e$ are almost the same in the adjusted and the low energy case they produce practically the same mass fraction of ${}^{11}\text{B}$ in the He shell. Still, the “full signal” leads to a significantly larger mass fraction. While the simulation based neutrino data increases the production in the most important regions for the total yield, we can see that not all regions of the star show the same trend. The mass fraction of ${}^{11}\text{B}$ in the outer C shell at a mass coordinate of around $6.1 M_{\odot}$ is lower for the calculations with the full signal than in all other cases. This is also particularly prominent for the mass fractions of ${}^7\text{Li}$ shown in the middle panel of Figure 5.30. While the “full signal” case leads to a significant increase of the mass fraction in the He

shell, it leads to a decrease of the - albeit small - mass fraction in the O/Ne shell. These differences do not affect the total yield because the mass fractions in these regions are very low but they in particular show that there are effects of using the full signal that cannot be captured by adjusting the neutrino temperature. Apparently, the total energy emitted in neutrinos as defined by equation (5.5) and the number of neutrinos defined by equation (5.6) are not sufficient to characterize the neutrino properties.

In order to include the effect of the position and expansion of a mass zone under consideration that affects how much the neutrino flux is geometrically diluted we can define the neutrino fluence F as time integral of the flux ϕ

$$F_\nu = \int_{t_{min}}^{\infty} \phi_\nu(t) dt. \quad (5.8)$$

Here t_{min} is taken as the time at which the temperature has decreased below a limiting value T_{lim} . The fluence is a measure for the neutrino exposure. It also takes into account that the exposure depends on the radius and hence decreases with time as the radius of a mass shell increases. For a mass zone that stays at a constant radius, the fluence is equal to the total number of neutrinos up to a constant factor of $1/(4\pi r^2)$. In the bottom panel of Figure 5.30 we can see that the fluence as defined by equation 5.8 is very similar for the adjusted parametric model and the full signal in for all mass zones. For finite values of T_{lim} the fluences for the full signal tend to be larger than in the parametric model which indicates that more neutrinos arrive at a given shell at later times. This is connected to the decreasing energies during the cooling phase in the full signal. Keeping the neutrino temperature constant in the parametric model requires less neutrinos to account for the same luminosity. While the number of neutrinos is larger for the full signal. Due to $\phi_\nu \propto L_\nu(t)/r(t)^2$ for the neutrino flux, the fluence decreases with radius and also depends on the expansion velocity.

Since also the fluences do not explain the differences between the full signal and our adjusted cooling model we need to take it one step further and look directly at the number of neutrino absorption reactions

$$\mathcal{R} = \int_{t_{min}}^{\infty} \phi_\nu(t) \sigma_\nu(T_\nu(t)) dt, \quad (5.9)$$

with the cross-section for neutral current reactions on ${}^4\text{He}$ which are the most important for ${}^7\text{Li}$ and ${}^{11}\text{B}$. This takes into account that the dependence of the cross-section on the neutrino temperature – here we still assume that all neutrinos follow a Fermi-Dirac spectrum – is at least quadratic or of higher order. This steep dependence on the neutrino temperature also explains why the changing the neutrino energies than changing only the luminosity.

The bottom panel of Figure 5.30 shows \mathcal{R}_{ν_x} for the whole range of the $27 M_\odot$ model for several values of T_{lim} . The total value integrated for the whole time of the calculation (full black line) is consistently larger for the full signal than for the adjusted parametrized approach shown as dashed black line. This shows, that even though the total number of neutrinos is the same for the different descriptions, the number of induced reactions is larger for the neutrino properties from the simulation because the higher than average neutrino temperatures during the early phase get a larger weight from the steep temperature dependence of the cross-sections. This explains why we can get a larger mass fraction of ${}^{11}\text{B}$ and ${}^7\text{Li}$ in the He shell. When we look at different values of T_{lim} we can also explain the lower mass fractions in the O/Ne and outer C shells. In this regions, the peak temperature in the shock is sufficient to destroy most of the ${}^{11}\text{B}$ and ${}^7\text{Li}$ that can be produced before the shock arrived. Therefore, the production depends only on those neutrinos that arrive at the mass zone after the material has cooled down. From the lower panel of Figure 5.30 we can see that \mathcal{R}_{ν_x} is lower for the full signal when we only consider neutrinos that arrive once the temperature has dropped below 1 GK.

In the He shell the temperature never gets very high, and therefore the larger total \mathcal{R}_{ν_x} has its full effect. In regions where the temperature is larger, the fragile light elements can only survive if they are produced below a certain threshold temperature. Since the neutrino signal from the simulation deposits a larger amount of neutrinos at early times, the ν process is less effective in regions where the temperature is high for the full signal. However, in such regions the mass fraction of the light elements is in any case low and therefore the net effect on the yield is an increase.

The spectral temperatures of the electron flavor neutrinos are even more important for ^{138}La and ^{180}Ta . As a reminder, these nuclei are only sensitive to electron neutrinos and are produced by $^{138}\text{Ba}(\nu_e, e^-)$ and $^{180}\text{Hf}(\nu_e, e^-)$ respectively. ^{138}Ba and ^{180}Hf are remains of the initial solar composition and γ process nucleosynthesis (see Section 5.2.4). Figure 5.31 shows the mass fraction profile for ^{138}La and ^{180}Ta for the $27 M_\odot$ model for the different description of the neutrino properties. Due to their large atomic number ^{138}La and ^{180}Ta are unaffected by charged particle reactions and the maximum abundance of free neutrons in the outer O/Ne shell is small. Therefore, when the temperature is too low for efficient photodissociation, ^{138}La and ^{180}Ta are almost unaffected by the supernova shock heating and the early component of the ν_e signal can fully contribute to the final yield. We found that the average energy of ν_e as defined in (5.7) corresponds to a $T_{\nu_e} = 3.4$ MeV - between the high and low energy cases studied so far. For the case “only cooling (adjusted)” this is also what we find for the mass fraction of ^{138}La which is between the low and high energy cases. The total yield is increased by 30% compared to the low energy case. However, for the full signal, the mass fraction of ^{138}La reaches values as large as the results with the high neutrino energies. This is again due to the fact that larger energies for a short time can induce more reactions than the average energy would suggest, due to the temperature dependence of the cross-section. The integrated yield is increased by 60% compared to the low energy case, reaching almost 90% of the high energy case (see Table 5.8).

Figure 5.31 also shows that the effect for ^{180}Ta is smaller. However, here we need to keep in mind that the $27 M_\odot$ model is special with respect to the production of ^{180}Ta which has a very strong contribution from the pre-explosive γ process and from neutral current spallation because of the large abundance of ^{181}Ta in the progenitor. This makes the production more sensitive to thermonuclear reactions and hence to the temperature as well as to the spectral temperature of the heavy flavor neutrinos. In our adjusted model T_{ν_x} for the heavy flavors is practically equal to the low energy case. Therefore, we only find an imperceptible increase of ^{180}Ta with our adjusted temperatures. However, the full signal leads to an increase of the ^{180}Ta yield by 20% compared to the low energy case. The stronger variation of the ^{180}Ta yields with the progenitor model is discussed in Section 5.2.4.

The resulting production factors are summarized in Table 5.8 and show that if we want to achieve the same production of ^{138}La with the parametric cooling approach as with the neutrino data from the simulation, we would need to choose almost the set of high neutrino energies, i.e. $T_{\nu_e} = 4$ MeV. However, if we do so, we would get an overproduction of ^{180}Ta as well as of the light elements ^{11}B and ^7Li . Remember that the ν process only needs to contribute around 30% to the solar ^{11}B abundance. Thus, we can conclude that defining an average temperature for a parametrized description of the neutrino properties is according to equation (5.7) is not able to capture the full range of effects that results from taking the neutrino properties from simulation data with differences of up to 50%.

In addition to that we also find that the time dependence of the luminosities has an impact on the nucleosynthesis, albeit mostly in the regions where that contribute little to the total yield because these effects arise from the timing of thermonuclear reactions that destroy the ν process products. Hence, even though the time dependence as such is not crucial for the nucleosynthesis, it makes defining an appropriate average for the neutrino temperature rather difficult. In particular, the elevated energies of the accretion phase and the electron neutrino burst would require to choose higher temperatures. The neutrinos emitted during these phases result from dynamical processes and are not directly connected to the proto-neutron star cooling. This cuts the connection to the gain of gravitational binding energy and makes the would make an appropriate choice of neutrino properties not only dependent on the remnant mass but on the dynamics of the explosion itself.

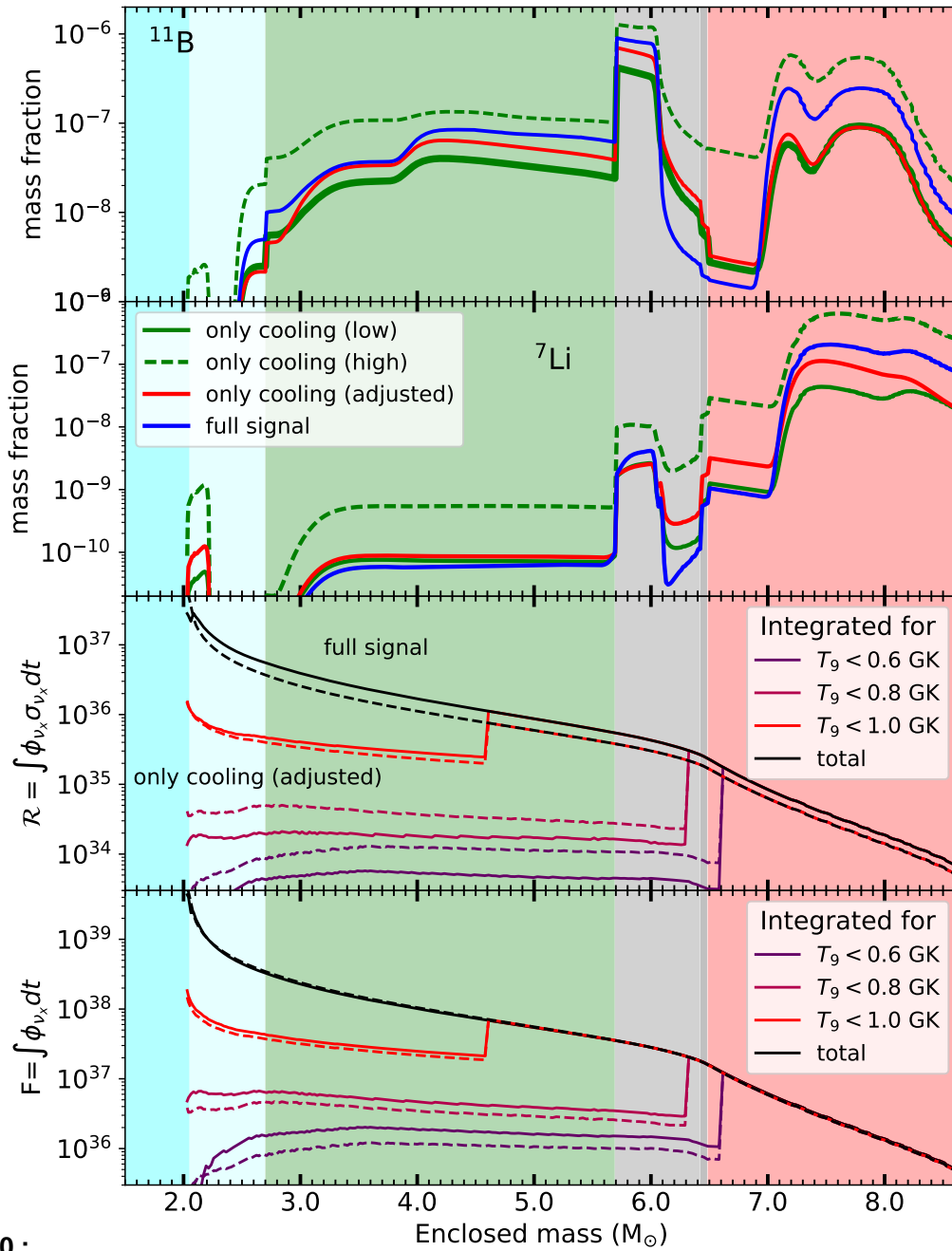


Figure 5.30.:

- *Top two panels:* mass fraction profile of ^{11}B for the $27 M_{\odot}$ model with different descriptions of the neutrino properties. “full signal” uses the data from the one-dimensional simulation as described in the text. “only cooling” use equation (4.6) with constant neutrino temperatures. Where “high” and “low” correspond to the temperatures used in Section 5.2 and “adjusted” employs the average values adjusted to the simulation data.
- *Third panel:* Number of neutrino-induced reactions on ^4He as define by equation (5.9) for the whole range of the star and different values of T_{lim} . The dashed lines are for the adjusted “only cooling” corresponding to the red line in the upper panels. The full lines results form the simulation data.
- *Bottom panel:* Neutrino fluences as defined by equation (5.8). Again dashed lines for the “only cooling” parametrization and full lines for the simulation data.

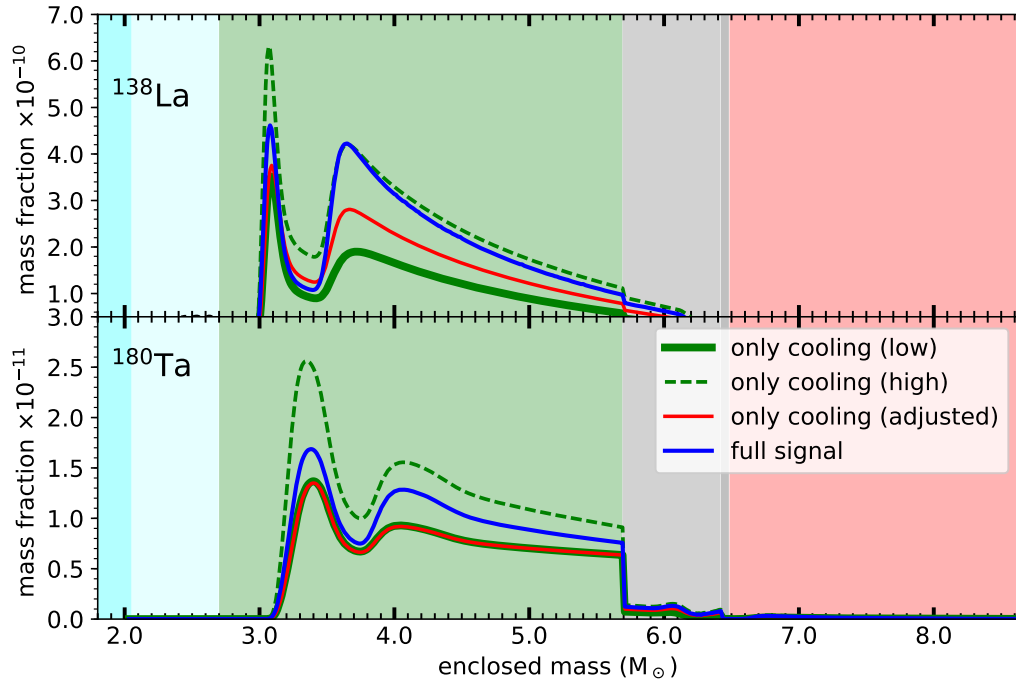


Figure 5.31.: Same as the top panel of Figure 5.30 but for ^{138}La and ^{180}Ta from the $27 M_{\odot}$ model calculated with the neutrino properties for the simulation discussed in the text. With the full neutrino signal the mass fraction of ^{138}La is almost as large as in the high energy case.

Having found that the neutrino properties from simulation data have a distinct effect, the question arises whether this can be used to put constraints on the physics that enter into the simulation from nucleosynthesis arguments. We have discussed in Section 3.3.2 that the neutrino properties are sensitive to the equation of state of nuclear matter. Figures 5.28 and 5.29 show the neutrino energies and luminosities for two different equations of state. On the one hand, the equation of state by [Lattimer & Douglas Swesty \(1991\)](#) which has become a standard reference case. It is based on a compressible liquid drop model that is characterized by the nuclear compressibility index $K = 3\partial P/\partial n$ at nuclear saturation density. For this case $K = 220$ MeV is set. The SFHo equation of state by [Steiner et al. \(2013\)](#) is based on a relativistic mean field model and in agreement with constraints from neutron star masses and nuclear properties at saturation density. It slightly differs with $K = 242$ MeV which in this case is not a parameter but results from the model. As discussed in Section 3.3.2, a softer equation of state leads to larger accretion luminosities because the core contracts faster. As a result, the core has already cooled down more once the accretion is over and therefore the luminosities during the cooling phase are larger for the calculation with SFHo. In total, with 3.57×10^{53} erg the energy emitted as neutrinos is also larger for the SFHo equation of state than in the calculation with LS220 where we find 3.42×10^{53} erg. The equation of state of hot and dense matter is not very well known and clues that can constrain the equation of state are highly sought after. The possible effect of the equation of state on the ν process has so far not been discussed in the literature and here we can see how the uncertainties due to the equation of state propagate into the ν process results. This comparison is also included in Table 5.8. The SFHo equation of state results in slightly lower neutrino energies and luminosities during the accretion phase, but it actually gives larger luminosities for $t > 1$ s. Despite the larger cooling luminosities for the SFHo equation of state, we find that the ν process production is weaker and the production factors for the ν process nuclei are by less than 10%. These changes are too small to draw any conclusion about the equation of state from nucleosynthesis, in particular by just considering a single stellar model. Here we have only included the effect of the equation of state on the neutrino properties. In nature, this also affects the dynamics of the explosion, changing the explosion energy and the mass cut.

In this Section we have now for the first time taken into account the full time dependence of neutrino properties based on supernova simulation with detailed neutrino transport. We find that there are distinctive effects that arise when we take into account the whole range of energies and including their time dependence that cannot be captured by the standard parametrization of the neutrino signal adjusted with the integrated luminosity and total number of neutrinos of each flavor. These effects can modify the integrated yield by up to 50% for ^{11}B and up to 20% for ^{138}La . While these effects are interesting for an individual stellar model, we would not expect a major effect on the nucleosynthesis of a whole stellar population. In nature the explosion dynamics and the neutrino emission are coupled and depend on the progenitor structure. Since there are only a few self-consistent simulations we present in the next section the outline of a toy model for the neutrino properties to include an extended accretion phase.

In this section we have assumed the same explosion energy and dynamics for all models with different neutrino properties. In the end, neutrino properties are tightly connected to the explosion energy. A fully consistent picture can only be obtained from a self consistent simulation, such as studied in the next Section.

5.5 Innermost ejecta and NSE

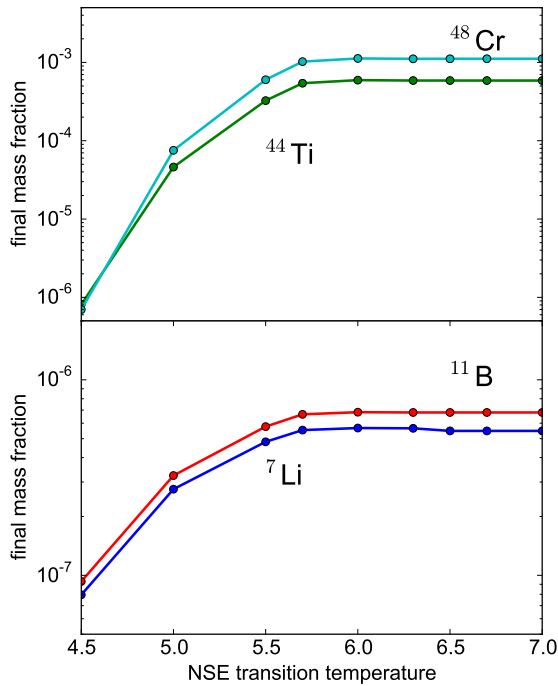


Figure 5.32.: Dependence on NSE freeze-out temperature

that need to minimize the computational cost of the nuclear reaction network that is included to account for energy generation by nuclear reactions. The production of ^{11}B and ^7Li by the ν process also requires a large abundance of ^4He in the freeze out. Therefore, the yields of ^{11}B and ^7Li are sensitive to the NSE transition temperature. This is illustrated in Figure 5.32, where the final mass fractions of ^{44}Ti and ^{48}Cr for one of the innermost zones of our stellar models are shown as function of the chosen transition temperature. The upper panel shows that lower transition temperatures reduce the mass fraction of ^{44}Ti and ^{48}Cr because the freeze is less α rich. The lower panel illustrates, that the same effect can be seen for ^{11}B and ^7Li . We choose the transition temperature to be $T_{NSE} = 6$ GK to make sure that the α rich freeze is well described.

In the next section we take a look at the innermost part of the supernova ejecta. This material is often heated by the shock to temperatures exceeding 10 GK. Under these conditions we do not calculate the composition with the reaction network but can safely assume nuclear statistical equilibrium (NSE, see Section 2.1.5). The temperature at which we then switch from the solving the NSE equations to solving the full reaction network needs to be chosen with some care. It is well known that ^{44}Ti and ^{48}Cr is mostly produced in the innermost supernova ejecta freezes out from NSE with a large abundance of α particles (α -rich freeze out, see section 2.1.5). The dependence of the production ^{44}Ti on the conditions has been studied in by [Magkotsios et al. \(2010\)](#). In practice, the temperature for transitioning between assuming NSE and using the full reaction network is chosen. A too low transition temperature means, that NSE is assumed for longer time and the abundances of ^4He at freeze out is lower. As a consequence, the abundance of nuclei that require an α rich freeze out are reduced. Reference [Harris et al. \(2017\)](#) have recently discussed the relevance of choosing an appropriate transition temperature which is of particular importance for multi dimensional supernova simulations



6 The ν process with tracer particles of a two-dimensional supernova simulation

In Section 3.3.2 we have pointed out that the explosion mechanism of core collapse supernovae hinges on effects of multi-dimensional fluid flows. In this section we study the ν process in the context of a two-dimensional axisymmetric but self consistent supernova simulation. While fully three dimensional supernova simulation are still computationally too expensive to run long enough to cover the whole domain relevant for nucleosynthesis (Müller, 2016), two-dimensional simulations just start to become a framework for extensive studies of the production of the elements (Wanajo et al., 2018; Eichler et al., 2018; Harris et al., 2017). One-dimensional explosion models currently have to employ schemes to artificially trigger explosions. Even though several models have been and are being developed to account for multi-D effects in 1D simulations, their predictive power remains to be confirmed. Most schemes to achieve an explosion in spherical symmetry impose or modify neutrino properties and are therefore not able predict the neutrino signal fully self-consistently. Furthermore, supernova explosions might significantly deviate from spherical symmetry, not only in the topology of the explosion itself, but also in the neutrino emission. Tamborra et al. (2014a) have reported a self-sustained asymmetry of lepton-number emission for some cases. Studying axisymmetric simulations for four different progenitors Bruenn et al. (2016) find that the development of asymmetries is very progenitor dependent and the development of pre-supernova asymmetries might even be the key to successful explosions (Müller et al., 2016b). Another caveat of one-dimensional supernova simulations is the requirement of a clearly defined mass cut, i.e. the innermost zone that is ejected. In self-consistent multi-dimensional simulations the distinction between ejecta and fallback does not need to be done by hand. Since the ν process mostly affects the O/Ne-, C- and He shells of a star, it has so far been assumed to be not very sensitive to the detailed dynamics of the explosion mechanism that determine the behavior of the innermost regions. However, we have seen in section 5.2 that there are indications of the production of light elements via the ν process from the α -rich freeze out of the innermost layers. This possibility has also been suggested by (Woosley et al., 1990) in the early studies of the ν process and it has also been mentioned in the context of two-dimensional simulations (Nishimura et al., 2015; Nagataki et al., 1997).

Wongwathanarat et al. (2017) have shown that it is possible to find three dimensional models to reproduce the topology of individual supernova explosions. However, from the point of view of nucleosynthesis as input for chemical evolution, we are in the end mostly interested in averaged yields for a whole range of progenitors. Therefore, the asymmetries and particular conditions that individual cases might provide need to be viewed as exemplary cases and we are mostly interested to see if general and systematic effects might arise that make a difference for the integrated nucleosynthesis of a whole stellar population. With the study of tracer particles we want to address two main aspects. First, a self-consistent simulation gives the best estimate for the innermost part of the supernova ejecta and allows us to explore the ν process in the region of the α -rich freeze out that was mentioned in section 5.2. In particular we want to see if the fluid dynamics of multi-dimensional simulations can significantly increase the production of the light elements by the ν process. Secondly, we can use neutrino properties consistent with the explosion dynamics. This removes the basically arbitrary choice of neutrino energies and luminosities that we have shown to be problematic in 5.4.

Here we want to focus on aspects related to the ν process as discussed in the previous sections. We also present an angle dependent extrapolation scheme that gives us a fast and computationally cheap estimate for the nucleosynthesis of the whole star. Since this simulation is still being continued to later times and larger radii, the extrapolation is to be viewed as a preliminary measure. However, the concept

can also be applied to extend the study of the nucleosynthesis based on data from three-dimensional simulations.

6.1 The simulation data and classification of tracer particles

The tracer particle method is the method of choice to study the detailed nucleosynthesis of scenarios that require computationally expensive simulations, that cannot carry out full reaction network calculations along with the hydrodynamic evolution (Nagataki et al., 1997; Nishimura et al., 2015). Tracer particles are records of the thermodynamic history of representative fluid elements. Important for our study, the tracer particles also keep a record of the neutrino exposure. We use tracer particles from an axisymmetric simulation of a $12 M_{\odot}$ star presented by Bruenn et al. (2016). Aspects of the nucleosynthesis with tracer particles have been discussed by Harris et al. (2017). Each tracer particle represents $1.87 \times 10^{-4} M_{\odot}$ of material and the tracer particles are initially distributed equally in mass along 40 radial columns or rays, each corresponding to a particular angle with respect to the symmetry axis. Note, that the equal distribution in mass does not correspond to an equal spacing of the angles. As the density decreases to larger radii, the volume represented by each tracer correspondingly increases, giving a wider spacing. The initial distribution of the tracers is illustrated in Figure 6.1. The evolution of the tracer particles has been followed throughout the simulation by advancing their position \vec{r} after each hydrodynamic time step according to the velocity \vec{v} of the surrounding fluid cell as

$$\vec{r}^{(n+1)} = \vec{r}^{(n)} + \vec{v}^{(n)} \Delta t. \quad (6.1)$$

For the new position the relevant physical quantities, such as temperature, density and neutrino exposure are interpolated from the values at the grid points of the simulation to the position of the tracer. The histories of these tracer particles cover 0.1 - $1.95 M_{\odot}$ in mass coordinate of the 1D progenitor model corresponding to initial radii from $890 - 15,000$ km, i.e. from the outer edge of the iron core to the lower edge of the O/C shell. Thus, they include already a major part of the explosive nucleosynthesis. Most of the outermost tracer particles are not subject to temperatures exceeding 2 GK. The lower panel of Figure 6.1 also shows the final configuration of the tracer particles. This shows that the explosion is dipolar, ejecting matter quickly along the axis while strong downstream pull matter in from the perpendicular direction. Still, the ν process is active in regions that are even further from the center. Furthermore, the simulation does not cover the evolution until the shock has reached the Hydrogen envelope. Even though the explosion is well developed and the explosion energy relatively well determined to be 0.3×10^{51} erg, the fate of individual tracer particles is still undecided. Even though this decision can only be made with certainty by continuation of the simulation, the velocity and energy of the particles give already an indications of the final fate. Since we want to study a broad range of scenarios for nucleosynthesis we choose a rather optimistic criterion for the ejection. We use the radial velocity as indicator for the fate of a tracer particle. If the radial velocity during the last 10 time steps of the simulation is positive and the radius coordinate of the particle has actually increased with respect to its initial position, we assume that the tracer is going to be ejected. This neglects the possibility that the tracer is moving outward at the end of the simulation but does not have sufficient energy to escape the gravity well of the remnant in the end.

We also have to account for the fact, that the explosion shock has not traveled through the whole simulation domain. Therefore, tracer particles at the edge of the domain are often unshocked. We identify those by requiring an increase in temperature of at least a factor 2 during the simulation time. Tracer for which this is not the case are tagged “unshocked” in Figure 6.1. Those tracers are not post-processed and instead we take the composition from the one-dimensional calculations based on the extrapolation of the shock evolution as described below. From a total set of 4000 tracer particles only 2109 fulfill these criteria and are post-processed for nucleosynthesis.

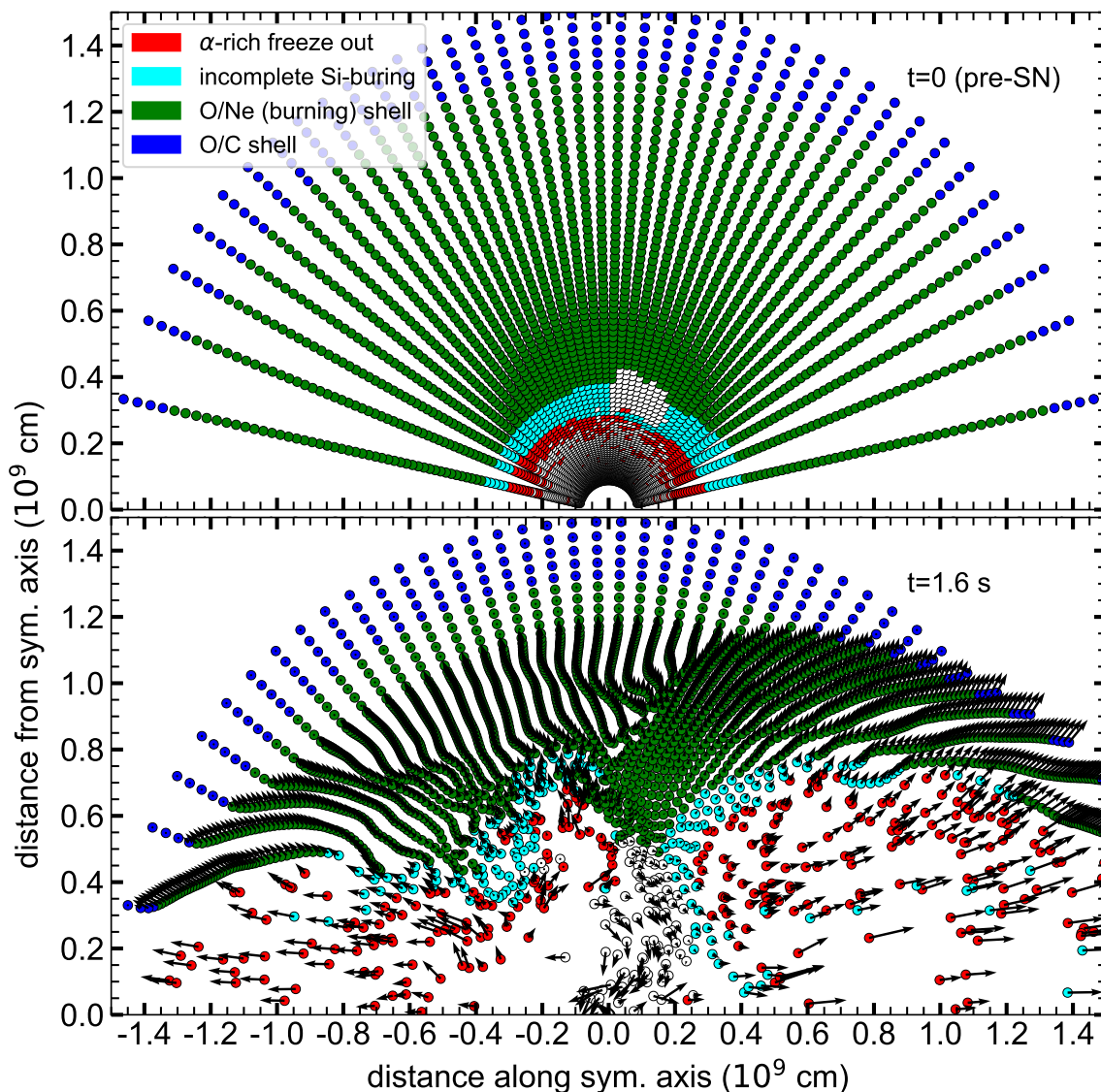


Figure 6.1.: Initial distribution of tracer particles and distribution at the end of the simulation. Colors classify the tracers according to their final composition. Tracers marked as Incomplete Si-burning include cases that end up dominated by ^{28}Si or ^{56}Ni . Tracers for which ^4He is the most abundant species are classified as α -rich freeze out. Tracers marked as O/Ne (burning) shell includes tracers consisting mainly of ^{20}Ne , ^{16}O and ^{24}Mg in the end. Tracers for which ^{12}C is among the two most abundant isotopes are included as O/C.

The lower panel shows the final distribution at the end of the simulation at around 1.6 s and arrows indicate the velocity at that time where the length of the arrow scales linear with the magnitude. The evolution after this time is extrapolated assuming an adiabatic expansion and constant velocity. For tracers that have left the simulation domain earlier, the extrapolation starts at an corresponding earlier time.

All the data is from [Bruenn et al. \(2016\)](#); [Harris et al. \(2017\)](#).

The tracer particles are initially arranged in 40 radial rays equally distributed in mass.

For the time after $t_{\text{last}} = 1.6$ s at which the simulation has been stopped, the temperature and density are extrapolated from the last values following (Ning et al., 2007) as:

$$T(t) = T_{\text{last}} \left(\frac{t}{t_{\text{last}}} \right)^{-2/3} \quad \text{and} \quad \rho(t) = \rho_{\text{last}} \left(\frac{t}{t_{\text{last}}} \right)^{-2}. \quad (6.2)$$

This is also consistent with the model we use for the regions outside the simulation domain, as explained below. The evolution of the neutrino luminosity is continued with equation (4.6) starting from the last value of the simulation data and $\tau_\nu = 3$ s.

6.2 Extrapolation of the simulation data

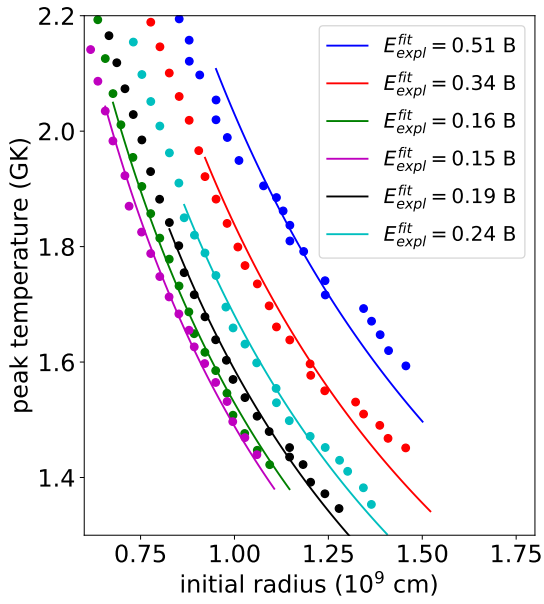


Figure 6.2.: Peak temperature over initial radius of the last 20 tracer particles at the outer edge of several columns (rays). Each of the rays was fitted as $T_{\text{peak}} = 2.4 \text{ GK} \times (E_{\text{expl}}^{\text{fit}})^{1/4} \times r_0^{-3/4}$ according to equation 4.2. Note that $1 \text{ B} = 10^{51} \text{ erg}$.

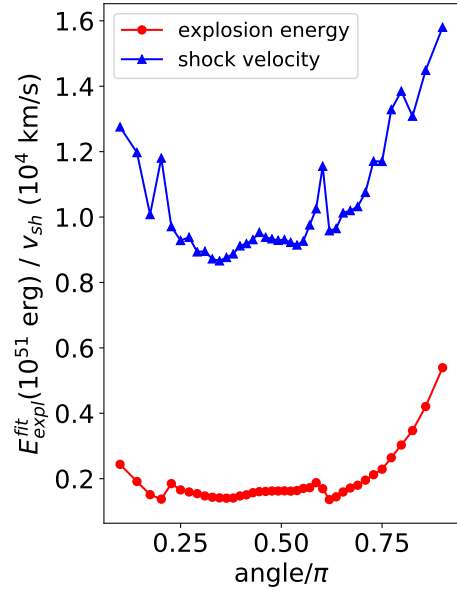


Figure 6.3.: Fitted results for $E_{\text{expl}}^{\text{fit}}$ and shock velocities that result from the fitting procedure.

The tracer particles cover almost the inner $2 M_\odot$ of the initially $12 M_\odot$ star with a He core mass of $3.1 M_\odot$. To judge the contribution of the α -rich freeze out to the production of ${}^7\text{Li}$ and ${}^{11}\text{B}$ we need an estimate for the nucleosynthesis yields of the whole star.

The explosion is not entirely symmetric and also the neutrino luminosity is not completely isotropic. In order to capture some of the effects of an asymmetric explosion, an extrapolation of the temperature and density evolution is necessary. The extrapolation is based on the initial position of the tracer particles as shown in the top panel of Figure 6.1. According to the initial position each tracer can be assigned to one of the 40 angles and the tracers can be grouped as rays or columns. Each of the 40 columns consists of all the 100 tracers that have the same initial angular position. Since the domain for which an extrapolation is needed starts relatively far out in the O/C shell, each column is assumed to evolve independently. We do not expect major effects of turbulence or convective overturns this far outside. Therefore, each angular ray is treated as a one dimensional problem, neglecting any non-radial motion. We use equation (4.2) to estimate the peak temperature for the regions beyond the simulation domain along each ray separately.

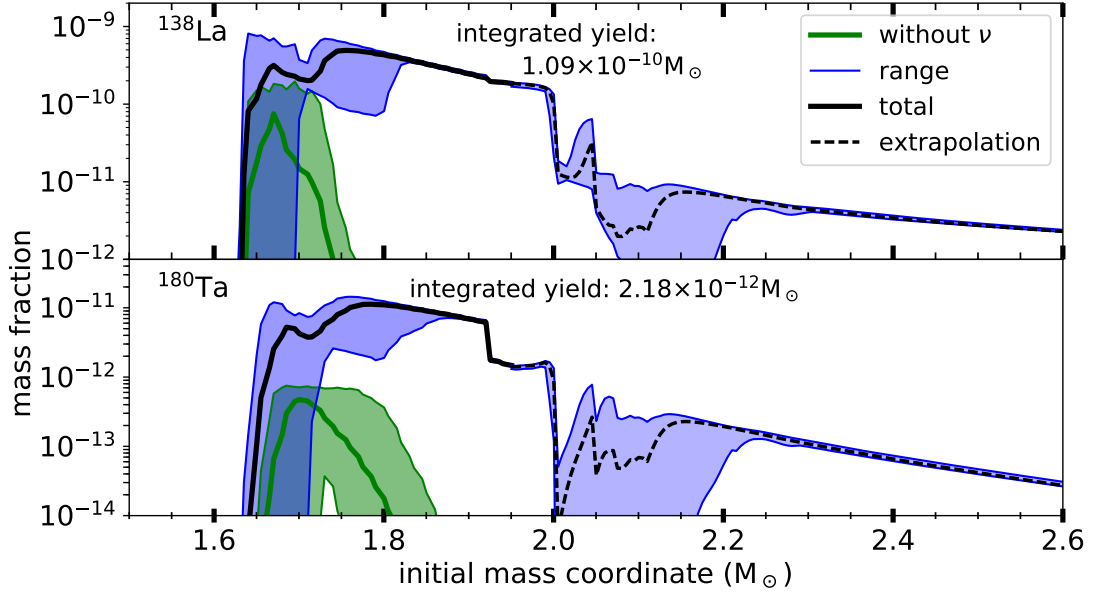


Figure 6.4.: Mass fraction profile for ^{138}La and ^{180}Ta projected onto the initial mass coordinate. The main production region is described by simulation data. Both nuclei turn out to be overproduced in this simulation. The range indicates the minimum and maximum mass fractions found for tracers initially located at a given mass coordinate.

The only parameter that is required for equation (4.2) is the explosion energy. Since we consider only a one dimensional ray out of a multi-dimensional setup, this explosion energy does not need to represent the total energy of the explosion. Instead it corresponds to the fraction of the total explosion energy in the radial direction of the angle under consideration. In order to find the appropriate value to represent the effective energy for each direction we fit equation (4.2) to the peak temperatures reached by the last twenty tracers that have experienced shock heating in the simulation and have originally been positioned along the ray. Figure 6.2 shows the peak temperature recorded by the tracers for exemplary four different rays as a function of the initial radial position of the corresponding tracer particle. The values can in all cases be described relatively well by equation 4.2. Fitting the last twenty tracer particles with equation 4.2 allows to extrapolate the peak temperature to radii beyond the simulation domain. We obtain a value for $E_{\text{expl}}^{\text{fit}}$ for each angular ray. Figure 6.3 shows the resulting fit parameters as a function of angle.

Furthermore, we need to estimate how fast the shock propagates in each direction. We use the time $t_{\text{Peak}}^{i,j}$ and position $r_{\text{sh}}^{i,j}$ for a tracer i in ray j at which the maximum temperature $T_{\text{peak}}^{i,j}$ is reached to define the evolution of the shock. This gives us the shock radius for each angular ray j as a function of time as covered by the simulation data. Figure 6.5 shows that shock moves already at a relatively constant

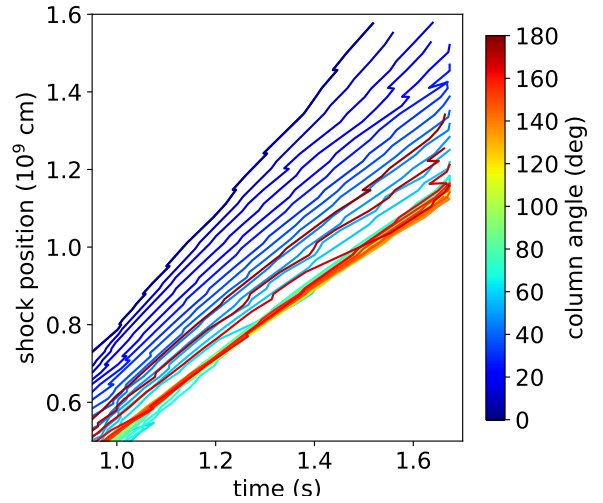


Figure 6.5.: Shock position r_{sh} , defined by time and radius of maximum temperature, over time for all the angular rays colored according to the angle. For the last ten tracers the shock velocity remains constant to a good approximation.

velocity towards later times. By taking the average velocity as finite differences we get an estimate for the shock velocity of ray j as

$$v_{sh}^j = \frac{1}{10} \sum_{i=N_j-11}^{N_j-1} \frac{r_{sh}^{i+1,j} - r_{sh}^{i,j}}{t_{Peak}^{i+1,j} - t_{Peak}^{i,j}}, \quad (6.3)$$

where N is the number of tracers for angle j . For the rays around $140^\circ - 160^\circ$ the motion of the particles has larger non-radial components that can also be seen in the lower panel of Figure 6.1. This leads to particles leaving the direction of their original ray and they do not move at the same velocity as other tracers associated with the same angle. This leads to the kinks in Figure 6.5 that result from tracers of the same ray “overtaking” each other. By averaging over the last ten tracers to get the velocities we are confident to get a representative estimate for the shock velocities.

The shock velocity is an important quantity if we want to extrapolate how the explosion propagates. Analytic formulas for the shock velocity in stellar explosions have also been developed in the past (Matzner & McKee, 1999) and would also provide a way to estimate the velocity. In order to get smooth transition between the tracer particles and the extrapolated trajectories, we take the velocities extracted from the data. One caveat of our approach is that we do not take into account the structure of the progenitor star that the shock encounters outside of the simulation domain. Large density gradients may speed up the shock, as it propagates further.

Following Ning et al. (2007) as explained in Section 4.1 we can use the estimate for the shock velocity v_{sh} to define a timescale for the expansion of a mass shell originally located at an radius r_0 as $\tau = r_0 / v_{sh}$ (see equation (4.5)). The evolution of temperature and density is then described by

$$T(t) = T_{peak} \left(1 + \frac{t - t_0}{\tau}\right)^{-2/3} \quad \text{and} \quad \rho(t) = \rho_{peak} \left(1 + \frac{t - t_0}{\tau}\right)^{-2}, \quad (6.4)$$

assuming an adiabatic expansion. The time of shock arrival t_0 is estimated from the time t_0^{last} and position r_0^{last} when the shock reaches the outermost tracer particle. With the shock velocity we get $t_0 = t_0^{last} + (r_0 - r_0^{last}) / v_{sh}$. Figure 6.3 summarizes the results for the fit parameters E_{expl}^{fit} and shock velocities as a function of angle. This shows that shock velocities and peak temperatures reflect the asymmetry of the explosion, which can be seen in Figure 6.1.

Two-dimensional supernova simulations tend to predict low explosion energies (see Section 3.3.2). Taking into account the geometrical factors, the fitted values E_{expl}^{fit} can be summed over all angles and we get a total explosion energy of 0.2×10^{51} erg. In the evaluation of the full hydrodynamic simulation data Bruenn et al. (2016) have found a total explosion energy of 0.3×10^{51} erg, taking into account gravitational overburden of the outer shells and nuclear recombination. Keeping in mind that our fit to equation 4.2 does not take into account the non-radial motion, a lower value is to be expected.

In order to include the ν process we need also an estimate for the neutrino fluxes. In order to be consistent with our extrapolation we use the recorded neutrino fluxes for the outermost tracer particle of each angular ray and assume that all the mass zones in this angular direction are subject to the same neutrino luminosity. This approach allows to account for the asymmetry of the neutrino emission and in particular also the correlation between the neutrino luminosity and strength of the explosion in the same direction. The neutrino fluxes are taken from the simulation until 1.6 s, when the simulation was stopped. We continue the evolution of the neutrino luminosity with equation (4.6) starting from the last value of the simulation data and $\tau_\nu = 3$ s. For the spectral temperature of the neutrinos we take also the last value from the tracer particles and keep it constant. This is also applied to the post-processing of the tracer particles themselves. In total this model gives an energy of 2.5×10^{53} erg emitted as neutrinos with little asymmetry. The angular variation of the neutrino luminosities is of the order of 10% with higher luminosities along the symmetry axis. While variations of this order are crucial for the revival of the explosion, it is negligible for the ν process. The average spectral temperatures as

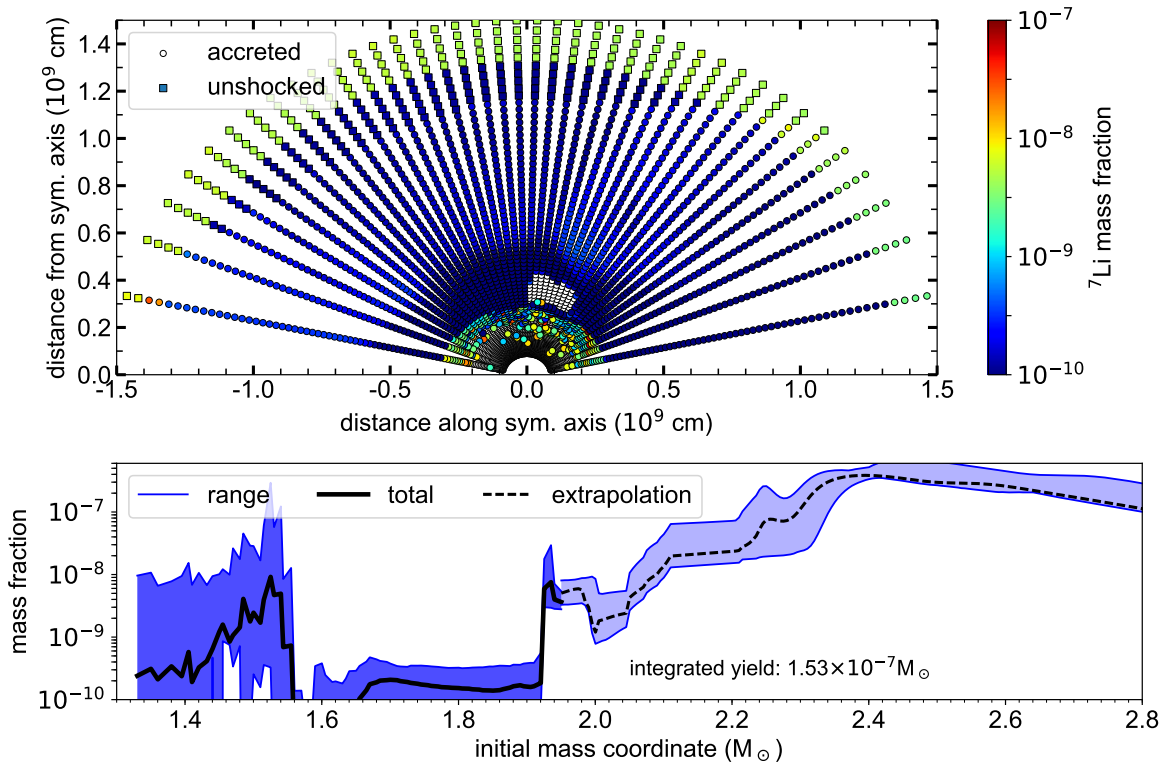


Figure 6.6.: Mass fraction of ${}^7\text{Li}$ for the tracer particles from a self-consistent axisymmetric supernova simulation. The upper panel shows the mass fraction as color code for the initial position of the tracer particles. The lower panel shows the total mass fraction as a function of initial mass coordinate and the spread between the maximum and minimum mass fractions for individual tracers is indicated by the shaded band.

defined by equation (5.7) are $T_{\nu_e} = 3.5$ MeV and $T_{\bar{\nu}_e} = 4.6$ MeV for the electron flavor neutrinos. The spectral temperature for the heavy flavor neutrinos and antineutrinos varies between 4.6 and 5.0 MeV depending on the angle. In total the neutrinos are more energetic than the what we find in the one-dimensional simulation used in Section 5.4.

6.3 Nucleosynthesis results

The motivation for the study of tracer particles is the question of possible effects of the ν process in the region of the α -rich freeze out that usually cannot be modeled reliably with one-dimensional calculations. The possibility of the light element production by the ν process in these innermost regions has already been hinted at by Nagataki et al. (1997) but has never been followed up on.

The composition of innermost zones is mostly given by nuclear statistical equilibrium (see section 2.1.5). Stellar structure then is important because it determines how fast the shocked material can expand. If the expansion is fast enough and low densities are quickly reached, the composition will reach an α -rich freeze-out. Figures 6.6 and 6.7 show the resulting mass fractions of ${}^7\text{Li}$ as a function of the initial position of the tracer particles and as projected onto the corresponding initial mass coordinate. We project everything onto the initial position because this makes it easy to distinguish the compositional layers. Note, that in a multi-dimensional calculation, the structure of the ejecta can deviate from this picture. Material from the deep interior can be ejected at high velocities and end up at larger radii

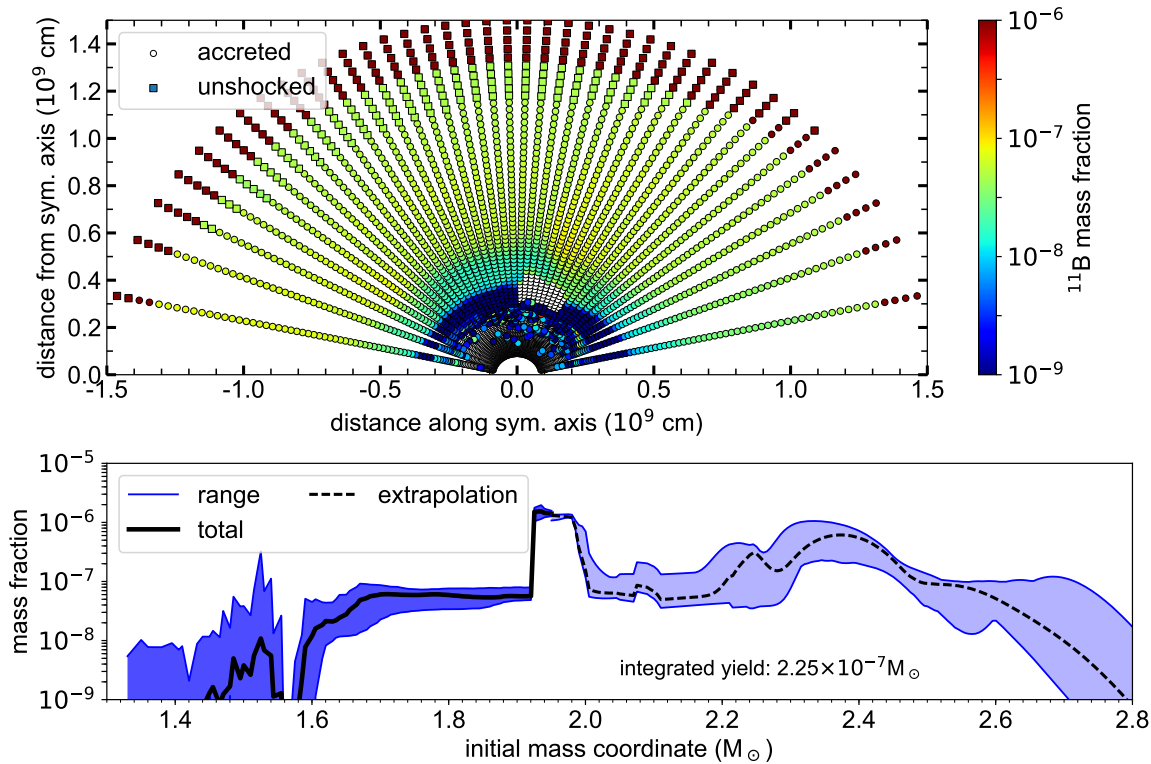


Figure 6.7.: Same as Figure 6.6 but for ^{11}B . The contribution from the innermost tracers is negligible compared to the production in the C shell.

in the final ejecta than material originally located in shells further out. This type of mixing has been observed in the supernova remnant Cassiopeia A (Grefenstette et al., 2014).

The total yield is calculated by combining the results of the tracer particles for the inner region with the average from the 1D calculations for the rest of the star. This continuation is shown as a dashed line in the lower panels of Figures 6.6 and 6.7. From these calculations we can first of all see that material from the α -rich freeze out, that gets enriched in ^7Li and ^{11}B is ejected. The contribution to the total yield from below $1.5 M_{\odot}$ is negligible for this progenitor model, in particular because the low effective explosion energies lead to very low peak temperatures in the He-shell that allow relatively large amounts of ^7Li and ^{11}B to survive in the outer layers. However, the lower panel of Figure 6.6 shows that even though the average mass fraction of ^7Li in the region of the α -rich freeze out is relatively low, there are individual tracer particles that lead to mass fractions larger than 10^{-7} , comparable to what is achieved in the He shell. For ^{11}B (see Figure 6.7) the contribution from the α -rich freeze-out is smaller than the production in the O/C shell, which is also partly covered by the simulation. From the upper panel of Figure 6.6 it is clear that the tracers that efficiently produce light elements are those located along the axis where the explosion is strongest. There are just a few tracer particles with large mass fractions of ^7Li of around 10^{-7} . Those tracers have first been ejected very fast and then decelerate to relatively low radial velocities between 400 and 1,600 km/s. Therefore, the material associated with these tracers is exposed longer to high neutrino fluxes when it has already reached regions with temperatures low enough for light elements to survive. Such tracer particles are on the edge of being ejected and depending on the dynamical evolution they might still fall back to the center. The removal of these rare cases would however not affect the integrated yields noticeably.

At the outer edge of the simulation domain, at the bottom of the O/C shell the average mass fractions smoothly match with our extrapolation results. From Figure 6.3 we see that only few columns along the axis have exceptionally large explosion energies while most are assigned rather low values in our extrapolation scheme. For the production of ^{11}B and ^7Li , the high explosion energy and associated high temperatures lead to the lowest yields, while the lower temperatures allow for larger yields. Since the majority of columns is described with a low energy, the average mass fraction is closer to the upper edge of the band shown in the lower panels of figures 6.6 and 6.7. For more energetic explosions, the production of light elements in the He-shell would also be more suppressed due to higher peak temperatures. In combination with our extrapolation method we find a production of radioactive ^{10}Be in the O/C shell that leads to a total amount of $3.49 \times 10^{-11} M_{\odot}$ to be ejected. This is about a factor 4 short of the yield required to explain the early solar system abundance (Banerjee et al., 2016). Since the simulation data reached up to the bottom of the O/C shell and the mass fraction at the interface matches very well we are confident that this yield is consistent with the explosion.

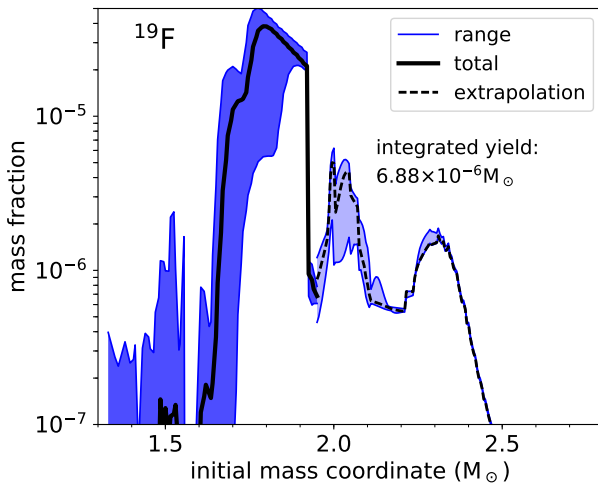


Figure 6.8.: ^{19}F mass fraction projected on the initial mass coordinate of the tracer particles. The ν process in the O/Ne shell dominates the production.

The final ^{19}F abundance is typically reached in less than 1.6 s which is the time domain covered by the simulation data. Hence, the result does not depend on the extrapolation of the evolution of the individual tracer particles. The production factor of 0.29 that is shown in Table 6.1 is in agreement with the finding that the ν process is not the most important contributor to the solar ^{19}F abundance. However, this value is now for the first time based on a fully self consistent supernova simulation, including consistent neutrino properties.

The production of ^{138}La and ^{180}Ta also occurs mostly in the O/Ne shells and is also covered by the simulation domain. The general pattern shown in Figure 6.4 is very similar to what we have found in the one-dimensional calculations. With and without neutrinos we find a peak of the mass fraction due to the γ process in explosive O/Ne burning. The low explosion energies lead to a small contribution of the γ process. The ν process is very efficient because only a small amount of ^{138}La and ^{180}Ta produced by neutrinos is destroyed by the shock passage and a large part of the O/Ne shell can contribute. The

Nucleus	Production factor
^7Li	0.28
^{11}B	0.98
^{15}N	0.11
^{19}F	0.29
^{138}La	1.30
$^{180}\text{Ta}^m$	1.96

Table 6.1.: Production factors for the ν process nuclei as discussed in section 5.2. ^{11}B , ^{138}La and ^{180}Ta are significantly overproduced.

The simulation domain covers most of the O/Ne shell which is the most important region for the production of ^{19}F by the ν process. In 5.2.3 we have shown that the main contribution to ^{19}F is in most cases a chain of thermonuclear reactions at the bottom of the He-shell. Due to the low explosion energy and the resulting low peak temperatures this mechanism is suppressed in this model. The final yield is determined almost entirely by the ν process in the O/Ne shell as illustrated by the profile in Figure 6.8. The production by the ν process still results in a production factor of 0.29, which is already relatively large compared to the average we find in our one-dimensional calculations (see Table 5.3). When looking at the angular distribution of the ^{19}F mass fraction, we find the lowest values for tracers along the symmetry axis that experience higher temperature and are ejected at higher velocities, reducing the neutrino exposure. The final

angular variation mostly affects the position of the inner edge of the production region that is set by the peak temperatures. The higher peak temperatures along the symmetry axis results in lower ^{138}La and ^{180}Ta mass fractions. In the upper part of the O/Ne shell the mass fraction is almost angle independent. In total this leads to an overproduction of both of these nuclei as shown in Table 6.1.

Table 6.1 summarizes the production factors normalized to ^{16}O for the ν process nuclei for this model. Taking into account that only a fraction of about 30% of the solar abundance of ^{11}B need to be accounted for by the ν process, while the rest can come from GCR irradiation, we find a production that is too large. The total yield of ^{11}B depends significantly on the production in the regions that are not covered by the simulation data and hence this is sensitive to the extrapolation. However, the production regions of ^{138}La and ^{180}Ta are completely included in the computational domain of the simulation and we also find a production that is larger than solar. This large production is possibly related to the nature of two-dimensional simulations. It has been found, that two-dimensional supernova models cannot properly describe turbulent energy cascades. The propagation of energy from small to large scales is exaggerated in 2D simulations which makes a successful explosion more likely (Kraichnan, 1967; Hanke et al., 2012; Couch, 2013; Couch & Ott, 2015) and in most cases faster to develop. In the absence of long lasting accretion flows that increase the energy of the explosion even after the shock has been launched (Müller, 2015) this leads to a tendency towards too low explosion energies. Higher temperature due to a more energetic explosion in turn would reduce the efficiency of the ν process and could ameliorate the overproduction of ^{11}B , ^{138}La and ^{180}Ta .

Additionally, a more reliable comparison to solar abundances requires a sufficient range of progenitor models because we can not expect to explain the chemical composition of the solar system with a single supernova explosion. As we have found in our one-dimensional calculations, low mass stars in general tend to overproduce ^{11}B .

Despite the caveats described above, we find two major conclusions. First, even though ^7Li and ^{11}B are found to be produced in the material from the α -rich freeze-out below the one-dimensional mass, this contribution is insignificant for the integrated yield, compared to the production in the C- and He shell. This means that we do not expect major changes of the expected yields predicted by one-dimensional simulations. Secondly, we can confirm that the ν process efficiently produces ^{138}La and ^{180}Ta in the O/Ne shell also in self-consistent supernova models. Also for these nuclei we do not find significant deviations of the averaged profiles and the integrated yield from the results of the one-dimensional models.

7 The νp process in neutrino driven winds

So far we have discussed the subtle effects of neutrinos during the explosive nucleosynthesis in core collapse supernova explosions. In this Section we further discuss the νp process in proton-rich neutrino driven winds, where the neutrinos are the dominant factors to determine the nucleosynthesis. In the aftermath of a supernova explosion the strong neutrino fluxes from the cooling proto-neutron star are expected to drive a mass outflow from the surface of the PNS. Even though this neutrino driven wind (NDW) would contribute only about $10^{-4} - 10^{-3} M_{\odot}$ to the total mass of ejected material, it is a potential site of very interesting nucleosynthesis. Modern simulations show that neutrino driven winds are most likely proton rich (Martínez-Pinedo et al., 2014), in particular in the late phase. Under these conditions, elements heavier than Iron can be produced via the νp process as discussed in Section 3.4.3. The nucleosynthesis in this scenario involves many neutron deficient nuclei far away from the valley of stability.

The properties of such nuclei are often not known and are in many cases based on extrapolations or completely on theoretical predictions. One of the important ingredients to nucleosynthesis are the nuclear masses. The masses affect the Q-values of the involved reactions, in this case especially the proton separation energies S_p , that determine the speed of the (p, γ) reactions that are here in competition with (n, p) . Additionally, the neutrino driven wind is ejected from very hot conditions and here the nuclear masses determine the initial composition in nuclear statistical equilibrium (NSE). As indicated in Section 5.3.2 the NDW could contribute a significant amount of ^{92}Nb to complement the production of the νp process and we find that this contribution is affected by recently determined nuclear masses and also by the inclusion of neutrino-induced spallation reactions.

To complete our picture of the role of neutrinos in supernova nucleosynthesis we want to discuss three aspects in the context of the neutrino driven winds in this section. First, we discuss the impact of recently measured masses on the νp process path and secondly we discuss the production of ^{92}Nb and other p -nuclei and combine the results with the supernova yields from Section 5.2. Before we discuss the nucleosynthesis results we introduce the model for the thermodynamic conditions. For the evolution of temperature, density and radius as well as for the initial composition (NSE) that is determined by Y_e , we use the results of a two-dimensional core-collapse supernova simulation

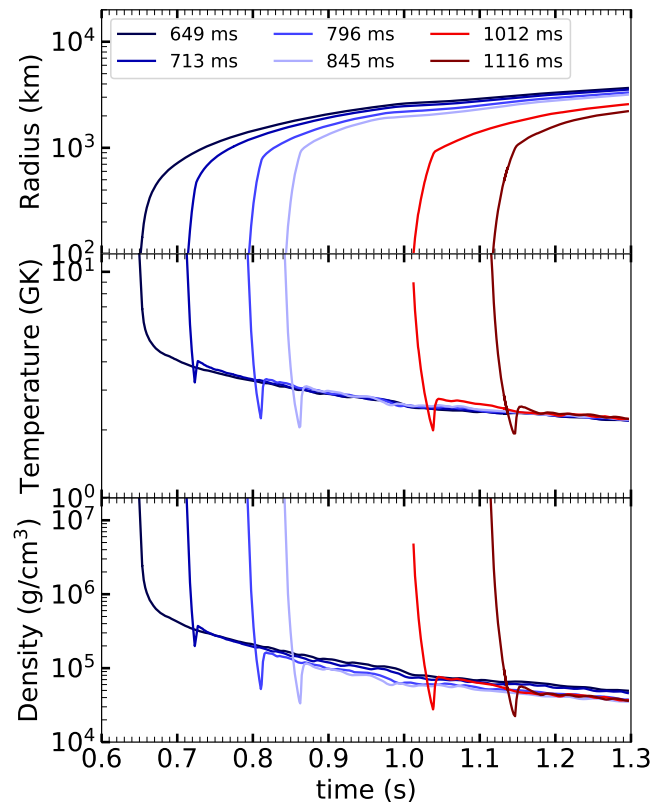


Figure 7.1.: Radius, temperature and density evolution for the neutrino driven wind models from a simulation by Janka et al. (2003).

of a $15 M_{\odot}$ star by [Janka et al. \(2003\)](#) (c.f. [Buras et al. \(2006\)](#) for details) including spectral neutrino transport. These calculations include neutrino transport in the “ray-by-ray plus” scheme but the explosion was only achieved by omitting velocity dependent terms corresponding to radiation compression, Doppler shift and fluid acceleration. Advection of neutrinos with the motion of the fluid is included. The neutrino driven winds appear in the late phase of the proto-neutron star evolution. The two-dimensional simulation follows the evolution for up to almost 468 ms after core-bounce. To follow the cooling phase of the proto-neutron star the results were then mapped to a one-dimensional grid and further evolved including then also the previously omitted term in the neutrino transport. The simulation then follows the evolution until 1.3 seconds. This includes the important collision of the supersonic wind with the slow moving supernova ejecta.

ejection time (ms)	Δ_n	initial Y_e
649	0.87	0.551
713	1.64	0.558
796	2.33	0.560
845	1.98	0.559
1012	10.25	0.600
1116	13.90	0.600

Table 7.1.: Values of Δ_n as defined in equation (7.1) and initial electron fraction Y_e for the six wind trajectories studied here. The latest ejecta are the most suitable for the synthesis of heavy elements.

Figure 7.1 shows the temperature, density and radius evolution for the NDW scenario we use in this section. Table 7.1 gives the initial values of the electron fraction. In all cases the wind is proton rich. The trajectories are classified by the time at which the material is ejected from the PNS. Due to their high velocity at which the material is launched, the expansion is first very fast and the temperature decreases rapidly. As soon as wind material collides with the earlier supernova ejecta, the expansion slows down and a reverse shock is formed, re-heating the matter. For the earliest wind phase the wind termination is relatively smooth, i.e. no significant heating occurs. For the trajectories considered here, the collision occurs at temperatures between 2 and 4 GK. The radius at which the collision occurs determines the neutrino flux and thus the potential to produce further neutrons after wind termination.

The idealized hot r -process proceeds along a path defined by (n, γ) - (γ, n) equilibrium [Qian \(2003\)](#) and most heavy nucleus that can be produced can already be estimated from the initial neutron-to-seed ratio. In the νp -process such a judgment is complicated by the competing timescales of (p, γ) and (n, p) reactions and the fact that the process does not end necessarily with the exhaustion of protons but as soon as the temperature is too low for proton captures or when the neutrino irradiation ends. The timescale of the (n, p) reactions is very sensitive to the neutrino flux and energies. Therefore, [Pruet et al. \(2006\)](#) have introduced the quantity

$$\Delta_n = \frac{y_p n_{\bar{\nu}_e}}{y_h} \quad \text{with} \quad n_{\bar{\nu}_e} = \int_{T_9 < 1.5} \lambda_{\bar{\nu}_e} dt \quad (7.1)$$

can be used to judge how suitable the conditions are for the νp process. This gives an estimate for how many neutrons can be produced by neutrinos after the temperature has dropped below 1.5 GK. This plays a similar role as the neutron-to-seed ratio for the r -process. Table 7.1 shows the values of Δ_n for the trajectories we study here, showing that we can expect the latest ejecta to exhibit the strongest νp process. This is also what we find in the final abundances shown in Figure 7.2.

The nucleosynthesis and in particular the νp process has already been studied for this simulation by [Pruet et al. \(2006\)](#). Their study has shown that the thermodynamic trajectories provide conditions suitable for the νp process. [Weber et al. \(2008\)](#) have also used the same model to study the effect of the newly measured masses. We follow the approach presented by [Pruet et al. \(2006\)](#) and recover most of their results.

flavor	$L_\nu(\text{erg/s})$	$\langle E_\nu \rangle$ (MeV)
ν_e	21.5×10^{51}	13.32
$\bar{\nu}_e$	21.5×10^{51}	15.94
$\nu_{\mu,\tau}, \bar{\nu}_{\mu,\tau}$	24.5×10^{51}	15.44

Table 7.2.: Neutrino properties for the νp process calculations. Since the wind expansion timescale is much shorter than the timescale of changes of the neutrino properties, we assume them to be constant here.

In order to follow the complete nucleosynthesis we still need to extrapolate the simulation data to later times. We employ the description used in reference [Wanajo et al. \(2011\)](#). Assuming an adiabatic expansion we find $\rho \propto T^3$ and extrapolate as

$$\rho(t) = \rho_0 \left(\frac{t}{t_0} \right)^{-2} \quad \text{and} \quad T(t) = T_0 \left(\frac{t}{t_0} \right)^{-2/3} \quad (7.2)$$

where ρ_0 and T_0 are the last points of the simulation data. In addition to the evolution of temperature and density, the radius is important because it determines the neutrino fluxes. While [Pruet et al. \(2006\)](#) have assumed a constant expansion velocity after the end of the simulation data, we follow again [Wanajo \(2006\)](#); [Wanajo et al. \(2011\)](#). From the last ten time steps of the simulation data we determine an initial velocity u_0 . With this we describe the evolution of the velocity as decelerating towards an asymptotic value

$$u(t) = u_0 \left[1 - \frac{u_0 t_0}{r_0} + \frac{u_0 t_0}{r_0} \left(\frac{t}{t_0} \right)^3 \right]^{-2/3} \times \left(\frac{t}{t_0} \right)^2 \quad (7.3)$$

This corresponds to an evolution of the radius as

$$r(t) = r_0 \left[1 - \frac{u_0 t_0}{r_0} + \frac{u_0 t_0}{r_0} \left(\frac{t}{t_0} \right)^3 \right]^{1/3}. \quad (7.4)$$

This description is based on the assumption of a constant mass outflow rate $\dot{M} = 4\pi r^2 \rho u = \text{const.}$ ([Wanajo, 2006](#)). The expansion timescale of the neutrino driven wind is short compared to the timescale of changes in the neutrino properties during the cooling phase. Therefore, following also the approach of [Pruet et al. \(2006\)](#), we assume the neutrino luminosities and energies to be constant. The values are shown in Table 7.2. [Pruet et al. \(2006\)](#) have extracted these values from the simulation at around 1 s. However, the neutrino properties given in [Pruet et al. \(2006\)](#) have been recorded at a radial position of 500 km. The wind trajectories start at around 80 km and therefore we correct the energies and luminosities for the geometrical flux factor and gravitational redshift following the approach by [Thompson et al. \(2001\)](#).

In addition to the modeling of the thermodynamic trajectory, we need to adjust the nuclear reaction network to include more nuclei on the neutron deficient side of the nuclear chart. For these calculations we include 2608 nuclei in the reaction network.

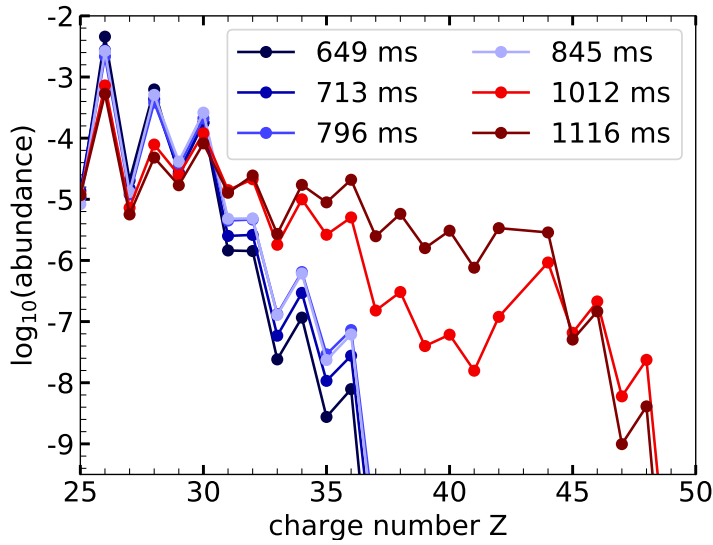


Figure 7.2.: Elemental abundances for the nucleosynthesis of the wind trajectories shown in Figure 7.1. The later ejecta produce more heavy elements. Note that there is no stable isotope of Tc ($Z=43$).

7.1 Impact of new experimental masses for neutron deficient Zr, Y and Nb isotopes

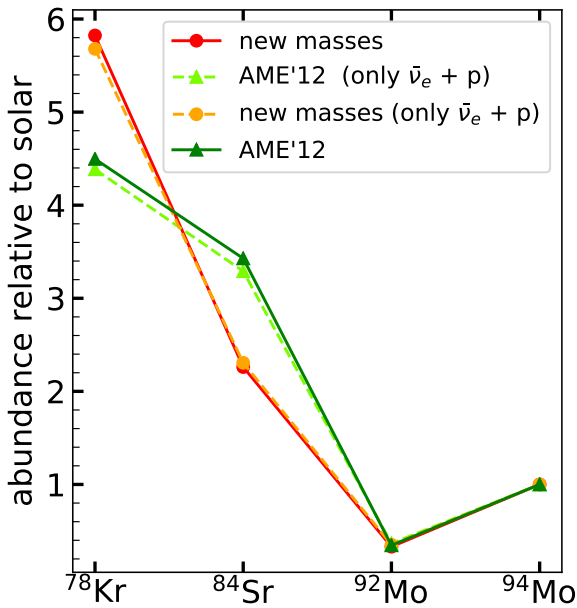


Figure 7.3.: Abundances of several p nuclei that are expected to have contributions from the NDW. The results of the calculations are normalized to the solar abundances of ^{92}Mo .

measurements have been adopted by the most recent Atomic Mass Evaluation 2016 (Huang et al., 2017). Extrapolating the systematics of two-neutron S_{2n} and two-proton S_{2p} separation energies, the masses of ^{78}Y , ^{80}Zr , ^{82}Nb , ^{84}Mo could also be estimated with significantly reduced uncertainty. The new ex-

The νp process involves many nuclei far away from stability and only modern experimental techniques are able to provide precise values for their properties. In this section we discuss the impact of a set of newly measured masses that affect the nucleosynthesis of p -nuclei in neutrino driven winds. Weber et al. (2008) have discussed the impact of newly measured masses of neutron deficient Tc, Ru, Rh and Pd isotopes. Despite rather moderate changes of the masses compared to extrapolated values of typically around a few hundred keV, significant effects on the reaction flows were identified. In a similar manner we explore here the impact of the nuclear masses of ^{79}Y , $^{81,82}\text{Zr}$ and $^{83,84}\text{Nb}$ that have been measured with isochronous mass spectroscopy at the experimental storage ring CSRe at Lanzhou (Hirfl-Csr Group et al., 2010; Xia et al., 2002). The ions of interest were produced by projectile fragmentation of the ^{112}Sn primary beam on a ^9Be target and then injected into the storage ring where the revolution time was measured with a dedicated timing detector (Mei et al., 2010). With this setup the nuclear masses could be determined with an accuracy of less than 150 keV. The results of these

Isotope	M_{ex} (MeV) AME12	M_{ex} (MeV) experiment	ΔS_p (keV)
^{79}Y	-58.360	-57.803	-557
^{81}Zr	-58.400	-57.524	-876
^{82}Zr	-63.940	-63.632	-308 [#]
^{83}Nb	-58.410	-57.613	-489 [#]
^{84}Nb	-61.020	-61.219	+199 [#]
$^{78}\text{Y}^{\#}$	-52.530	-52.397	-133 [#]
$^{80}\text{Zr}^{\#}$	-55.520	-54.176	-787 [#]
$^{82}\text{Nb}^{\#}$	-52.200	-51.790	+466 [#]
$^{84}\text{Mo}^{\#}$	-54.500	-53.958	+255 [#]

Table 7.3.: Values for mass excess M_{ex} from [M. et al. \(2012\)](#) and the new values from [Xing et al. \(2018\)](#) and the change of proton separation energies $\Delta S_p = S_p^{\text{new}} - S_p^{\text{AME12}}$ with respect to AME'12. Isotopes marked with # are extrapolations based on the new data as explained by [Xing et al. \(2018\)](#).

perimental values compared to the Atomic Mass Evaluation 2012 are shown in Table 7.3. The largest changes of proton separation energies result for ^{81}Zr and ^{83}Nb . Those changes have the largest impact on the nucleosynthesis. Based on these masses we have re-calculated the reaction rates for (p, γ) , (α, γ) , (p, α) and (n, p) reactions and their reverse reactions with a statistical model nuclear reaction code ([Koning et al., 2007](#)). Details of the experiment and the implications for the rp - and νp process are also discussed in [Xing et al. \(2018\)](#). Here we give more details about the effect on the νp process.

In order to evaluate the effects that the new measurements have on the νp process, we compare to reaction rates based on the masses of the Atomic Mass Evaluation 2012 (AME'12, [M. et al. \(2012\)](#)) because the measured masses are already included in the more recent Atomic Mass Evaluation 2016. To exclude effect from different ways of calculating the cross-sections, we also re-calculate the reaction rates within the same framework ([Koning et al., 2007](#)), with the same input parameters for the masses from AME'12. Our calculations show that the new masses mainly have an effect on the mass fractions in the mass region of $A = 76 - 86$. Figure 7.3 shows the final abundances for the p -nuclei in this mass region integrated over the six trajectories discussed above, relative to their solar abundances. Since we cannot tell how much of the solar material has been enriched by such as scenario we can scale the abundances by a constant factor. The new masses affect neither ^{92}Mo nor ^{94}Mo significantly and we normalize the results to its abundance. In our calculation ^{94}Mo is more abundant than ^{92}Mo which is contrary to what is observed in the solar abundances, where ^{92}Mo is almost 70% more abundant than the heavier isotope. This trend has been observed in previous studies and the production of ^{92}Mo may require a contribution from slightly neutron-rich winds with Y_e values between 0.47 and 0.49 ([Hoffman et al., 1996](#); [Wanajo, 2006](#)).

The new masses have significant effects on the production of the light p -nuclei ^{78}Kr and ^{84}Sr which are among the most abundantly produced heavy nuclei in this scenario, as shown in Figure 7.6. The final abundance of ^{78}Kr increases due to the reduced proton separation energy of ^{79}Y which decreases the $^{78}\text{Sr}(p, \gamma)$ rate enhancing the production of ^{78}Sr which is the progenitor of ^{78}Kr . Furthermore, the abundance of ^{84}Sr , which appears overproduced with respect to the Mo isotopes in our calculations, is reduced.

Figures 7.4 and 7.5 show the reaction flows in this region, comparing the calculations with the previously estimated masses and the new experimental masses. The most important flows are due to (p, γ) and (n, p) reactions. Additionally (n, α) reactions play a role. The change in the final abundance of ^{84}Sr is largely related to the decrease of the proton separation energy of ^{83}Nb by around 500 keV. As a consequence, the largest reaction flow changes from $^{82}\text{Zr}(p, \gamma)^{83}\text{Nb}(p, \gamma)^{84}\text{Mo}$ to $^{82}\text{Zr}(p, \gamma)^{83}\text{Nb}(n, p)^{83}\text{Zr}(p, \gamma)^{84}\text{Nb}$. Hence, ^{84}Nb becomes the progenitor of ^{84}Sr with the new masses instead of ^{84}Mo with the AME12 masses. This change alone will lead to a substantial decrease in the production of ^{84}Sr . However, it is partly compensated by an increase in the proton separation energy

of ^{82}Nb that allows for the reaction sequence $^{81}\text{Zr}(p, \gamma)^{82}\text{Nb}(n, p)^{82}\text{Zr}$, feeding into the reaction chain described above. The proton separation energies of ^{82}Nb is based on extrapolation and rather close to the value defining the νp process path assuming $(p, \gamma) \rightleftharpoons (\gamma, p)$ equilibrium, which is about 1.65 MeV for the conditions considered here. Therefore, a experimental determination will be highly welcome. The reduced proton separation energy of ^{79}Y leads to a weaker flow through ^{79}Y and increases the flow to ^{78}Rb . This results in an increase of the final abundance of ^{78}Kr .

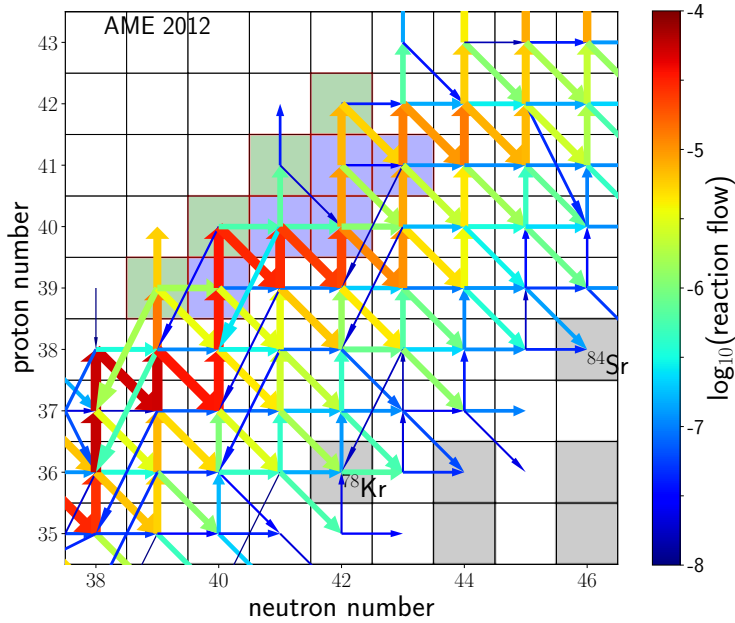


Figure 7.4.: Reaction flows affected by the newly measured masses but here with reaction rates based on the masses from AME 2012. The reaction flows have been integrated over the first 200 seconds and do not include β decay and electron capture flows. All diagonal reactions flow are therefore due to (n, p) reactions. The nuclei for which the new experimental values for the masses have been obtained are marked red. Those, for which new extrapolated masses are now available are in green. The stable nuclei are in gray. Here the flow goes to ^{84}Mo which will finally decay to ^{84}Sr .

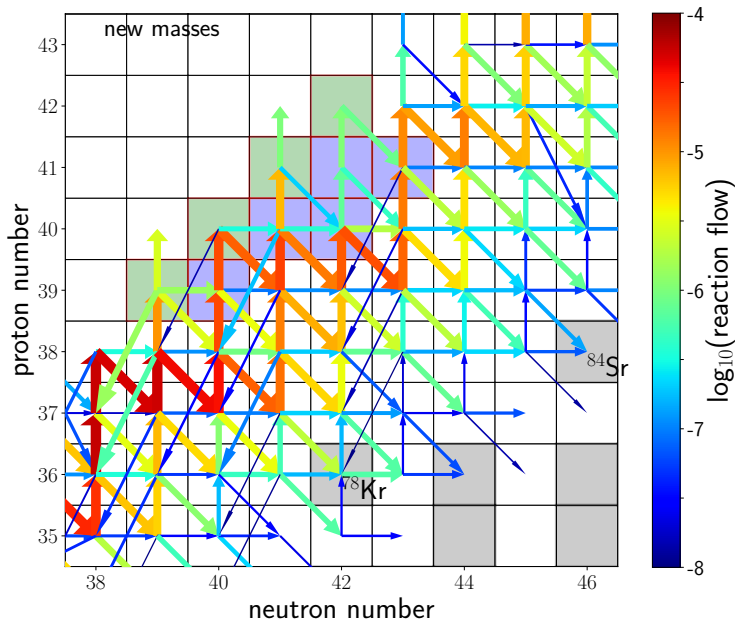


Figure 7.5.: Same as Figure 7.4 but with the reaction rates based on the new nuclear masses. There is now very little flow to ^{84}Mo . Instead the flow through ^{84}Nb is enhanced. The flow to ^{82}Nb is also significantly increased. A weaker flow through ^{79}Y increases the flow to ^{78}Rb , that gives the increase in the production of ^{78}Kr

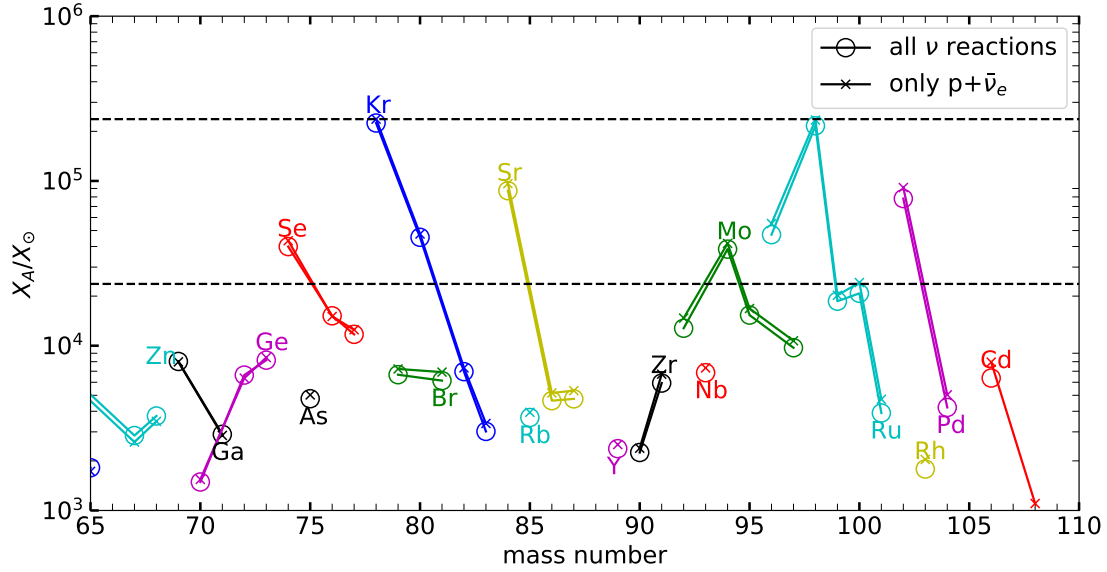


Figure 7.6.: Comparison of the νp process yield with and without including the full set of neutrino reactions. $\bar{\nu}_e + p$ is always included. Isotopes of the same elements are connected by lines and marked with the same color. The abundances are divided by their solar values and the dashed lines indicate the range of a factor 10 down from the most abundant species.

7.2 Production of ^{92}Nb

The effect of including a full set of neutrino-nucleus reactions in calculations of the νp -process has already been discussed to some extent in by [Huther \(2014\)](#) for a different setup of wind conditions leading to the conclusion that there is no significant impact of the neutrino reactions. The additional release of free neutrons due to spallation reactions is negligible compared to the production of free neutrons from neutrino reactions on free protons, because protons are much more abundant than heavy nuclei. However, spallation reactions on ^4He , which is also very abundant in the α -rich freeze out, lead to the production of ^3H which can induce the reaction chain $^3\text{H}(\alpha, \gamma)^7\text{Be}(\alpha, \gamma)^{11}\text{C}$, bypassing the triple- α bottle-neck reaction for the production of heavier nuclei. This reaction lead to a reduction of the ratio of free particles to seeds. Therefore, [Pruet et al. \(2006\)](#) have also included neutrino reactions on ^4He and we also find that this is the most important part of the effects due reactions on nuclei. For the trajectory launched at 1116 ms, we find that the final abundance of ^{12}C is increased by more than a factor two to 4.4×10^{-6} by the neutrino reactions on α particles. This increased number of intermediate mass are ideal targets for proton capture reactions because of the lower Coulomb barrier compared to the Fe group nuclei. Therefore, including the spallation reactions decreases the supply of free protons faster, and hence the supply of neutrons, particularly at late times. As This effect does not introduce significant changes in the overall abundance pattern of p -nuclei after decay, as can be seen in Figure 7.6

However, we find that it does indeed affect the production of ^{92}Nb . Since we have already extensively discussed the production of ^{92}Nb in the ν -process and the γ -process, we want to complete the picture here with the contribution from the νp -process in neutrino driven winds. Just as in the case of neutron capture nucleosynthesis, the production of ^{92}Nb in proton rich nucleosynthesis is also problematic because it is shielded from the decay of neutron deficient nuclei by the stable isobar ^{92}Mo . Therefore, ^{92}Nb cannot be produced in the rp -process. Instead, ^{92}Nb requires neutron captures on ^{91}Nb . The progenitor of ^{91}Nb in the νp process is ^{91}Ru with a half-life of 8 s. Once ^{91}Ru is available, the production of ^{92}Nb first requires a sufficient supply of neutrons to get to ^{91}Nb via (n, p) and even more for $^{91}\text{Nb}(n, \gamma)$. Therefore, the final abundance of ^{92}Nb is sensitive to the neutron abundance at late times. The reaction

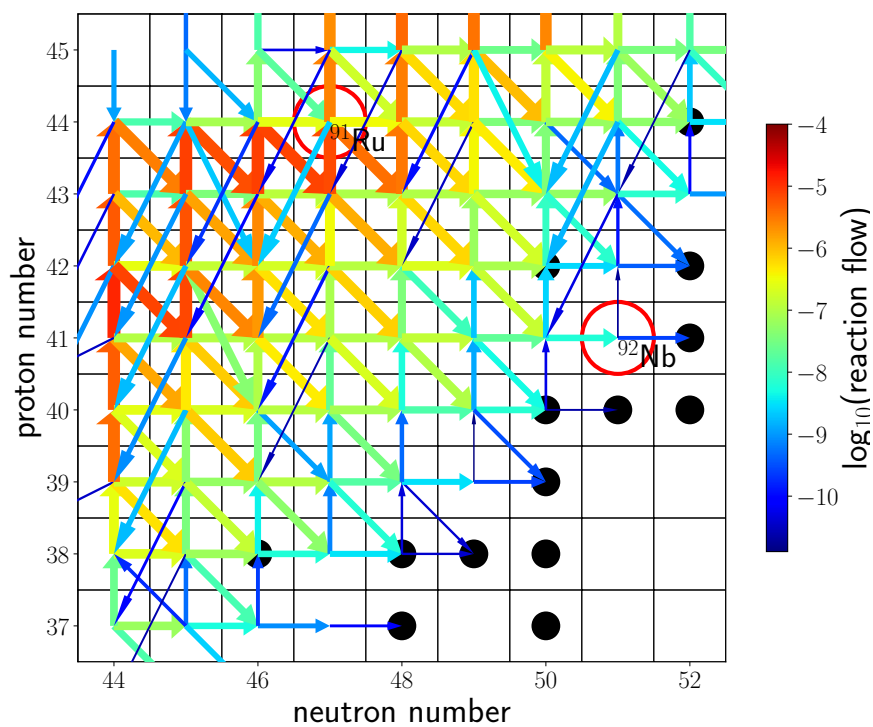


Figure 7.7.: Time integrated reaction flows contributing to ^{92}Nb for the 1116 ms ejecta and reaction rates based on the new masses. Filled black circles mark the stable isotopes. ^{92}Nb is shielded from the decay of neutron deficient nuclei by ^{92}Nb and only a small branch from $^{91}\text{Nb}(n, \gamma)$ contributes.

masses	only $\bar{\nu}_e + p$	incl. ${}^4\text{He}(\nu, \nu'np)$	incl. only c.c. reactions	incl. all reactions
AME'12	9.04	6.99	8.95	5.6
new masses	8.40	6.51	8.33	5.2

Table 7.4.: Integrated yield of ${}^{92}\text{Nb}$ in units of $10^{-10} M_{\odot}$. The combined effect of including all neutrino reactions and the new masses decreases the yield by almost a factor of two.

flows are illustrated in Figure 7.7 for the late 1116 ms wind trajectory. This case provides the largest abundance of Ru isotopes in the end (see Figure 7.2) and is the only case where we find a significant production of ${}^{92}\text{Nb}$. Table 7.4 illustrates the sensitivity of the ${}^{92}\text{Nb}$ yield to the nuclear masses on the one hand on to the inclusion of more neutrino reactions. This shows that the spallation reactions on ${}^4\text{He}$ have the largest impact. The most relevant nucleus for the yield of ${}^{92}\text{Nb}$ is the production of ${}^{91}\text{Ru}$ which is already quite far from the region of masses that have now been measured. Therefore, ${}^{92}\text{Nb}$ is only marginally affected by the slight reduction of the reaction flow through ${}^{83}\text{Nb}$. The effect of the additional neutrino reactions is however quite significant. Including all the neutrino reactions reduces the ${}^{92}\text{Nb}$ yield by almost a factor of 2. Neutrino spallation reactions on ${}^4\text{He}$ effectively reduce the amount of free protons and hence the production of neutrons. Therefore, (n, p) reactions are reduced and the less material arrives in ${}^{91}\text{Nb}$ before the neutrino irradiation ceases. We find that the maximum ${}^{91}\text{Nb}$ abundance reached at around 10s is reduced by almost 40% when the spallation reactions are included. Additionally, the abundance of neutrons is reduced by 15% at that time, inhibiting ${}^{91}\text{Nb}(n, \gamma)$. This results in the reduction of the ${}^{92}\text{Nb}$ abundance shown in Table 7.4. We find a significant production of ${}^{92}\text{Nb}$ only in one of the six wind trajectories. This shows that the production is quite sensitive to the conditions and we cannot expect it to give a robust contribution when we consider a range of stars.

In the context of the late input scenario discussed in Section 5.3.2 the ${}^{92}\text{Nb}$ yields we find here are very important. We have seen in Section 5.3.2 that even with the ν process enhancement the $13 M_{\odot}$ model does not yield a sufficient amount of ${}^{92}\text{Nb}$ to explain the ${}^{92}\text{Nb}/{}^{93}\text{Nb}$ ratio found in meteoritic grains for values of the delay time Δ and the dilution factor f that would be in agreement with previous studies. However, adding now the contribution from the νp -process with the yields given in Table 7.4 overproduces ${}^{92}\text{Nb}$ for $\Delta = 1 \text{ Myr}$ and $f = 5 \times 10^{-4}$. The lowest yield here still corresponds to an estimated ratio of ${}^{92}\text{Nb}/{}^{93}\text{Nb}$ in the early solar system of 12.5×10^{-5} . Scaling the wind contribution down by a factor 0.1 we can get a good agreement with the observed ratio of 1.6×10^{-5} . The neutrino luminosities for the wind scenario we study here are relatively high and most modern simulations, such as the cases discussed in Section 5.4, would suggest lower luminosities. Therefore, it seems reasonable to take our results as an upper limit. Furthermore, we consider here only proton rich conditions and ${}^{92}\text{Nb}$ may have further contribution from the early, neutron-rich wind phase (Hoffman et al., 1996).

From equation 5.3 there is a value of f for any value Δ such that the observed ratio is reproduced for any given yield of the radioactive isotope Y_R . Hence, this condition alone does not allow to pin down the parameters. However, if one event that is characterized by one particular combination of f and Δ is responsible for the enrichment of the early solar system with short-lived radioactive isotopes, this event is required to reproduce the ratios for all of the SLRs at once. The combination of these constraints gives a very stringent condition for the viability of a given model. Figure 7.8 illustrates this approach. It shows the possible combinations of f and Δ to reproduce the measured isotopic ratios of several short-lived radionuclei. From the uncertainties in the determination of the pre solar ratios, the error bands are calculated. We find that with a contribution of the neutrino driven wind multiplied by a factor 0.1, we can find a combination of f and Δ to reproduce the inferred ratios of ${}^{92}\text{Nb}$, ${}^{36}\text{Cl}$, ${}^{41}\text{Ca}$ and ${}^{107}\text{Pd}$ at the same time. These values also satisfy the constraints on ${}^{98}\text{Tc}$. However, ${}^{10}\text{Be}$ is not sufficiently produced. For this model we also find an amount of ${}^{53}\text{Mn}$ that is by far too large and would formally require $f > 1$. However, ${}^{53}\text{Mn}$ is produced in the innermost layer and can be affected significantly by fallback as suggested by Banerjee et al. (2016), which we do not consider here. The neutrino driven

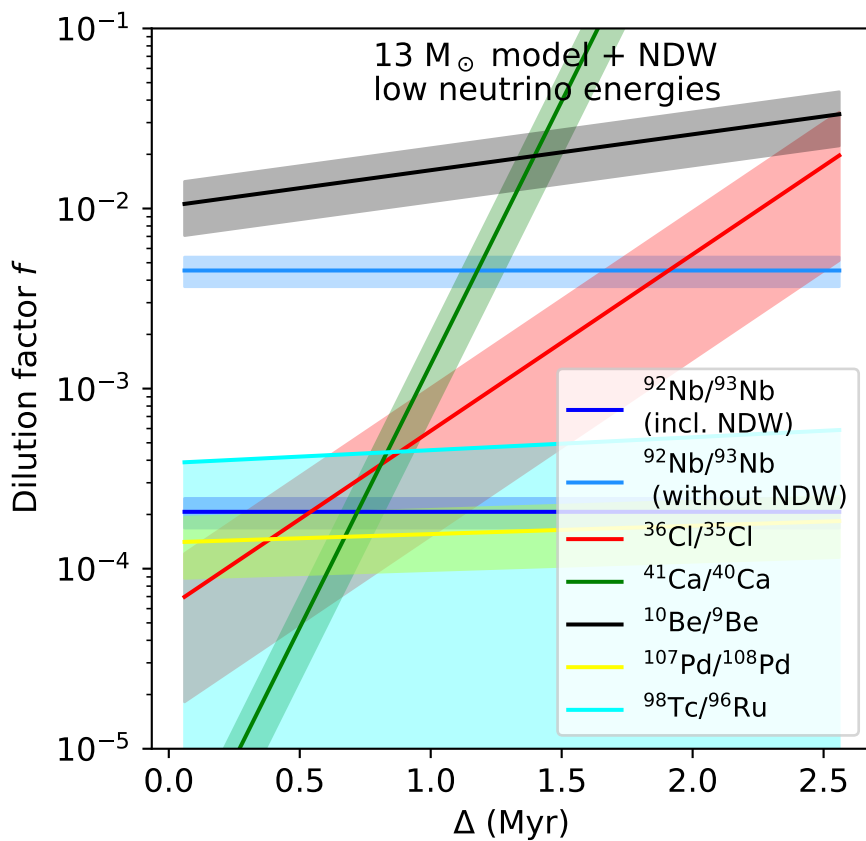


Figure 7.8.: Values of Δ and f that reproduce the measured isotopic ratios within their respective error bars. In many cases as suitable combination of Δ and f can be found but agreement between several ratios is required for a realistic scenario. Here we have added 10% of the NDW contribution to ^{92}Nb .

wind contribution is not very sensitive to the progenitor mass and could be similar for a less massive star that could produce more ^{10}Be and less ^{53}Mn .

7.3 Combined nucleosynthesis

Finally, we can combine our results from the neutrino driven wind with the supernova nucleosynthesis including the γ process, ν process and the νp process to explore the role of supernovae for the solar abundances of the so-called p -nuclei. The yields from the NDW calculations with the new masses and the full set of neutrino-induced reactions are added to the IMF averaged supernova yields from Section 5.2. This assumes that the NDW is independent of the progenitor star.

Another promising scenario for the production of a range of p -nuclei are type Ia supernovae, which are thermonuclear explosions that are commonly associated with the accretion of material on white dwarfs, see [Thielemann et al. \(2004\)](#) for a recent review. The numerical modeling of type Ia supernova has recently been significantly improved by [Röpke \(2005\)](#), leading to the first multi-dimensional explosion models [Röpke & Niemeyer \(2007\)](#). [Travaglio et al. \(2011\)](#) have studied the nucleosynthesis for two-dimensional simulations of delayed detonation and deflagration models, assuming that the white dwarf is enriched in s -process material during the accretion phase. This enrichment provides in their calculations the seeds for an efficient γ -process and that efficiently produces most of the heavy p -nuclei (see also [Travaglio et al. \(2014\)](#)). For comparison Table 7.5 shows the production factors normalized to ^{144}Sm for all the 35 p -nuclei. Recently, [Travaglio et al. \(2018\)](#) have combined core collapse supernova nucleosynthesis with contributions from type Ia supernovae but without including neutrino driven winds and with the standard setup of high neutrino energies. We cannot draw conclusions at the same level here because we do not include the dynamics of a chemical evolution model and only look at stars with solar metallicity, but we can make some general observations.

Without the explosive nucleosynthesis induced by the supernova shock, most of the p -nuclei are not produced to a significant fraction of the solar abundances. ^{84}Sr is produced by several progenitors already during hydrostatic O and Ne burning. While most of it is located below the mass cut and a significant amount is destroyed by the shock, it is also re-created during explosive burning. Hence, the production is sensitive to the explosion dynamics and fallback. With additional contributions from the neutrino driven wind and type Ia supernovae, we find the overproduction is even increased. The newly measured masses discussed in Section 7.1 only slightly ameliorate this problem and as suggested by [Wanajo et al. \(2011\)](#), a mechanism or an update of nuclear properties seems necessary to reduce the yield. For ^{74}Se the explosive burning leads to an increase of the yield and just as ^{84}Sr it is mostly located in the innermost layers and is sensitive to fallback and details of the explosion dynamics. However, even if the supernova nucleosynthesis contribution was reduced, the neutrino driven wind results in an overproduction by itself. While the mass fraction of ^{78}Kr is increased by a factor 1000 in the O/Ne shell, the yield is dominated by a contribution for O-burning. The overproduction of ^{78}Kr in NDWs is increased further by the recently measured masses as discussed in Section 7.1.

We find $(^{92}\text{Mo}/^{94}\text{Mo}) < 1$ and it has been found before ([Wanajo, 2006](#); [Pruet et al., 2006](#)) that the νp process can produce ^{94}Mo but not ^{92}Mo in sufficient amounts. However, ^{92}Mo could have further contribution from a neutron-rich wind outflow ([Hoffman et al., 1996, 1997](#)) that we have not considered here. In [Travaglio et al. \(2018\)](#) the final abundances of ^{92}Mo and ^{94}Mo including a detailed calculation of galactic chemical evolution exhibit almost the solar ratio, but are underproduced with respect to the solar value in absolute terms by more than a factor 3. This also suggests a the need for an additional source. Note, that [Fisker et al. \(2009\)](#) and also [Bliss et al. \(2018\)](#) have concluded that the NDW cannot account for the full solar abundances of ^{92}Mo and ^{94}Mo . Here it is also important that the νp process in the NDW is a primary process that would not depend directly on the initial metallicity of the star. The light p -nuclei up to ^{106}Cd can be produced to solar proportion or even more by Supernova nucleosynthesis including the neutrino driven winds. However, [Travaglio et al. \(2015\)](#) also find a significant production of these nuclei in type Ia supernovae and in particular ^{84}Sr is overproduced in all cases. In

contrast to the overproduction of the light p -nuclei, many of the heavier p isotopes are barely produced to solar proportions. Type Ia Supernovae are clearly the favored site for $^{130,132}\text{Ba}$, $^{124,126}\text{Xe}$. For ^{144}Sm we could also find a production to half of the solar abundance but note that this production is secondary, i.e. it requires the presence of seed for the γ -process that are provided here by the initially solar composition. For lower metallicity, this contribution would be reduced accordingly. In core-collapse supernovae the heaviest p isotope ^{196}Hg results from the decay of ^{206}Pb that is produced by (γ, n) reactions on ^{207}Pb and ^{208}Pb and including yields obtained with the KEPLER code in galactic chemical evolution [Travaglio et al. \(2018\)](#) conclude that supernovae could provide an important contribution to the solar abundance. From this comparison we see that Type Ia supernovae are more efficient in the production of most of the heavier p nuclei including ^{180}Ta . As only exception, [Travaglio et al. \(2015\)](#) find ^{138}La which is produced more efficiently in supernovae by the ν process. This gives emphasis to our conclusion from Section 5.4 that the ν process contribution to ^{138}La is increased significantly by detailed neutrino properties from detailed simulations, while the production of ^{180}Ta is less affected. [Travaglio et al. \(2018\)](#) conclude that core-collapse supernovae contribute only a minor fraction to the solar abundances of p -nuclei. Including the contribution from a proton-rich neutrino driven wind we find a significant overproduction of the light p -nuclei by supernovae. For heavier p nuclei the γ process in type Ia supernovae based on [Travaglio et al. \(2011\)](#) is more efficient. Realistic neutrino spectra may help to prevent an overproduction of ^{180}Ta while allowing for a sufficient contribution of ^{138}La , which is in our current understanding the only p -nucleus that requires the ν process to explain its solar abundance.

Nucleus	pre-SN	post-SN			SN Ia Travaglio et al. (2011)
		without ν	including ν	+wind	
⁷⁴ Se	0.85	2.70	2.73	7.24	0.85
⁷⁸ Kr	0.29	1.09	1.09	27.11	0.72
⁸⁴ Sr	2.10	2.16	2.20	12.24	3.46
⁹² Mo	0.04	0.29	0.29	1.77	0.88
⁹⁴ Mo	0.02	0.31	0.31	4.78	0.15
⁹⁶ Ru	0.02	0.29	0.29	5.76	1.24
⁹⁸ Ru	0.07	0.32	0.32	25.39	1.64
¹⁰² Pd	0.42	0.43	0.43	9.49	1.09
¹⁰⁶ Cd	0.14	0.46	0.46	1.20	1.13
¹⁰⁸ Cd	0.20	0.57	0.57	0.66	0.41
¹¹² Sn	0.29	0.46	0.46	0.46	0.03
¹¹³ In	0.03	0.29	0.30	0.30	0.75
¹¹⁴ Sn	0.09	0.43	0.43	0.43	0.37
¹¹⁵ Sn	0.02	0.29	0.29	0.29	0.00
¹²⁰ Te	0.02	0.46	0.45	0.45	0.51
¹²⁴ Xe	0.04	0.62	0.61	0.61	1.00
¹²⁶ Xe	0.03	0.67	0.65	0.65	1.29
¹³⁰ Ba	0.04	1.20	1.18	1.18	1.12
¹³² Ba	0.03	0.99	0.97	0.97	0.84
¹³⁶ Ce	0.03	0.48	0.48	0.48	0.04
¹³⁸ La	0.02	0.35	0.95	0.95	0.43
¹³⁸ Ce	0.03	0.51	0.51	0.51	0.55
¹⁴⁴ Sm	0.03	1.00	1.00	1.00	1.00
¹⁵² Gd	0.04	0.76	0.76	0.74	0.02
¹⁵⁶ Dy	0.03	0.44	0.43	0.43	0.33
¹⁵⁸ Dy	0.02	0.40	0.40	0.40	0.18
¹⁶² Er	0.03	0.50	0.50	0.50	0.43
¹⁶⁴ Er	0.02	0.37	0.36	0.36	0.12
¹⁶⁸ Yb	0.03	0.96	0.90	0.90	1.35
¹⁷⁴ Hf	0.05	1.15	1.10	1.10	1.23
¹⁸⁰ W	0.08	2.18	2.10	2.05	0.16
¹⁸⁰ Ta	0.03	1.09	1.61	1.61	2.63
¹⁸⁴ Os	0.05	1.19	1.17	1.17	1.16
¹⁹⁰ Pt	0.02	0.44	0.45	0.45	0.39
¹⁹⁶ Hg	0.03	1.78	1.72	1.75	1.58

Table 7.5.: Production factors normalized to ¹⁴⁴Sm (post-SN) for the 35 *p*-nuclei before the explosion, i.e. without the γ -process, after the explosion but without neutrino, including neutrinos and also including the νp -process yield discussed in this section with the updated masses. We compare to the production of *p*-nuclei in Type Ia supernova presented by [Travaglio et al. \(2011\)](#)

8 Conclusions and outlook

We have compiled a full set of neutrino-induced charged- and neutral current reactions including multi-particle emission channels for nuclei with charge numbers $Z < 76$. We have improved the values for the charged current reactions $^{26}\text{Mg}(\nu_e, e^-)^{26}\text{Mg}$, $^{22}\text{Ne}(\nu_e, e^-)^{22}\text{Na}$, $^{36}\text{S}(\nu_e, e^-)^{36}\text{Cl}$ and $^{36}\text{Ar}(\bar{\nu}_e, e^+)^{36}\text{Cl}$ by including experimental data and shell model calculations.

With these results we have performed an updated study of ν process nucleosynthesis taking into account for the first time the results from recent supernova simulations [Hüdepohl et al. \(2010\)](#); [Martínez-Pinedo et al. \(2012\)](#); [Martínez-Pinedo et al. \(2014\)](#) that predict noticeably lower average energies particularly for μ and τ (anti)neutrinos. As a results we found charged current processes to be now more relevant due to reduced neutrino energies. Such reactions are more sensitive to the details of the transition strength distribution at low energies. We have performed this study for a range of progenitor models for massive stars with ZAMS masses in the range between 13 and 30 M_\odot , highlighting sensitivities and trends with respect to stellar structure and composition. Our nucleosynthesis study confirms the contribution of the ν process to the production of ^{11}B , ^{138}La , and ^{180}Ta and avoids the overproduction of these elements that has been found in previous studies due to insights on supernova physics. Furthermore, we discuss the interplay between γ process and ν process production and find that for individual progenitor models, in particular for the 27 M_\odot model, neutral current neutrino interactions leading to the emission of neutrons have a major effect on the production of ^{180}Ta .

We confirm that the ν process cannot be the primary origin of ^{19}F even when a various progenitor models are considered. However, we also emphasize remaining uncertainties with respect to thermonuclear reaction cross-sections. We find that neutrino-induced reactions, directly and indirectly, contribute to the production of long- and short-lived radioactive nuclei.

Even though we include a complete set of neutrino interactions in our calculations we do not find changes of the integrated yields exceeding the 10% level for any nuclei that have not been discussed here and in previous studies. For the purpose of the calculation of yield tables for models of galactic chemical evolution is not necessary to include any further reactions.

For ^{92}Nb and ^{98}Tc we also discuss the competition thermonuclear and neutrino-induced production and the role of the ν process to explain the abundance of ^{92}Nb in pre-solar grains. We find that a significant amount of ^{36}Cl can be produced mostly by electron antineutrino captures on ^{36}Ar that is produced in explosive O/Ne burning. We also suggest that neutrinos could explain the observed abundances ^{36}Cl in meteorites.

The yields of ^{22}Na and ^{26}Al , both prime candidates for gamma-ray astronomy, are enhanced. For ^{26}Al the magnitude of this enhancement is of the order of a few percent. ^{22}Na is increased on average by 30% and by more than 60% for individual progenitor models. In particular we find large mass fractions of ^{22}Na in C-rich zones and suggest the ν process in the O/C shell of massive stars as the origin of the Ne-E(L) component found in low density graphite grains.

In addition to discussing the standard treatment of the ν process with one-dimensional models, we have explored the effects of more detailed models. By comparing the standard approach to calculations using the full information about the neutrino properties from as detailed simulation we conclude that the assumption of a constant spectral temperature for the neutrinos is problematic for two reasons. First, is not straightforward to define an appropriate temperature. Secondly, there identify small effects on the mass fraction profiles that cannot be captured by using constant neutrino temperatures. The next generation of supernova models for nucleosynthesis already includes more information about the neutrino properties that can be used in the future for supernova yield tables.

Furthermore, we have for the first time addressed the question of the ν process in the region of the α -rich freeze out with tracer particles from a self-consistent two-dimensional supernova simulation. We find, that the contribution of to the integrated yield of ${}^7\text{Li}$ and ${}^{11}\text{B}$ are negligible for this model. For the production of ${}^{19}\text{F}$, ${}^{138}\text{La}$ and ${}^{180}\text{Ta}$ we find a good agreement with the results from one-dimensional calculations, suggesting that multi-dimensional effects do not have a major impact on the production of these nuclei in the ν process. To complete our picture of neutrino-induced nucleosynthesis we study contributions from the νp process in neutrino driven winds. We include and update of recently measured nuclear masses for several nuclei on the νp process path. These new values affect in particular the production of the p -nuclei ${}^{84}\text{Sr}$ and ${}^{78}\text{Kr}$. For particular conditions we find that the NDW could contribute a substantial amount of ${}^{92}\text{Nb}$. This production is sensitive to neutrino-induced spallation reactions, in particular on ${}^4\text{He}$. We finally combine the contribution to the production p -nuclei from explosive nucleosynthesis, the ν process and the νp process in the neutrino driven wind. In combination with results from the Type Ia supernovae, we find that the solar abundance of most p nuclei can be explained and the lightest p -nuclei are potentially overproduced. We confirm the conclusions by [Travaglio et al. \(2018\)](#) that the most Important contributions from core-collapse supernovae are ${}^{138}\text{La}$ and ${}^{94}\text{Mo}$. Important uncertainties remain related to the progenitor structure [Woosley et al. \(2002\)](#), helium burning rates [Austin et al. \(2014\)](#), and the long term evolution of the neutrino spectra and neutrino oscillations [Wu et al. \(2015\)](#).

The neutrino cross-sections we have compiled are about to be published and could become a new standard database for ν process nucleosynthesis. The lower neutrino energies call for more attention with respect to charged current reactions. With a better nuclear model several other reactions are to be improved. We have found that a combination of the ν process and a contribution from neutrino driven winds are promising to explain multiple isotopic ratios found in primitive meteorites with one single event. If a similarly good agreement can be found for a less massive progenitor, we could provide further support for the suggestion that a low mass supernova is responsible for the formation of the solar system, as suggested by [Banerjee et al. \(2016\)](#). Since we have shown that the static treatment of neutrino properties is insufficient, future work includes the proper incorporation of neutrino properties from modern simulations into nucleosynthesis calculations. This can for example be achieved by employing the PUSH scheme ([Perego et al., 2015](#)) for artificially triggered explosions in one dimension or parametric descriptions of the neutrino properties, following e.g. [Müller et al. \(2016a\)](#). In this study it has been neglected that modern calculations do not only provide the neutrino luminosities and average energies but actually provide the full spectral distribution which can deviate from a Fermi-Dirac distribution. In particular, the high energy tail that is important for spallation reactions, has been found to be reduced ([Tamborra et al., 2014b](#); [Janka & Hillebrandt, 1989](#); [Giovanoni et al., 1989](#)). The impact of such spectral properties has not been studied in detail before and requires either the calculations of the cross-section by integrating over the neutrino spectrum at each time step, or the tabulation of the cross-sections for deformed spectra.

Regarding the ν process in the region of an α -rich freeze-out we have so far only considered one single self-consistent simulation in two dimensions. For final conclusions, it is necessary to investigate a range of progenitors and also look at three dimensional simulations.

Appendices



A REACLIB reaction rates

Detailed nucleosynthesis calculations involve typically 1000 - 8000 species of nuclei. Including all different reaction channels between those nuclei requires an extended database that is compiled from a large range of sources. One of the most successful such compilations is the REACLIB reaction rate library that includes reaction cross-sections bases on experimental evaluations where available and complements those with theoretical calculations otherwise. The origin of this tabulation lies in large scale statistical model calculations by [Rauscher & Thielemann \(2000\)](#) that covers basically the whole range of nuclei between neutron and proton dripline. The REACLIB library is kept updated an regularly new measurements or improved calculations are included ([Cyburt et al., 2010](#)).

For efficient numerical evaluation of the cross-sections at different temperatures of the astrophysical plasma they are fitted with one or several sets of seven parameters $a_{0...6}^j$ as

$$N_A \langle \sigma v \rangle (T_9) = \sum_j \exp \left[a_0^j + a_1^j T_9^{-1} + a_2^j T_9^{-1/3} + a_3^j T_9^{+1/3} + a_4^j T_9 + a_5^j T_9^{5/3} + a_6^j \ln(T_9) \right] \quad (\text{A.1})$$

While non-resonant reactions and neutron captures can mostly be described by a single seven-parameter fit, reactions that are dominated by resonances often require several such fits. This format allows for an efficient implementation because the evaluation of the exponent for a whole range of reactions can be implemented as a matrix multiplication. Let $\vec{a}^j = (a_0, \dots, a_6)$ be the fit coefficients for one reaction and $\vec{T} = (T_9, T_9^{-1/3}, T_9^{+1/3}, T_9, T_9^{5/3}, \ln(T_9))^T$ are the required powers of the temperature as a column vector. We can construct a matrix for n reactions

$$\hat{a} = \begin{pmatrix} \vec{a}^1 \\ \dots \\ \vec{a}^n \end{pmatrix}, \quad (\text{A.2})$$

Note that usually $n \gg 7$, so the matrix is very asymmetric. In this way the calculation of the cross-sections for all reactions can be written as

$$\begin{pmatrix} (N_A \langle \sigma v \rangle)_1(T_9) \\ \dots \\ (N_A \langle \sigma v \rangle)_n(T_9) \end{pmatrix} = \exp \left[\hat{a} \vec{T} \right]. \quad (\text{A.3})$$

where the exponential acts on each component on the vector.



B Galactic cosmic ray contribution

Cosmic rays are high energy particles and nuclei that have mostly been accelerated by supernova explosions and now form a isotropic background. In addition to proton and α particles, cosmic rays themselves can also be CNO nuclei or even heavier. $\alpha + \alpha$ fusion reactions lead to the production of Li and Be isotopes. (p, α) on CNO elements can occur either on the CNO abundances in the interstellar medium or can be induced by the CNO component of cosmic rays on Hydrogen and Helium in the ISM. In the latter case, it is less likely that the reaction products thermalize with the ISM and accumulate (Meneguzzi et al., 1971; Prantzos, 2012) The fluxes of cosmic rays are relatively low, but material is usually exposed to it timescales on the order of 10^9 yr. Therefore, it has been suggested that several rare species, that have been found in the solar system, could have been produced by cosmic rays. This mechanism has been discussed in particular for ${}^6,7\text{Li}$, ${}^{10,11}\text{B}$ (Prantzos, 2007, 2012). Neither the ν process nor any other stellar processes are able to explain the solar abundances of ${}^6\text{Li}$ and ${}^{10}\text{B}$. Therefore, it is necessary to include an estimate for the contribution from cosmic ray exposure, which also contributes to ${}^7\text{Li}$ and ${}^{11}\text{B}$. Since absolute numbers would require the knowledge of the total mass, it is useful to look mainly at abundance ratios. Assuming that two isotopes a and b for which the solar abundance ratio $R_{\odot}^{a,b} = \frac{N^a}{N^b_{\odot}}$ is known can be produced in supernovae as well as by cosmic ray irradiation, we require that these contributions fulfill:

$$\begin{aligned} N_{CR}^a + N_{SN}^a &= N_{\odot}^a \\ N_{CR}^b + N_{SN}^b &= N_{\odot}^b \end{aligned} \quad (\text{B.1})$$

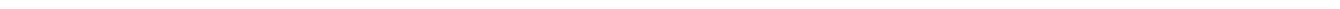
For these isotopes we know the solar ratio and we can get the ratio of their production in either supernovae or by cosmic rays from models, i.e. $R_x^{i,j} = \frac{N_x^i}{N_x^j}$ for $x = SN, CR, \odot$ are known. From this we can get an estimate how large the supernova production factor $R_{SN}^{i,i} = \frac{N_{SN}^i}{N_{\odot}^i}$ needs to be in order to explain the observed abundance ratio. Inserting the ratios in equation (B.1) we obtain

$$\begin{aligned} R_{CR}^{a,b} N_{CR}^b &= N_{\odot}^a (1 - R_{SN}^{a,a}) \\ N_{CR}^b &= N_{\odot}^a (R_{\odot}^{b,a} - R_{SN}^{b,a} R_{SN}^{a,a}) \end{aligned} \quad (\text{B.2})$$

Dividing the two equations in (B.2) and rearranging finally gives

$$R_{SN}^{a,a} = \frac{1 - (R_{CR}^{a,b} / R_{\odot}^{a,b})}{1 - (R_{CR}^{a,b} / R_{SN}^{a,b})} \quad (\text{B.3})$$

where we have used that $R^{a,b} = 1 / R^{b,a}$.



Bibliography

- Abbott, B. P., Abbott, R., Abbott, T. D., et al. 2017, *ApJ* , 848, L12
- Adande, G. R., & Ziurys, L. M. 2012, *ApJ* , 744, 194
- Alastuey, A., & Jancovici, B. 1978, *ApJ* , 226, 1034
- Almqvist, E., Bromley, D. A., Ferguson, A. J., Gove, H. E., & Litherland, A. E. 1959, *Physical Review*, 114, 1040
- Amari, S. 2009, *ApJ* , 690, 1424
- Anderson, B. D., Tamimi, N., Baldwin, A. R., et al. 1991, *Phys. Rev. C*, 43, 50
- Angulo, C., Arnould, M., Rayet, M., et al. 1999, *Nuclear Physics A*, 656, 3
- Arcones, A., Janka, H.-T., & Scheck, L. 2007, *A&A* , 467, 1227
- Arnett, W. D. 1969, *ApJ* , 157, 1369
- . 1971, *ApJ* , 166, 153
- . 1987, *ApJ* , 319, 136
- Arnett, W. D., Truran, J. W., & Woosley, S. E. 1971, *ApJ* , 165, 87
- Athanassopoulos, C., Auerbach, L. B., Burman, R. L., et al. 1997, *Phys. Rev. C* , 55, 2078
- Audouze, J., Lequeux, J., & Vigroux, L. 1975, *A&A* , 43, 71
- Austin, S. M., Heger, A., & Tur, C. 2011, *Phys. Rev. Lett.*, 106, 152501
- Austin, S. M., West, C., & Heger, A. 2014, *Phys. Rev. Lett.*, 112, 111101
- Banerjee, P., Haxton, W. C., & Qian, Y.-Z. 2011, *Physical Review Letters*, 106, 201104
- Banerjee, P., Qian, Y.-Z., Heger, A., & Haxton, W. C. 2016, *Nature Communications*, 7, 13639
- Baron, E., & Cooperstein, J. 1990, *ApJ* , 353, 597
- Bartl, A., Bollig, R., Janka, H.-T., & Schwenk, A. 2016, *Phys. Rev. D* , 94, 083009
- Bartl, A., Pethick, C. J., & Schwenk, A. 2014, *Physical Review Letters*, 113, 081101
- Battino, U., Pignatari, M., Ritter, C., et al. 2016, *ApJ* , 827, 30
- Becker, H., & Walker, R. J. 2003, *Nature* , 425, 152
- Belic, D., Arlandini, C., Besserer, J., et al. 2002, *Phys. Rev. C*, 65, 035801
- Bemmerer, D., Akhmadaliev, S., Al-Abdullah, T., et al. 2016, in *Journal of Physics Conference Series*, Vol. 665, *Journal of Physics Conference Series*, 012030
- Bethe, H. A. 1990, *Reviews of Modern Physics*, 62, 801

-
- . 1993, *ApJ* , 412, 192
- Bethe, H. A., Brown, G. E., Applegate, J., & Lattimer, J. M. 1979, *Nuclear Physics A*, 324, 487
- Bethe, H. A., & Wilson, J. R. 1985, *ApJ* , 295, 14
- Black, D., & Pepin, R. 1969, *Earth and Planetary Science Letters*, 6, 395
- Bliss, J., Arcones, A., & Qian, Y.-Z. 2018, ArXiv e-prints. <https://arxiv.org/abs/1804.03947>
- Bollig, R., Janka, H.-T., Lohs, A., et al. 2017, *Physical Review Letters*, 119, 242702
- Broggini, C., Bemmerer, D., Caciolli, A., & Trezzi, D. 2018, *Progress in Particle and Nuclear Physics*, 98, 55
- Brown, B. A., & Richter, W. A. 2006, *Phys. Rev. C*, 74, 034315
- Bruenn, S. W. 1985, *ApJS* , 58, 771
- Bruenn, S. W., Lentz, E. J., Hix, W. R., et al. 2016, *ApJ* , 818, 123
- Brussaard, P., & Glaudemans, P. 1977, *Shell model Applications in nuclear spectroscopy* (Elsevier/North-Holland, New York)
- Bühring, W. 1982, *Electron radial wave functions and nuclear beta-decay*
- Buras, R., Rampp, M., Janka, H.-T., & Kifonidis, K. 2006, *A&A* , 447, 1049
- Burbidge, E. M., Burbidge, G. R., Fowler, W. A., & Hoyle, F. 1957, *Rev. Mod. Phys.*, 29, 547
- Burrows, A., & Lattimer, J. M. 1987, *ApJ* , 318, L63
- Burrows, A., & Sawyer, R. F. 1998, *Phys. Rev. C* , 58, 554
- Byelikov, A., Adachi, T., Fujita, H., et al. 2007, *Phys. Rev. Lett.*, 98, 082501
- Cameron, A. G. W. 1957, *Stellar Evolution, Nuclear Astrophysics, and Nucleogenesis*, Report CRL-41, Chalk River
- Cassé, M., Lehoucq, R., & Vangioni-Flam, E. 1995, *Nature* , 373, 318
- Caughlan, G. R., & Fowler, W. A. 1988, *Atomic Data and Nuclear Data Tables*, 40, 283
- Cheoun, M.-K., Ha, E., Hayakawa, T., et al. 2012, *Phys. Rev. C*, 85, 065807
- Cheoun, M.-K., Ha, E., Lee, S. Y., et al. 2010, *Phys. Rev. C* , 81, 028501
- Clayton, D. D. 1975, *Nature* , 257, 36
- Clayton, D. D., Liu, W., & Dalgarno, A. 1999, *Science*, 283, 1290
- Colgate, S. A., & White, R. H. 1966, *ApJ* , 143, 626
- Côté, B., Ritter, C., O’Shea, B. W., et al. 2016, *ApJ* , 824, 82
- Couch, R. G., Schmiedekamp, A. B., & Arnett, W. D. 1974, *ApJ* , 190, 95
- Couch, S. M. 2013, *ApJ* , 775, 35
- Couch, S. M., & O’Connor, E. P. 2014, *ApJ* , 785, 123

-
- Couch, S. M., & Ott, C. D. 2015, *ApJ* , 799, 5
- Cowan, J., Thielemann, F.-K., & Truran, J. in prep., NUCLEAR EVOLUTION OF THE UNIVERSE
- Cowperthwaite, P. S., Berger, E., Villar, V. A., et al. 2017, *ApJ* , 848, L17
- Cyburt, R. H., Amthor, A. M., Ferguson, R., et al. 2010, *Astrophys. J. Suppl.*, 189, 240
- Descouvemont, P., Adahchour, A., Angulo, C., Coc, A., & Vangioni-Flam, E. 2004, *Atomic Data and Nuclear Data Tables*, 88, 203
- Diehl, R. 2013, *Astron. Rev.*, 8, 19
- Diehl, R., & Timmes, F. X. 1998, *Publ. Astron. Soc. Pacific*, 110, 637
- Diehl, R., Halloin, H., Kretschmer, K., et al. 2006, *Nature*, 439, 45
- Dilg, W., Schantl, W., Vonach, H., & Uhl, M. 1973, *Nuclear Physics A*, 217, 269
- Dillmann, I., Rauscher, T., Heil, M., et al. 2008, *Journal of Physics G Nuclear Physics*, 35, 014029
- Dillmann, I., Szücs, T., Plag, R., et al. 2014, *Nuclear Data Sheets*, 120, 171
- Doherty, C. L., Gil-Pons, P., Lau, H. H. B., Lattanzio, J. C., & Siess, L. 2014, *MNRAS* , 437, 195
- Domogatskii, G. V., & Nadezhin, D. K. 1980, *Ap&SS* , 70, 33
- Domogatskij, G. V., & Nadezhin, D. K. 1980, *Soviet Astronomy Letters*, 6, 127
- Domogatsky, G. V., & Nadyozhin, D. K. 1977, *MNRAS* , 178, 33P
- Duan, H., Fuller, G. M., & Qian, Y.-Z. 2010, *Annual Review of Nuclear and Particle Science*, 60, 569
- Duncan, R. C., Shapiro, S. L., & Wasserman, I. 1986, *ApJ* , 309, 141
- Ebinger, K., Curtis, S., Fröhlich, C., et al. 2018, ArXiv e-prints. <https://arxiv.org/abs/1804.03182>
- Edelmann, P. V. F., Röpke, F. K., Hirschi, R., Georgy, C., & Jones, S. 2017, *A&A* , 604, A25
- Eichler, M., Nakamura, K., Takiwaki, T., et al. 2018, *Journal of Physics G Nuclear Physics*, 45, 014001
- Ekström, S., Georgy, C., Eggenberger, P., et al. 2012, *A&A* , 537, A146
- Engel, J. 1998, *Phys. Rev. C* , 57, 2004
- Engel, J., Kolbe, E., Langanke, K., & Vogel, P. 1993, *Phys. Rev. D* , 48, 3048
- Epstein, R. I., Colgate, S. A., & Haxton, W. C. 1988, *Physical Review Letters*, 61, 2038
- Ertl, T., Janka, H.-T., Woosley, S. E., Sukhbold, T., & Ugliano, M. 2015, ArXiv e-prints. <https://arxiv.org/abs/1503.07522>
- . 2016, *Astrophys. J.*, 818, 124
- Fermi, E. 1934, *Zeitschrift für Physik*, 88, 161
- Fernandez, B., Gaarde, C., Larsen, J. S., Pontoppidan, S., & Videbaek, F. 1978, *Nuclear Physics A*, 306, 259
- Firestone, R. B. 1991, *Nuclear Data Sheets*, 62, 101

-
- Fischer, T., Whitehouse, S. C., Mezzacappa, A., Thielemann, F.-K., & Liebendörfer, M. 2009, *Astron. & Astrophys.*, 499, 1
- Fischer, T., Whitehouse, S. C., Mezzacappa, A., Thielemann, F.-K., & Liebendörfer, M. 2010, *Astron. & Astrophys.*, 517, A80
- Fischer, T., Sagert, I., Pagliara, G., et al. 2011, *ApJS* , 194, 39
- Fisker, J. L., Hoffman, R. D., & Pruet, J. 2009, *ApJ* , 690, L135
- Frebel, A., Aoki, W., Christlieb, N., et al. 2005, *Nature* , 434, 871
- Fröhlich, C., Martínez-Pinedo, G., iebendörfer, M., et al. 2006, *Physical Review Letters*, 96, 142502
- Fujita, Y., Akimune, H., Daito, I., et al. 1999, *Phys. Rev. C* , 59, 90
- Fuller, G. M., Fowler, W. A., & Newman, M. J. 1982, *ApJS* , 48, 279
- Fuller, G. M., & Meyer, B. S. 1995, *Astrophys. J.*, 453, 792
- Gade, A., & Sherrill, B. M. 2016, *Phys. Scr*, 91, 053003
- Gazit, D., & Barnea, N. 2007, *Phys. Rev. Lett.*, 98, 192501
- Gilbert, A., & Cameron, A. G. W. 1965, *Canadian Journal of Physics*, 43, 1446
- Giovanoni, P. M., Ellison, D. C., & Bruenn, S. W. 1989, *ApJ* , 342, 416
- Goriely, S. 1996, *Nuclear Physics A*, 605, 28
- Goriely, S., Arnould, M., Borzov, I., & Rayet, M. 2001a, *A&A* , 375, L35
- Goriely, S., Tondeur, F., & Pearson, J. M. 2001b, *Atomic Data and Nuclear Data Tables*, 77, 311
- Graboske, H. C., Dewitt, H. E., Grossman, A. S., & Cooper, M. S. 1973, *ApJ* , 181, 457
- Grefenstette, B. W., Harrison, F. A., Boggs, S. E., et al. 2014, *Nature*, 506, 339
- Guman, V. N., & Birbrair, B. L. 1965, *Nucl. Phys. A*, 70, 545
- Hanke, F., Marek, A., Müller, B., & Janka, H.-T. 2012, *ApJ* , 755, 138
- Harris, J. A., Hix, W. R., Chertkow, M. A., et al. 2017, *ApJ* , 843, 2
- Hashimoto, M., Iwamoto, K., & Nomoto, K. 1993, *ApJ* , 414, L105
- Haxton, W. C., Langanke, K., Qian, Y.-Z., & Vogel, P. 1997, *Physical Review Letters*, 78, 2694
- Haxton, W. C., Stephenson, Jr., G. J., & Strottman, D. 1982, *Phys. Rev. D* , 25, 2360
- Hayakawa, T., Nakamura, K., Kajino, T., et al. 2013, *ApJ* , 779, L9
- Heger, A., Kolbe, E., Haxton, W., et al. 2005, *Phys. Lett. B*, 606, 258
- Heger, A., & Woosley, S. E. 2010, *Astrophys. J.*, 724, 341
- Hertzsprung, E., & Herrmann, D. B. 1976, *Zur Strahlung der Sterne*
- Hirfl-Csr Group, Zhan, W. L., Xu, H. S., et al. 2010, *Nuclear Physics A*, 834, 694
- Hirschi, R., Meynet, G., & Maeder, A. 2004, *A&A* , 425, 649

-
- Hix, W. R., & Thielemann, F.-K. 1999, *Journal of Computational and Applied Mathematics*, 109, 321
- Hoffman, R. D., Woosley, S. E., Fuller, G. M., & Meyer, B. S. 1996, *Astrophys. J.*, 460, 478
- Hoffman, R. D., Woosley, S. E., & Qian, Y.-Z. 1997, *ApJ*, 482, 951
- Hoffman, R. D., Woosley, S. E., & Weaver, T. A. 2001, *ApJ*, 549, 1085
- Hoyle, F. 1954, *ApJS*, 1, 121
- Huang, W., Audi, G., Wang, M., et al. 2017, *Chinese Physics C*, 41, 030002
- Hüdepohl, L., Müller, B., Janka, H., Marek, A., & Raffelt, G. G. 2010, *Phys. Rev. Lett.*, 104, 251101
- Huss, G. R., Meyer, B. S., Srinivasan, G., Goswami, J. N., & Sahijpal, S. 2009, *Geochim. Cosmochim. Acta*, 73, 4922
- Huther, L. 2014, PhD thesis, TU Darmstadt
- Hynes, K. M., & Gyngard, F. 2009, in *Lunar and Planetary Science Conference*, Vol. 40, Lunar and Planetary Science Conference, 1198
- Iliadis, C. 2007, *Nuclear Physics of Stars* (Wiley-VCH Verlag Weinheim)
- Iliadis, C., Champagne, A., Chieffi, A., & Limongi, M. 2011, *ApJS*, 193, 16
- Iliadis, C., D'Auria, J. M., Starrfield, S., Thompson, W. J., & Wiescher, M. 2001, *ApJS*, 134, 151
- Iliadis, C., Longland, R., Champagne, A. E., Coc, A., & Fitzgerald, R. 2010, *Nucl. Phys. A*, 841, 31
- Iyudin, A. F. 2010, *Astronomy Reports*, 54, 611
- Iyudin, A. F., Diehl, R., Bloemen, H., et al. 1994, *Astron. & Astrophys.*, 284, L1
- Jacobsen, B., Matzel, J., Hutcheon, I. D., et al. 2009, in *Lunar and Planetary Science Conference*, Vol. 40, Lunar and Planetary Science Conference, 2553
- Jacobsen, B., Matzel, J., Hutcheon, I. D., et al. 2011, *Astrophys. J.*, 731, L28
- Janka, H.-T. 2001, *A&A*, 368, 527
- . 2012, *Annual Review of Nuclear and Particle Science*, 62, 407
- Janka, H.-T., Buras, R., & Rampp, M. 2003, *Nuclear Physics A*, 718, 269
- Janka, H.-T., Hanke, F., Hüdepohl, L., et al. 2012, *Progress of Theoretical and Experimental Physics*, 2012, 01A309
- Janka, H.-T., & Hillebrandt, W. 1989, *A&A*, 224, 49
- Jones, S., Röpkke, F. K., Pakmor, R., et al. 2016, *A&A*, 593, A72
- Jönsson, H., Ryde, N., Spitoni, E., et al. 2017, *Astrophys. J.*, 835, 50
- Kappeler, F., Beer, H., & Wisshak, K. 1989, *Reports on Progress in Physics*, 52, 945
- Käppeler, F., Arlandini, C., Heil, M., et al. 2004, *Phys. Rev. C*, 69, 055802
- Karakas, A. I. 2016, *Mem. Soc. Astron. Italiana*, 87, 229

-
- Kelic, A., Valentina Ricciardi, M., & Schmidt, K.-H. 2009, ArXiv e-prints. <https://arxiv.org/abs/0906.4193>
- Kheswa, B. V., Wiedeking, M., Giacoppo, F., et al. 2015, *Physics Letters B*, 744, 268
- Kippenhahn, R., Weigert, & A., Weiss, A. 2012, *Stellar Structure and Evolution* (Springer-Verlag, Berlin Heidelberg)
- Kiss, G. G., Mohr, P., Fülöp, Z., et al. 2013, *Phys. Rev. C* , 88, 045804
- Kitaura, F. S., Janka, H.-T., & Hillebrandt, W. 2006, *A&A* , 450, 345
- Kneller, J. P., Phillips, J. R., & Walker, T. P. 2003, *ApJ* , 589, 217
- Kobayashi, C., Izutani, N., Karakas, A. I., et al. 2011, *ApJ* , 739, L57
- Kolbe, E., Langanke, K., Krewald, S., & Thielemann, F.-K. 1992, *Nucl. Phys. A*, 540, 599
- Kolbe, E., Langanke, K., Martínez-Pinedo, G., & Vogel, P. 2003, *J. Phys. G: Nucl. Part. Phys.*, 29, 2569
- Kolbe, E., Langanke, K., & Vogel, P. 1999, *Nuclear Physics A*, 652, 91
- Koning, A. J., Hilaire, S., & Duijvestijn, M. C. 2007, in *International Conference on Nuclear Data for Science and Technology*, International Conference on Nuclear Data for Science and Technology, 211–214
- Kotake, K. 2013, *Comptes Rendus Physique*, 14, 318
- Kotake, K., Takiwaki, T., Fischer, T., Nakamura, K., & Martínez-Pinedo, G. 2018, *ApJ* , 853, 170
- Kozma, C., & Fransson, C. 1998, *ApJ* , 496, 946
- Kraichnan, R. H. 1967, *Physics of Fluids*, 10, 1417
- Krane, K. 1988, *Introductory Nuclear Physics* ("John Wiley & Sons Inc., New York")
- Kuo, T. T. S., & Brown, G. E. 1968, *Nuclear Physics A*, 114, 241
- Lamers, H. J. G. L. M., & Levesque, E. M. 2017, *Understanding Stellar Evolution*
- Landau, L. D., & Lifshitz, E. M. 2012, *Fluid Mechanics* (Pergamon Press)
- Langanke, K., & Martínez-Pinedo, G. 2000, *Nuclear Physics A*, 673, 481
- Langer, N. 2012, *ARA&A* , 50, 107
- Lattimer, J. M., & Douglas Swesty, F. 1991, *Nuclear Physics A*, 535, 331
- Lattimer, J. M., Schramm, D. N., & Grossman, L. 1978, *ApJ* , 219, 230
- Liebendörfer, M., Mezzacappa, A., Messer, O. E. B., et al. 2003, *Nuclear Physics A*, 719, C144
- Liebendörfer, M., Mezzacappa, A., Thielemann, F.-K., et al. 2001, *Phys. Rev. D* , 63, 103004
- Liebendörfer, M., Rampp, M., Janka, H.-T., & Mezzacappa, A. 2005, *ApJ* , 620, 840
- Limongi, M., & Chieffi, A. 2006, *Astrophys. J.*, 647, 483
- Lisetskiy, A. F., Caurier, E., Langanke, K., et al. 2007, *Nuclear Physics A*, 789, 114
- Lodders, K. 2003, *Astrophys. J.*, 591, 1220

-
- Loens, H. P. 2010, PhD thesis, TU Darmstadt
- Longland, R., Iliadis, C., Champagne, A. E., et al. 2010, *Nuclear Physics A*, 841, 1
- M., W., Audi, G., A. H., W., et al. 2012, *Chinese Physics C*, 36, 003
- Maeder, A. 2009, *Physics Formation and Evolution of Rotating Stars* (Springer-Verlag Berlin Heidelberg)
- Magkotsios, G., Timmes, F. X., Hungerford, A. L., et al. 2010, *ApJS*, 191, 66
- Martínez-Pinedo, G., Fischer, T., & Huther, L. 2014, *J. Phys. G: Nucl. Part. Phys.*, 41, 044008
- Martínez-Pinedo, G., Fischer, T., & Huther, L. 2014, *Journal of Physics G Nuclear Physics*, 41, 044008
- Martínez-Pinedo, G., Fischer, T., Lohs, A., & Huther, L. 2012, *Phys. Rev. Lett.*, 109, 251104
- Martínez-Pinedo, G., Fischer, T., Lohs, A., & Huther, L. 2012, *Physical Review Letters*, 109, 251104
- Matzner, C. D., & McKee, C. F. 1999, *ApJ*, 510, 379
- Mei, B., Tu, X., Wang, M., et al. 2010, *Nuclear Instruments and Methods in Physics Research A*, 624, 109
- Meier, M. M. M., Heck, P. R., Amari, S., Baur, H., & Wieler, R. 2012, *Geochim. Cosmochim. Acta*, 76, 147
- Melson, T., Janka, H.-T., Bollig, R., et al. 2015, *ApJ*, 808, L42
- Meneguzzi, M., Audouze, J., & Reeves, H. 1971, *A&A*, 15, 337
- Mercer, D. J., Austin, S. M., Brown, J. A., et al. 2001, *Phys. Rev. C*, 63, 065805
- Metzger, B. D., Martínez-Pinedo, G., Darbha, S., et al. 2010, *MNRAS*, 406, 2650
- Mirizzi, A., Tamborra, I., Janka, H.-T., et al. 2016, *Nuovo Cimento Rivista Serie*, 39, 1
- Mohr, P. 2016, *Phys. Rev. C*, 93, 065804
- Mohr, P., Käppeler, F., & Gallino, R. 2007, *Phys. Rev. C*, 75, 012802
- Möller, P., Nix, J. R., & Kratz, K.-L. 1997, *Atomic Data and Nuclear Data Tables*, 66, 131
- Mösta, P., Ott, C. D., Radice, D., et al. 2015, *Nature*, 528, 376
- Müller, B. 2015, *MNRAS*, 453, 287
- . 2016, *PASA*, 33, e048
- Müller, B., Heger, A., Liptai, D., & Cameron, J. B. 2016a, *MNRAS*, 460, 742
- Müller, B., & Janka, H.-T. 2014, *ApJ*, 788, 82
- Müller, B., Viallet, M., Heger, A., & Janka, H.-T. 2016b, *ApJ*, 833, 124
- Murty, S. V. S., Goswami, J. N., & Shukolyukov, Y. A. 1997, *Astrophys. J.*, 475, L65
- Nagataki, S., Hashimoto, M.-a., Sato, K., & Yamada, S. 1997, *ApJ*, 486, 1026
- Nieuwenhuijzen, H., & de Jager, C. 1990, *A&A*, 231, 134
- Ning, H., Qian, Y.-Z., & Meyer, B. S. 2007, *ApJ*, 667, L159

-
- Nishimura, N., Takiwaki, T., & Thielemann, F.-K. 2015, *ApJ* , 810, 109
- Nomoto, K., & Hashimoto, M. 1988, *Phys. Rep.*, 163, 13
- O'Connor, E., & Ott, C. D. 2011, *ApJ* , 730, 70
- . 2013, *ApJ* , 762, 126
- O'Connor, E. P., & Couch, S. M. 2018, *ApJ* , 854, 63
- Oertel, M., Hempel, M., Klöhn, T., & Typel, S. 2017, *Reviews of Modern Physics*, 89, 015007
- Olive, K. A., Prantzos, N., Scully, S., & Vangioni-Flam, E. 1994, *ApJ* , 424, 666
- Ott, C. D. 2009, *Classical and Quantum Gravity*, 26, 063001
- Paar, N., Tutman, H., Marketin, T., & Fischer, T. 2013, *Phys. Rev. C* , 87, 025801
- Papish, O., & Soker, N. 2014, *MNRAS* , 438, 1027
- Perego, A., Hempel, M., Fröhlich, C., et al. 2015, *ApJ* , 806, 275
- Petra, C., Schenk, O., Lubin, M., & Gaertner, K. 2014, *SIAM Journal on Scientific Computing*, 36, C139
- Pignatari, M., Zinner, E., Hoppe, P., et al. 2015, *Astrophys. J.*, 808, L43
- Pignatari, M., Herwig, F., Hirschi, R., et al. 2016, *ApJS* , 225, 24
- Plumley, M. R., Watson, J. W., Anderson, B. D., et al. 1997, *Phys. Rev. C* , 56, 263
- Prantzos, N. 2007, *Space Sci. Rev.*, 130, 27
- . 2012, *A&A* , 542, A67
- Prantzos, N., Hashimoto, M., Rayet, M., & Arnould, M. 1990, *A&A* , 238, 455
- Pruet, J., Hoffman, R. D., Woosley, S. E., Janka, H.-T., & Buras, R. 2006, *ApJ* , 644, 1028
- Qian, Y.-Z. 2003, *Progress in Particle and Nuclear Physics*, 50, 153
- Qian, Y.-Z., & Wasserburg, G. J. 2007, *Phys. Rep.*, 442, 237
- Qian, Y.-Z., & Woosley, S. E. 1996, *ApJ* , 471, 331
- Radice, D., Ott, C. D., Abdikamalov, E., et al. 2016, *ApJ* , 820, 76
- Rakavy, G., Shaviv, G., & Zinamon, Z. 1967, *ApJ* , 150, 131
- Rampp, M., & Janka, H.-T. 2002, *A&A* , 396, 361
- Rauscher, T., Heger, A., Hoffman, R. D., & Woosley, S. E. 2002, *Astrophys. J.*, 576, 323
- Rauscher, T., & Thielemann, F.-K. 2000, *Atomic Data and Nuclear Data Tables*, 75, 1
- Rauscher, T., Thielemann, F.-K., & Kratz, K.-L. 1997, *Phys. Rev. C* , 56, 1613
- Rayet, M., Arnould, M., Hashimoto, M., Prantzos, N., & Nomoto, K. 1995, *A&A* , 298, 517
- Reeves, H. 1970, *Nature* , 226, 727
- Renda, A., Fenner, Y., Gibson, B. K., et al. 2004, *MNRAS* , 354, 575

-
- Ring, P., & Schuck, P. 2000, *The nuclear many-body problem* (Springer, Berlin Heidelberg)
- Rinker, G. A., & Speth, J. 1978, *Nuclear Physics A*, 306, 360
- Ritter, C., Andrassy, R., Côté, B., et al. 2018, *MNRAS*, 474, L1
- Roberts, L. F., Reddy, S., & Shen, G. 2012, *Phys. Rev. C*, 86, 065803
- Roig, O., Jandel, M., Méot, V., et al. 2016, *Phys. Rev. C*, 93, 034602
- Romano, D., Matteucci, F., Zhang, Z.-Y., Papadopoulos, P. P., & Ivison, R. J. 2017, *MNRAS*, 470, 401
- Röpke, F. K. 2005, *A&A*, 432, 969
- Röpke, F. K., & Niemeyer, J. C. 2007, *A&A*, 464, 683
- Rukeya, R., Lü, G., Wang, Z., & Zhu, C. 2017, *PASP*, 129, 074201
- Russell, H. N. 1914, *Popular Astronomy*, 22, 275
- Sallaska, A. L., Iliadis, C., Champagne, A. E., et al. 2013, *ApJS*, 207, 18
- Salpeter, E. E. 1955, *ApJ*, 121, 161
- Sbordone, L., Bonifacio, P., Caffau, E., et al. 2010, *Astron. & Astrophys.*, 522, A26
- Schatz, H., Aprahamian, A., Goerres, J., et al. 1998, *Phys. Rep.*, 294
- Schatz, H., Aprahamian, A., Barnard, V., et al. 2001, *Physical Review Letters*, 86, 3471
- Scheck, L., Kifonidis, K., Janka, H.-T., & Müller, E. 2006, *A&A*, 457, 963
- Schönbächler, M., Rehkämper, M., Halliday, A. N., et al. 2002, *Science*, 295, 1705
- Schwab, J., Quataert, E., & Kasen, D. 2016, *MNRAS*, 463, 3461
- Seitenzahl, I. R., Timmes, F. X., Marin-Laflèche, A., et al. 2008, *ApJ*, 685, L129
- Shimizu, Y., Kobayashi, T., Kubo, T., et al. 2011, in *Journal of Physics Conference Series*, Vol. 312, *Journal of Physics Conference Series*, 052022
- Sieverding, A., Huther, L., Martínez-Pinedo, G., Langanke, K., & Heger, A. 2018a, in *Journal of Physics Conference Series*, Vol. 940, *Journal of Physics Conference Series*, 012054
- Sieverding, A., Martínez-Pinedo, G., Huther, L., Langanke, K., & Heger, A. 2018b, *ArXiv e-prints*. <https://arxiv.org/abs/1805.10231>
- Spite, F., & Spite, M. 1982, *Astron. & Astrophys.*, 115, 357
- Steiner, A. W., Hempel, M., & Fischer, T. 2013, *ApJ*, 774, 17
- Strieder, F., & Rolfs, C. 2007, *Progress in Particle and Nuclear Physics*, 59, 562
- Sukhbold, T., Woosley, S., & Heger, A. 2017, *ArXiv e-prints*. <https://arxiv.org/abs/1710.03243>
- Summa, A., Hanke, F., Janka, H.-T., et al. 2016, *ApJ*, 825, 6
- Suwa, Y., & Müller, E. 2016, *MNRAS*, 460, 2664
- Takahashi, K., Witt, J., & Janka, H. T. 1994, *Astron. Astrophys.*, 286, 857

-
- Takigawa, A., Miki, J., Tachibana, S., et al. 2008, *ApJ* , 688, 1382
- Tamborra, I., Hanke, F., Janka, H.-T., et al. 2014a, *ApJ* , 792, 96
- Tamborra, I., Raffelt, G., Hanke, F., Janka, H.-T., & Müller, B. 2014b, *Phys. Rev. D* , 90, 045032
- Tatischeff, V., Tavani, M., von Ballmoos, P., et al. 2016, in *Proc. SPIE*, Vol. 9905, *Space Telescopes and Instrumentation 2016: Ultraviolet to Gamma Ray*, 99052N
- Teegarden, B. J., & Watanabe, K. 2006, *ApJ* , 646, 965
- The, L.-S., El Eid, M. F., & Meyer, B. S. 2000, *ApJ* , 533, 998
- Thielemann, F.-K., Arnould, M., & Truran, J. 1987, in *Advances in Nuclear Astrophysics*, eds. E. Vagioni-Flam et al. p. 525, ed. E. Vagioni-Flam (Editions frontieres (Gifs-sur-Yvette)), 525 ff.
- Thielemann, F.-K., Brachwitz, F., Höflich, P., Martinez-Pinedo, G., & Nomoto, K. 2004, *New Astronomy Reviews*, 48, 605
- Thomas, J., Chen, Y. T., Hinds, S., Meredith, D., & Olson, M. 1986, *Phys. Rev. C* , 33, 1679
- Thompson, T. A., Burrows, A., & Meyer, B. S. 2001, *ApJ* , 562, 887
- Timmes, F. X., Woosley, S. E., Hartmann, D. H., et al. 1995a, *Astrophys. J.*, 449, 204
- Timmes, F. X., Woosley, S. E., & Weaver, T. A. 1995b, *ApJS* , 98, 617
- Towner, I., & Hardy, J. 1995, in I.S. Towner and J.C. Hardy, in: W.C. Haxton, E.M. Henley (Eds), *Symmetries and Fundamental Interactions in Nuclei* (World Scientific, Singapore, 1995) p. 183, ed. W. Haxton & E. Henley (World Scientific, Singapore), 183
- Travaglio, C., Gallino, R., Arnone, E., et al. 2004, *ApJ* , 601, 864
- Travaglio, C., Gallino, R., Rauscher, T., et al. 2014, *ApJ* , 795, 141
- Travaglio, C., Gallino, R., Rauscher, T., Röpke, F. K., & Hillebrandt, W. 2015, *ApJ* , 799, 54
- Travaglio, C., Rauscher, T., Heger, A., Pignatari, M., & West, C. 2018, *ApJ* , 854, 18
- Travaglio, C., Röpke, F. K., Gallino, R., & Hillebrandt, W. 2011, *ApJ* , 739, 93
- Truran, J. W., Arnett, W. D., & Cameron, A. G. W. 1967, *Canadian Journal of Physics*, 45, 2315
- Truran, J. W., & Cameron, A. G. W. 1971, *Ap&SS* , 14, 179
- Ugliano, M., Janka, H.-T., Marek, A., & Arcones, A. 2012, *ApJ* , 757, 69
- Väänänen, D., & McLaughlin, G. C. 2016, *Phys. Rev. D* , 93, 105044
- van Wormer, L., Görres, J., Iliadis, C., Wiescher, M., & Thielemann, F.-K. 1994, *ApJ* , 432, 326
- Vangioni-Flam, E., Casse, M., Fields, B. D., & Olive, K. A. 1996, *ApJ* , 468, 199
- Walecka, J. 1975, in *Muon Physics, Volume II: Weak Interactions*, ed. H. V.W. & C. Wu (Academic Press, New York), 114
- Wanajo, S. 2006, *ApJ* , 647, 1323
- Wanajo, S., Janka, H.-T., & Kubono, S. 2011, *ApJ* , 729, 46

-
- Wanajo, S., Müller, B., Janka, H.-T., & Heger, A. 2018, *ApJ* , 852, 40
- Wang, M., Audi, G., Kondev, F. G., et al. 2014, *Nuclear Data Sheets*, 120, 6
- Ward, R. A., & Newman, M. J. 1978, *ApJ* , 219, 195
- Wasserburg, G. J., Busso, M., Gallino, R., & Nollett, K. M. 2006, *Nuclear Physics A*, 777, 5
- Weaver, T. A., & Woosley, S. E. 1993, *Phys. Rep.*, 227, 65
- Weaver, T. A., Zimmerman, G. B., & Woosley, S. E. 1978, *ApJ* , 225, 1021
- Weber, C., Elomaa, V.-V., Ferrer, R., et al. 2008, *Phys. Rev. C* , 78, 054310
- Weinberg, S. 1996, *The Quantum Theory of Fields* (Cambridge University Press), 511
- Winteler, C., Käppeli, R., Perego, A., et al. 2012, *ApJ* , 750, L22
- Wisshak, K., Voss, F., Arlandini, C., et al. 2018, *Progress in Particle and Nuclear Physics*, 98, 55
- Wongwathanarat, A., Janka, H.-T., Müller, E., Pllumbi, E., & Wanajo, S. 2017, *ApJ* , 842, 13
- Woosley, S. E. 1977, *Nature* , 269, 42
- Woosley, S. E., Hartmann, D., & Pinto, P. A. 1989, *ApJ* , 346, 395
- Woosley, S. E., Hartmann, D. H., Hoffman, R. D., & Haxton, W. C. 1990, *Astrophys. J.*, 356, 272
- Woosley, S. E., & Heger, A. 2007, *Phys. Rep.*, 442, 269
- . 2015a, *ApJ* , 810, 34
- . 2015b, *ApJ* , 806, 145
- Woosley, S. E., Heger, A., & Weaver, T. A. 2002, *Rev. Mod. Phys.*, 74, 1015
- Woosley, S. E., & Weaver, T. A. 1986, *ARA&A* , 24, 205
- . 1995, *ApJS* , 101, 181
- Woosley, S. E., Wilson, J. R., Mathews, G. J., Hoffman, R. D., & Meyer, B. S. 1994, *Astrophys. J.*, 433, 229
- Wu, M.-R., Duan, H., & Qian, Y.-Z. 2016, *Physics Letters B*, 752, 89
- Wu, M.-R., Qian, Y.-Z., Martínez-Pinedo, G., Fischer, T., & Huther, L. 2015, *Phys. Rev. D*, 91, 065016
- Xia, J. W., Zhan, W. L., Wei, B. W., et al. 2002, *Nuclear Instruments and Methods in Physics Research A*, 488, 11
- Xing, Y. M., Li, K. A., Zhang, Y. H., et al. 2018, *Physics Letters B*, 781, 358
- Yoshida, T., Kajino, T., & Hartmann, D. H. 2005, *Phys. Rev. Lett.*, 94, 231101
- Yoshida, T., Kajino, T., Yokomakura, H., et al. 2006, *ApJ* , 649, 319
- Young, P. A., & Fryer, C. L. 2007, *ApJ* , 664, 1033
- Zegers, R. G. T., Akimune, H., Austin, S. M., et al. 2006, *Phys. Rev. C*, 74, 024309
- Zinner, E. 1998, *Annual Review of Earth and Planetary Sciences*, 26, 147
- Zinner, N. 2007, PhD thesis, University of Aarhus



Acknowledgements

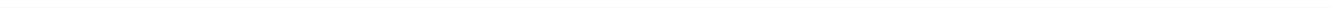
First of all I would like to thank Gabriel Martínez Pinedo as advisor of my Ph.D. project for giving me the opportunity to work on this topic at TU Darmstadt and GSI. He has always had an open ear for my questions and generously shared his immense knowledge on all aspects of neutrino interactions in supernovae. Furthermore, I would like to express my gratitude to Karlheinz Langanke, who has despite an enormous workload and huge responsibilities always found the time for regular committee meetings to discuss interesting physics. As members of the examination committee, I also need to thank Thomas Aumann and Barbara Drossel for taking the time during the busy conference and vacation season.

Special thanks also goes to Lutz Huther, who has initiated this project with his own Ph.D. project and taught me all I needed to get started in the beginning — He is responsible for me using Vim. People change offices a lot and so I can thank the whole working for being friendly office mates. With their experience and live examples Lutz, Andreas, Heiko, Samuel, Gang, and Alexander were able to show me the way. Special thanks goes to Heiko and Alexander for their extensive lessons on the secrets of professional cycling and to Andreas for heated political discussions. Samuel's charming modesty and enthusiastic liveliness have made him a dear partner in and outside the office. I have to thank Meng-Ru for many interesting discussions and a live-saving support on my first trip to China. With his amazing sense of humor Dag has made me smile even in the worst hours of writing and I am thankful to Stylianos for sharing his enthusiasm and BoWen for his questions. Furthermore, I would like to thank Kevin for interesting discussions about astrophysics and also Bastian who is always in a good mood.

I am also indebted to Alexander Heger, who has hosted me for one month in Melbourne and provided access to the monumental KEPLER code and his progenitor models. For my Ph.D. project and also for future work I have received data from many people. I am indebted to Austin Harris and Raphael Hix for the 2D simulation data and to Hans-Thomas Janka and Robert Bollig for the neutrino data. On my travels to conferences, schools and workshop I have enjoyed the company of many people. A special connection remains with Projjwal Banerjee, who is sharing my interest in neutrino nucleosynthesis. None of this would have been possible without the administrative and technical infrastructure of TU Darmstadt and GSI. In particular I would like to express my gratitude towards Genette Kluckner, Carina Seeger, Gabriele Menge and Marco Brunken.

Beyond the working environment, I also have to thank my family and friends at home for their support in spite of my persistent absence. Finally, my greatest gratitude goes to my wife for providing ample distraction, loving care and the world's best food for the long working hours.

Thank you all!



Curriculum Vitae

Andre Sieverding

Contact

GSI Helmholtz Centre for Heavy Ion Research, Planckstraße 1

64291 Darmstadt, Germany

a.sieverding@gsi.de

+49-6159-71 2744

Personal data

- *Date of birth:* 13.12.1988
- *Place of birth:* Heppenheim
- *Citizenship:* German

Education

PhD. in Nuclear Astrophysics

- *Since 2014:* Technische Universität Darmstadt
- *Title:* Neutrinos in Core-Collapse Supernova Nucleosynthesis
- *Advisors:* Prof. Dr. Martínez-Pinedo and Prof. Karlheinz Langanke

B.Sc. and M.Sc. in Physics

- *2009–2014:* Technische Universität Darmstadt, Germany
- *M.Sc. Thesis on:* Neutrino Nucleosynthesis in the outer layers of Supernovae
- *B.Sc. Thesis on:* Structure of White Dwarfs and Neutron Stars
 - Supervisor *Prof. Dr. Martínez-Pinedo*



Erklärung zur Dissertation

Hiermit versichere ich, die vorliegende Dissertation ohne Hilfe Dritter nur mit den angegebenen Quellen und Hilfsmitteln angefertigt zu haben. Alle Stellen, die aus Quellen entnommen wurden, sind als solche kenntlich gemacht. Diese Arbeit hat in gleicher oder ähnlicher Form noch keiner Prüfungsbehörde vorgelegen.

Darmstadt, den July 12, 2018

(Andre Sieverding)